PLASMA SPECTROSCOPY OF HIGHLY CHARGED IONS BY THE METHOD OF COLLISIONAL-RADIATIVE MODEL

Tetsuya Kawachi

Department of Engineering Science

Kyoto University

1995

Preface

So it goes

This thesis is the summary of my study of plasma spectroscopy for six years in Kyoto university. During these years, I studied under professor Fujimoto, and I could promote the better understanding about not only the spectroscopic study but also the style of the study, "How to reach the essence of nature."

From now on, I should struggle to establish the identity and originality as an physist or scientist, though it may be a rocky road.

This thesis means the starting point.

Tetsuya Kawachi

Feb. 1995 at Kyoto

The present thesis is based on the contents of the following papers :

I **"Collisional-Radiative Model for Lithium-like Ions in Plasma"**
T Kawachi, T Fujimoto and G Csanak,*Phys. Rev. E* (1995) (in press)

II **"Population Kinetics in Lithium-like Ions in Plasma"**
T Kawachi and T Fujimoto,*Phys. Rev. E* (1995) (in press)

III **"I*n Situ* Sensitivity Calibration of Xuv Spectrometer for Plasma Spectroscopy: Branching Ratio Method and Collsional-Radiative Model**
T Kawachi, H Suemitsu, K Sawada, T Fujimoto, T Maehara, S Yoshimura, T Maekawa, and Y Terumichi, *Rev, Sci, Inst* (1995) (in press)

IV **"Effect from Enhancement of Excitation Process on the Excited Level Population in High Dense Plasma"**
T Kawachi and T Fujimoto (to be published in J. Phys. B.)

V **"Observation of the Polarization of the Soft X-Ray Laser Line in Neon-Like Germanium Ions"**
T Kawachi, K Murai, G Yuan, S Ninomiya, R Kodama, H Daido, Y Kato and T Fujimoto, *Phys. Rev. Lett* (submitted)

VI **"Plasma Polarization Spectroscopy"**
T Fujimoto and T Kawachi
APS topical conference in San Antonio (1993)

VII **"Amplification Gain of the Lithium-like Aluminum Ions"**
T Fujimoto and T Kawachi
APS topical conference in San Antonio (1993)

CONTENTS

List of Symbols

$A(p,q)$: Einstein A coefficient from level p to level q.
A_a : Autoionization probability.
A_L : Longitudinal alignment.
A_r : Radiative decay probability from a doubly excited level.
a : Minor radius of the WT-3.
a_0 : Bohr radius.
$B(p,q)$: Rate coefficient from level p to level q.
$B'(p,q)$: Rate coefficient for creation of population imbalance from population in p.
$B''(p,q)$: Rate coefficient for creation of population imbalance in q from population imbalance in p.
$B'''(p,q)$: Correction term for the population imbalance in the fine-structure levels for the collisional-radiative model with fine-structure unresolved.
B_T : Toroidal magnetic field strength.
b : Impact parameter.
c : Light velocity in vacuum.
$C(p,q)$: Electron impact excitation rate coefficient from level p to level q.
$E(p)$: Energy of level p measured from the ground state.
$F(p,q)$: Electron impact deexcitation rate coefficient from level p to level q.
F : Total angular momentum of a Zeeman multiplet.
$f(p,q)$: Absorption oscillator strength for the transition from level p to level q.
G : Relaxation matrix.
G : Total angular momentum of a Zeeman multiplet.
$g(p)$: Statistical weight of level p.
$g_{/\!/}\ g_{\perp}$: Amplification gain for the parallel and perpendicular components of the polarized light, respectively.
$g_q(kk')$: Relaxation rate from rank k' to rank k.
$g_q^{kk'}(p, r)$: Relaxation rate from rank k' in p to rank k in r.
I : Nuclear spin angular momentum quantum number.
$I_{/\!/}\ I_{\perp}$: Intensity of the parallel and perpendicular components of the polarized light, respectively.
j : Total angular momentum quantum number.
k : Boltzmann constant.
k , q : Rank of a tensor operator and its z-component.
l : Orbital angular momentum quantum number.
M , m_j : Projection of J or F onto the quantization axis. (Azimuthal quantum number.)
M_{ion} : Mass of the ion.
N_p : Number of parturbers.
n : Principal quantum number.
n_e : Electron density.
$n(p)$: Population of the level p .
$n(nl)_M$: Population of the magnetic sublevel M of level nl .
n_{He} : Ground state density of helium-like ions.
n_{Li} : Ground state density of lithium-like ions.
n_{Be} : Ground state density of beryllium-like ions.
p^* : Effective principal quantum number. (Section IV. in Chapter II)
p_1, p_2 : Fine structure sublevels of level p.
p_B^* : Byron's boundary.
R : Major radius of the WT-3.
R_y : One Rydberg. (13.6eV)
$R_0(p)$: Population coefficient of level p for the recombining plasma component.
$R_1(p)$: Population coefficient of level p for the ionizing plasma component.
$r_1(p)$: Reduced population coefficient of level p for the ionizing plasma component.
$r_d(p, nl)$: Dielectronic capture rate coefficient into level (p, nl).
S : Collision S-matrix.
$S(p)$: Electron impact ionization rate coefficient from level p .
S_{CR} : Collisional-radiative ionization rate coefficient.
S_{eff} : Effective ionization rate coefficient.
$S_{/\!/}\ S_{\perp}$: Relative transmittance of the HIREFS spectrometer for the parallel and perpendicular components of the polarized light, respectively
T_e : Electron temperature.
T_{et}, T_{ep} : Electron temperature in the toroidal and poloidal directions, respectively.
$T(F,G)_{kq}$: Irreducible tensor operator with rank k.
$V(p)$: Electron impact j-changing rate coefficient of level p .
v_a : Velocity of the orbital electron of the initial level.
v_{tor}, v_{pol} : Electron velocity in the toroidal and poloidal directions, respectively.
$X_{eff}(p)$: Effective excitation rate coefficient into level p.
z : Nuclear charge.
z_{eff} : Effective nuclear charge.
z_{col} : Nuclear charge of the colliding ions.

α_{CR} : Collisional-radiative recombination rate coefficient.

α_{eff} : Effective recombination rate coefficient.

$\alpha(p)$: Three body recombination rate coefficient into level p .

β : Population ratio of the $2p^2P$ level to the ground state of the lithium-like ions.

$\beta(p)$: Radiative recombination rate coefficient into level p .

$\Gamma(a)$: Γ-function.

$\gamma(p)$: Dielectronic recombination rate coefficient into level p .

η : Reduced electron density.

Θ : Reduced electron temperature.

Θ_{IB} : Optimum temperature.

λ : Wavelength of a spectral line.

$\mu(p)$: Population imbalance in level p .

Π, Π' : Super operator and intermediate super operator. (Vector in the Liouville space.)

ρ : Density Operator.

$\rho^k{}_q(F,G)$: Irreducible component of the density matrix (State multipole).

σ : Excitation cross section.

$|\psi\rangle$: Wave function or state vector.

$\omega(p)$: Population of level p divided by its statistical weight.

CHAPTER I.

General Introduction

Plasma spectroscopy has been one of the powerful techniques in diagnosing plasmas of various kinds, laboratory and astrophysical. Atoms and ions in a plasma emit optical radiation in the form of spectral lines and continuum. Their intensities and spectral profiles, and spatial distributions of these characteristics reflect the state of the atoms and ions and its spatial variation, and therefore contain information of the plasma acting as the environment of these atoms and ions. It is thus possible and is our objective to investigate from spectral observations various attributes of the plasma, *e.g.*, electron temperature and density, spatial distribution of atoms and ions in it and thus the particle transport. For this reason, plasma spectroscopy has played an important role in plasma research. With the recent progress in producing and controlling high temperature plasmas, especially magnetically confined plasmas and laser-produced plasmas, the importance of highly charged ions is increasing in plasma spectroscopy.

In actual experiments and observations, the number of quantities directly measured is rather small, and sometimes experimental uncertainties are large. In order to accomplish our objective under these conditions and, more importantly, in order to construct a general perspective of our plasma, we have to have a model with which we can deduce, estimate or infer the properties of the plasma under study. The collisional-radiative model is the most important tool in combining the spectroscopic observations and the properties of the plasma, and is indispensable in quantitative plasma spectroscopy.

The collisional-radiative (CR) model was first proposed for atomic hydrogen to account for the experimentally observed rate of recombination of protons in plasma. [1-3] It was then recognized that it is also suitable to describe the excited-level populations and the effective ionization rate. It is now generally accepted that, when we treat atoms and ions in a plasma having a finite density, we have to rely on a CR model. By improving the cross section data in the code, the CR model of hydrogen has been highly refined. [4] Helium and neutral and singly ionized argon have also been treated by the respective CR models. [5-7] For highly charged ions, however, CR model treatment has been rather scanty except for hydrogen-like and helium-like ions. [8, 9] Recently, neon-like germanium in the ionizing plasma phase and lithium-like aluminum in the recombining plasma have been treated in relation to the x-ray laser amplifications. [10, 11] In order to expand the variety of plasmas and the range of plasma parameters, especially of temperature, which we can treat, we have to have reliable CR models for various ions which may be present in these plasmas. In this respect, scaling properties are useful for CR models of ions in an isoelectronic sequence.

With the progress in the techniques of producing, heating and controlling plasmas, it is becoming clear that the plasmas under current investigations have sometimes nonthermal properties, *e.g.*, a non-Maxwellian velocity distribution of plasma electrons. Furthermore, it should be noted that these plasmas are almost always necessarily anisotropic. Neutral beam injection creates highly anisotropic situation, too. These characteristics of the plasmas endow plasma spectroscopy with another importance, *i.e.*, the importance of observing polarization. In these plasmas, excited atoms and ions may be polarized, aligned in the case of one directional excitation. The emitted radiation from these atoms and ions are polarized, linearly polarized in the above example. Until now, however, polarization properties of radiation emitted from plasma have called little attention in plasma spectroscopy experiment except for the pioneering investigations made mainly by Russian researchers. [12-14] In view of the present situation of the magnetically confined plasmas and the laser-produced plasmas, spectroscopic studies in which emphasis is placed on the polarization properties of radiation appear quite promising. This new dimension of spectroscopy may be called Plasma Polarization Spectroscopy (PPS). These studies would give information concerning primarily anisotropic and therefore non-thermal properties of the plasma.

In this study, I construct a collisional-radiative model for lithium-like ions. The background of this attempt is: 1) We have already reliable CR models for hydrogenic and helium-like ions. [4, 8] It would be natural to extend our study to lithium-like ions. 2) These ions are common impurity ions in tokamak plasmas or serve as the x-ray laser media in laser-produced plasmas. In **Chapter II**, I describe the details of the formulation of this model, the atomic parameters which I employ, the validity and uncertainty of this model and the comparison with the experimental results.

I apply this CR model to the analysis of the xuv spectra of lithium-like oxygen and carbon ions observed in the WT-3 tokamak in Kyoto University. The experimental apparatus is described in **chapter III**. In **chapter IV**, from the comparison of the photoelectron count ratios of these xuv spectra with the expected values from our CR model, I calibrate absolutely the sensitivity of our xuv spectrometer. Furthermore, by observing the spectra from the edge (Scrape-off) plasma, the rate coefficients of the charge exchange recombination between the helium-like ions and the neutral hydrogen atoms or molecules are estimated.

In **Chapter V**, the anisotropic characteristics of plasmas and polarization of emitted radiation are treated. I assume that the plasma is axially symmetric, and we show the formulation of the polarization (or alignment) CR model on this assumption. As an example, I conduct a preliminary experiment on the WT-3 tokamak, and observe polarization of the emission lines from beryllium-like oxygen (OV) ions. I make simplified alignment CR model for these ions, and calculate the alignment for the above lines on the assumption of several electron velocity distributions.

In **Chapter VI**, the measurement of the polarization of the x-ray laser line from the laser-produced plasma is reported. This work has been done in collaboration with the x-ray laser group in *ILE* (Institute of Laser Engineering) of Osaka University.

References

[1] D.R. Bates, A.E. Kingstone, and R.W.P. McWhirter, *Proc.R.Soc. London* **267**, 297 (1962)

[2] D.R. Bates, A.E. Kingstone, *Planet. Space Sci.* **11**,1 (1963)

[3] R.W.P. McWhirter and A.G. Hearn, *Proc. Phys. Soc.* **82**, 641 (1963)

[4] T. Fujimoto, *J. Phys. Soc. Jpn*, **47**, 265 (1979); **47**, 273 (1979); **49**, 1561 (1980); **49**, 1569 (1980), **54**, 2905 (1985)

[5] T. Fujimoto, *J. Quant. Spectrosc. Radiative Transfer*, **21**, 439 (1979)

[6] J. Vlcék and V. Pelikán, *J. Phys. D*, **19**, 1879 (1986)

[7] T. Fujimoto, *Jpn. J. Appl. Phys.* **11**, 1501 (1972)

[8] N. N. Ljepojevic, R.J. Hutcheon and R. W. P. McWhirter, *J. Phys. B* **17**, 3057 (1984)

[9] T. Fujimoto and T. Kato, *Phys. Rev. A* **30**, 379 (1984)

[10] A. Klisnick, A. Sureau, H. Guennou, C. Moller and J. Virmont, *Appl. Phys.* **B50**. 153 (1990)

[11] P.B. Holden, S.B. Healy, M.T.M. Lightbody, G.J. Pert, J.A. Plowes, A.E. Kingston, E. Robertson, C.L.S. Lewis and D. Neely, *J. Phys. B* **27**, 341 (1994)

[12]. S.A. Kazantev, A.G. Petrashen, N.T. Polezhaeva, V.N. Rebane and T.K. Rebane, *Opt. Spectrosc.* (USSR) **68**, 544 (1990)

[13]. S.A. Kazantev, A.G. Petrashen, N.T. Polezhaeva, V.N. Rebane, *Opt. Spectrosc.* (USSR) **68**, 740 (1990)

[14]. A.G. Petrashen, V.N. Rebane and T.K. Rebane, *Opt. Spectrosc.* (USSR) **58**, 481 (1985)

CHAPTER II.

Collisional-Radiative Model for Lithium-Like Ions in Plasma

Abstract We have constructed a collisional radiative model for lithium-like ions. For low-lying levels with principal quantum number $n \leq 5$, different l -levels are treated separately and the fine structure is taken into account. Electron impact excitation cross section of oxygen ion (OVI) is calculated for virtually all the transitions among the $n \leq 5$ levels and it is scaled for other elements. We calculate populations of excited levels of lithium-like ions (oxygen and aluminum) both for the ionizing plasma and the recombining plasma under appropriate plasma conditions. For both the plasmas, characteristics of the population distribution over the excited levels and the population kinetics are examined in detail. In the high-density region, a simple approximate distribution function is derived for both the plasmas on the basis of the multistep ladderlike excitation or deexcitation mechanism, combined with the thermodynamic equilibrium distribution. As examples of applications, we present intensity ratios of emission lines from impurity ions in tokamaks, and the population inversion and gain for x-ray laser of the recombining plasma. We also calculate the effective excitation and ionization rate coefficients, and they are compared with experimental results available.

I. INTRODUCTION

Population distribution among excited atoms and ions in a plasma reflects the nature of the plasma concerned, and is the subject of plasma spectroscopy through observation of the spectral emission from these atoms and ions. A wide variety of population characteristics, *e.g.*, thermodynamic equilibrium and population inversion, could be realized depending on various collisional and radiative processes in the plasma. A comprehensive investigation of the characteristics of the population and its kinetics for hydrogen atoms and hydrogenic ions has been done several years ago [1]. It divides an excited level population into the ionizing plasma component and the recombining plasma component, and then proposes a classification scheme of the population distribution into several categories: the corona phase and the ladderlike excitation-ionization phase for ionizing plasma and the capture-radiative-cascade phase, LTE phase and the ladderlike deexcitation phase for the recombining plasma. Depending on the particular condition of the plasma in question one, two or even more than two of these phases would manifest itself in the observed spectrum.

The above treatment, however, is rather limited in several respects. The first is the energy level structure of hydrogen. The ionization potential of the ground state is four times larger than that of the first excited level, or the ground state potential is rather "deep". This feature is shared by helium-like ions, which have an even deeper ground state, but is rather exceptional for many atomic and ionic species which have "shallow" potentials. The second is: the s, p, d, ... levels, or different-l levels, are bundled together, or they are assumed to be populated according to their statistical weights. This assumption obviously breaks down in low density plasmas in which collisional population mixing among these levels are slower than radiative decay. It is even not entirely clear whether this assumption is valid in high density ionizing plasmas, since they are not equlibrium in nature. In view of these limitations and questions, it was decided to extend the investigation of the population characteristics to atoms and ions having a rather "shallow" potential and with the above assumption removed.

Lithium-like ions have the next simpler energy level structure to hydrogen. Furthermore, the importance of these ions in plasma research is increasing now. In tokamak plasmas, for example, prominent impurity lines are emitted by lithium-like ions of oxygen, carbon and other elements, and in laser produced plasmas, an x-ray laser based on the recombining lithium-like ion scheme is being extensively studied. Determination of the absolute density of these ions

for the purpose of studying their transport for the former plasma and evaluation of the population inversion and gain for the latter plasma are subjects of plasma spectroscopy.

For the above purposes, a reliable collisional-radiative (CR) model for lithium-like ions is indispensable. Klisnick *et al.* [2] first constructed a CR model for these ions. The cross section data in their model, however, are rather unsophisticated and the model has been applied only to the low temperature recombining plasma.

In this chapter, the details of our CR model are described. We summarize the atomic data we employ in section III. We investigate and discuss the population kinetics of lithium-like ions in section IV. As examples, we present the calculation results of the photon emission ratio of the dominant transitions for the carbon, nitrogen and oxygen ions in tokamak plasmas, and amplification gain for the recombining lithium-like aluminum ions. A comparison of the result of our CR model calculation with the available plasma experiments is made in section V. The validity range of our present model and uncertainties of the results are discussed in section VI.

II. COLLISIONAL-RADIATIVE MODEL

The population density of the ground and excited levels of ions in plasma is determined by various collisional and radiative atomic processes taking place in the plasma. For level p, the temporal development of its population $n(p)$ is expressed by the differential equation,

$$\begin{aligned}\frac{dn(p)}{dt} &= \sum_{q<p} C(q,p)n_e n(q) \\ &-\{[\sum_{q<p} F(p,q)+\sum_{q>p} C(p,q)]n_e+\sum_{q<p} A(p,q)\}n(p) \\ &+\sum_{q>p}[F(q,p)n_e+A(q,p)]n(q)-S(p)n_e n(p) \\ &+\{\alpha(p)n_e+\beta(p)+\gamma(p)]n_e n_{He} \qquad (1)\end{aligned}$$

which is coupled with similar equations for other levels. Here "$q < p$" means that level q lies energetically lower than level p. $A(p,q)$ is the spontaneous transition probability from p to q, $C(p,q)$, $F(q,p)$ and $S(p)$ are the rate coefficients for electron impact excitation, deexcitation, and ionization, respectively, and $\alpha(p)$, $\beta(p)$ and $\gamma(p)$ are the rate coefficients for three-body, radiative and

dielectronic recombination, respectively. n_e is electron density, and we express the ground state helium-like ion density as n_{He}. According to the method of the quasi steady state solution, the time derivative of the population of excited levels is put equal to 0, so that the set of coupled differential equations for excited levels reduces to a set of coupled linear equations. The solution is expressed as the sum of the two terms;

$$n(p)=R_0(p)n_e n_{He}+R_1(p)n_e n_{Li} \qquad (2)$$

where $R_0(p)$ and $R_1(p)$ are the population coefficients which are determined by the actual collisional and radiative processes and are functions of n_e and electron temperature T_e. The ground state lithium-like ion density *i.e.*, $n(2^2S)$, has been expressed as n_{Li}. The first term may be called the recombining plasma component and the second term is the ionizing plasma component [3].

We define an effective ionization rate coefficient (S_{eff}) and recombination rate coefficient (α_{eff}) as

$$S_{eff}=\frac{\sum_{p=1,2}\left[S(p)R_1(p)+\sum_{q\geq 3}C(p,q)R_1(p)-\sum_{q\geq 3}F(q,p)R_1(q)\right]}{[R_1(1)+R_1(2)]}$$

$$\alpha_{eff}=\sum_{p=1,2}\left[\alpha(p)n_e+\beta(p)+\gamma(p)+\sum_{q\geq 3}F(q,p)R_0(q)n_e\right] \qquad (3)$$

where p = 1 and 2 are understood to denote the ground state and the 2^2P level, respectively. $R_1(1)$ is put equal to 1. S_{eff} is different from the collisional-radiative rate coefficient S_{CR} defined for hydrogen by Bates *et al.* [3]. In S_{CR} the summation in the denominator of S_{eff} is replaced by $R_1(1)=1$. In the low density limit, S_{eff} becomes identical to S_{CR}.

A. Collisional-radiative model with fine structure unresolved

In the case of a CR model with fine structure unresolved, we assume that the fine structure sublevels belonging to a level are populated according to their statistical weights. Let p in eq.(1) represent the principal quantum number n and the angular momentum quantum number l, and $n(p)$ is the sum of the populations of the fine structure sublevels. Each of the rate coefficients in eq.(1) refers to level p or q, and is related to the rate coefficients for transitions connecting individual fine structure sublevels; *i.e.*, it is the average over the initial fine structure sublevels and the sum over the final sublevels.

$$B(p,q)=\frac{g(p_1)}{g(p)}\{B(p_1,q_1)+B(p_1,q_2)\}+\frac{g(p_2)}{g(p)}\{B(p_2,q_1)+B(p_2,q_2)\} \tag{4}$$

where $B(p,q)$ stands for $C(p,q)$, $A(p,q)$ or $F(p,q)$ and p and q denote the initial and final levels, respectively. Here p_1 and p_2 mean the fine structure sublevels with total angular momentum $j=l-1/2$ and $j=l+1/2$, respectively, and $g(p)$ is the statistical weight of level p. In the case of an S state, p_1 or q_1 term is absent. The ionization rate coefficient is defined as

$$S(p)=\frac{g(p_1)}{g(p)}S(p_1)+\frac{g(p_2)}{g(p)}S(p_2) \tag{5a}$$

and the recombination rate coefficient is defined as

$$\alpha(p)=\alpha(p_1)+\alpha(p_2) \tag{5b}$$

for $\alpha(p)$ and similarly for $\beta(p)$ or $\gamma(p)$.

B. Collisional-radiative model with fine structure resolved

When the nuclear charge z is large, the energy splittings between the fine structure sublevels are substantial for low lying levels. At the same time, the individual rate coefficients in the right hand side of eq.(4) deviate from those expected from the pure L-S coupling scheme, and a population imbalance may develop in these levels. We introduce a quantity $\mu(p)$ which describes the population imbalance.

$$\mu(p)=\omega_1-\omega_2 \tag{6a}$$

with

$$\omega_1=\frac{n(p_1)}{g(p_1)},\quad \omega_2=\frac{n(p_2)}{g(p_2)} \tag{6b}$$

In the extreme case that only level p_1 is populated with no population in level p_2, the quantity μ reduces to ω_1, and in the opposite case, μ is equal to $-\omega_2$. In the case that the populations are distributed according to the statistical weights, μ is 0.

The quantity μ is described by the coupled equation,

$$\begin{aligned}\frac{d\mu(p)}{dt}=&[\sum_{q<p}C'(q,p)n_e+\sum_{q>p}\{F'(q,p)n_e+A'(q,p)\}]n(q)\\&-[\sum_{q<p}\{F''(p,q)n_e+A''(p,q)\}+\sum_{q>p}C''(p,q)n_e+S''(p)n_e]n(p)\\&+[\sum_{q<p}K(q,p)n_e+\sum_{q>p}\{M(q,p)n_e+U(q,p)\}]\mu(q)\\&-[\sum_{q<p}\{M(p,q)n_e+U(p,q)\}+\{\sum_{q>p}K(p,q)+I(p)+V(p)\}n_e]\mu(p)\\&+\{\alpha'(p)n_e+\beta'(p)+\gamma'(p)\}n_e n_{He}\end{aligned} \tag{7}$$

where $C'(q,p)$, $F'(q,p)$, $A'(q,p)$ are the imbalance creation rate coefficients in level p from population of another level q by collisional excitation, deexcitation, and radiative decay, respectively, and they are defined as follows;

$$B'(q,p)=\frac{g(q_1)}{g(q)}\{\frac{B(q_1,p_1)}{g(p_1)}-\frac{B(q_1,p_2)}{g(p_2)}\}+\frac{g(q_2)}{g(q)}\{\frac{B(q_2,p_1)}{g(p_1)}-\frac{B(q_2,p_2)}{g(p_2)}\} \tag{8}$$

and $C''(q,p)$, $F''(q,p)$, $A''(q,p)$ are the rate coefficients for imbalance destruction or creation in level p by depopulation, and they are defined as;

$$B''(p,q)=\frac{1}{g(p)}\{B(p_1,q_1)+B(p_1,q_2)-B(p_2,q_1)-B(p_2,q_2)\} \tag{9}$$

and

$$S''(p)=\frac{1}{g(p)}(S(p_1)-S(p_2)) \tag{9 a}$$

$K(q,p)$, $M(q,p)$, $U(q,p)$ are the imbalance transfer rate coefficients from level q to p by excitation, deexcitation and radiative decay, respectively,

$$B(q,p)=\frac{g(q_1)g(q_2)}{g(q)}\{\frac{B(q_1,p_1)}{g(p_1)}-\frac{B(q_1,p_2)}{g(p_2)}-\frac{B(q_2,p_1)}{g(p_2)}+\frac{B(q_2,p_2)}{g(p_2)}\} \tag{10}$$

The imbalance in p is decreased by the depopulation processes

$$B(p,q)=\frac{g(p_1)g(p_2)}{g(p)}\{\frac{B(p_1,q_1)}{g(p_1)}+\frac{B(p_1,q_2)}{g(p_1)}+\frac{B(p_2,q_1)}{g(p_2)}+\frac{B(p_2,q_2)}{g(p_2)}\} \tag{11}$$

$I(p)$ is the imbalance destruction rate coefficient by ionization, and $\alpha'(p)$, $\beta'(p)$ and $\gamma'(p)$ are the imbalance creation rate coefficients by recombination. These rate coefficients are defined as,

$$I(p)=\frac{g(p_1)g(p_2)}{g(p)}\left(\frac{S(p_1)}{g(p_1)}+\frac{S(p_2)}{g(p_2)}\right)$$
$$\alpha'(p)=\left(\frac{\alpha(p_1)}{g(p_1)}-\frac{\alpha(p_2)}{g(p_2)}\right) \qquad (12)$$

$\beta'(p)$, $\gamma'(p)$ are defined similarly to $\alpha'(p)$. $V(p)$ is the collisional j-changing rate coefficient between the fine-structure sublevels of level p.

According to the spirit of the CR model, the time derivative of the population imbalance is put equal to 0. This quantity is described, with the help of eq.(2), as

$$\mu(p)=\rho_0(p)\,n_e\,n_{1Be}+\rho_1(p)\,n_e\,n_{Li} \qquad (13)$$

When the population imbalance is different from zero, the treatment presented in the preceding subsection becomes inadequate, and correction terms are added to the right hand side of eq.(1),

$$\frac{dn(p)}{dt}=\sum_{q<p}C(q,p)n_e n(q)-\sum_{q<p}[F(p,q)n_e+A(p,q)]n(p)$$
$$-\sum_{p<q}C(p,q)n_e n(p)+\sum_{p<q}[F(q,p)n_e+A(q,p)]n(q)$$
$$-S(p)n_e n(p)+(\alpha(p)n_e+\beta(p)+\gamma(p))n_e n_{He}$$
$$+\sum_{q<p}C'''(q,p)n_e\mu(q)-\sum_{q<p}[F'''(p,q)n_e+A'''(p,q)]\mu(p)$$
$$-\sum_{p<q}C'''(p,q)n_e\mu(p)+\sum_{p<q}[F'''(q,p)n_e+A'''(q,p)]\mu(q)$$
$$-S'''(p)\mu(p) \qquad (14)$$

Triple primed terms are the correction terms due to the imbalance of the populations of other excited levels, and the rate coefficients are defined as,

$$B'''(p,q)=[B(p_1,q_1)+B(p_1,q_2)+B(p_2,q_1)+B(p_2,q_2)] \qquad (15)$$

This iterative procedure may be repeated further.

III. ATOMIC PROCESSES

In this section, a detailed account is given of the atomic data employed in our calculation. We use two kinds of notations to describe the levels; n^2L refers to a level with fine structure unresolved, and $nl^2L_{l\pm1/2}$ refers to the fine structure sublevels.

In our calculation code, we use fitting formulae for atomic parameters and rate coefficients for collisional processes. These formulae are described in appendix A.

A. Energy level

Figure 1 shows the energy level diagram of the OVI ion taken as an example. We consider excited levels as high as $n = 40$. The levels for $n \le 5$ are treated separately according to their angular momentum quantum number, and we may include the fine structure for these levels. For the CR model with fine structure unresolved, we define the level energy by taking the weighted average of the energies of the fine structure sublevels with their statistical weights. All the higher lying levels of $n \ge 6$ are treated as hydrogenic and the populations of different-l levels are assumed to be distributed according to their statistical weights; validity of these approximations will be discussed later.

The ionization potential of the ground state and the transition energy from the ground state to $2p^2P_{1/2}$, $2p^2P_{3/2}$ and $3p^2P_{1/2}$ are taken from Zhang *et al.* [4] and shown in Fig.2 against the effective nuclear charge z_{eff}, which is the nuclear charge z subtracted by 2. It is seen that the ionization potential of these low-lying levels has an approximately z_{eff}^2 dependence, whereas the transition energies from the ground state to $2p^2P_{1/2}$ and $2p^2P_{3/2}$ have a z_{eff}^{+1} dependence for $z < 15$. (See Appendix A-I and Table A-1.)

B. Oscillator strength

Absorption oscillator strength is given by Lindgard and Nielsen [5], by Zhang *et al.* [4] and in the compilation by Wiese [6]. We use the data by Zhang *et al.* for the transitions from the ground state and the $2p^2P_{1/2,3/2}$ levels, and we use the data by Lindgard and Nielsen for transitions from $n = 3$, 4 and 5 levels. Figure 3 shows examples of the oscillator strengths for transitions $2s^2S_{1/2}$-$2p^2P_{1/2}$, -$2p^2P_{3/2}$, -$3p^2P_{1/2}$, -$3p^2P_{3/2}$ and $2p^2P_{1/2}$-$3s^2S_{1/2}$, $2p^2P_{3/2}$-$3s^2S_{1/2}$. A large deviation of the $2s^2S_{1/2}$-$2p^2P_{3/2}$ oscillator strength from the z^{-1} dependence in the range of $z > 20$ is due to the relativistic effects. (See Fig.2.) This suggests that the population of $2p^2P_{1/2}$ and $2p^2P_{3/2}$ may deviate substantially from their statistical weights under certain conditions.

We include an optically forbidden transition, $2p^2P_{1/2}$-$2p^2P_{3/2}$. (See Appendix A-II and Table A-2, 3 and 4.)

C. Excitation cross section

For transitions $2s^2S_{1/2}$-$2p^2P_{1/2,3/2}$, $2s^2S_{1/2}$-$3p^2P_{1/2,3/2}$ and $2s^2S_{1/2}$-$3s^2S_{1/2}$, there are many theoretical, experimental and semi-empirical cross section data [4,7-12]. Comprehensive data for oxygen to uranium are given by Zhang *et al.* [4] who treat the fine structure sublevels separately. For transitions between excited levels or between the ground state and highly excited levels, however, there are few published data. We have calculated cross sections for virtually all the transitions among the levels from $2s^2S_{1/2}$ to $5g^2G_{7/2,9/2}$ for OVI ion taken as an example. These cross section data are referred to as Clark, Abdallah and Csanak (C,A,C), and details of the calculation method is given in [13].

Figure 4 (a) and (b) shows excitation cross section of 2^2S-3^2P and 2^2P-3^2S of OVI, respectively (optically allowed transitions). Here the fine-structure resolved data ([4] and C,A,C) have been reduced by eq.(4) to the unresolved data shown. The results by Zhang *et al.* [4] and C,A,C are in good agreement. In the high energy range, the hydrogenic approximation by Clark *et al.* [12] for 2^2S-3^2P is larger by a factor 1.5 than the result by Zhang *et al.* and for 2^2P-3^2S, smaller by a factor 2.5. These differences may be attributed to the oscillator strength values of hydrogenic 2^2S-3^2P and 2^2P-3^2S transitions which are larger and smaller than those of OVI approximately by those amounts, respectively. (See Fig.3)

For other lithium like ions with nuclear charge z, we use Zhang's cross section data for the transitions from the ground state and from $2p^2P_{1/2,3/2}$. For other transitions among the $n \le 5$ levels, we assume the following scaling formula,

$$\sigma(E/E_{\rm th})=\sigma_{\rm oxygen}(E/E_{\rm th})\left(\frac{z-s}{8-s}\right)^{-4}\frac{f_z}{f_{\rm oxygen}} \qquad (16\ a)$$

where $\sigma_{\rm oxygen}$ refers to the C,A,C cross section expressed in the threshold units $E/E_{\rm th}$, s is the screening constant given by Mayer [14] for the lower level, and f_z is the absorption oscillator strength for ion z.

Figure 5 shows 2^2S-3^2S cross section (optically forbidden transition). All the cross sections agree well. For other z ions, we scale the data by Zhang *et al.* and by C,A,C in the similar way to the optically allowed transition,

$$\sigma(E/E_{\rm th})=\sigma_{\rm oxygen}(E/E_{\rm th})\left(\frac{Z-s}{8-s}\right)^{-4} \qquad (16\ b)$$

For transitions from $n \le 5$ levels to $n \ge 6$ levels, we scale these excitation cross sections by threshold energies and their absorption oscillator strengths. For transitions between the excited levels whose principal quantum number is $n \ge 6$, we assume these to be hydrogenic and choose the semi-empirical cross section by Vriens and Smeets [15].

Figure 6 (a) and (b) shows 3^2S-3^2P and 3^2P-3^2D excitation cross sections, respectively, taken as examples of the l-changing transitions. Results by C,A,C, Sampson and Parks [16] and semi-empirical results by Jacobs and Davis [17] agree well. In these figures also given is that calculated from the formula derived by Dickinson [18] for Rydberg states of neutral carbon and generalized by Fujima [19] to other transitions. In Fig 6(b), the discontinuity of the data by Dickinson-Fujima at E = 4~5 eV corresponds to the boundary between the non-sudden collision and sudden collision approximations. These low energy regions are unimportant in practical situations. In view of the good agreements even for these low-lying levels, we decide to use the latter formula for the l-changing transitions $l \leftrightarrow l+1$ between the levels with same n.

In many cases lithium-like ions are observed as an impurity in, say, a tokamak hydrogen plasma. In these cases, the electron temperature is too high for the l-changing process to be effective. (See Fig.6) Rather, proton or other ion collisions may become dominant. We take these collision process into our code when it is appropriate. In this case, we basically assume the velocity scaling for electron and ion collisions. For the case that the collision velocity v is larger than the threshold value $v_{\rm th,e}$, the cross section for the ions with z is given by

$$\sigma_z(v)=z_{\rm col}^2\sigma_{\rm e}(v) \qquad (17\ a)$$

where $z_{\rm col}$ is the effective nuclear charge of the projectile ion. For the case of $v \le v_{\rm th,e}$, we assume

$$\sigma_z(v)=z_{\rm col}^2\,\sigma_{\rm e}(v_{\rm th,e})\times\left(\frac{v}{v_{\rm th,e}}\right) \qquad (17\ b)$$

(See Appendix A-III, and Table A-5, 6, 7 and 8.)

D. Ionization cross section

Cross section is given by Sampson and co-workers [20-25] for ionization of 2^2S through 5^2G and by Kunc [26] for ionization of 2^2S, 2^2P and 3^2L levels. Hofmann

et al. [27] measured by a crossed beam technique the ionization cross section from the ground state including the processes *via* doubly and triply excited levels for lithium-like carbon, nitrogen, and oxygen ions. These cross sections are small compared with the direct ionization cross section, and we neglect these processes in our calculation. We use the hydrogenic approximation by Sampson and co-workers, which agree with the semi-empirical cross section by Lotz [28]. For $n \geq 6$ levels, we use the hydrogenic cross sections by Vriens and Smeets [15].

E. Recombination processes

Burgess [29] gives radiative recombination rate coefficient for hydrogenic ions and MacLaughlin and Hahn [30] modify the results to non-hydrogenic ions. In the case of the lithium-like ion, the free-bound oscillator strength of each level is rather close to that of hydrogen and we use the calculation by Burgess, which is in good agreement with the total radiative recombination rate coefficient measured by Andersen and Bolko. [31].

Dielectronic recombination is an important process in the high temperature region. This process proceeds by two-step processes; *i.e.*, electron capture into a doubly excited level (dielectronic capture), and a radiative decay which competes with autoionization. The electron capture rate coefficient r_d is associated with the autoionization probability A_a through the detailed balance,

$$[n_{He} n_e r_d(p, nl) = n_{Li}(p, nl) A_a]_E \tag{18}$$

where $n_{Li}(p,nl)$ is the density of the doubly excited lithium-like ions. Here $[\ ]_E$ means that this equality holds in thermodynamic equilibrium; *i.e.*, these densities are given by the Saha-Boltzmann relationship. Dielectronic recombination rate coefficient is given by,

$$\gamma(nl) = \sum_p r_d(p, nl) \frac{A_r}{A_r + A_a} \tag{19}$$

where A_r is the radiative decay probability. We consider $2pnl$ and $3pnl$ ($n \geq 2$) levels as the doubly excited levels, and we use the autoionization probability and radiative decay probability given by Bely and Dubau [32] for the OVI ion. For other z elements, we estimate the autoionization probability and the radiative decay probability by a scaling [33] from those of OVI. (See Appendix A-IV, and Table A-9.)

The three body recombination rate coefficient is given from the ionization rate coefficient from the principle of detailed balance.

IV. CALCULATION RESULT AND POPULATION KINETICS

By the collisional-radiative (CR) model we have calculated populations of excited levels of lithium-like ions (oxygen and aluminum) both for the ionizing plasma and the recombining plasma under appropriate plasma conditions. In many actual situations, excited level populations are given by the ionizing plasma component or the recombining plasma component. We therefore discuss these components separately.

A. Ionizing plasma

We take OVI ion as an example. Figure 7 shows the n_e-dependence of the population of some of the excited levels. The electron temperature T_e is assumed to be 50eV (Θ=1.4eV, $\Theta = T_e/(z\text{-}2)^2$ is the reduced temperature, where z is the nuclear charge.); this T_e corresponds to that of tokamak plasmas where the OVI ions in this ionization stage are present predominantly. Effect of proton collisions are included, where the ion temperature is assumed to be equal to T_e.

In the low density region of $n_e < 10^{20}\mathrm{m}^{-3}$ ($\eta < 10^{15}\mathrm{m}^{-3}$; η is the reduced or equivalent density for neutral isoelectronic species and is defined as $\eta = n_e/(z - 2)^7$), the populations of low-lying excited levels with $n \leq 10$ are proportional to n_e; these levels are in the corona phase as explained later, and the magnitude of the populations of the s, p, d,... levels per unit statistical weight is in the order s, p, d,... for the n = 3, 4 and 5 levels. For higher lying excited levels with $n > 10$, deviation from the linear relation has already taken place. In the region of $10^{21}\mathrm{m}^{-3} < n_e < 10^{25}\mathrm{m}^{-3}$ ($10^{16}\mathrm{m}^{-3} < \eta < 10^{20}\mathrm{m}^{-3}$), a deviation from the linear relation occurs for the low-lying levels. At the same time, the populations in the different-l levels tend to be proportional to their statistical weights. This is because the collisional transitions between neighboring excited levels having different-l and same n become substantial compared with the radiative transitions. In the high density region, $n_e > 10^{25}\mathrm{m}^{-3}$ ($\eta > 10^{20}\mathrm{m}^{-3}$), all the populations reach the high density limit values.

We examine the n_e-dependent populations shown in Fig.7 in more detail. We take 4^2P level as an example. Figure 8 (a) and (b) shows the magnitude of population flows into and out of the 4^2P level. For convenience, the population flow has been divided by electron density, and the values at the high density limit is given by numbers. In the low density region, the dominant flow into this level is the direct excitation from the ground state 2^2S, and a contribution

from cascade from higher-lying levels is about 20%. This value is typical for low density ionizing plasmas and Appendix B discusses this characteristic. The dominant flow out of 4^2P is the radiative decay, 80% of which is the transition to the ground state. This is consistent with the linear relationship in Fig.7 in this region and the nomenclature of the corona phase. At about $n_e = 10^{21}m^{-3}$ the contribution from the excitation from 2^2P begins to be substantial. At the same time, the l-changing transitions become substantial. These additional contributions result in the slight upward deviation of the population from the linear relation in Fig.7. In $n_e > 10^{21}m^{-3}$, the population of the 2^2P level becomes almost equal to or even larger than that of the 2^2S state. (Remember that the population in Fig.7 has been divided by the statistical weight; $g(2^2S) = 2$, $g(2^2P) = 6$.) The population flow from 2^2P into 4^2P becomes larger than that from the ground state 2^2S. In such a situation, the 2^2S and the 2^2P levels altogether may be regarded as the ground level.

In the higher density region $n_e > 10^{21}m^{-3}$, the dominant flows both into and out of 4^2P are l-changing collisions $4^2S \leftrightarrow 4^2P$ and $4^2P \leftrightarrow 4^2D$.. It might be assumed that, at the high density limit, the populations of 4^2S, 4^2P, 4^2D and 4^2F are in thermodynamic equilibrium, or almost equivalently determined by their statistical weights. We look at Figure 8 (a) and (b) carefully; the population flow from 4^2S to 4^2P is larger than the inverse flow by 4% and the flow from 4^2P to 4^2D is larger than the inverse flow by 3%. This means that there exists a small but substantial net 'upward' flow of $4^2S \Rightarrow 4^2P \Rightarrow 4^2D \Rightarrow 4^2F$. This may be called the generalized ladder-like excitation-ionization established among the different-l levels in the same n. Figure 8 shows that the magnitude of the population flows of $n = 3 \rightarrow n = 4$ and $n = 4 \rightarrow n = 5$ is about one order of magnitude smaller than the individual l-changing flow, but is larger than the net l-changing flow or the generalized ladder-like excitation-ionization flow. Strictly speaking, therefore, these different-l levels would never be in thermal equilibrium each other. Figure 9 shows the population distribution at the high density limit or $n_e = 10^{26}m^{-3}$. Abscissa is the effective principal quantum number p^* of the levels in a logarithmic scale. Ordinate is the normalized population coefficient $r_1(p)$ which is related to the population coefficient as,

$$r_1(p) = \frac{R_1(p)\, g(1)}{g(p)} \exp\left(\frac{E(p)}{k T_e}\right) \qquad (20)$$

where $E(p)$ is the energy of level p measured from the ground state. In the case of the ground state 2^2S, $r_1(2^2S)$ is put equal to 1. If thermal equilibrium were

established among a group of levels, $r_1(p)$ for these levels would be equal. On the contrary, for $n = 2$, 3, 4 and 5 levels, the different-l levels are not in thermal equilibrium. In the study for hydrogen or hydrogen-like ions, it is assumed that, at high density, the collisional l-changing rate coefficients are sufficiently larger than those of the $\Delta n \neq 0$ transitions and the population of different-l levels with same n are populated according to their statistical weights. Sampson [34] suggests that the critical electron density for the statistical distribution is determined from the comparison between the smallest collisional l-changing rate and the largest radiative decay rate. In the present case of the $n = 4$ levels, the smallest collisional l-changing rate coefficient for proton collisions is for 4^2S-4^2P and is $10^{-13}m^3sec^{-1}$ for 50eV. The largest spontaneous transition rate for 2^2P - 4^2D is $2.9\times10^{10}sec^{-1}$. The critical density is about $n_e = 3\times10^{23}m^{-3}$. This appears consistent with the result shown in Fig.7, but, as we have seen, the statistical population distribution has not been established. So the question is open for hydrogen or hydrogen-like ions, whether thermal equilibrium is actually established or not under the high density conditions.

Figure 9 shows that $r_1(p)$ has a monotonic p-dependence and is given approximately by,

$$r_1(p) \propto p^{*-6} \qquad (21)$$

starting from $r_1(2^2S) = 1$. (In this paragraph, p is understood to denote the principal quantum number.) The p^{*-6} dependence was first shown theoretically for neutral hydrogen [1, 35], and verified experimentally for neutral argon [36] and for helium [37]. This dependence is the result of establishment of the ladder-like excitation ionization process with the approximate relationship of the excitation rate coefficients $C(p,p+1) \propto p^4$. It is interesting to find here a similar relation also in the case of a highly charged ion. The slight failure of eq.(21) between $n = 2$ and $n = 3$ is the result of the failure of the above approximation of the excitation rate coefficients. As has been noted, a generalized ladder-like mechanism is established among the different-l levels. These populations show a slope intermediate between eq.(21) and thermodynamic equilibrium. It is also noted that the fine-structure components of $2^2P_{1/2}$ and $2^2P_{3/2}$ are not in thermal equilibrium, that is; $n(2^2P_{3/2})/g(2^2P_{3/2}) < n(2^2P_{1/2})/g(2^2P_{1/2})$.

The relationship expressed by eq.(21) suggests the method of estimating the excited-level populations in high density plasmas; *i.e.* if we know the ground state density $n(2^2S)$ or a low-lying level population, we can derive approximate populations of the high-lying excited levels from eq.(21).

In Fig.7, the population of 2^2P shows a slight maximum hump at about $n_e = 10^{23}m^{-3}$. The reason is as follows; in the range of $n_e < 10^{23}m^{-3}$, in the population flow into the 2^2P level, the cascade contribution from 3^2D is substantial (15%) besides the collisional excitation from the ground state. As the electron density become higher than $10^{24}m^{-3}$, the 3^2D population saturates (Fig.7). The relative cascade contribution from 3^2D decreases, resulting in a decrease in the 2^2P population. Finally the 2^2P level population becomes to be determined only by the collisional processes, $2^2S \rightarrow 2^2P \rightarrow 3^2D$.

We may apply our collisional radiative model calculation to actual plasmas. We take a tokamak plasma, which is a typical example of the ionizing plasma considered here. Figure 10 shows the photon emission ratio of transitions 2^2S-3^2P to 2^2P-3^2S and that of 2^2P-3^2D to 2^2P-3^2S of CIV, NV and OVI ions against electron temperature. We assume electron density of $10^{19}m^{-3}$, which is the typical value for a tokamak plasma where these ions are present. In such a low density plasma, as shown in Fig.7, there is no significant density effect on the n = 3 level populations. In Fig.10, two sets of results of calculation are shown. They are based on the two different cross section data for 2^2S-3^2P, as shown in Fig.4(a). A similar calculation result by Zastrow *et al.*[38] is also given. They treat the individual l-levels for $n \leq 5$, and neglect levels with $n \geq 6$. Our results based on the C,A,C calculation agree with those by Zastrow *et al.* The slight difference between the two calculations would be explained as due to the cascade contribution from the $n \geq 6$ levels which is neglected in Zastrow *et al.*

B. Recombining plasma

We take AlXI ion as an example and T_e is assumed to be 30eV (Θ=0.25eV). We include the ion collisions. We assume that the average charge of aluminum ions is 10 and its density is 10% of the electron density. The n_e-dependence of the populations of the n = 3, 4 and 5 levels are shown in Fig.11. We again take the 4^2P level as an example and show in Fig.12(a) and (b) the n_e-dependence of the amount of population flows divided by electron density into and out of the 4^2P level. In the low density region than $n_e = 10^{20}m^{-3}$ ($\eta < 10^{13}m^{-3}$), the excited levels shown in Fig.11 are in the capture-radiative-cascade phase, in which they are populated predominantly by the direct radiative recombination plus cascade and depopulated through the radiative decay. It may be interesting to remember that, in the case of hydrogen, the contributions from the direct recombination and the cascade are approximately 2 : 1. [1] As Fig.11 shows, the n^2S level has the largest population per unit statistical weight among the different-l levels for n = 3, 4 and 5. At this temperature, the radiative recombination rate coefficient into

the s, p and d levels are approximately proportional to their statistical weights (that for the s is slightly smaller) and those for f and especially g are much smaller. The n^2S level has the smallest decay probability, resulting in the largest population. In lithium-like ions, the n^2D level has the largest radiative decay probability among the same n levels and the dominant transition is 2^2P -n^2D for the $n \leq 5$ levels. This results in the smallest population per unit statistical weight of n^2D among the same n levels for n = 3, 4 and 5. In the intermediate density region $10^{21}m^{-3} < n_e < 10^{25}m^{-3}$ ($10^{14}m^{-3} < \eta < 10^{18}m^{-3}$), the populations of the levels with same n converge with each other by the l-changing collisions, and they approach the high density limit values.

In the high density limit, there is a different characteristic from the ionizing plasma case; as seen in Fig.12 the "net" upward or downward flow in $4^2S \leftrightarrow 4^2P \leftrightarrow 4^2D$, is less than 0.1 % of the individual flow. This is consistent with the near Boltzmann distribution of these levels as shown in Fig.9: the same slope of these populations to the Saha-Boltzmann distribution. Similar feature is seen in $4^2P \leftrightarrow n \geq 5$ levels. (0.5% is the net flow.) For $4^2P \leftrightarrow n$ = 2 and 3, however, the 'net' downward population flow is substantial. This suggests that thermal equilibrium would be established for the $n \geq 4$ levels but not with the n = 2 and 3 levels. This is actually the case as seen in Fig.9.

The overall population distribution in Fig.9 is interpreted in the following. We introduce Byron's boundary in high density plasma [1, 39]; this gives the boundary between the levels in LTE and those for which the ladderlike deexcitation mechanism is established. This boundary is given approximately by

$$p_B^* = \left(\frac{(z-2)^2 R_y}{3kT_e} \right)^{1/2} \qquad (22)$$

where R_y is one Rydberg (13.6eV) and kT_e is the temperature in eV. (In this paragraph, we use "p" for principal quantum number.) For levels lying above this with principal quantum number p, the collisional excitation to the p +1 level is more frequent than deexcitation to the p -1 level and for levels below that, the relation is reversed. Under this plasma conditions, $p_B^* \cong 4.2$. The population distribution in the ladderlike deexcitation mechanism has been shown for hydrogen to be given approximately by $n(p)/g(p) \propto p^{-6}$. This is based on the characteristics of the deexcitation rate coefficient similar to that for the excitation rate coefficient mentioned earlier. Appendix C shows that in Fig.9 the curve representing the Saha-Boltzmann distribution (S-B) has slope -6 at p^* =

p_B^*. The overall population distribution is therefore given by the curve S-B for $p^* \geq p_B^*$ and by its linear extrapolation for $p^* \leq p_B^*$ with slope -6. In Fig. 9, populations of the levels $n \geq 3$ are well approximated by this simple relationship. The gross deviation of $n(2^2P)$ from this line is the result of the failure of the approximation for the deexcitation rate coefficients from this level, $F(2^2P, 2^2S)$.

We note one thing; Figure 12 (a) shows that in the low density region, the dominant direct recombination process is radiative recombination. In the high density region the contribution from three-body recombination becomes much larger than that from the radiative recombination. In such a high density region, however, collisional excitation and deexcitation processes between excited levels become dominant. It is concluded that the three-body recombination can never be the dominant mechanism for low lying levels. Dielectronic recombination process is insignificant in the present low temperature region.

An important application of the recombining plasma is the x-ray laser of the recombining plasma scheme. Figure 11 shows that in the density region of $n_e \leq 2\times10^{25}m^{-3}$, the population inversion is established between the 3^2P and 3^2D levels and $n = 4$ or 5 levels. We assume that the spectral broadening is determined by thermal Doppler broadening and the helium-like aluminum ion density is 10% of electron density. We define the absolute amplification gain as,

$$\text{gain} = (8\pi c)^{-1}\sqrt{\frac{M_{\text{ion}}c^2}{2\pi kT_e}}\left[n(p) - \frac{g(p)}{g(q)}n(q)\right]A(p,q)\lambda^3 \qquad (23)$$

where p and q are the upper and lower excited levels, respectively, M_{ion} and λ are the mass of the ion and the wavelength of the transition line, respectively. We resolve the levels into the fine structure components and assume the L-S coupling scheme for the transition probabilities of the component lines. Hyperfine structure (nuclear spin of aluminum is $I = 5/2$) is neglected. We take the strongest line among the fine structure component levels in our calculation of the gain.

Figure 13 shows the n_e-dependence of the gain for 3^2D-4^2F, -5^2F, -4^2P, -5^2P, 3^2P-4^2D, -5^2D, -4^2S and 3^2P-5^2S lines of AlXI ion. Although population inversion is realized between many pairs of levels, their amplification gain for many of them is very small. Only the two transitions 3^2D-4^2F and 3^2P-4^2D show substantial gain at about $n_e = 10^{25}m^{-3}$. Carillon *et al.* [40] measured the gain in a laser produced aluminum plasma. They found that four transitions 3^2D-4^2F, -5^2F, 3^2P-4^2D and -5^2D had significant gain; gains of the 3^2D-5^2F, 3^2P-4^2D and 3^2P-5^2D transitions were about equal and the gain of the 3^2D-4^2F transition was about as twice as larger than those of the other three transitions.

Our results of the gain of 3^2D-4^2F and 3^2P-4^2D are smaller than those of the experimental result [40] by a factor of 2, and the gain of 3^2P-5^2D and 3^2D-5^2F are more than 10 times smaller than those of the experiment. The calculation by Klisnick *et al.* [2, 41] is in accordance with our result. If we assume the calculated populations for the $n = 3$ levels, in order for our calculated gain to be consistent with experiment the 4^2D population should be larger by 20% and the 5^2D and 5^2F populations by an order. As shown in Fig.11 together with Fig. 9, under the experimental conditions, the $n = 5$ levels are almost in LTE, and the $n = 4$ levels are close to that. Therefore, the larger populations, especially, in the $n = 5$ levels are unlikely. Our failure of reproducing experiment may be related with our neglect of the excitation and deexcitation processes which involve doubly excited states and are predicted to play an important role in high density plasma [42]. The $n = 3$ level populations might be decreased by these processes. We will investigate this possibility in near future.

C. Ionization balance

In lithium-like ions, the $n = 1$ orbitals are filled and the ground state is 2^2S. This makes the system of the lithium-like ion energetically "shallow" compared with hydrogen or helium-like ions. For example, both the lithium-like oxygen (OVI) and the hydrogen-like carbon (CVI) ions have the effective nuclear charge $z_{\text{eff}} = 6$, but the ionization potentials of these ions are 138eV and 489eV, respectively, nearly about a factor of 4 difference. This makes the ionization balance characteristics of lithium-like ions substantially different from those of hydrogen or helium-like ions. Ionization balance is defined as

$$S_{\text{eff}}\, n_e\, n_{\text{Li}} = \alpha_{\text{eff}}\, n_e\, n_{\text{He}} \qquad (24)$$

where the effective ionization and recombination rate coefficient S_{eff} and α_{eff} are defined in eq.(3). The temperature at which eq.(24) leads to $n_{\text{He}} = n_{\text{Li}}$ is called the "optimum temperature" T_{IB} or Θ_{IB}. Figure 14 shows the z-dependence of the optimum temperature for low density of $\eta = 10^{14}m^{-3}$ and the corresponding temperature for hydrogenic ions [1]. The optimum temperature for lithium-like ions is about a factor 5 lower compared with hydrogenic ions.

It has been shown that, for hydrogen atom and hydrogenic-ions in low density plasma, the recombining plasma component in eq.(2) is of the order of 0.1 of that of the ionizing plasma component, independent of temperature [1].

We now discuss the relative contributions for the lithium-like ions. We limit our discussion to the low-density limit and to the high temperature case, but low enough in which dielectronic recombination can be neglected. Equation (24) reduces to

$$S(2^2S)\, n_e\, n_{Li} = \sum_p \beta(p)\ n_e\, n_{He} \qquad (25)$$

The population ratio between the ionizing and recombining plasma component is approximately given by

$$\frac{n_{He}\,\beta(p)}{n_{Li}\,C(2^2S,p)} = \frac{S(2^2S)}{\sum_p \beta(p)}\,\frac{\beta(p)}{C(2^2S,p)} = \frac{S(2^2S)}{C(2^2S,3)}\,\frac{C(2^2S,3)}{C(2^2S,p)}\,\frac{\beta(p)}{\sum_p \beta(p)} \qquad (26)$$

where "3" means the principal quantum number. In eq.(26), in the case of the OVI ions, $S(2^2S)/C(2^2S,3) \approx 0.2$ for T_e=50eV. The last factor may be approximated to $\beta(p)/\Sigma\beta(p) \approx p^{-3}/0.2$. $C(2^2S,3)/C(2^2S,p)$ is approximated to $3.5 \times 3^{-3}/p^{-3}$ for high-lying levels ($n \geq 7$). The population ratio would be about 3.5×3^{-3} (=0.13) for these levels.

Figure 15 shows the calculated population ratios in ionization balance. n_e is assumed to be 10^{13}m^{-3}. In the case of OVI (Θ=1.4eV), the ratio is n_{He}/n_{Li}=49. It is concluded that, for the condition of n_{He}/n_{Li} <10 (*i.e.*, the ionizing plasma), the ionizing plasma component in eq.(2) predominates over the recombining plasma component by more than a factor 10 for all the excited levels. For recombining plasma of $n_{He}/n_{Li}>5\times10^5$, the situation is reversed. For ionization balance plasma in the high density limit, it has been shown [1] that, in eq.(2), both the components together constitute the LTE population (the Saha-Boltzmann distribution against n_{He} and the Boltzmann distribution against n_{Li}, in the present case). Figure 9 shows the relative contribution from the ionizing plasma component, *i.e.*, $r_1(p)$, and that from the recombining plasma component, $r_0(p)$, is given by $[1-r_1(p)]$, where $r_0(p)$ is defined as

$$r_0(p) = \frac{2g_{He}\,R_0(p)}{g(p)}\left[\frac{h^2}{2\pi mkT_e}\right]^{-3/2}\exp\left(-\frac{\chi(p)}{kT_e}\right) \qquad (27)$$

where g_{He} and $\chi(p)$ is the statistical weight of the ground state of helium-like ions and the ionization potential of the level p, respectively. It is straightforward to estimate for plasmas out of ionization balance the relative magnitude of both the contributions.

Figure 15 contains the ratios for low temperature (AlXI T_e=30eV, Θ=0.25eV). The ratio is $n_{He}/n_{Li}=2.5\times10^{-6}$. Even for recombining plasma of $n_{He}/n_{Li}>2.5\times10^{-6}$, the ionizing plasma component tends to persist especially for low-lying levels. For a strongly recombining plasma with $n_{He}=n_{Li}$, for example, the population $n(2^2P)$ is still determined by the ionizing plasma component as given in Fig.7. For ionization balance plasma in the high-density limit, where the relation $r_0(p)+r_1(p)=1$ holds, a similar argument to the above indicates that, in Fig.9, the population of the recombining plasma component with respect to the curve "S-B" gives the relative contribution from the recombining plasma component and that from the ionizing plasma component corresponds to the difference between the curve and the recombining plasma population.

D. The population imbalance in the fine structure sublevels

We assume the ionizing plasma with the reduced temperature Θ=3eV and the reduced electron density η is from 10^{14}m^{-3} to 10^{20}m^{-3}. Figure 16 shows the degree of the population imbalance between the fine structure sublevels of $2p^2P_{1/2,3/2}$ and $3p^2P_{1/2,3/2}$. The ordinate is the imbalance normalized to ±1, $\mu(p)/(\omega_1+\omega_2)$. The abscissa is nuclear z. A large imbalance develops between the $2p^2P_{1/2,3/2}$ levels for large nuclear charge ($z > 20$). This is mainly due to the difference in the radiative decay probabilities from the $2p^2P_{1/2,3/2}$ levels. In the high electron density regions, the imbalance disappears; this is because of the collisional depopulation to the $2s^2S_{1/2}$ level. However, a small imbalance remains even for small z. The $3p^2P_{1/2,3/2}$ levels show very small imbalance throughout the electron density region for $z \leq 40$.

V. COMPARISON WITH EXPERIMENTS

Several plasma experiments have been reported which are relevant to the present calculation.

Datla and Kunze [43] measured spectral line intensities from OVI and NV ions in a theta pinch plasma and deduced the relative effective excitation rate coefficient for several levels. In this experiment, they regard the sum of the populations of the ground state and the 2^2P level as the lithium-like ion density. The population ratio $\beta = n(2^2P)/n(2^2S)$ which they use is calculated by Sampson

to be 0.88 for NV ions and 0.58 for OVI ions. They present the effective rate coefficients X_{eff} according to

$$X_{\rm eff}(p) = \frac{n(p)\sum_{q<p} A(p,q)}{n_e[n(2^2S)+n(2^2P)]} \qquad (28)$$

and it was normalized by the effective excitation rate coefficient of 3^2S. Table 1(a) reproduces the result. In this table, proton collisions are included in our calculation. Their plasmas for NV and OVI ions happen to have nearly the same reduced temperature and the identical reduced density. As seen from Fig.7, at this density, these levels, especially $n = 5$ levels, are not in the corona phase. Rather, the "density effect" is substantial. However, the density effect is minimal for 3^2S (See the last three columns in Table 1(a); for explanation see later) and its excitation cross section has little uncertainties. It is judged that the choice of this level as the denominator for comparison is suitable. By using eq.(28) we reinterpret the result and retrieve the population ratio. Figure 17 shows the "experimental" relative populations of excited levels of OVI and NV ions and the calculated ones as functions of the reduced density. The curves for OVI are nothing but a different plot of Fig.7. Uncertainty of the experiment is claimed to be about 50% for OVI and for $n = 5$ levels of NV ions and 30% for other levels of NV ions. Our results agree with the experimental results within the experimental uncertainties except for 3^2D of OVI ion; for this level the experimental population is smaller by a factor 1.9. The experimental population divided by its statistical weight is even smaller than that of 4^2S by a factor 1.5. For NV ions, discrepancy is the same direction but its magnitude is smaller. For 3^2P and 4^2P, the experimental results are larger than our results in the case of NV ions and smaller in the case of OVI.

Collisional depopulation processes from the excited levels are ignored by Datla and Kunze, as seen in eq.(28). The same is true for populating process except from 2^2P. In Table 1(a), the last three columns show the contributions to the population flow into the excited levels from the ground state, the 2^2P level and the same n levels, *i.e.* the three dominant contributions, calculated under the experimental plasma conditions. The relative contribution from the l-changing processes to the population flow into an excited level is approximately equal to that to the depopulation flow out of this level in this electron density region. It may thus be concluded that collisional depopulation is substantial in the experimental conditions, especially for higher-lying levels, and that eq.(28), with

its neglect of collisional population and depopulation flows from and to other levels than 2^2S and 2^2P levels, is inappropriate for a definition of the excitation rate coefficient.

In order for our calculated 3^2D population of OVI ions to be consistent with the experiment [43], the l-changing cross section, Fig 6(b) should be decreased by at least by one order. It may be interesting to note that if the experimental n_e for OVI were reduced by a factor 2 or 3, the experimental population would be in almost complete agreement with the calculation except for levels 4^2S and 5^2P.

Ionization rate coefficient of lithium-like ions are measured by Kunze [44], Jones *et.al.* [45, 46], Rowan and Roberts [47], Hinnov [48] and Datla and Roberts [49] in theta pinch plasmas. These results are summarized in Table 1 (b), and are compared with the effective ionization rate coefficients S_{eff} expressed by eq.(3), which include the indirect ionization through the excited levels (the ladder-like process [1]) as explicitly shown in Table 1 (b). Proton collisions are included in our calculation. Table 1 (b) shows that the experimental results of [46] and [49] are in agreement with our calculation within the experimental uncertainties. References [47] and [48] for OVI ions give larger values, while [47] for NV agree with our calculation. References [44] and [45] give smaller values; especially [44], although with large uncertainty of a factor 2, gives consistently smaller values for CIV, NV and OVI ions. Figure 18 summarizes the comparison for OVI. It is noted that the experimental ionization rate coefficient of [44] is smaller than the low density limit value, or the direct ionization rate coefficient.

There are few experiments available for comparison of the recombination processes. Datla and Kunze [43] report the effective recombination rate coefficients $\alpha_{eff}(p)$ for the $n = 4$ and 5 excited levels in a theta pinch plasma for OVI and NV ions. The electron density of their experiment, (n_e=2.5×10^{22}m^{-3} (η=0.9×10^{17}m^{-3}) for OVI and n_e=1.0×10^{22}m^{-3} (η=1.4×10^{17}m^{-3}) for NV), corresponds in Fig.11 approximately to n_e=2~3×10^{24}m^{-3} in terms of η. This range of n_e is in the transition region between the intermediate and high density regions, and the picture that the population of an individual level is determined by the balance between recombination and radiative and collisional decay is clearly inappropriate. Rather, as shown in Fig.11 the levels with $n = 4$ are almost statistically populated; this is the case even in the absence of proton collisions. We derive the "experimental" populations from their $\alpha_{eff}(p)$ values, where the helium-like ion density n_{He} = 1m^{-3} is assumed for convenience of presentation. We compare in Fig.19 the experimental and theoretical populations (proton collisions are included) in the Boltzmann plot. The discrepancies between our results and experiment are about two orders of magnitude. It may be unrealistic

to try to bring our calculation into agreement with the experiment by introducing an additional recombination process, because these levels, especially n=5 are almost in LTE with respect to the helium-like ions.

VI. VALIDITY RANGE AND UNCERTAINTIES

A. Atomic data

The uncertainty in the level energy calculated by Zhang *et al.*[4] is claimed to be less than 1%. The uncertainty due to the fitting formula (eqs. (A1-3)) adopted in this study is less than 0.5%.

The uncertainty in the absorption oscillator strength data by Zhang *et al.*[4] is about 1% and that by Lindgard and Nielsen [5] is about 1% for $z \leq 18$, and within 10% for $z \geq 20$. The uncertainty due to the fitting formula (eqs. (A4-8)) is less than 5%. The resulting uncertainty in the A coefficient for the transitions into n = 3, 4 and 5 levels is 10% in the case of high z ions. The irregularities of the $2s^2S_{1/2}$-$2p^2P_{1/2,3/2}$ absorption oscillator strengths at z = 21 seen in Fig.3 and that of energies in Fig.2 are ignored in our code.

The results of various calculations except the hydrogenic approximation [4,8-11 and 13] for excitation cross section of OVI are in good agreement for all the transitions except for 2^2S-3^2P.(See Figs.4-5) For this transition, the cross section by Mann is larger than those by C,A,C and Zhang *et al.* by a factor 2 near the threshold. (Fig.4(a))

B. Validity of eq.(2)

In eqs.(1) and (2), we have assumed that production of excited ions directly from the beryllium-like ions is insignificant; that is, its flow is less than, say, 10% of the contributions given in the right hand side of eq.(1). We take OVI as an example. In the low density region ($\eta \leq 10^{13}\mathrm{m}^{-3}$), where the excited level populations of beryllium-like ion are low, the ionization-excitation process from $2s^2\,{}^1S$ to n^2L is considered; the ratio of the rate coefficients to those for $2s^2S$ to n^2L is estimated to be of the order of 10^{-5}. Thus, a conservative estimate leads to a condition $n_{\mathrm{Be}}/n_{\mathrm{Li}} < 10^2$~$10^3$. In the region of $10^{13}\mathrm{m}^{-3} < \eta < 10^{18}\mathrm{m}^{-3}$, the ratio of the metastable $2s2p^3P$ population to the ground-state population is 0.3 [50]. From the comparison of ionization of $2s2p^3P$ creating 2^2P and excitation 2^2S -2^2P, it is concluded that $n_{\mathrm{Be}}/n_{\mathrm{Li}} < 20$ should be satisfied. In the high density limit ($\eta > 10^{18}\mathrm{m}^{-3}$), the ladder-like excitation-ionization mechanism through the $2snl$ and $2pnl$ rydberg states may create the 2^2S and 2^2P ions, respectively. The ratio of the production rate of 2^2P to that of 2^2S is estimated to be 0.9. (In eq.(1) we have assumed this to be zero.) In the extreme case that only the 2^2P ions were created all the populations in Fig.7 and in Fig.9 except for $n(2^2S)$ would be shifted by 20% upward and S_{eff} in Fig.18 would increase by 10%.

C. Assumption of hydrogenic approximation and statistical distribution for $n \geq 6$ levels

We assume the hydrogenic approximation for the $n \geq 6$ levels. As the nuclear z becomes large, quantum defects of excited levels become small. For lithium like ions with $z \geq 6$, the quantum defects of the $n \geq 6$ levels are smaller than 0.05, and this approximation may be justified.

For the levels with $n \geq 6$, we assume that all the different-l levels are populated according to their statistical weights. As we show in Figs.7 and 11, in the low density region, the populations of the different-l levels for n = 3, 4 and 5 largely deviate from the statistical distributions. A similar deviation is expected for the $n \geq 6$ levels in the corresponding density regions. For the purpose of estimating errors in the populations of the low-lying levels caused from our assumption for the $n \geq 6$ levels, we compare the results of a calculation in which the n = 5 levels are assumed to be statistically populated. For ionizing plasma of low density, this population is close to that of 5^2P in Fig.7. In this case, the 4^2P population is smaller by 10% and the 4^2F population, which is affected most, is larger by 20%. These changes are due to the lower 5^2S population and the enhanced 5^2G population, respectively, in this calculation. In recombining plasma, the statistical population is close to 5^2G in Fig.11. The discrepancy of the 4^2F population, which is affected most, is smaller (2%), because the 5^2G population does not change substantially between the two calculations. The populations of the n = 3 and 2 levels are little affected for both the ionizing and recombining plasmas. Judging from the above observations, we may conclude that, in our present model, the n = 5 levels are, in low density regions, overpopulated at most by 20% for 5^2G in the ionizing plasma and reasonably accurate in the recombining plasma. The populations of the n = 4, 3 and 2 levels are little affected by our assumption. Our assumption would be substantiated in the high density region where the l-changing collisions are frequent enough for the n = 6 levels. The critical density would be given from comparison of the radiative decay rate and the l-changing collisional rate of 6^2D. In the case that proton collisions are neglected, the critical density is $n_e \cong 5\times10^{22}\mathrm{m}^{-3}$ for the condition of Fig.7 and in the case that proton collisions are included, the critical density is $n_e \cong 1\times10^{21}\mathrm{m}^{-3}$.

APPENDIX A. THE ATOMIC PARAMETERS AND RATE COEFFICIENTS IN THE CR MODEL

In this appendix, the fitting formulae of the atomic parameters which are used in our collisional-radiative model are shown.

A-I. Energy level

The ionization potential for ion z is expressed as

$$E\,(2^2S\,)\,(\mathrm{eV}) = 2.60910 \times (z-2) + 3.39323 \times (z-2)^2 + 1.94126 \times 10^{-3} \times (z-2)^3$$
$$\text{for } z: 6 \le z \le 50 \tag{A1}$$

The energy of the excited levels are given by [4] and [5]. The fitting formula for the energy of the nl levels ($n \le 5$) measured from the ionization limit of the ion z is expressed by the polynomial,

$$E\,(n^2L)\,(\mathrm{eV}) = \sum_{k=1}^{4} C_k \times (z-2)^k \tag{A2}$$

The fitting parameters C_k's are listed in Table A-1. (See also Fig.2)

For the $n \ge 6$ levels, we assume the hydrogenic approximation, *i.e.*, the energy levels measured from the ionization limit are described as

$$E\,(n) = \frac{(z-2)^2 Ry}{n^2} \tag{A3}$$

where the Ry is one Rydberg.

A-II. Absorption oscillator strength

1. $\Delta n \neq 0$ transitions

The absorption oscillator strength is given by [4-6].

The value between the levels with $n \le 5$ for ion z are described by

$$f\,(i\,,\,f\,) = C_1 + \frac{C_2}{(z-2)^2} + C_3 \times \exp\left(-C_4 \times (z-2)^{0.4}\right) \tag{A4}$$

and the fitting parameters C_k's are listed in Table A-2.

For transitions from a level with $n \le 4$ to a level with $6 \le n \le 10$, we adopt

$$f\,(n^2L, n'^2L')_z = f\,(n^2L, 5^2L')_z \times \left(\frac{n'}{5}\right)^{\alpha}$$
$$\text{for } n \le 4,\ 6 \le n' \le 10 \tag{A5}$$

the fitting parameter α are listed in Table A-3.

For transitions from the $n=5$ levels to levels with $6 \le n \le 10$,

$$\begin{aligned} f\,(5^2S, n\,) &= 0.608 \times (n/6)^{-3} \\ f\,(5^2P, n\,) &= 0.700 \times (n/6)^{-3} \\ f\,(5^2D, n\,) &= 0.700 \times (n/6)^{-3} \\ f\,(5^2F, n\,) &= 1.208 \times (n/6)^{-3} \\ f\,(5^2G, n\,) &= 1.683 \times (n/6)^{-3} \end{aligned} \tag{A6}$$

and in the case of $n \ge 11$,

$$f\,(n^2L, n'^2L')_z = f\,(n^2L, 10^2L')_z \times \left(\frac{n'}{10}\right)^{-3}$$
$$\text{for } n' \ge 11 \tag{A7}$$

For transitions among the $n \ge 6$ levels, we assume those of hydrogenic [15].

2. $\Delta n=0$ (l-changing) transition

The oscillator strengths of $2s^2S_{1/2}$-$2p^2P_{1/2,3/2}$ are given by

$$f\,(2s^2S_{1/2}\text{–}2\,p^2P_{1/2}) = 0.82900 + \frac{1.3392}{(z-2)^2} - 0.77803 \times \exp\left(1.2187\times10^{-2} \times (z-2)^{0.4}\right)$$
$$f\,(2s^2S_{1/2}\text{–}2\,p^2P_{3/2}) = 8.8928 \times 10^{-2} + \frac{2.4051}{(z-2)^2} - 3.4939 \times 10^{-3}\,(z-2) - 6.6531 \times 10^{-5}\,(z-2)^2$$

and for other transitions

$$f\,(n^2L, n'^2L')_z = C_1 \times \left(\frac{8-2}{z-2}\right) \tag{A8}$$

where the parameter C_1 is identical to the absorption oscillator strength for the lithium-like oxygen ions. (See table A-4.)

Forbidden transition ($2p^2P_{1/2}$-$2p^2P_{3/2}$) probability for the ions from z=26 to 36 are given in [52]. The results are shown in Fig. A-1. These data are scaled ($\propto z_{\mathrm{eff}}{}^{12}$) for other z ions.

A-III. Electron impact excitation cross sections and rate coefficients

1. Cross section

$\Delta n \neq 0$ transition

The cross sections for transitions from the 2^2S and the 2^2P levels are given by [4], and those for transitions between all the levels with $n \le 5$ are calculated by C, A, C. [13] The fitting formula is

$$\sigma(i, f) = \pi a_0^2 [A \frac{\ln E}{E} + \frac{B}{E} + C \times \exp(-DE)] \quad \text{(A9)}$$

The parameters of these transitions for lithium-like oxygen ions are listed in Table A-5 together with those for 2^2S-2^2P.

The cross sections for transitions from a level with $n \leq 4$ to those with $n \geq 6$ are calculated from

$$\sigma(E/E_{th})_{n\,l \to n'\,l'} = \sigma(E/E_{th})_{n\,l \to 5\,l'} \times (\frac{f(nl, n'l')}{f(nl, 5l')}) \quad \text{for } n \leq 4,\ n' \geq 6 \quad \text{(A10)}$$

where $f(i,f)$ is the absorption oscillator strength for the transition from i to f.

The cross sections for the transitions from a level with $n = 5$ to those with $n \geq 6$ are calculated by

$$\sigma(E/E_{th})_{5\,l \to n'} = \sum_{l=0}^{4} \sigma(E/E_{th})_{4\,l \to n'\,l'} \times (\frac{5}{4})^3 \times \frac{f(5l, n')}{f(4l, n')} \quad \text{for } n' \geq 6 \quad \text{(A11)}$$

For transitions among the levels with $n \geq 6$, we use the data by ref. [15].

Δn=0 transition

For the transitions of the $3s^2S$-$3p^2P_{1/2,3/2}$, $3p^2P_{1/2,3/2}$-$3d^2D_{3/2,5/2}$, 4^2S-4^2P, 5^2S-5^2P, we use eq.(A9) and show the fitting parameters in Table A-6.

For other transitions, we use the Dickinson-Fujima formula which is expressed as

$$\sigma(nl,nl+1) = \frac{1}{(z-2)^2} \times 6\pi a_0^2 \times n^4 \times (\frac{v_a}{v})^2 \times (\frac{l+1}{2l+1}) \times \ln[\frac{E}{2E_{th}}] \quad \text{(A12)}$$

where v_a is the velocity of the classical orbital electron in the initial level and v is the velocity of the colliding electron.

2. Excitation and deexcitation rate coefficients

$\Delta n \neq 0$ transition

We integrate numerically the cross section which is expressed by eq.(A9) over a Maxwellian velocity distribution to calculate the deexcitation rate coefficients for all the transitions. Each of them is fitted by the formula

$$F(i, f)_{\text{oxygen}}\ (\text{m}^3\,\text{s}^{-1}) = [K \times \frac{\log(T_e)}{T_e^L} + \frac{M}{T_e} + N \times \exp(-P \times T_e)] \times \text{factor} \quad \text{(A13)}$$

The parameters for lithium-like oxygen ions are listed in Table A-7.

For transitions among the levels with $n \geq 6$, we use the data by ref. [15].

Δn=0 transition

Equation (A13) is used. The fitting parameters for the deexcitation rate coefficients are shown in Table A-8.

Excitation rate coefficient is calculated from the deexcitation rate coefficient from the principle of detailed balance.

The accuracy of the fitting is estimated to be 5%.

A-IV. Dielectronic recombination rate coefficient

The autoionization probability, A_a, and the radiative decay probability from the doubly excited levels, A_r, are referred to Dubau *et al.* [32] for the levels with $n \leq 5$ of oxygen ions. For other elements, Veinstein and Safronova [33] give A_a and A_r including the relativistic effects. The A_a and A_r for lithium-like oxygen are listed in Table A-9.

For the $n \geq 6$ levels, we employ the threshold value of the hydrogenic excitation cross section of 1^2S-2^2P and 1^2S-3^2P to estimate A_a. (See also Table A-9.)

APPENDIX B. CONTRIBUTION FROM CASCADE

We assume hydrogenic ions for the purpose of simplifying argument. The excitation rate coefficient from the ground state is approximately given as

$$C(1, q) \cong C_0\, q^{-3} \quad \text{(B1)}$$

with a constant C_0 and the principal quantum number q.

The radiative decay rate from level q is expressed by using a constant H ($= (2^8/3\sqrt{3})\,\pi e^2 z^4 R^2/h^2 mc^3$)

$$\sum_{q>k}^{q-1} A(q, k) \cong \int_1^{q-1} \frac{H}{q^3 k (q^2 - k^2)}\, dk = \frac{H}{2q^5} \log\left(\frac{(2q-1)(q+1)}{q-1}\right) \cong H\, q^{-4.5} \quad \text{(B2)}$$

In the low density ionizing plasma or in the corona phase, the population of level q is approximately given as,

$$n(q) = \frac{C(1,q)n_e n(1)}{\sum_{k<q} A(q,k)} \cong \frac{C_0}{H} q^{1.5} n_e n(1) \tag{B3}$$

where cascade contribution has been neglected. The cascading population flow from level q to p is

$$n(q)\ A(q,p)$$

and the total cascading flow from all the levels q ($>p$) is

$$\text{Cascade} \cong \int_{p+1}^{\infty} n(q)\ A(q,p)\,dq$$

$$\cong \int_{p+1}^{\infty} \frac{C_0\, n_e n(1)}{p q^{1.5}(q^2 - p^2)}\,dq$$

$$= \frac{C_0 n_e n(1)}{p^2}\left[\frac{2}{p\alpha} + \frac{1}{2p\sqrt{p}}\ln\left(\frac{\alpha-\sqrt{p}}{\alpha+\sqrt{p}}\right) + \frac{1}{2p\sqrt{p}}\arctan\frac{\alpha}{\sqrt{p}}\right]_{\alpha=\sqrt{p+1}}^{\infty}$$

$$= \frac{C_0 n_e n(1)}{p^3}\left(\frac{\pi}{2\sqrt{p}} - \frac{2}{\sqrt{p+1}} - \frac{1}{2\sqrt{p}}\ln\left(\frac{\sqrt{p+1}-\sqrt{p}}{\sqrt{p+1}+\sqrt{p}}\right) - \frac{1}{\sqrt{p}}\arctan\frac{\sqrt{p+1}}{\sqrt{p}}\right) \tag{B4}$$

By using eq.(B1) and eq.(B4), we obtain the relative contribution ζ from the cascading to the population flow into level p,

$$\zeta = \frac{\text{cascade}}{C(1,\ p)\ n_e n(1) + \text{cascade}}$$

$$= \frac{\left(\frac{\pi}{2\sqrt{p}} - \frac{2}{\sqrt{p+1}} - \frac{1}{2\sqrt{p}}\ln\left(\frac{\sqrt{p+1}-\sqrt{p}}{\sqrt{p+1}+\sqrt{p}}\right) - \frac{1}{\sqrt{p}}\arctan\frac{\sqrt{p+1}}{\sqrt{p}}\right)}{1 + \left(\frac{\pi}{2\sqrt{p}} - \frac{2}{\sqrt{p+1}} - \frac{1}{2\sqrt{p}}\ln\left(\frac{\sqrt{p+1}-\sqrt{p}}{\sqrt{p+1}+\sqrt{p}}\right) - \frac{1}{\sqrt{p}}\arctan\frac{\sqrt{p+1}}{\sqrt{p}}\right)} \tag{B5}$$

The values of ζ for p = 4, 6 and 10 is 0.187, 0.190 and 0.193, respectively. If we take into account the cascade contribution in eq. (B3), ζ would be slightly larger than 20%.

APPENDIX C. POPULATION DISTRIBUTION OF HIGH-DENSITY RECOMBINING PLASMA

The Saha-Boltzmann population for lithium-like ions with nuclear charge z is

$$n(p) = \frac{g(p)}{2g_{1\mathrm{e}}}\left(\frac{h^2}{2\pi m k T_e}\right)^{3/2} \exp\left(\frac{(z-2)^2 R/p^{*2}}{kT_e}\right) \tag{C1}$$

where p^* is the effective principal quantum number and R is one Rydberg. We express $n(p)$ and p^* in a common logarithmic scale (Fig.9) and transform eq.(C1) to

$$\log_{10}\frac{n(p)}{g(p)} = \log_{10}\frac{1}{2g_{\mathrm{He}}}\left(\frac{h^2}{2\pi m k T_e}\right)^{3/2} + \frac{1}{t}\left[\frac{(z-2)^2 R}{kT_e}\exp(-2t\alpha)\right] \tag{C2}$$

where

$$t = \log_e 10\,,\quad \alpha = \log_{10} p^* \tag{C3}$$

We differentiate eq.(C2) with α

$$\frac{d}{d\alpha}\left(\log_{10}\frac{n(p)}{g(p)}\right) = -2\,\frac{(z-2)^2 R}{kT_e}\exp(-2t\alpha) \tag{C4}$$

At Byron's critical level p^*_{B}, eq.(C4) is expressed as

$$\left(\frac{(z-2)^2 R}{3kT_e}\right)^{1/2} = \exp(t\alpha) \tag{C5}$$

Substitution of eq.(C5) into eq.(C4) yields slope -6 at $p^*=p^*_{\mathrm{B}}$.

References

[1] T. Fujimoto, *J. Phys. Soc. Jpn.* **47**, 265 (1979); **47**, 273 (1979); **49**, 1561 (1980); **49**, 1569 (1980), **54**, 2905 (1985)

[2] A. Klisnick, A. Sureau, H. Guennou, C. Moller and J. Virmont, *Appl. Phys. B* **50** 153 (1990)

[3] D.R. Bates, A.E. Kingston, and R.W.P. McWhirter, *Proc.R.Soc. London* **267**, 297 (1962)

[4] H.L.Zhang, D.H.Sampson and C.J.Fontes, *At.Data & Nucl.Data Table* **44**, 31(1990)

[5] A. Lindgard and S.E. Nielsen, *At. Data & Nucl. Data Table* **19**, 533 (1977)

[6] W.L. Wiese, M.W. Smith and B.M. Glennon, *NSRDS-NBS 4* (1966)

[7] C.M. Varsavski, *Planet. Space Sci.* **11**, 1001 (1963)

[8] J.B. Mann, IPPJ-AM-**27**, *Inst.Plasma Phys.,Nagoya Univ.*, Nagoya, (1983)
[9] R. Mewe, *Astron. & Astrophys.* **20**, 215 (1972)
[10] R.E.H.Clark, A.L.Merts, J.B.Mann and L.A.Collins,*Phys.Rev.A* **27**,1812 (1983)
[11] K. Bhadra and R.J.W. Henry, *Phys. Rev.A* **26**, 1848 (1982)
[12] R.E.H. Clark, D.H. Sampson and S.J. Goett, *Astrophys. J Sppl.* **49**, 545 (1982)
[13] R.E.H.Clark, G. Csanak and J. Abdallah,Jr., *Phys.Rev. A* **44**, 2935 (1991)
[14] H. Mayer, *Los Alamos Scientific Laboratory Report* No **LA-607** (1947)
[15] L. Vriens and A.H.M. Smeets *Phys. Rev. A* **22**,940 (1980)
[16] D.H. Sampson and A.D. Parks, *Astrophys. J. Suppl.* **28**, 323 (1974)
[17] V.L.Jacobs and J.Davis, *Phys.Rev.A* **18**,697(1978)
[18] A.S. Dickinson, *Astron. & Astrophys.* **100**, 302 (1981)
[19] K. Fujima, (Private communication)
[20] L.B. Golden and D.H. Sampson *J. Phys. B* **10**,2229 (1977)
[21] L.B. Golden, D.H. Sampson and K. Omidvar, *J. Phys. B* **11**, 3235 (1978)
[22] D.L. Moore, L.B. Golden and D.H. Sampson, *J. Phys. B* **13**, 385 (1980)
[23] D.H. Sampson and L.B. Golden, *J. Phys. B* **12**, L785 (1979)
[24] L.B. Golden and D.H. Sampson, *J. Phys. B* **13**, 2645 (1980)
[25] R.E.H. Clark and D.H. Sampson, *J. Phys. B* **17**, 3311 (1984)
[26] J.A. Kunc, *J. Phys. B* **13**, 587 (1980)
[27] G. Hofmann, A. Muller, K. Tinschert, E. Salzborn, *Z. Phys. D* **16**, 113 (1990)
[28] W. Lotz, *Astrophys. J. Suppl.* **14**, 207 (1967)
[29] A. Burgess, *Mem. Roy. Astr. Soc.* **69**, 1 (1964)
[30] D.J. MacLaughlin and Y. Hahn, *Phys. Rev. A* **43**, 1313 (1991)
(Errata; *Phys. Rev. A* **45**, 5317 (1992))
[31] L.H. Andersen and J. Bolko, *J. Phys. B* **23**, 3167 (1990)
[32] F. Bely-Dubau, J. Dubau, P. Faucher and L. Steenman-Clark, *J. Phys. B* **14**,3313 (1981)
[33] L.A. Vainshtein and U.I. Safronova, *Atomic Data & Nuclear Data Table***21**, 49 (1978)
[34] D.H. Sampson, *J.Phys.B* **10**, 749, (1977)
[35] T. Fujimoto, Y. Ogata, I. Sugiyama, K. Tachibana and K. Fukuda, *Jpn. J. Appl. Phys.* **12**, 718 (1972)
[36] K. Tachibana and K. Fukuda, *Jpn. J. Appl. Phys,* **12**, 895 (1973)
[37] A.Hirabayashi, Y.Nambu, M.Hasuo and T.Fujimoto,*Phys.Rev.A* **37**, 77(1988)
[38]K-D. Zastrow, J.H. Brzozowski, E. Källne and H. P. Summers, **TRITA-PFU-91-09,** Stockholm (1991)
[39] S. Byron, R.C. Stabler and P.I. Bortz, *Phys.Rev.Lett.* **8**, 376 (1962)

[40] A. Carillon, M.J. Edwards, M. Grande, M.J.de C. Henshaw, P.Jaegle, G. Jamelot, M.H. Key, G.P. Kiehn, A. Klisnick, C.L.S.Lewis, D. O'Neill, G.J. Pert, S.A. Ramsden, C.M.E.Regan, S.J.Rose, R.Smith, and O.Willi, *J. Phys.B* **23**, 147 (1990)
[41] A. Klisnick, A. Sureau, H. Guennou, C. Moller, and J. Virmont, *Inst. Phys. Conf. Ser.* No116, 17 (1990)
[42] T. Fujimoto and T. Kato, *Phys. Rev. A* **32** 1663 (1985)
[43] R.U. Datla and H.J. Kunze, *Phys.Rev. A* **37**, 4614 (1989)
[44] H.-J. Kunze, *Phys. Rev. A* **3**,937 (1971)
[45] L.A. Jones, E. Källne, and D.B. Thomson, *J. Phys. B* **10**, 187 (1977)
[46] E. Källne and L.A. Jones, *J. Phys. B* **10**, 3637 (1977)
[47] W.L. Rowan and J.R. Roberts *Phys. Rev. A* **19**, 90 (1979)
[48] E. Hinnov, *J. Opt. Soc. Am.* **56**, 1179 (1966); **57**, 1392 (1962)
[49] R.U. Datla and J.R. Roberts, *Phys. Rev. A* **28**, 2201 (1983)
[50] T. Kato, **NIFS-DATA-2**, (1990)
[51] T. Nishikawa, T. Kawachi, K. Nishihara and T. Fujimoto, *NIFS report* (to be published)
[52] V. Kaufman and J. Sugar, *J. Phys. Chem. Ref. Data* **15**, 321 (1986)

Table 1 (a). Relative effective excitation rate coefficient (m^3s^{-1})

Comparison of the rate coefficients of the experiment [43] and the present calculation. The last three columns show the relative contributions from the population flows from various levels.

	T_e (eV)	n_e (m^{-3})	level	Datla and Kunze[a]	$\beta_{sampson}$ (n(2P)/n(2S))	present β_{ours}	contribution 2S	2P	I-changing
NV			5D	0.14		0.17	2%	5%	92%
			5P	0.06		0.05	2%	2%	95%
	45	5.5 (21)	4D	0.58		0.70	11%	27%	59%
			4P	0.22		0.28	18%	11%	69%
			4S	0.13	0.88	0.10	21%	27%	49%
	Θ=1.8	η=7.0 (16)	3D	3.7		5.3	22%	68%	7%
			3P	1.4		1.8	25%	43%	30%
			3S	1		1	57%	24%	17%
OVI			5D	0.15		0.14	2%	6%	92%
			5P	0.06		0.05	1%	2%	96%
	50	2.0 (21)	4D	0.96		0.68	11%	30%	56%
			4P	0.34		0.28	15%	15%	66%
			4S	0.08	0.54	0.09	21%	27%	48%
	Θ=1.4	η=7.0 (16)	3D	5.02		6.3	20%	71%	6%
			3P	2.75		2.1	18%	54%	25%
			3S	1		1	58%	24%	16%

a: ref [43]

β is the ratio of the population of $n\,(2^2P)$ and $n\,(2^2S)$, i.e., $\beta = n\,(2^2P)/n\,(2^2S)$

TABLE 1 (b). Effective ionization rate coefficient (m^3s^{-1})

Comparison of the rate coefficients between the several experimental results and the present calculation. The last column shows the relative contribution from the ladderlike excitation-ionization process.

	ref	T_e (eV)	n_e (m^{-3})	experiments	present	indirect
CIV	44	120	3.0 (21)	1.3± b (-9)	3.2 (-9)	38%
N V	47	80	4.0 (21)	7.4±2.2 (-10)	8.8 (-10)	35%
N V	46	100	1.0 (22)	9.7±2.9 (-10)	1.2 (-9)	43%
N V	44	188	4.0 (21)	5.9± b (-10)	1.5 (-9)	27%
OVI	49	55	2.5 (22)	1.4±0.3 (-10)	1.6 (-10)	55%
OVI	47	80	4.0 (21)	4.1±1.2 (-10)	2.7 (-10)	29%
OVI	46	110	1.8 (22)	3.9±1.2 (-10)	5.0 (-10)	40%
OVI	46	120	1.4 (22)	4.4±1.3 (-10)	5.6 (-10)	36%
OVI	44	200	4.0 (21)	3.4± b (-10)	6.9 (-10)	20%
NeVIII	48	65	6.0 (18)	1.4±0.7 (-11)	9.1 (-12)	3%
NeVIII	45	230	1.0 (22)	1.1±0.4 (-10)	2.0 (-10)	17%

b: factor 2

Table A-1. Fitting parameters for the energy of the excited level measured from the ground state (eV)

transition	C_1	C_2	C_3	C_4
$2s^2S$-$2p^2P_{1/2}$	2.02360	7.63516 (-3)	4.03435 (-4)	3.50523 (-6)
$2s^2S$-$2p^2P_{3/2}$	1.86034	2.09641 (-2)	9.96515 (-4)	6.54990 (-5)
$2s^2S$-$3s^2S_{1/2}$	2.03012	1.86053	2.15764 (-3)	
$2s^2S$-$3p^2P_{1/2}$	2.57010	1.86074	2.18833 (-3)	
$2s^2S$-$3p^2P_{3/2}$	2.64457	1.84622	3.02400 (-3)	
$2s^2S$-$3d^2D_{3/2}$	2.80616	1.85040	2.95088 (-3)	
$2s^2S$-$3d^2D_{5/2}$	2.82538	1.84642	3.19623 (-3)	
$2s^2S$-$4s^2S$	2.50127	2.51293	2.80191 (-3)	
$2s^2S$-$4p^2P$	2.72231	2.51292	2.82370 (-3)	
$2s^2S$-$4d^2D$	2.82148	2.50884	3.13175 (-3)	
$2s^2S$-$4f^2F$	2.85063	2.50632	3.24800 (-3)	
$2s^2S$-$5s^2S$	2.66090	2.81601	3.04306 (-3)	
$2s^2S$-$5p^2P$	2.76940	2.81645	3.04064 (-3)	
$2s^2S$-$5d^2D$	2.81834	2.81454	3.19541 (-3)	
$2s^2S$-$5f^2F$	2.83717	2.81267	3.27143 (-3)	
$2s^2S$-$5g^2G$	2.85217	2.81149	3.30877 (-3)	

* (-p) means $\times 10^{-p}$.

Table A-2. Fitting parameters for the absorption oscillator strength.

transition	C_1	C_2	C_3	C_4
2^2S-$3^2P_{1/2}$	0.13796	-0.15043	-0.38835	1.0560
2^2S-$3^2P_{3/2}$	0.24421	6.8560	-19.572	2.1160
2^2S-4^2P	9.4591 (-2)	0.75369	-2.3790	1.9990
2^2S-5^2P	7.5024 (-2)	-0.22318	-3.6884 (-2)	8.8471 (-3)
$2^2P_{1/2}$-3^2S	0.18187	0.29300	-0.15963	-1.0173 (-2)
$2^2P_{1/2}$-4^2S	0.14546	5.5335 (-2)	-0.14093	-1.9114 (-3)
$2^2P_{1/2}$-5^2S	0.13893	1.9218 (-2)	-0.13713	-7.6803 (-4)
$2^2P_{1/2}$-$3^2D_{3/2}$	0.10485	-2.0162	0.56994	6.6767 (-3)
$2^2P_{1/2}$-$4^2D_{3/2}$	0.19421	2.7930 (-2)	-6.8550 (-2)	-1.3520 (-2)
$2^2P_{1/2}$-$5^2D_{3/2}$	0.16453	4.6981 (-2)	-0.11788	-3.4209 (-3)
$2^2P_{3/2}$-3^2S	0.16013	0.34780	-0.14292	1.39333 (-3)
$2^2P_{3/2}$-4^2S	0.14563	6.3087 (-2)	-0.14200	4.2164 (-4)
$2^2P_{3/2}$-5^2S	0.14337	2.1549 (-2)	-0.14185	1.8398 (-5)
$2^2P_{3/2}$-$3^2D_{3/2}$	6.7235 (-2)	0.14974	-0.40673	1.8056
$2^2P_{3/2}$-$3^2D_{5/2}$	-0.18942	-1.4983	0.76625	-1.0197 (-2)
$2^2P_{3/2}$-4^2D	0.19102	2.4880 (-2)	-6.5457 (-2)	-1.2836 (-2)
$2^2P_{3/2}$-5^2D	0.16450	4.1760 (-2)	-0.11738	-4.7800 (-3)
3^2S-4^2P	-1.2232	-2.0861	1.4285	-4.3588 (-2)
3^2S-5^2P	0.1481	-5.4063 (-2)	-0.2166	0.58345
$3^2P_{1/2}$-4^2S	4.6238 (-2)	-0.27642	3.2633	2.3769
$3^2P_{1/2}$-5^2S	1.2355 (-2)	-0.80070	6.3012	2.7435
$3^2P_{1/2}$-4^2D	-2.1699	-0.52680	2.7021	-6.9282 (-3)
$3^2P_{3/2}$-5^2D	0.23246	-1.9082 (-2)	-0.10674	3.9274 (-2)
$3^2P_{3/2}$-4, $5\,^2S$	same as $3^2P_{1/2}$			
$3^2P_{3/2}$-4, $5\,^2D$	same as $3^2P_{1/2}$			
$3^2D_{3/2}$-4^2P	7.2805 (-3)	1.7312	-16.312	2.9344
$3^2D_{3/2}$-5^2P	1.8186 (-3)	0.25527	-2.3983	2.9326
$3^2D_{3/2}$-4^2F	1.015	0.0000	0.0000	------
$3^2D_{3/2}$-5^2F	0.1565	0.0000	0.0000	------

Table A-2. (Continued)

transition	C_1	C_2	C_3	C_4
$3^2D_{5/2}$-4, 5 ^2P	same as $3^2D_{3/2}$			
$3^2D_{5/2}$-4, 5 ^2F	same as $3^2D_{3/2}$			
4^2S-5^2P	-3.0129	-1.5386	3.1378	-3.2640 (-2)
4^2P-5^2S	4.8882 (-2)	6.2580	-66.580	3.0805
4^2P-5^2D	-2.4693	-0.13835	2.9084	-1.5923 (-2)
4^2D-5^2P	2.4435 (-2)	2.2772	-23.664	3.0081
4^2D-5^2F	0.8855	0.0000	0.0000	-------
4^2F-5^2D	8.8392 (-3)	2.5175 (-2)	-0.64736	3.5608
4^2F-5^2G	1.346	0.0000	0.0000	-------

Table A-3. Absorption Oscillator Strength

transition	$2^2S_{1/2}$ - n^2P	$2^2P_{1/2,3/2}$ - n^2S	$2^2P_{1/2,3/2}$ - n^2D	$3^2S_{1/2}$ - n^2P
a	-3.8	-3.48	-3.50	-4.25
transition	$3^2P_{1/2,3/2}$ - n^2S	$3^2P_{1/2,3/2}$ - n^2D	$3^2D_{3/2,5/2}$ - n^2P	$3^2D_{3/2,5/2}$ - n^2F
a	-4.08	-4.21	-5.40	-4.41
transition	4^2S - n^2P	4^2P- n^2S	4^2P - n^2D	4^2D - n^2P
a	-5.08	-5.95	-5.27	-6.83
transition	4^2D - n^2F	4^2F- n^2D	4^2F - n^2G	
a	-6.00	-5.94	-5.95	

Table A-4. Absorption Oscillator Strength for Δn=0 transitions

transition	$3^2S_{1/2}$ - $3^2P_{1/2}$	$3^2S_{1/2}$ - $3^2P_{3/2}$	$3^2P_{1/2}$ - $3^2D_{3/2}$	$3^2P_{3/2}$ - $3^2D_{3/2}$
O.S.	0.112	0.224	0.0488	4.78 (-3)
transition	$3^2P_{3/2}$ - $3^2D_{5/2}$	4^2S - 4^2P	4^2P - 4^2D	4^2D - 4^2F
O.S.	0.0433	0.4616	8.555 (-2)	2.374 (-3)
transition	5^2S - 5^2P	5^2P - 5^2D	5^2D - 5^2F	5^2F - 5^2G
O.S.	0.5860	0.1184	5.606 (-3)	4.18 (-4)

O.S. means the oscillator strength.

Table A-5. Excitation cross section fitting parameters.

transition	A	B	C	D	Ref
2^2S - 2^2P	2.234 (-1)	5.625 (1)	- 1.648	3.00 (-2)	4
2^2S - 3^2S	0.000	1.481	5.694 (-1)	6.50 (-2)	4
2^2S - 3^2P	1.706 (-1)	- 5.800 (-1)	6.250 (-2) 1.800 (1)	1.40 (-2) 9.60 (-2)	4
2^2S - 3^2D	0.000	3.470	- 5.860 (-2)	1.50 (-2)	4
2^2S - 4^2S	0.000	2.961 (-1)	- 2.278 (-2)	3.70 (-2)	4
2^2S - 4^2P	9.634 (-3)	1.760 (-1)	- 6.534 (-3)	8.00 (-2)	4
2^2S - 4^2D	0.000	6.030 (-1)	- 5.400 (-3)	1.30 (-2)	4
2^2S - 4^2F	0.000	1.424 (-1)	0.000	0.00	4
2^2S - 5^2S	0.000	1.139 (-1)	- 2.278 (-3)	1.98 (-2)	4
2^2S - 5^2P	4.043 (-3)	8.610 (-2)	- 2.468 (-3)	6.50 (-3)	4
2^2S - 5^2D	0.000	2.097 (-1)	- 1.502 (-3)	1.20 (-2)	4
2^2S - 5^2F	0.000	8.030 (-2)	- 1.141 (-4)	1.00 (-2)	4
2^2S - 5^2G	0.000	3.417 (-3)	5.695 (-3)	4.00 (-2)	4
2^2P - 3^2S	5.826 (-3)	1.642 (-1)	- 4.358 (-3)	7.90 (-3)	4
2^2P - 3^2P	0.000	1.987	0.000	0.000	4
2^2P - 3^2D	1.240 (-1)	7.270	1.280 (-1)	9.20 (-3)	4
2^2P - 4^2S	8.076 (-4)	3.911 (-2)	- 4.632 (-4)	5.00 (-3)	4
2^2P - 4^2P	0.000	3.673 (-1)	1.708 (-2)	2.98 (-2)	4
2^2P - 4^2D	1.756 (-2)	1.279	- 1.200 (-2)	7.20 (-3)	4
2^2P - 4^2F	0.000	2.707 (-1)	- 2.500 (-3)	9.00 (-3)	4
2^2P - 5^2S	2.764 (-4)	1.726 (-2)	- 1.534 (-4)	3.88 (-3)	4
2^2P - 5^2P	0.000	1.481 (-1)	1.162 (-2)	3.00 (-2)	4
2^2P - 5^2D	5.876 (-3)	5.340 (-1)	- 5.200 (-3)	7.20 (-3)	4
2^2P - 5^2F	0.000	1.139 (-1)	0.000	0.000	4
2^2S - 5^2G	0.000	5.125 (-3)	6.834 (-2)	6.99 (-2)	4
3^2S - 4^2S	0.000	4.320	0.000	0.000	13
3^2S - 4^2P	1.627 (-1)	1.263 (1)	- 2.721 (-1) - 1.174	1.28 (-2) 6.01 (-2)	13
3^2S - 4^2D	0.000	8.200	- 3.209 (-1)	3.00 (-2)	13
3^2S - 4^2F	0.000	3.880	0.000	0.00	13
3^2S - 5^2S	0.000	7.652 (-1)	0.000	0.00	13
3^2S - 5^2P	1.638 (-1)	2.270 (-1)	- 2.800 (-2)	2.00 (-2)	13
3^2S - 5^2D	0.000	1.260	- 1.000 (-2)	2.00 (-2)	13
3^2S - 5^2F	0.000	3.270 (-1)	6.843 (-2)	4.73 (-2)	13
3^2S - 5^2G	0.000	7.830 (-1)	1.580 (-1)	6.70 (-2)	13

Table A-5. (Continued)

transition	A	B	C	D	ref
3^2P - 4^2S	3.758 (-2)	7.956 (-1)	- 1.621 (-2) - 5.930 (-2)	1.12 (-1) 5.20 (-2)	13
3^2P - 4^2P	0.000	5.030	- 3.998 (-2)	2.50 (-2)	13
3^2P - 4^2D	0.3014	6.100	- 2.170 (-1)	2.41 (-2)	13
3^2P - 4^2F	0.000	1.013 (1)	- 4.000 (-1)	4.00 (-2)	13
3^2P - 5^2S	9.502 (-3)	- 3.300 (-1)	3.500 (-2)	5.20 (-2)	13
3^2P - 5^2P	0.000	9.697(-1)	7.600 (-1)	1.80 (-1)	13
3^2P - 5^2D	9.832 (-2)	- 2.856	1.476 (-1)	4.40 (-2)	13
3^2P - 5^2F	0.000	7.921 (-1)	1.134	1.20 (-1)	13
3^2P - 5^2G	0.000	1.090	1.130	1.20 (-1)	13
3^2D - 4^2S	0.000	9.000 (-1)	7.000 (-3)	2.00 (-1)	13
3^2D - 4^2P	8.954 (-3)	4.900 (-1)	- 6.600 (-3)	1.55 (-2)	13
3^2D - 4^2D	0.000	4.170	4.950 (-2)	1.00 (-1)	13
3^2D - 4^2F	5.776 (-1)	2.049 (1)	- 4.200 (-1)	1.50 (-2)	13
3^2D - 5^2S	0.000	2.280 (-2)	8.400 (-3)	5.00 (-2)	13
3^2D - 5^2P	2.144 (-3)	1.800 (-2)	3.300 (-2)	4.30 (-2)	13
3^2D - 5^2D	0.000	7.600 (-1)	1.240 (-1)	5.50 (-2)	13
3^2D - 5^2F	2.448 (-1)	- 5.884	1.402 (-1) 4.401	1.50 (-2) 1.02 (-1)	13
3^2D - 5^2G	0.000	1.588	- 1.881 (-2)	1.50 (-2)	13
4^2S - 5^2S	0.000	2.340 (1)	0.000	0.000	13
4^2S - 5^2P	1.299	- 9.879	- 7.421	1.56 (-1)	13
4^2S - 5^2D	0.000	2.233 (1)	- 7.493 (-1)	2.50 (-2)	13
4^2S - 5^2F	0.000	1.046 (1)	0.000	0.000	13
4^2S - 5^2G	0.000	9.112	0.000	0.000	13
4^2P - 5^2S	7.736 (-2)	0.000	4.408 (-1)	1.55 (-1)	13
4^2P - 5^2P	0.000	2.847 (1)	0.000	0.000	13
4^2P - 5^2D	2.320	- 3.234	8.876	1.40 (-1)	13
4^2P - 5^2F	0.000	3.840 (1)	- 3.102	6.00 (-2)	13
4^2P - 5^2G	0.000	1.481 (1)	0.000	0.00	13
4^2D - 5^2S	0.000	4.320 (-1)	- 1.000 (-2)	5.50 (-2)	12

Table A-5. (Continued)

transition	A	B	C	D	Ref
4^2D - 5^2P	1.642 (-1)	- 2.897	2.570 (-1) 1.164	4.50 (-2) 1.45 (-1)	13
4^2D - 5^2D	0.000	1.396 (1)	- 1.200 (-1)	5.50 (-2)	12
4^2D - 5^2F	3.854	- 6.663 (1)	5.911 2.401 (1)	4.50 (-2) 1.45 (-1)	12
4^2D - 5^2G	0.000	2.247 (1)	- 9.480 (-1)	5.50 (-2)	12
4^2F - 5^2S	0.000	6.282 (-2)	5.180 (-2)	1.25 (-1)	12
4^2F - 5^2P	0.000	3.021 (-1)	1.498 (-1)	1.25 (-1)	12
4^2F - 5^2D	3.959 (-2)	5.031 (-1)	1.000	1.45 (-1)	12
4^2F - 5^2F	0.000	1.119 (1)	8.680 (-1)	1.25 (-1)	12
4^2F - 5^2G	5.858	-7.367	7.064 3.834 (1)	4.50 (-2) 1.45 (-1)	12

TableA-6. The fitting parameters for the *l*-changing process

transition	A	B	C	D	Ref
3^2S-3^2P	5.345	2.180 (2)	4.172 (1)	1.56 (-1)	13
4^2S-4^2P	2.511 (1)	7.912 (2)	4.960 (2)	2.86 (-1)	13
5^2S-5^2P	6.308 (1)	1.962 (3)	1.240 (3)	2.86 (-1)	13

Table A-7. Deexcitation Rate Coefficients

transition	K	L	M	N	P	factor
2^2S - 2^2P	25.0	0.55	60.2	0.0		1.0e-15
2^2S - 3^2S	290.0	0.62	600.	0.0		1.0e-17
2^2S - 3^2P	11.0	0.2	185.	0.0		1.0e-17
2^2S - 3^2D	58.0	0.5	360.	0.0		1.0e-17
2^2S - 4^2S	48.0	0.6	200.	0.0		1.0e-17
2^2S - 4^2P	11.7	0.43	50.0	5.7	0.01	1.0e-17
2^2S - 4^2D	14.0	0.55	77.1	0.0		1.0e-17
2^2S - 4^2F	35.0	0.6	150.0	0.0		1.0e-18
2^2S - 5^2S	14.5	0.58	120.0	0.0		1.0e-17
2^2S - 5^2P	10.0	0.5	15.0	-4.15	0.005	1.0e-17
2^2S - 5^2D	8.3	0.62	21.3	0.0		1.0e-17
2^2S - 5^2F	38.0	0.7	40.0	0.0		1.0e-18
2^2S - 5^2G	28.0	0.8	70.0	560.0	0.52	1.0e-19
2^2P - 3^2S	101.0	0.5	403	-44.0	0.01	1.0e-17
2^2P - 3^2P	165.0	0.5	2640	0.0		1.0e-17
2^2P - 3^2D	63.0	0.5	231.6	-12.0	0.01	1.0e-16
2^2P - 4^2S	15.5	0.5	80.0	-3.0	0.005	1.0e-16
2^2P - 4^2P	33.25	0.5	550.0	8.0	0.01	1.0e-17
2^2P - 4^2D	12.0	0.5	78.0	-3.0	0.005	1.0e-16
2^2P - 4^2F	9.5	0.5	50.0	0.0		1.0e-17
2^2P - 5^2S	800.0	0.5	2.0e3	-160.0	0.003	1.0e-19
2^2P - 5^2P	34.8	0.65	130.5	0.0		1.0e-17
2^2P - 5^2D	32.0	0.45	238.0	0.0		1.0e-17
2^2P - 5^2F	12.0	0.65	45.0	0.0		1.0e-17
2^2P - 5^2G	60.0	0.7	240.5	0.0		1.0e-19
3^2S - 4^2S	6.00	0.5	74.0	1.0	0.01	1.0e-15
3^2S - 4^2P	70.5	0.5	30.0	-30.0	0.007	1.0e-16
3^2S - 4^2D	22.5	0.5	110.0	0.0	0.00	1.0e-16
3^2S - 4^2F	8.00	0.5	100.0	2.0	0.01	1.0e-16

Table A-7. (Continued)

transition	K	L	M	N	P	factor
3^2S - 5^2S	13.0	0.6	45.0	0.0	0.0	1.0e-16
3^2S - 5^2P	10.0	0.5	0.5	-4.2	0.05	1.0e-16
3^2S - 5^2D	48.0	0.6	80.0	0.0	0.0	1.0e-17
3^2S - 5^2F	18.0	0.7	0.0	270.0	0.4	1.0e-17
3^2S - 5^2G	18.0	0.62	50.0	0.0	0.0	1.0e-17
3^2P - 4^2S	17.2	0.35	77.0	-7.3	0.01	1.0e-16
3^2P - 4^2P	280.0	0.7	350.0	0.0		1.0e-16
3^2P - 4^2D	55.0	0.3	500.0	0.0		1.0e-16
3^2P - 4^2F	110.0	0.6	180.3	0.0		1.0e-16
3^2P - 5^2S	56.7	0.5	83.3	-19.3	0.0038	1.0e-17
3^2P - 5^2P	220.0	0.65	450.0	0.0		1.0e-17
3^2P - 5^2D	24.8	0.5	36.12	-6.4	0.0045	1.0e-16
3^2P - 5^2F	8.0	0.65	20.0	0.0		1.0e-16
3^2P - 5^2G	8.0	0.65	20.0	0.0		1.0e-16
3^2D - 4^2S	140.0	0.6	600.0	0.0		1.0e-17
3^2D - 4^2P	145.0	0.5	1100.0	-25.0	0.01	1.0e-17
3^2D - 4^2D	40.0	0.85	400.0	-2.0	0.01	1.0e-17
3^2D - 4^2F	50.0	0.5	190.0	-13.0	0.01	1.0e-15
3^2D - 5^2S	24.0	0.62	144.0	0.0		1.0e-17
3^2D - 5^2P	24.0	0.55	230.0	4.0 (3)	0.8	1.0e-17
3^2D - 5^2D	170.0	0.65	800.0	0.0		1.0e-17
3^2D - 5^2F	400.0	0.5	1900.0	-70.0	0.005	1.0e-17
3^2D - 5^2G	8.0	0.5	90.0	850.0	0.32	1.0e-16
4^2S - 5^2S	50.0	0.65	700.0	4.0e4	0.8	1.0e-15
4^2S - 5^2P	6.0	0.42	0.0	112.0	0.22	1.0e-15
4^2S - 5^2D	7.0	0.6	66.0	84.0	0.2	1.0e-15
4^2S - 5^2F	6.0	0.7	60.0	78.0	0.2	1.0e-15
4^2S - 5^2G	1.5	0.6	50.0	59.0	0.2	1.0e-15
4^2P - 5^2S	60.0	0.55	-1	-24.3	0.013	1.0e-15
4^2P - 5^2P	65.0	0.65	216.0	0.0		1.0e-15

Table A-7. (Continued)

transition	K	L	M	N	P	factor
4^2P - 5^2D	45.0	0.5	50.0	-12.0	0.01	1.0e-15
4^2P - 5^2F	36.0	0.65	50.0	0.0		1.0e-15
4^2P - 5^2G	12.0	0.65	45.0	0.0		1.0e-15
4^2D - 5^2S	50.0	0.62	190.0	0.0		1.0e-16
4^2D - 5^2P	50.0	0.5	60.0	100.0	0.20	1.0e-16
4^2D - 5^2D	298.0	0.65	1490	0.0		1.0e-16
4^2D - 5^2F	300.0	0.4	0.0	1000	0.2	1.0e-16
4^2D - 5^2G	240.0	0.6	995.0	0.0		1.0e-16
4^2F - 5^2S	50.0	0.88	302.0	784.0	0.5	1.0e-16
4^2F - 5^2P	24.0	0.7	333.0	0.0		1.0e-16
4^2F - 5^2D	20.0	0.5	487.0	0.0		1.0e-16
4^2F - 5^2F	250.0	0.65	1800	0.0		1.0e-16
4^2F - 5^2G	120.0	0.5	380	-25.0	0.005	1.0e-15

Table A-8. Deexcitation Rate Coefficients for *l*-changing transition

transition	K	L	M	N	P	factor
3^2S-3^2P	2.5	0.6	0.0	4.1	0.3	1.0e-13
3^2P-3^2D	3.5	0.7	0.0	37.0	0.5	1.0e-13
4^2S-4^2P	5.0	0.5	20.0	0.0		1.0e-13
4^2P-4^2D	1.3	0.6	0.0	3.0	0.4	1.0e-12
4^2D-4^2F	1.0	0.6	0.0	2.0	0.3	1.0e-12
5^2S-5^2P	2.7	0.6	0.0	5.0	0.3	1.0e-12
5^2P-5^2D	3.3	0.6	0.0	6.3	0.3	1.0e-12
5^2D-5^2F	4.1	0.6	0.0	8.0	0.3	1.0e-12
5^2F-5^2G	4.3	0.6	0.0	8.23	0.3	1.0e-12

Table A-9. Dielectronic recombination rate coefficient

Dielectronic recombination rate coefficient by ref [33]

$$\alpha_d(1,nl) = \sum_p^{\infty} Z(p,nl)\,\frac{A_a A_{r1}}{A_a + A_{r2}}$$

$$= \sum_p^{\infty} \frac{g_z(p,nl)}{2g_z}\left(\frac{h^2}{2\pi m k T_e}\right)^{1.5} \exp[E(p,nl)/T_e]\,\frac{A_a A_{r1}}{A_a + A_{r2}}$$

$$= 2.07\times 10^{-16} \sum_p^{\infty} \frac{g_z(p,nl)}{2} T_e^{-1.5} \exp[E(p,nl)/T_e]\,\frac{A_a A_{r1}}{A_a + A_{r2}}$$

$$E(p,nl)\ [\mathrm{eV}] = (550 - E(nl))/[(z-2)/(8-2)]^2$$

The transition to the 2^2P

transition	weight	autoionization	radiative decay A_{r1}	rad. decay A_{r2}
a	4	9.44e10	3.97e12	4.71e12
b	4	9.44e10	7.21e11	4.71e12
j	6	9.80e13	1.48e12	1.48e12
k	4	9.79e13	1.29e12	1.49e12
l	4	9.79e13	1.88e11	1.49e12
m	2	8.71e12	9.28e11	1.38e12
n	2	8.71e12	4.37e11	1.38e12
p	2	1.02e14	1.22e11	1.90e11

The transitions are expressed by Gabriel notation

The transition to the 3^2S

transition	weight	autoionization	A_{r1}	A_{r2}
$1s^2 3s$ - $1s2p3s$	6	6.9e12	2.47e12	2.73e12
- $1s2p3s$	6	2.65e13	3.68e11	3.97e11
- $1s2s3p$	6	4.45e11	2.13e11	6.43e11
- $1s2p3d$	6	9.06e10	1.38e11	3.43e11

The transition to the 3^2P

transition	weight	autoionization	A_{r1}	A_{r2}
$1s^2 3p$ - $1s2p3p$	2	5.87e12	2.27e12	2.31e12
	2	1.61e12	6.10e11	1.55e12
	10	2.43e13	2.39e12	2.57e12
	10	1.75e13	7.66e11	1.35e12
- $1s2s3s$	2	1.68e13	3.43e11	4.27e11

The transition to the 3^2D

transition	weight	autoionization	A_{r1}	A_{r2}
$1s^2 3d$ - $1s2p3d$	6	7.65e10	2.93e12	2.93e12
	6	9.06e10	1.11e11	3.43e11
	14	6.32e12	2.63e12	2.76e12
	14	7.65e10	6.09e11	6.73e12
- $1s2p3s$	6	2.65e13	1.22e11	6.43e11

The transition to the 4^2S

Transition	weight	autoionization	A_{r1}	A_{r2}
$1s^2 4s$ - $1s2p4s$	6	1.89e12	2.60e12	2.71e12

The transition to the 4^2P

transition	weight	autoionization	A_{r1}	A_{r2}
$1s^2 4p$ - $1s2p4p$	2	1.16e12	2.92e12	3.00e12
-	10	7.07e12	3.12e12	3.29e12
- $1s2s4s$	10	6.01e12	1.49e11	1.90e11

The transition to the 4^2D

transition	weight	autoionization	A_{r1}	A_{r2}
$1s^2 4d$ - $1s2p4d$	6	1.62e11	3.19e12	3.28e12
	6	2.19e11	3.07e10	3.07e10
	14	3.20e12	3.13e12	3.13e12
	14	3.01e11	5.39e10	9.47e10

The transition to the 4^2F

transition	weight	autoionization	A_{r1}	A_{r2}
$1s^2 4f$ - $1s2p4f$	10	4.47e10	3.33e12	3.36e12
-	18	1.46e11	3.28e12	3.30e12

The transition to the levels with n=5

transition	weight	autoionization	A_{r1}	A_{r2}
$1s^2 5s$-$1s2p5s$	6	2.80e11	3.26e12	3.32e12
$1s^2 5p$-$1s2p5p$	2	1.05e12	3.27e12	3.32e12
	10	3.39e12	3.23e12	3.37e12
$1s^2 5d$-$1s2p5d$	6	1.28e11	3.31e12	3.37e12
	14	1.70e12	3.27e12	3.30e12
$1s^2 5f$-$1s2p5f$	10	5.95e10	3.36e12	3.38e12
	18	1.17e11	3.30e12	3.31e12
$1s^2 5g$-$1s2p5g$	22	9.53e9	3.30e12	3.31e12

For the transition to the level with $n \geq 6$, we assume hydrogenic approximation, and the autoionization probability is given as

$$A_a = \frac{4}{h\,n^3}\,\frac{R}{g(p,nl)}\,z^2\Omega\ (1s^2 \rightarrow 1s\,2p)$$

where $z^2\Omega\ (1s^2 \rightarrow 1s\,2p) = 2.355$ at the threshold.

transition	weight	autoionization	A_{r1}	A_{r2}
$1s^2 n$-$1s2pn$	$2n^2$+4n		3.30e12	3.30e12

Figure Captions

Fig. 1. Energy level diagram of the lithium-like oxygen (OVI or O^{5+}) ion.

Fig. 2. Energy levels of the excited levels of ions z measured from the ground state and the ionization potential of the ground state. The abssissa is the effective nuclear charge; z_{eff}=z-2.

Fig. 3. z_{eff}-dependence of the absorption oscillator strength for several transitions. Corresponding oscillator strength values for neutral hydrogen are given for the $n = 2 - n = 3$ transitions.

Fig. 4. Electron impact excitaion cross section of optically allowed transitions; (a) for transition of 2^2S-3^2P ; (b) 2^2P-3^2S.

Fig. 5. Electron impact excitaion cross section of optically forbidden transition of 2^2S-3^2S.

Fig. 6. Electron impact l-changing cross section; (a) for 3^2S-3^2P ; (b) for 3^2P-3^2D. The results by Jacobs and Davis has been derived from their semiempirical rate coefficient.

Fig. 7. The ionizing plasma component of the excited level populations of OVI ions. $n(2^2S)$ and T_e are assumed to be $1cm^{-3}$ and 50eV, respectively. Proton (ion) collisions are included.

Fig. 8. Population flow (a) into and (b) out of level 4^2P for the ionizing plasma component in Fig.7. The magnitude of the flow has been divided by electron density for convenience. The number attached on the right side is the magnitude at the high density limit.

Fig. 9. Population distribution against the effective principal quantum number for both the ionizing plasma component (OVI; open circle) and the

recombining plasma component (AlXI; open triangle). The Solid curve ('S-B') denotes the Saha-Boltzmann distribution. The straight lines have slope -6, indicating the ladder-like excitation or deexcitation.

Fig. 10. Photon emission ratios from lithium-like carbon, nitrogen and oxygen ions for the transitions of 2^2P-3^2D to 2^2P-3^2S and 2^2S-3^2P to 2^2P-3^2S. Electron density is assumed to be $n_e = 10^{19}m^{-3}$. We compare the calculation results for the two different 2^2S-3^2P excitation cross sections.

Fig. 11. The recombining plasma component of the excited level populations of AlXI ions (Al^{10+}). T_e is assumed to be 30eV. Ion collisions are included.

Fig. 12. population flow (a) into and (b) out of level 4^2P for the recombining plasma component in Fig.11. The magnitude of the flow has been divided by electron density for convenience. The number attached on the right side is the magnitude at the high density limit.

Fig. 13. Absolute amplification gain for several transitions in recombining lithium-like aluminum ions. All the gains have been multiplized by 10 except for those for the 3^2P-4^2D and 3^2D-4^2F transitions.

Fig. 14. Optimum temperature is shown as a function of effective nuclear charge z_{eff}, where z_{eff}=z-2 for lithium-like ions and z_{eff}=z for hydrogenic ions.

Fig. 15. The ratios of the recombining plasma component $n_0(p)$ $(=R_0(p)n_e n_{He})$ to the ionizing plasma component $n_1(p)$ $(=R_1(p)n_e n_{Li})$ under the condition of ionization balance. T_e=50eV and n_e=$1.0\times10^{13}m^{-3}$ for OVI (open circle), T_e=30eV and n_e=$1.0\times10^{13}m^{-3}$ for AlXI (closed circle).

Fig. 16. z-dependence of the population imbalance; (a) between the $2p^2P_{1/2}$ and $2p^2P_{3/2}$ levels for several reduced electron densities; (b) between the $3p^2P_{1/2}$ and $3p^2P_{3/2}$ levels.

Fig. 17. Comparison of the relative population of several excited levels of OVI and NV ions in ionizing plasma with the experimental results by Datla and Kunze [43]. OVI and NV populations are expressed by the open and closed symbols, respectively. The plasma conditions are referred to table 1(a).

Fig. 18. The n_e-dependence of S_{eff} of OVI for several temperatures. Experimental results are compared.

Fig. 19. Comparison of the calculated population of several levels of OVI and NV ions in recombining plasma with the experimental results by Datla and Kunze [43] in Boltzmann plots. The calculation results has been multiplized by a factor 100.

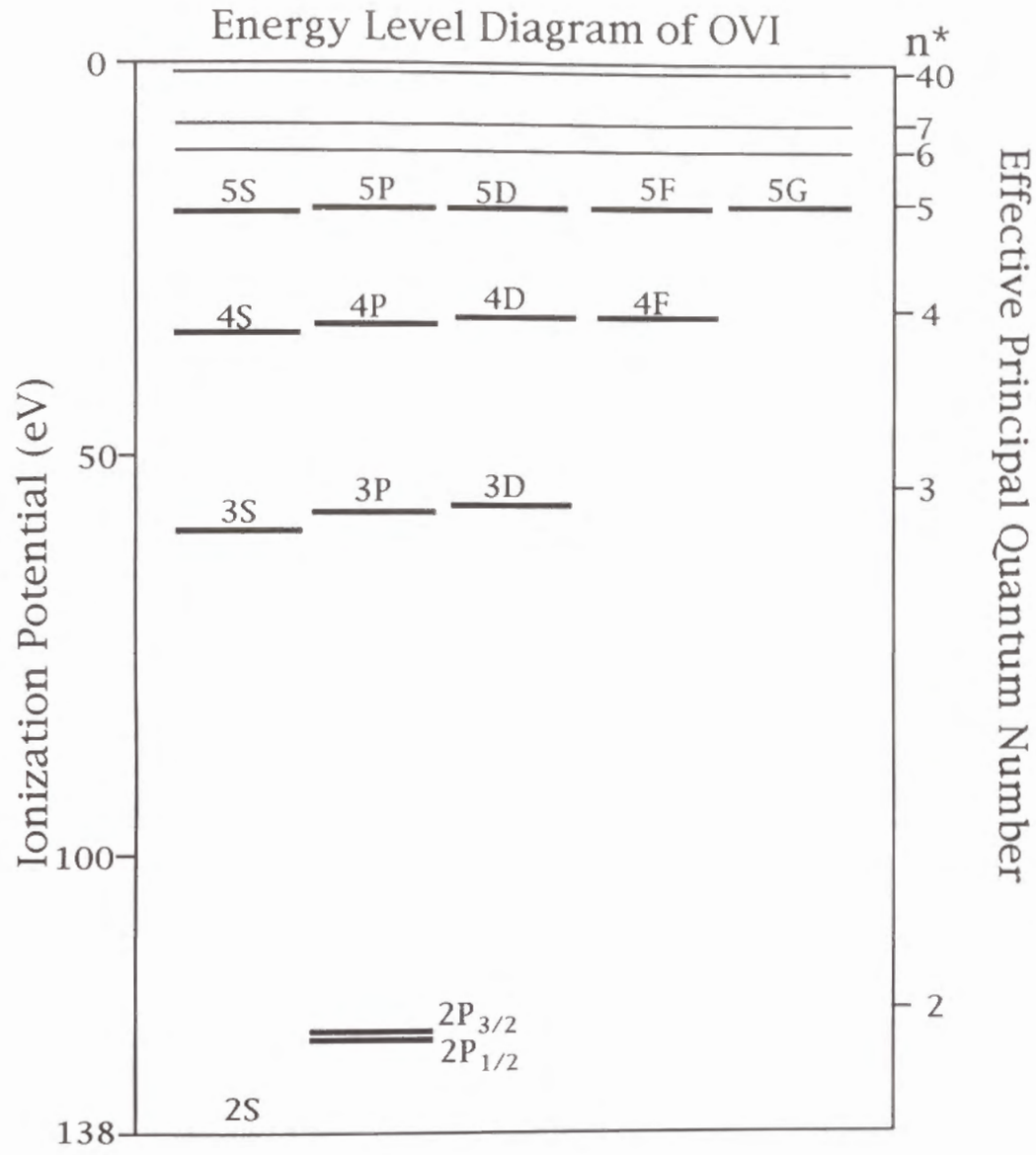

Fig. 1

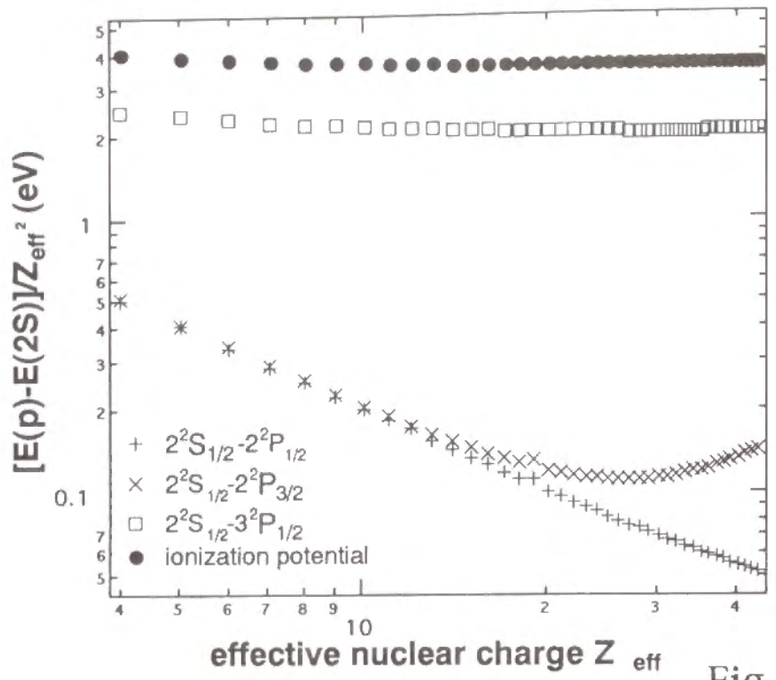

Fig. 2

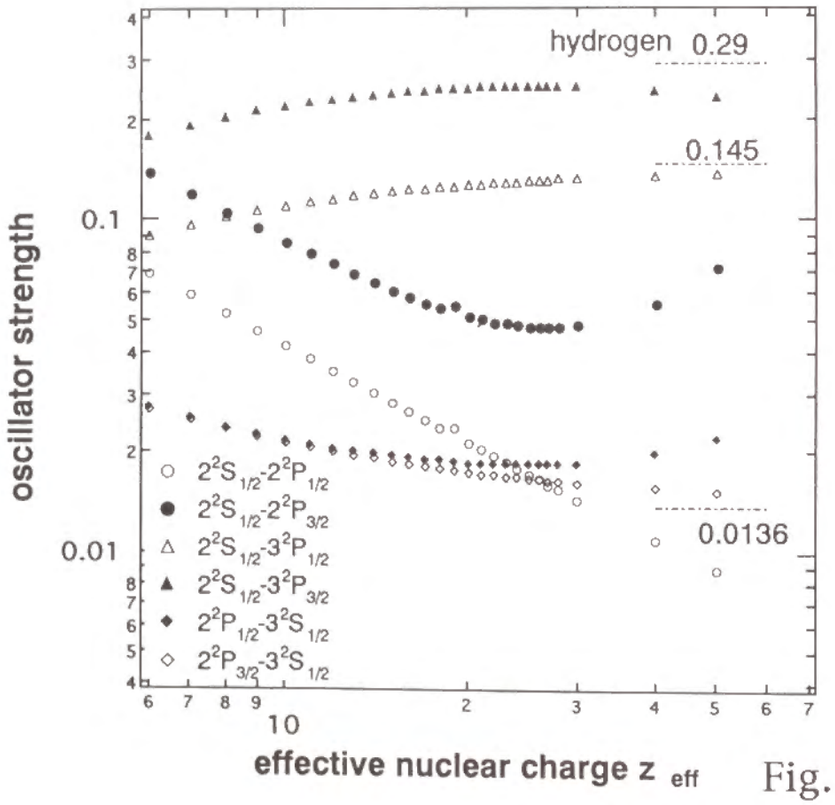

Fig. 3

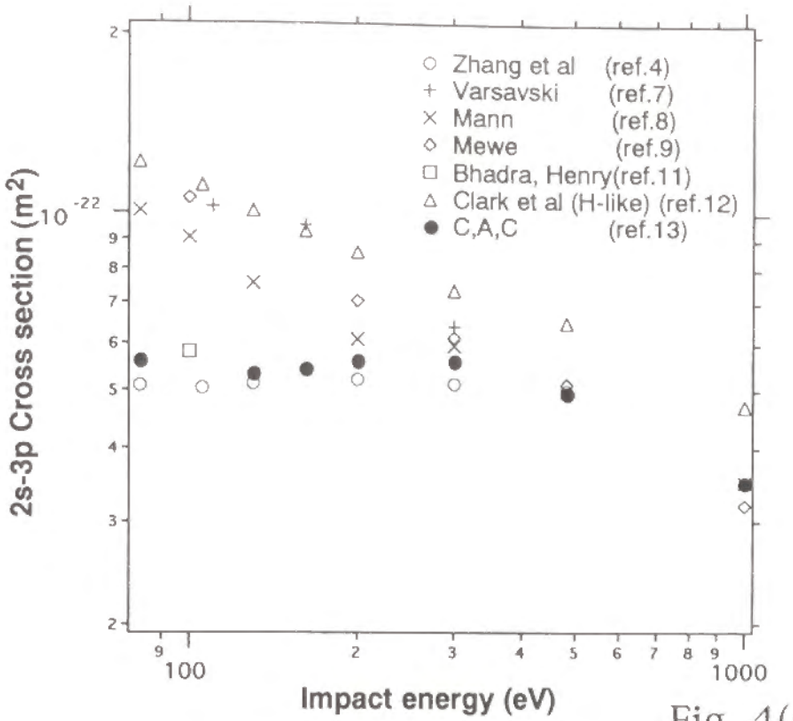

Fig. 4(a)

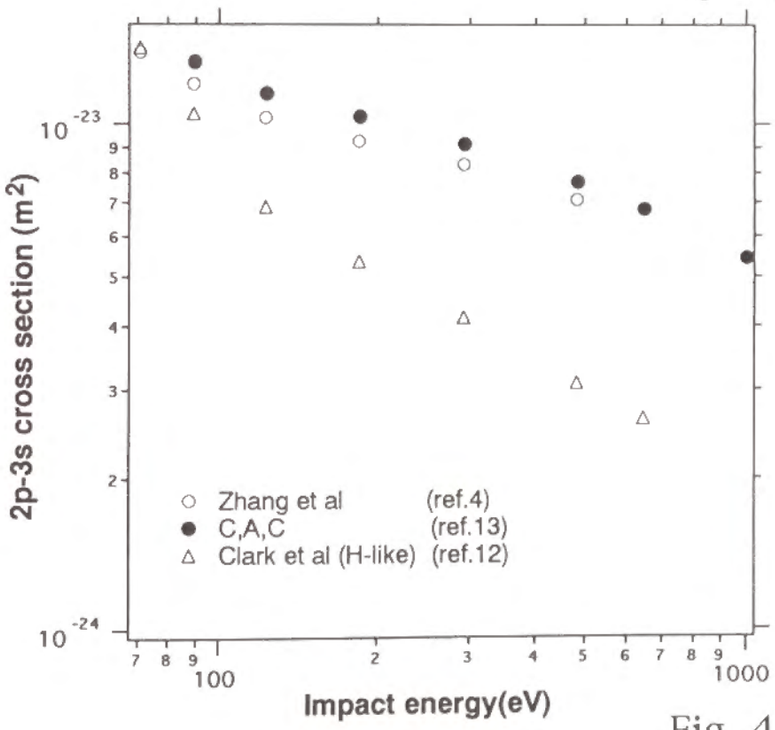

Fig. 4(b)

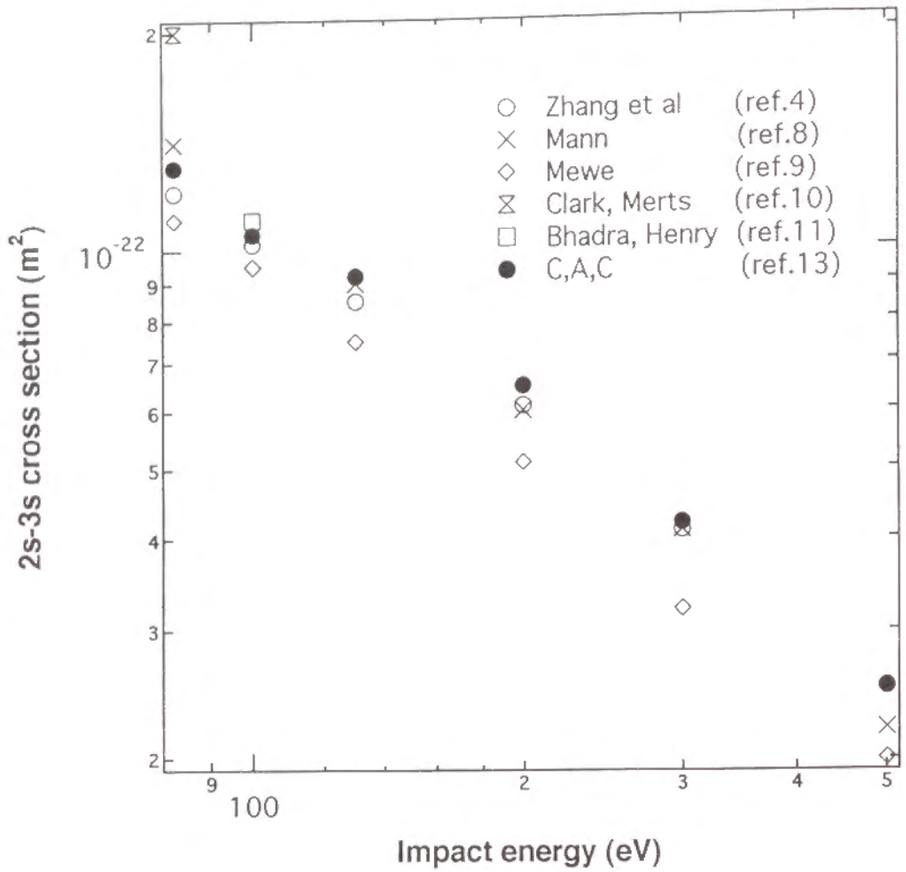

Fig.5

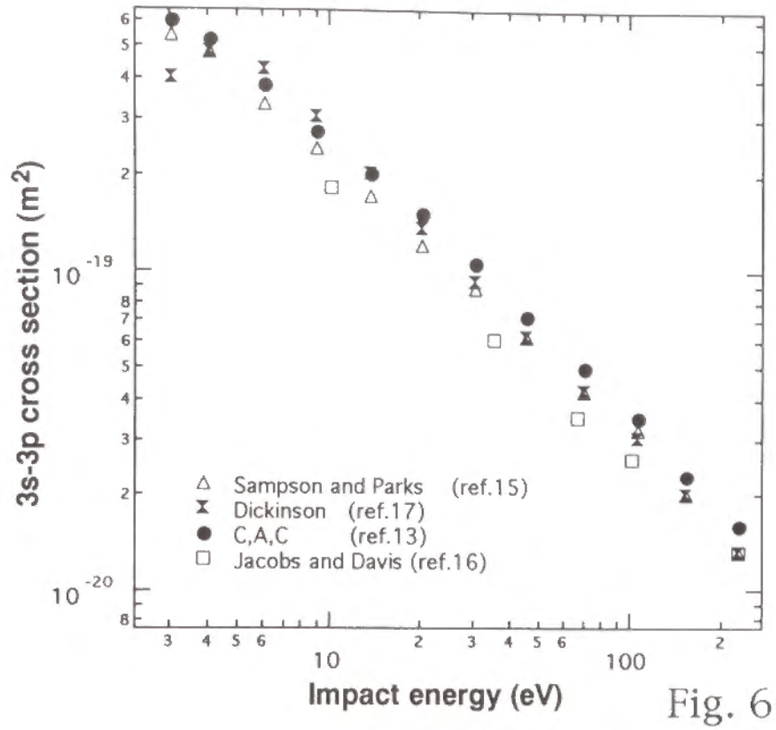

Fig. 6(a)

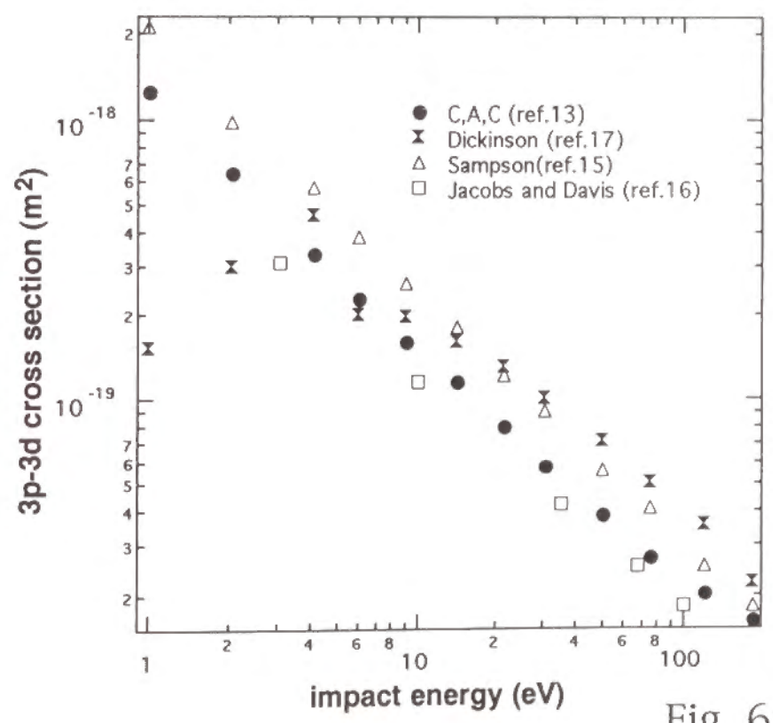

Fig. 6(b)

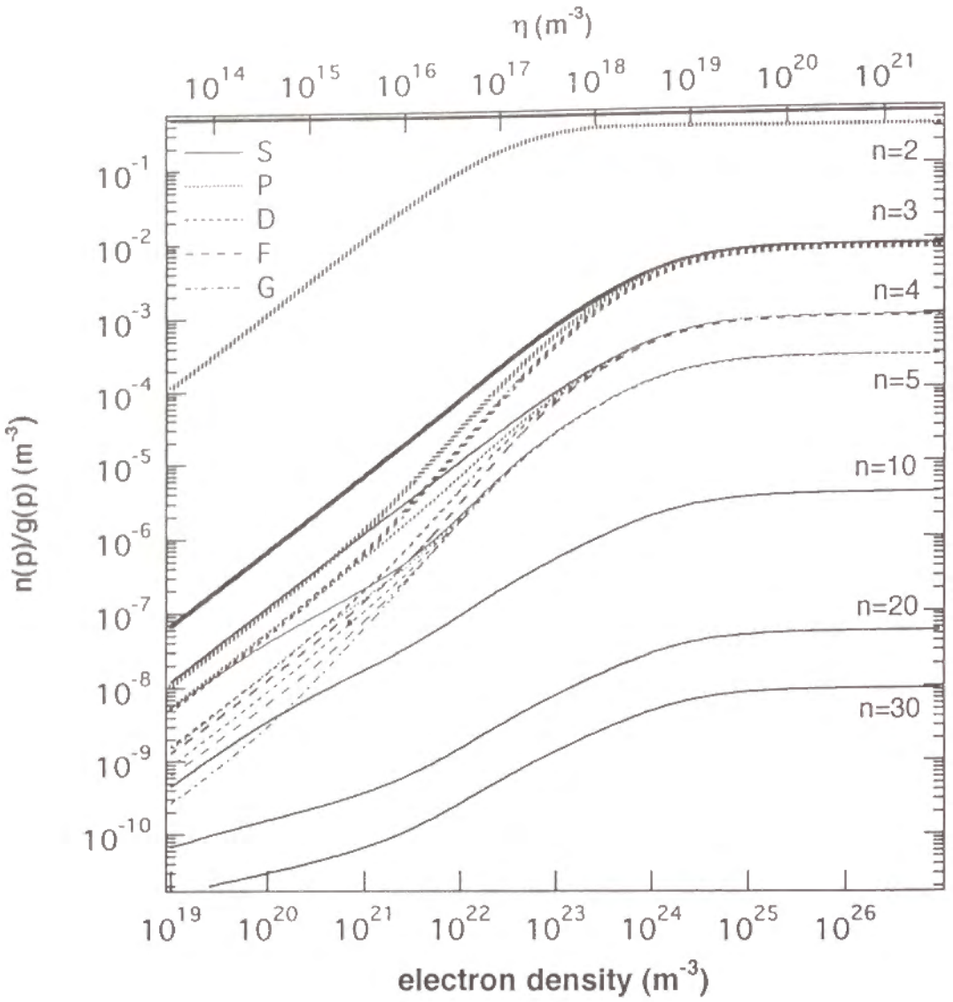
η (m⁻³)
10¹⁴ 10¹⁵ 10¹⁶ 10¹⁷ 10¹⁸ 10¹⁹ 10²⁰ 10²¹
S
P
D
F
G
n=2
n=3
n=4
n=5
n=10
n=20
n=30
n(p)/g(p) (m⁻³)
10⁻¹ 10⁻² 10⁻³ 10⁻⁴ 10⁻⁵ 10⁻⁶ 10⁻⁷ 10⁻⁸ 10⁻⁹ 10⁻¹⁰
10¹⁹ 10²⁰ 10²¹ 10²² 10²³ 10²⁴ 10²⁵ 10²⁶
electron density (m⁻³)

Fig.7

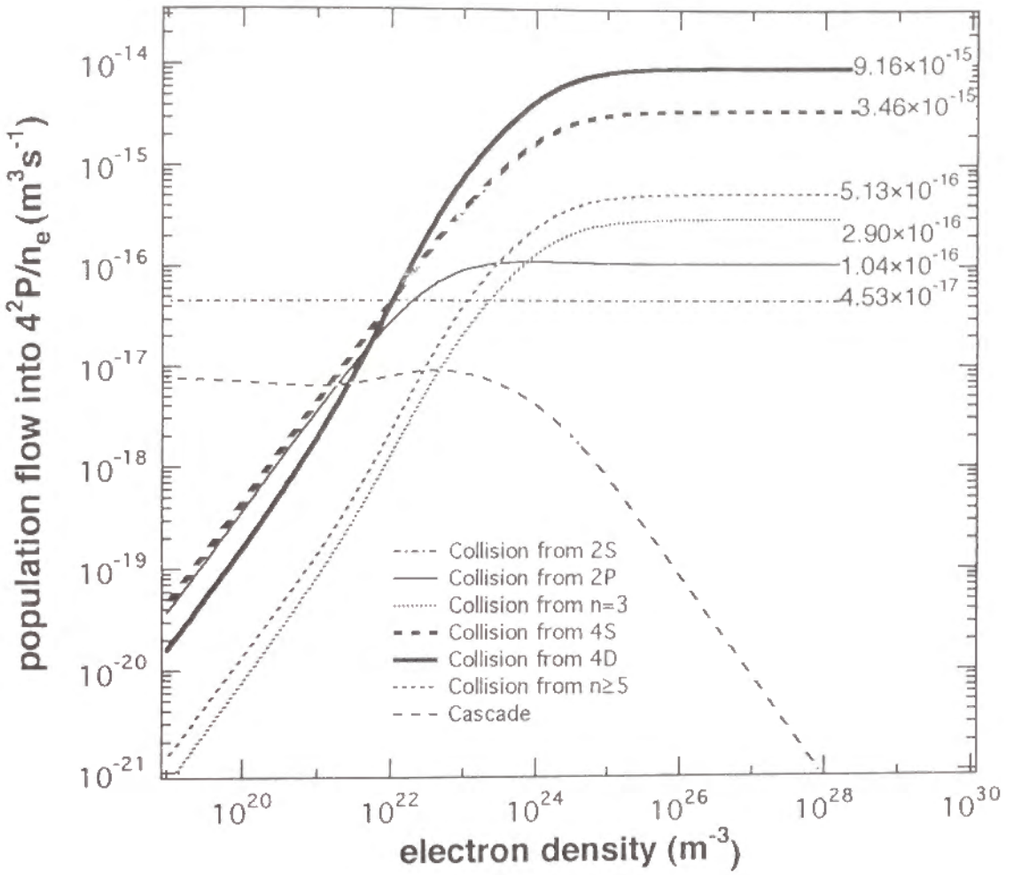
population flow into 4²P/nₑ (m³s⁻¹)
10⁻¹⁴ 10⁻¹⁵ 10⁻¹⁶ 10⁻¹⁷ 10⁻¹⁸ 10⁻¹⁹ 10⁻²⁰ 10⁻²¹
9.16×10⁻¹⁵
3.46×10⁻¹⁵
5.13×10⁻¹⁶
2.90×10⁻¹⁶
1.04×10⁻¹⁶
4.53×10⁻¹⁷
Collision from 2S
Collision from 2P
Collision from n=3
Collision from 4S
Collision from 4D
Collision from n≥5
Cascade
10²⁰ 10²² 10²⁴ 10²⁶ 10²⁸ 10³⁰
electron density (m⁻³)

Fig.8(a)

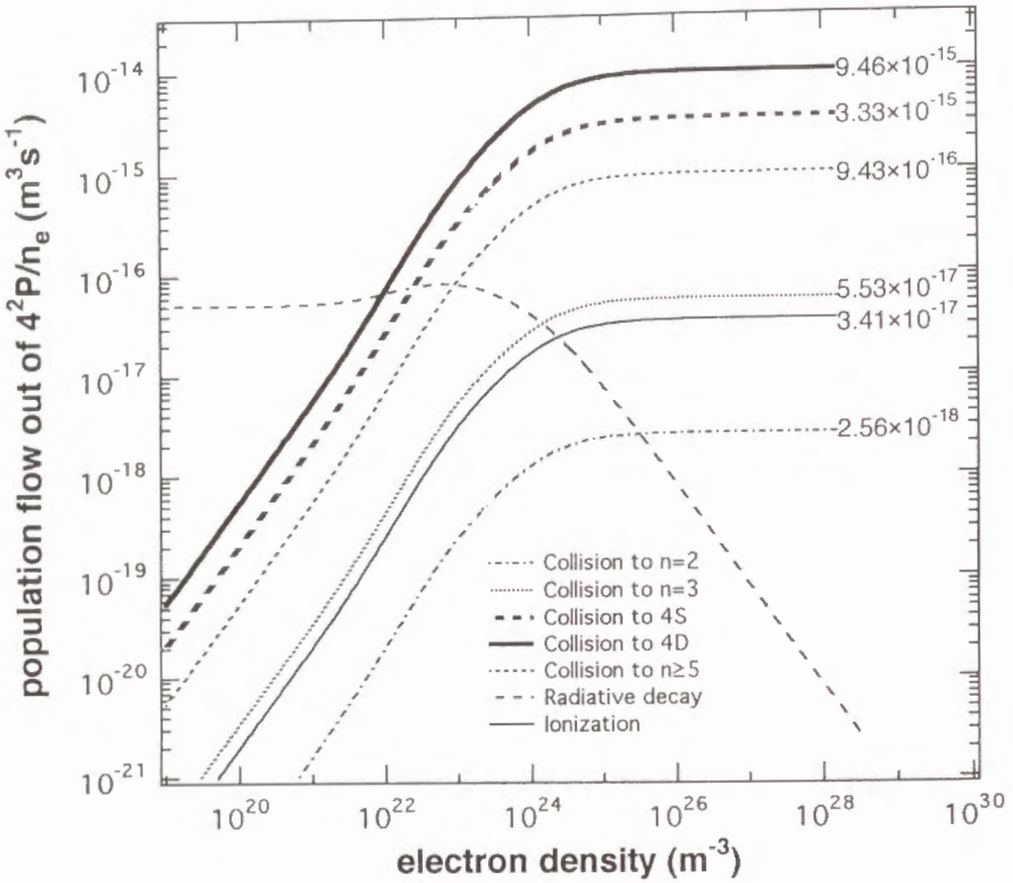
population flow out of $4^2P/n_e$ (m^3s^{-1})
10^{-14}
10^{-15}
10^{-16}
10^{-17}
10^{-18}
10^{-19}
10^{-20}
10^{-21}
9.46×10^{-15}
3.33×10^{-15}
9.43×10^{-16}
5.53×10^{-17}
3.41×10^{-17}
2.56×10^{-18}
Collision to n=2
Collision to n=3
Collision to 4S
Collision to 4D
Collision to n≥5
Radiative decay
Ionization
10^{20}
10^{22}
10^{24}
10^{26}
10^{28}
10^{30}
electron density (m^{-3})

Fig.8(b)

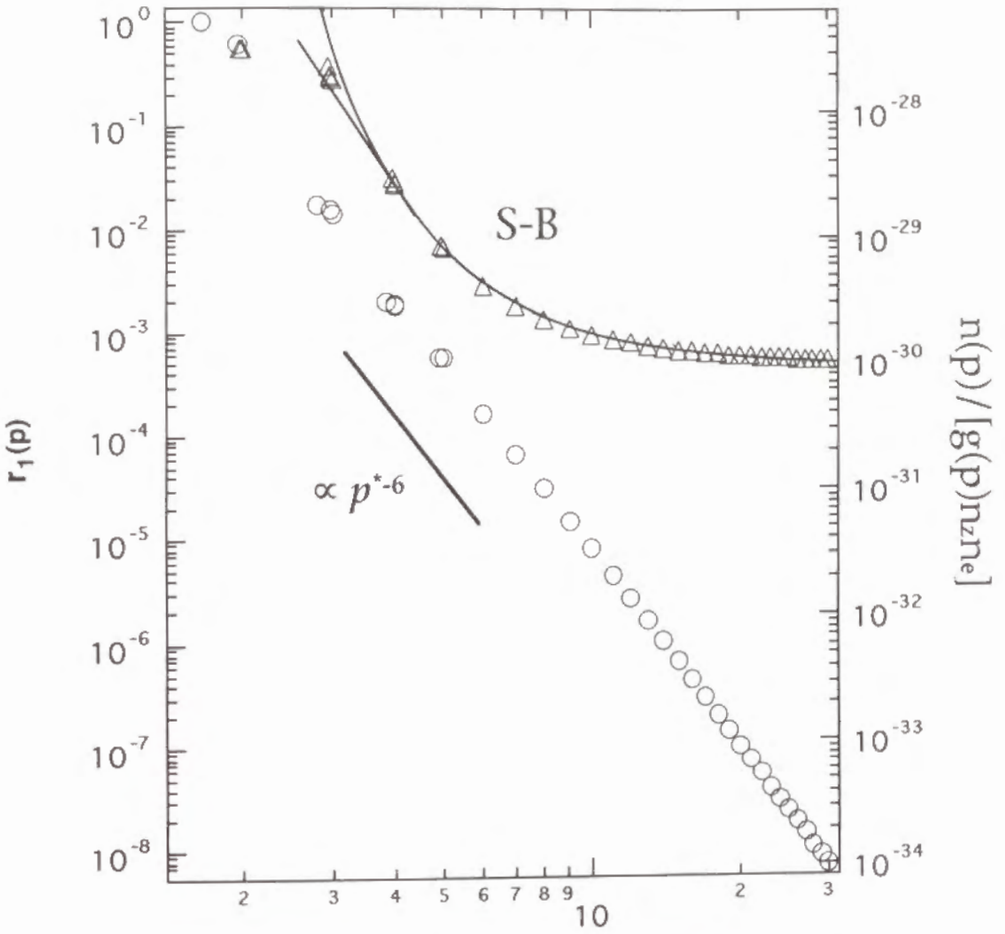
$r_1(p)$
10^{0}
10^{-1}
10^{-2}
10^{-3}
10^{-4}
10^{-5}
10^{-6}
10^{-7}
10^{-8}
S-B
$\propto p^{*-6}$
n(p)/[g(p)nn$_e$]
10^{-28}
10^{-29}
10^{-30}
10^{-31}
10^{-32}
10^{-33}
10^{-34}
2 3 4 5 6 7 8 9 10 2 3
effective principal quantum number

Fig. 9

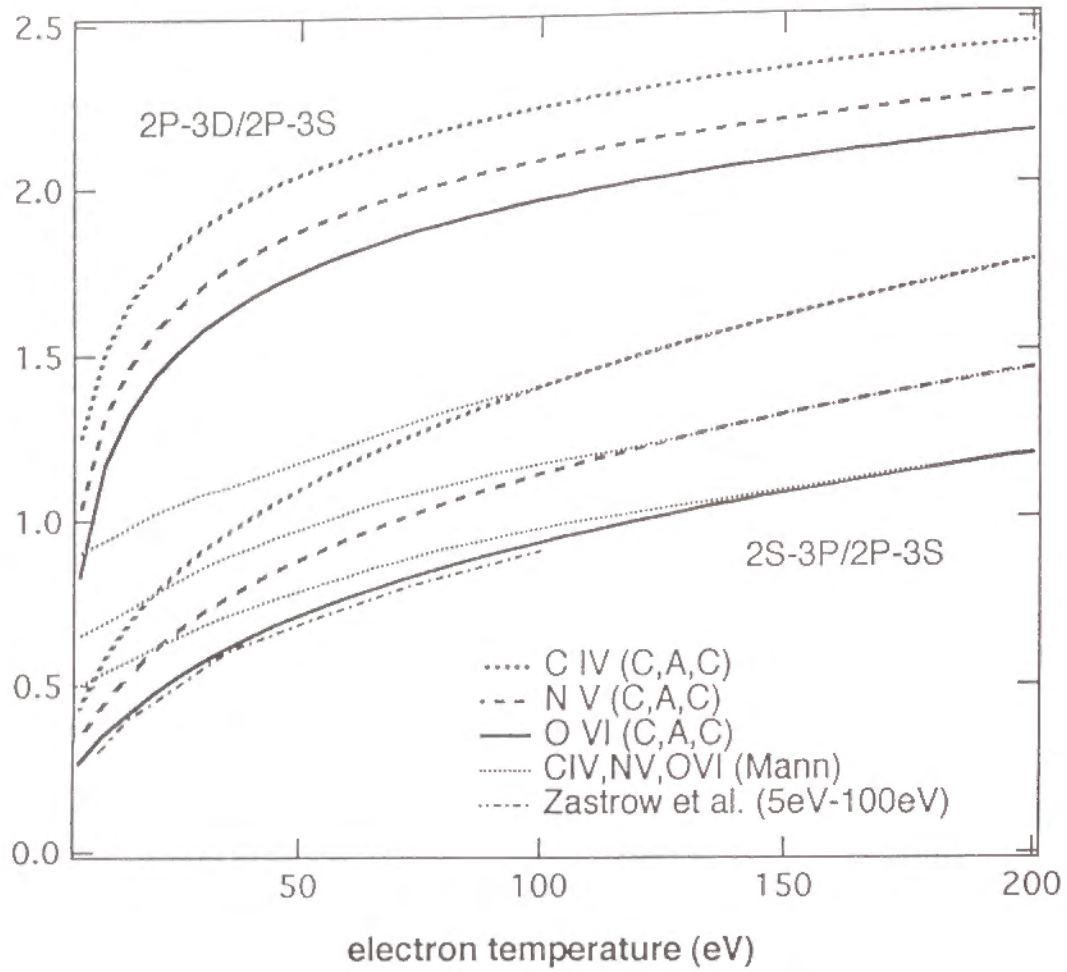
2P-3D/2P-3S
2S-3P/2P-3S
C IV (C,A,C)
N V (C,A,C)
O VI (C,A,C)
CIV,NV,OVI (Mann)
Zastrow et al. (5eV-100eV)
photon emission ratio
electron temperature (eV)
0.0
0.5
1.0
1.5
2.0
2.5
50
100
150
200

Fig.10

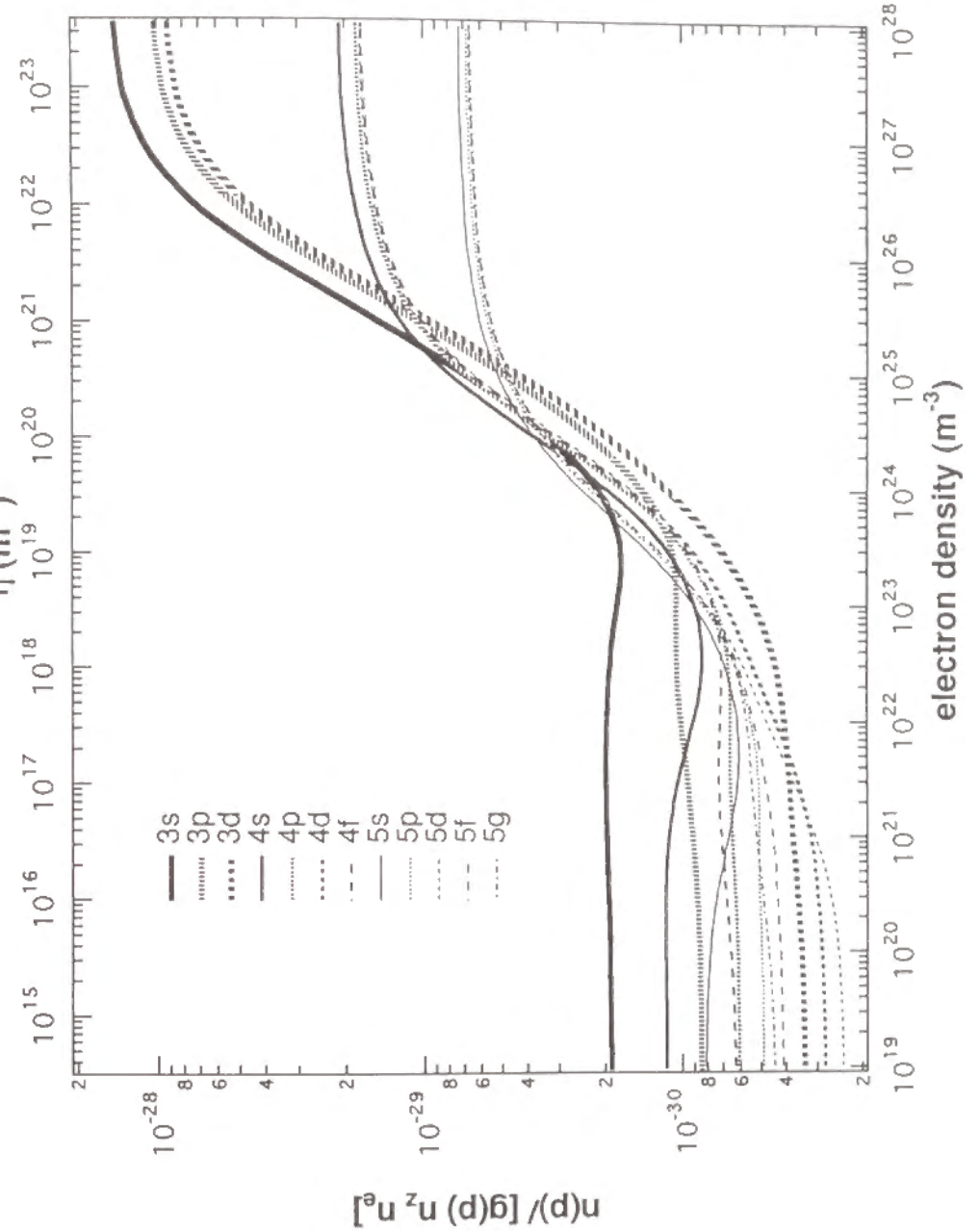
3s
3p
3d
4s
4p
4d
4f
5s
5p
5d
5f
5g
η (m-3)
electron density (m-3)
n(p)/ [g(p) nz na]

Fig.11

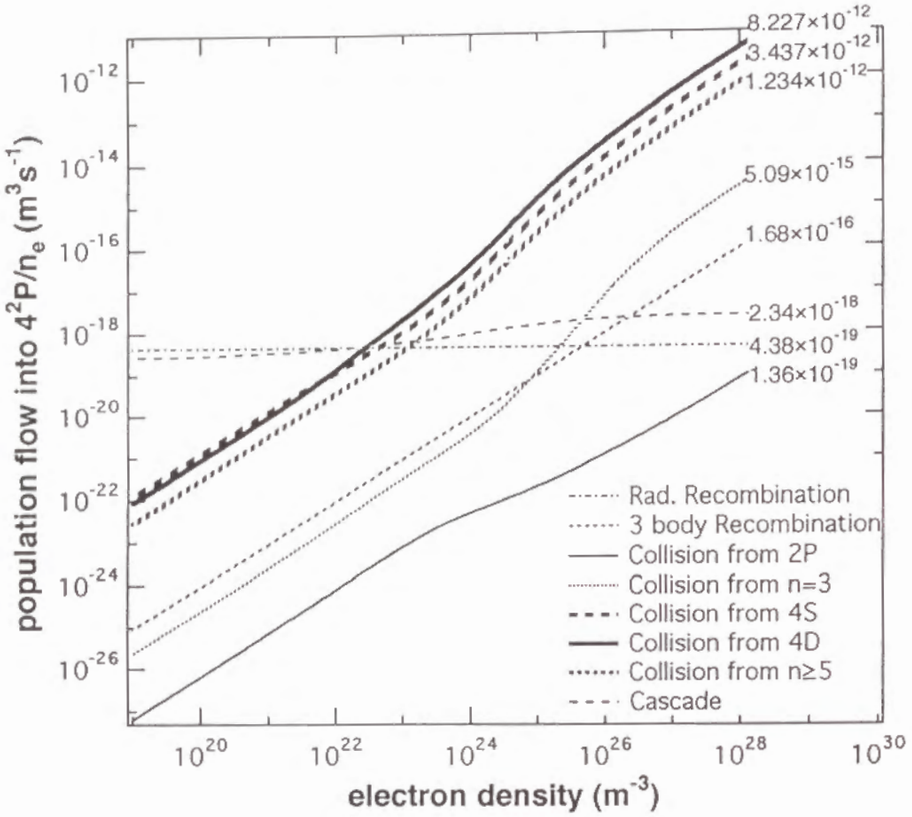

Fig.12(a)

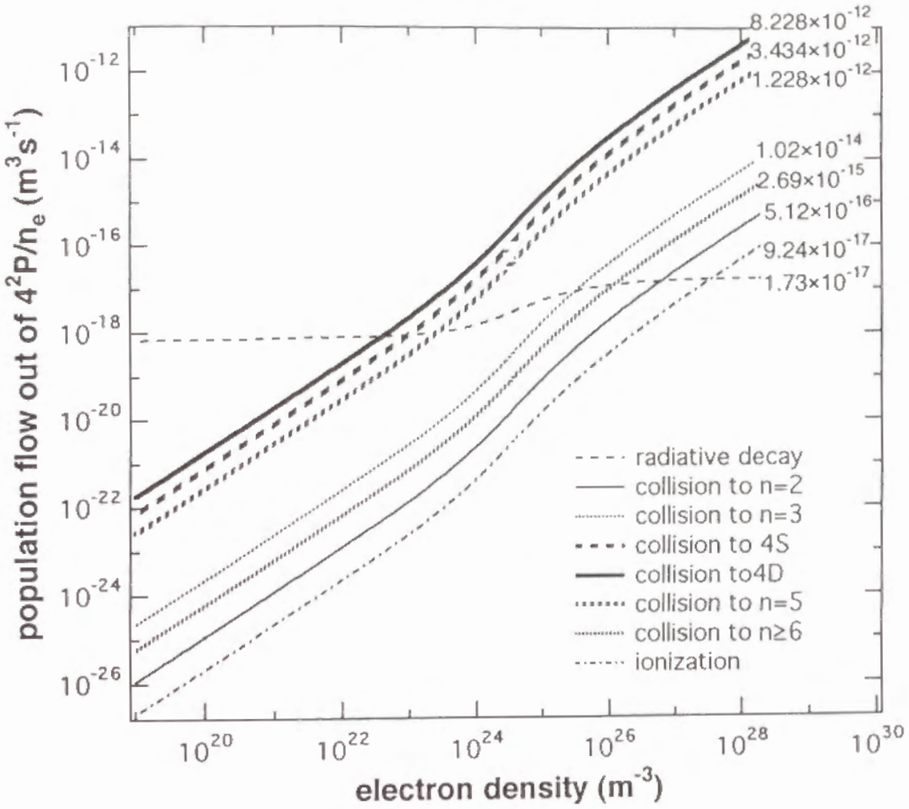

Fig.12(b)

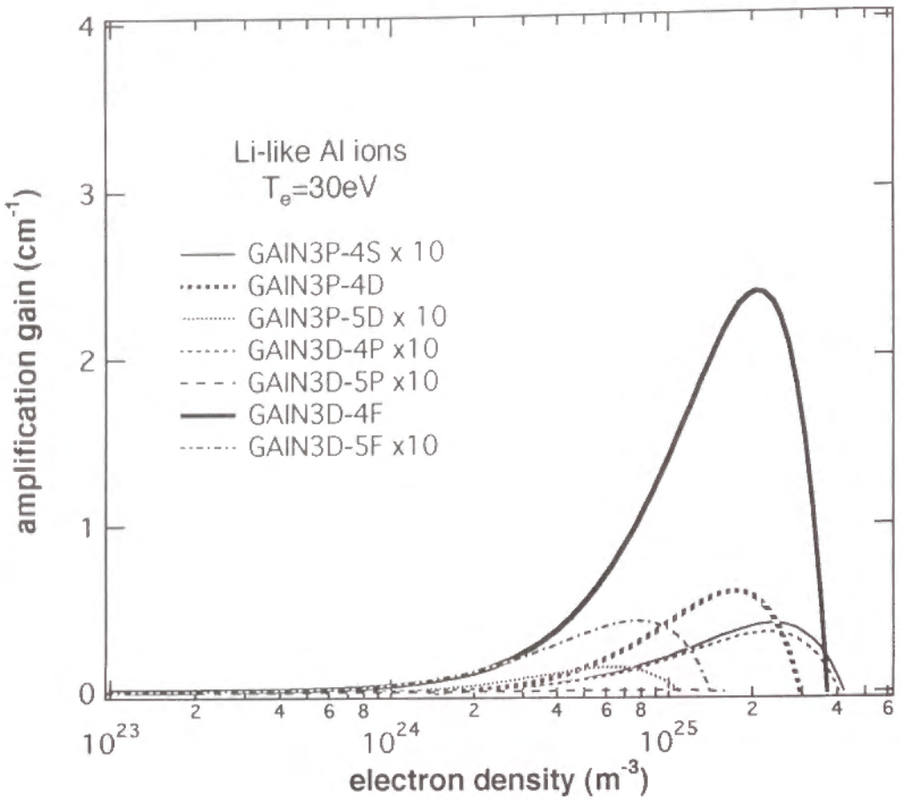
Li-like Al ions
T_e=30eV
GAIN3P-4S x 10
GAIN3P-4D
GAIN3P-5D x 10
GAIN3D-4P x10
GAIN3D-5P x10
GAIN3D-4F
GAIN3D-5F x10
amplification gain (cm^{-1})
electron density (m^{-3})

Fig. 13

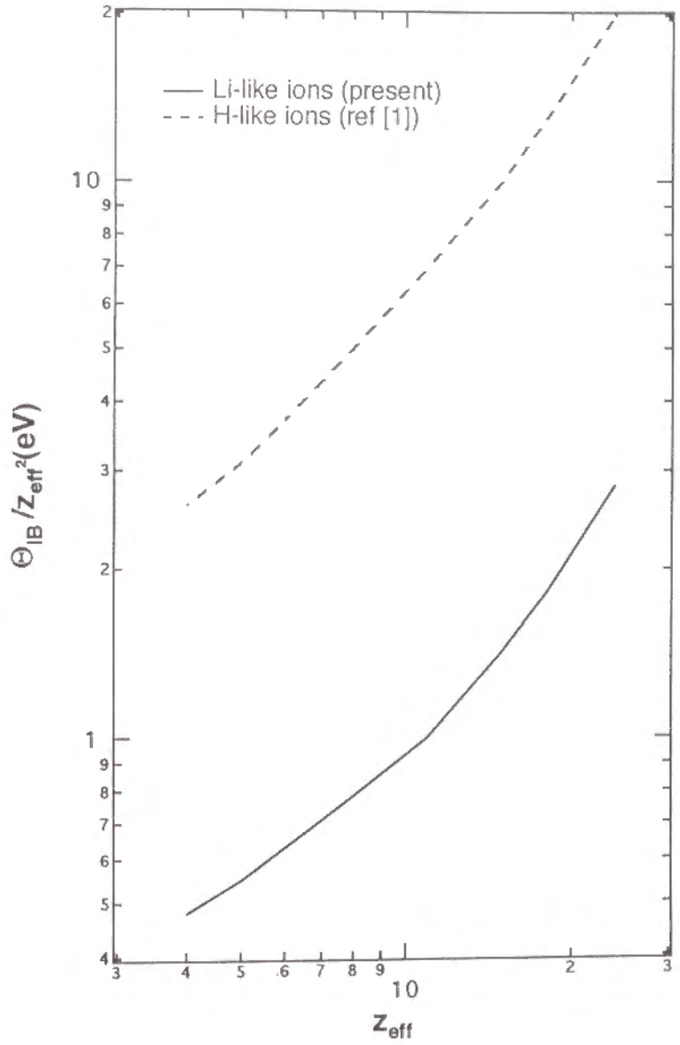
Li-like ions (present)
H-like ions (ref [1])
Θ_{IB}/Z_{eff}^2(eV)
Z_{eff}

Fig.14

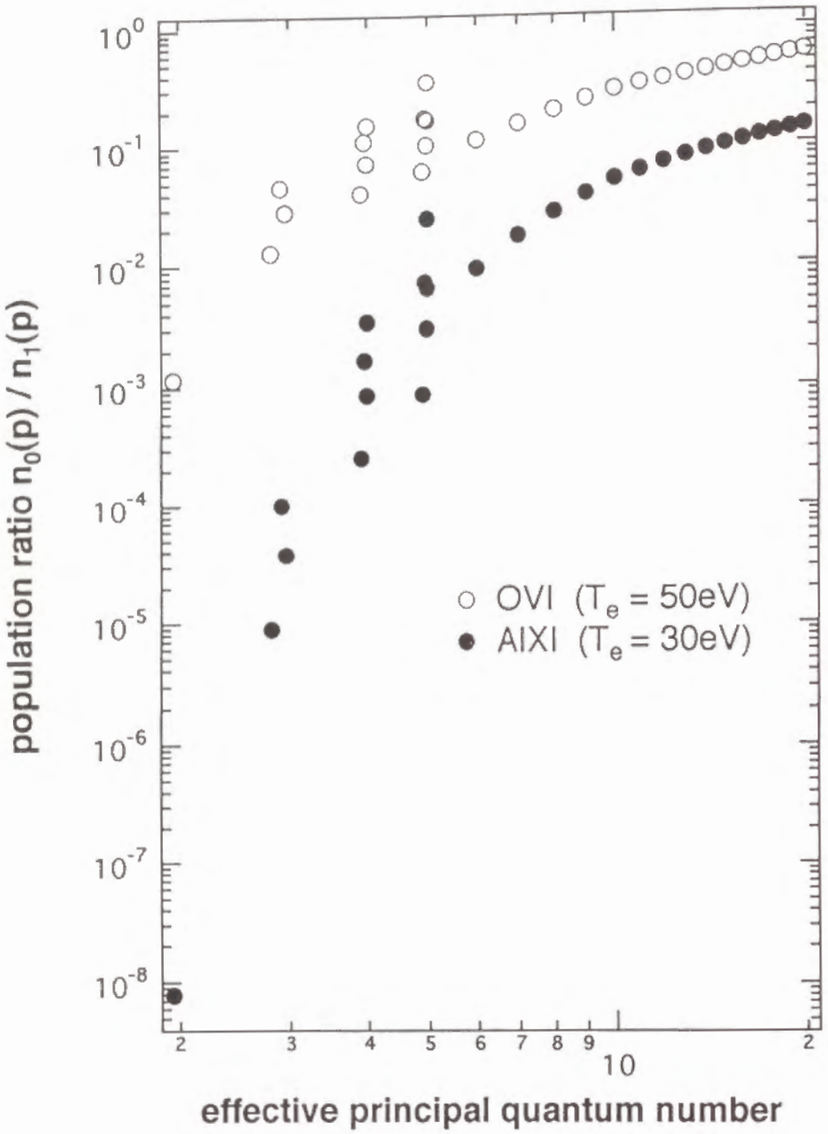

Fig.15

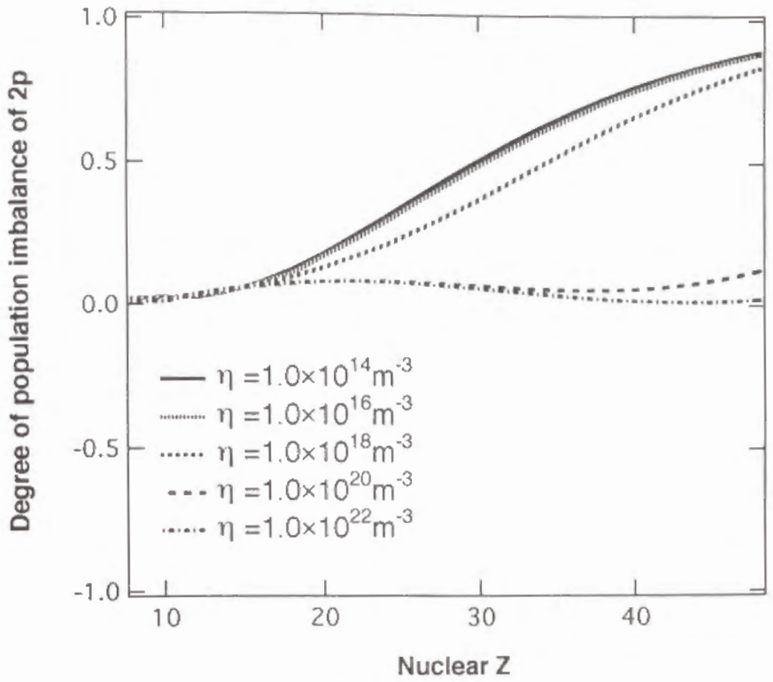

Fig.16(a)

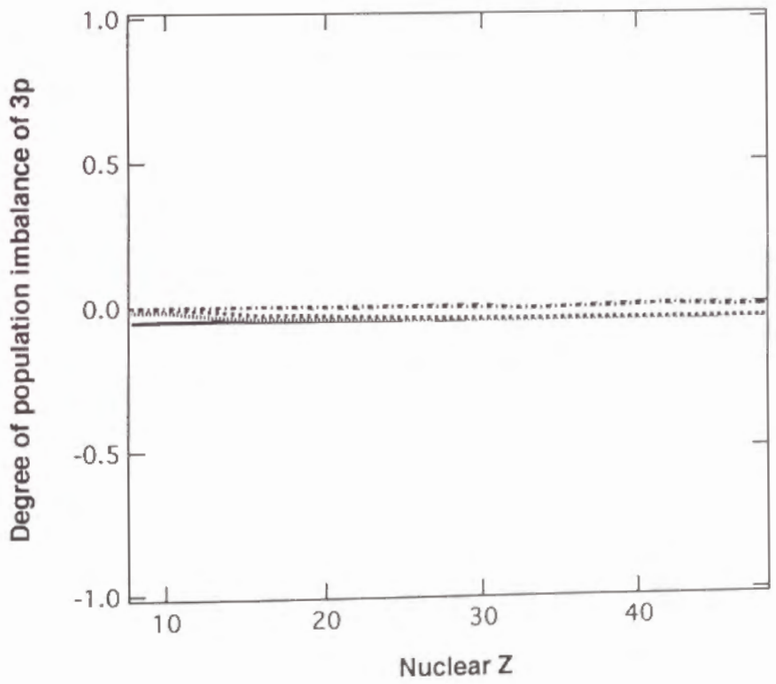

Fig.16(b)

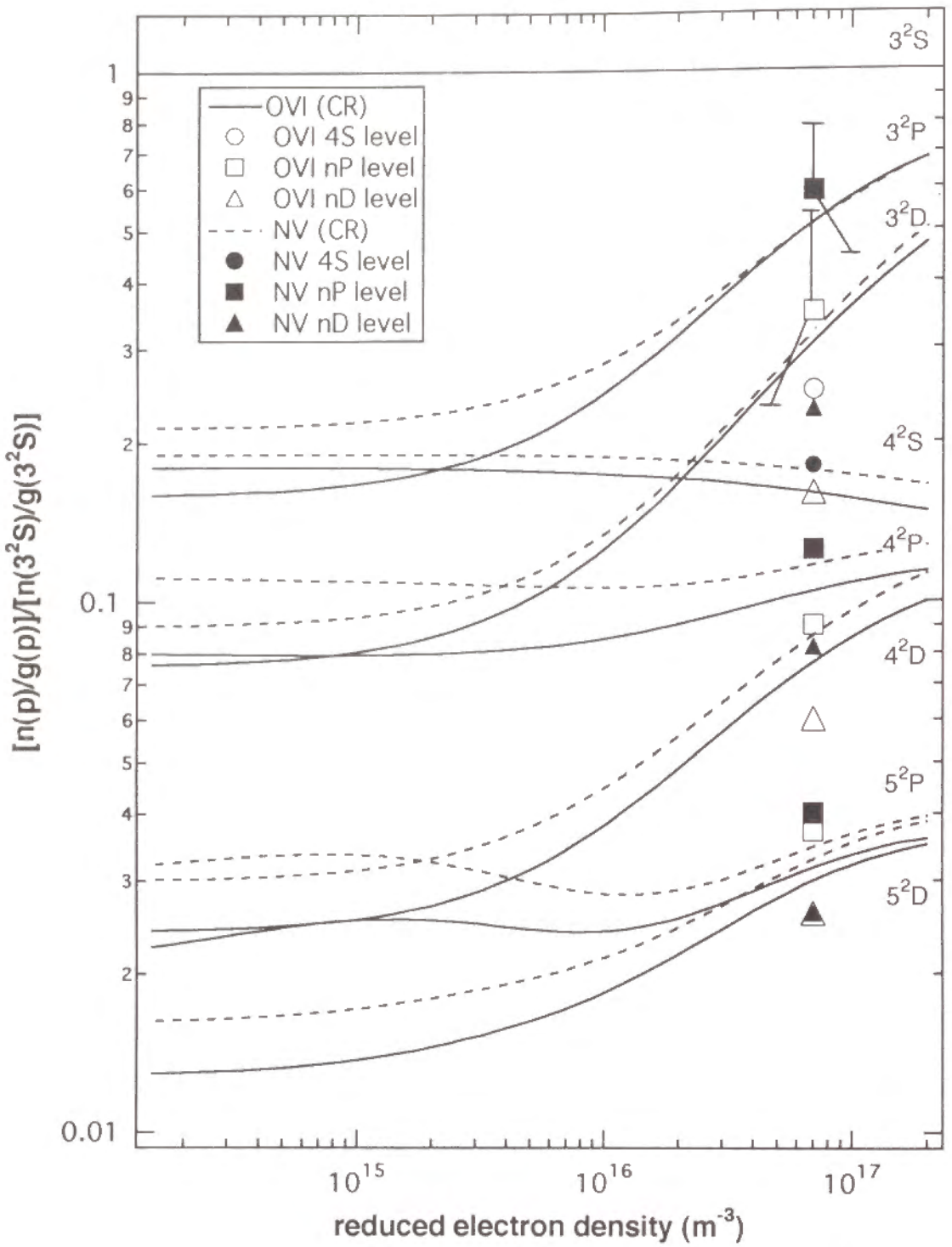
3²S
3²P
3²D
4²S
4²P
4²D
5²P
5²D
OVI (CR)
OVI 4S level
OVI nP level
OVI nD level
NV (CR)
NV 4S level
NV nP level
NV nD level
[n(p)/g(p)]/[n(3²S)/g(3²S)]
reduced electron density (m⁻³)

Fig.17

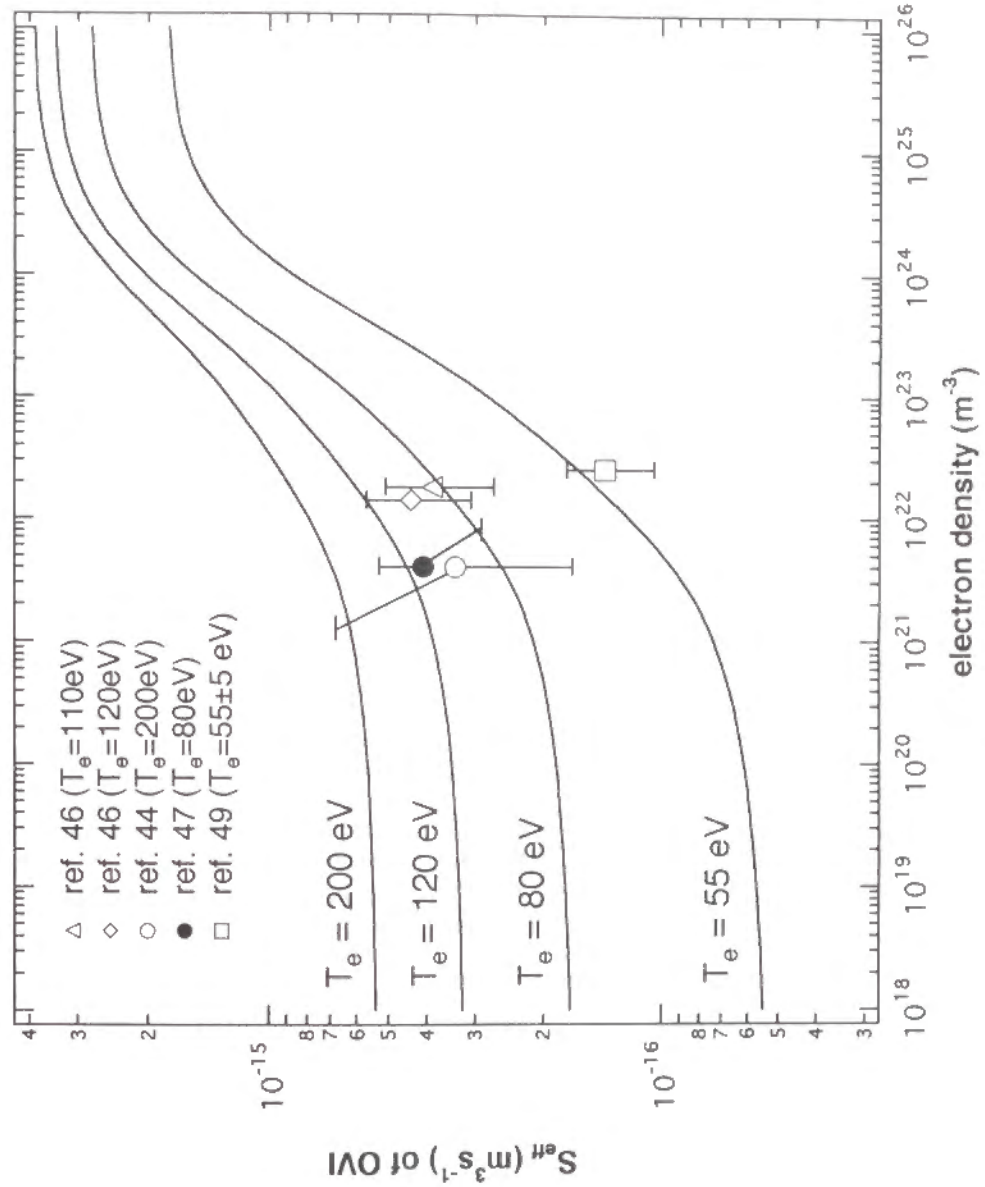
ref. 46 (Te=110eV)
ref. 46 (Te=120eV)
ref. 44 (Te=200eV)
ref. 47 (Te=80eV)
ref. 49 (Te=55±5 eV)
Te = 200 eV
Te = 120 eV
Te = 80 eV
Te = 55 eV
Seff (m³s⁻¹) of OVI
electron density (m⁻³)

Fig.18

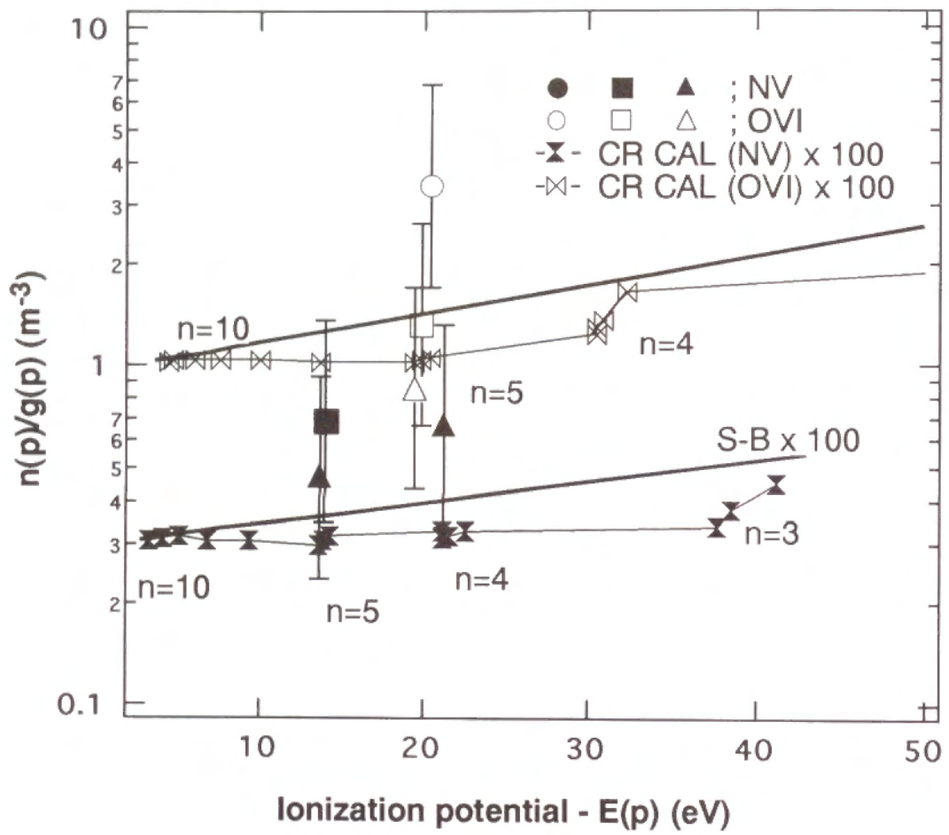

Fig. 19

CHAPTER III.

Experimental Apparatus

Abstract The experimental apparatus for the present study, *i.e.*, the plasma source (WT-3 tokamak), the visible-uv spectrometer, and the xuv spectrometer are described in detail.

I. PLASMA SOURCE (WT-3 TOKAMAK)

Almost all of the experiments described in this thesis have been conducted on plasmas in the WT-3 tokamak. The WT-3 tokamak is located at the Department of Physics, Kyoto University, and we are responsible for the spectroscopic studies of the plasma.

The top view of the tokamak is shown in Fig.1. The WT-3 tokamak has a major radius, R, of 0.65m, and the minor radius, a, can be changed by movable top and side molybdenum limiters from 0.15m to 0.21m. The maximum toroidal magnetic field, $B_T(0)$, is 1.7T, and the poloidal magnetic field is about 0.1T. Plasma current is, for typical cases, 80kA in the joule heating mode. In the WT-3 tokamak, additional plasma heating and current drive modes can be performed, *i.e.*, lower hybrid heating (LHH), lower hybrid current drive (LHCD), electron cyclotron heating (ECH) and electron cyclotron current drive (ECCD). For LHH and LHCD, the RF power for LH wave is generated by a klystron (the frequency: f =2GHz, the input power: P_{LH}< 300kW) and is fed into the plasma by two launchers, each consisting of four waveguides. One launcher is mounted above the midplane and the other below the midplane on the low field side at the same toroidal location. [1] The RF power of ECH or ECCD is generated by two gyrotrons (40GHz, 20kW, 56GHz, 200kW). [2] Although the plasma current can be sustained for 300ms, the discharge time is typically 100ms, in which the plasma can reach a steady-state in all the discharge and current drive modes. Shot by shot interval is 110 s for a normal operation.

The gas puff system is constituted from two gas tanks and three piezo valves. Usually the gas is molecular hydrogen which is contained in the first gas tank and one of the three valves is used. When we use a mixture gas, *i.e.*, helium or molecular nitrogen with hydrogen, we use the second gas tank and valve system. The third valve is reserved for emergency case.

The exhaust system is constituted from a turbomolecular pump (Osaka Vacuum TH-1500) and a rotary pump (Yasukawa Electric FELQ-5). The pumping efficiency of this system is 1.5×10^3 litres/s. The vacuum of the chamber is kept better than 2×10^{-6} torr during the shot interval. From the mass analysis of the pumped gas, dominant impurity atoms and molecules are found to be O_2, H_2O and C.

Electron density of the main plasma is measured by an HCN laser interferometer system. [3] This system has 5 channels and each channel is separeted by 2.5cm. The system can be moved over 7.5cm along the minor radius. Thus we can measure the chord dependence of line-integrated electron density. By use of the Abel inversion for these chord dependent data, we derive the radial (r-) dependence of electron density. Electron temperature of the main plasma is measured by a Ruby laser scattering system (Thomson scattering) and electron cyclotron emission (ECE) radiometer. [4] The electron density and temperature of the edge plasma, *i.e.*, the scrape-off layer (SOL) plasma, are measured by use of the electric probe at location from the chamber wall to r = 0.2m. Soft x-ray emissions are observed by silicon surface barrier diodes (SSB). Four SSB diodes are used to view the whole plasma in one poloidal plane. By use of the beryllium absorbers with various thicknesses, we detect soft x-ray emissions in different energy ranges; the detectable energy range is from 0.2keV to 30keV. Hard x-ray emissions, which result from the high energy tail electrons, can be detected by pulse height analyzer (PHA) systems. We use two NaI scintillators. The detectable photon energy is from 35keV to 500keV [5].

II. VISIBLE-UV SPECTROMETER

Figure 2 shows the schematic diagram of our optics for visible-uv light spectroscopy. We observe the plasma emission through a 15mm-thick window which is made of high quality fused quartz (sprasil I). The transmittance of this window against the wavelength is shown in Fig. 3. We set the light damper on the opposite side of the poloidal plane to prevent the reflection of the plasma light from coming into the spectrometer. (See Fig.2)

A light collecting optics with three plane mirrors and two concave mirrors (f = 1m) are set before the spectrometer. (see Fig. 2) By use of this light collecting system, we determine the chord (z-) dependence of the spectral line intensity. We derive the r-dependence of the spectral intensity by Abel inversion. [7]

A visible-uv spectrometer is NIHON BUNKO CT-100 type (See Fig. 4) with the focal length of 1m. The height and the width of the entrance slit can be changed from 0mm to 20mm and from 0mm to 5mm, respectively. The accuracy of the hight and width are within 10μm. We set a low-pass filter in

front of the entrance slit when it is necessary to cut off the higher order light. We use two gratings, 3600 grooves/mm (grating 1) and 300 grooves/mm (grating 2). The spectra of 200nm through 457nm can be observed by grating 1 and 200nm-700nm spectra by grating 2. The reciprocal linear dispersion is 0.27nm/mm in the former case and 3.3nm/mm in the latter case. We have an aperture in front of the first mirror and we can choose the full size of the grating 102mm×102mm (without the aperture) or 60mm×60mm (with the aperture).

We have two detectors; "Optical Multichannel Analyzer" (OMA) with a micro channel plate (MCP) and a 512ch photodiode array (Tractor Northern Inc. TN-6130) and a photomultiplier (HAMAMATSU R376).

The size of the photodiode array is 12.8mm×2.5mm. The maximum temporal resolution of this detector is 2.56ms, which is determined by the time necessary to read the photo electron signal of each channel and send it to the controller (SMD-201, SMD-501). The instrumental function of the spectrometer has been measured by use of the emission lines from a mercury lamp, for which the Doppler broadening is negligibly small compared with the instrumental width. The full width at half-intensity-maximum (FWHM) of the 238nm line of mercury atoms corresponds to 5.5ch on the MCP. Figure 5 shows a typical example of the *z-chord dependence of the spectral line*. (the λ 381.1nm ($3s^2S_{1/2}$-$3p^2P_{3/2}$) line of lithium-like oxygen ions (OVI).) The plasma is in the Joule heating mode, and we take these data in the peroid of 70ms-84ms from the start of the discharge.

The photomultiplier R376 is a head-on type. The temporal resolution is 10μs. The high voltage applied is 650 V.

Absolute sensitivity calibrations of the spectrometer for these two detectors have been done by use of a tungsten standard lamp and a deuterium lamp. [6] The results are shown in Fig. 6 (a-e).

All the operations of the spectrometer and the collecting optics system, and the data accumulation are done by use of the PC-9801 personal computer with the software "MDS" created by SEKI Inc.

III. XUV SPECTROMETER

Figure 7 shows the schematic diagram of our xuv spectrometer. This spectrometer is of a grazing incidence type. The position of the entrance slit is

1079mm from the plasma center. The width and height of the entrance slit are fixed at 100μm and 10mm, respectively. The distance from the entrance slit to the grating is 238mm. The toroidal grating is unevenly-ruled with 1200 grooves/mm (Hitachi 001-0450). The radius of the curvature is 5.6m and the angle of incidence is 87° with respect to its surface normal. The focal plane is virtually flat in the wavelength range of 8nm-34nm at the distance of 241mm from the grating. The reciprocal linear dispersion is 0.6nm/mm. The detector is a 1024-channel photodiode array with two MCPs and PbS-coated-phospher plate. (HAMAMATSU C2321) whose size is 45mm×12mm. The incident xuv photons are transformed into the photoelectrons and the number of the photoelectrons is amplified in MCPs. The maximum voltage applied to the MCPs is 1.9kV. These photoelectrons are accelalated by the electric field between the MCPs and the phospher plate (the maximum voltage between the MCPs and the phospher plate is 3.85kV), and hit the PbS-coated phospher plate without losing their position information. On the phospher plate, these accelalated electrons are transformed into the photons of the visible light. These photons are guided by a bundle of optical fibers into the 1024ch photo-diode-array. The temporal resolution of this detector is 20ms which is determined by the time to send the data from the 1024 channel diodes to the controller (HAMAMATSU C3633).

The spectrometer is located at 150° of the toroidal angle from the visible-uv spectrometer and observes normally the plasma in the equatorial plane. The vacuum of the spectrometer is separated from the WT-3 main chamber by a magnetic gate valve (OSAKA Vacuum MGV-100). The high vacuum level of the spectrometer is sustained by two molecular turbo pumps (Osaka Vacuum TH-162) and two rotary pumps (ULVAC GVD-100A); the back pressure is better than 1×10^{-6} torr.

We can change the sight area of the spectrometer to observe the SOL plasma. In this case, the observed area is from r=0.17m to 0.21m.

The wavelength calibration of the spectrometer for the region from 9nm to 31.2nm has been accomplished by use of the impurity spectral lines from the plasma, *i.e.*, lithium-like oxygen (OVI), beryllium-like oxygen (OV) and corresponding carbon ion lines for a typical joule heating discharge, and lithium-like and beryllium-like neon ions (NeVIII and NeVII) for the discharge for which we used the mixture gas of neon atoms and hydrogen

molecules (the ratio of the neon atom concentration to molecular hydrogen was 20%.). Figure 8 shows the xuv spectra of the discharge with and without the Ne gas. We refer the wavelengths of these xuv lines to Kelly [8] and the NSRD data compiled by Wiese [9]. For OV ions, the intensity ratios for the lines [10] were taken into consideration in the calibration. The result of the wavelength calibration is shown in Fig.9.

The absolute sensitivity of this spectrometer has been calibrated. The details are described in the next chapter.

References

[1] Y. Terumichi, H. Tanaka, A. Ando, K. Ogura, S. Ide, M. Iida, K. Cho, S. Ozaki,
K. Iwamura, A. Yamazaki, M. Nakamura, T. Maekawa and S. Tanaka,
INT. J. Electronics. **65**, 691 (1988)

[2] K. Ogura, H. Tanaka, S. Ide, M. Iida, K. Hanada, M. Yoshida, T. Minami, M. Nakamura, T. Maekawa, Y. Terumichi and S. Tanaka, *Nucl. Fusion* **30**, 611 (1990)

[3] T. Maekawa, T. Minami, K. Makino, S. Tanaka, S. Kubo and M. Iguchi, *Rev. Sci. Instr.* **62**, 304 (1991)

[4] S. Ide, M. Iida, K. Ogura, H. Tanaka, A. Yamazaki, K. Iwamasa, A. Ando, M. Nakamura, T. Maekawa, Y. Terumichi and S. Tanaka, *J. Phys. Soc. Japan.* **57**, 2605 (1988)

[5] H. Tanaka, K. Ogura, A. Ando, S. Ide, M. Iida, K. Hanada, T. Minami, M. Yoshida,M. Nakamura, T. Maekawa, Y. Terumichi and S. Tanaka, *Nucl. Fusion.* **31**, 1673 (1991)

[6] K. Sawada, *thesis*, Kyoto University (1994)

[7] T. Miyamoto, "Plasma physics for fusion" (in Japanese) Iwanami (1978)

[8] R.L. Kelly, *J. Phys. Chem. Ref. Data* **16**, 1 (1987)

[9] W.L. Wiese, M.W. Smith and B.M. Glennon, National Bureau of Standard, *NSRD-NBS 4*, (1966)

[10] T. Kato, J. Lang and K.E. Berirington, Nuclear Institute of Fusion and Science, *NIFS-DATA-2* (1990)

Figure Captions

Fig. 1. Top view of the WT-3 Tokamak Device.

Fig. 2. Schematic diagram of the light collecting system of the visible-uv spectrometer. M1 and M5: concave mirrors with focal length of 1m, M2, M3 and M4: flat mirrors. We measure the chord depenfence of the spectral line by moving M1 and M2 in the z-direction.

Fig. 3. Transmittance of the window in the wavelength region of 200nm through 800nm.

Fig. 4. Schematic diagram of CT-100, uv-visible spectrometer. M and G are the mirrors and the grating, respectively.

Fig. 5. Chord dependence of the spectral line intensity of OVI ions in a typival joule heating discharge.

Fig. 6. Result of the absolute sensitivity calibration of the spectrometer with the OMA, (a); the case of the grating 1 without the aperture, (b); grating 1 with the aperture, (c); grating 2 without the aperture, (d); grating 2 with the aperture. (e); The sensitivity for the case of the photomultiplier. (We use grating 2 without the aperture.)

Fig. 7. Schematic diagram of the xuv spectrometer.

Fig. 8. Typical spectra in the wavelength region of 9nm through 15nm. (a): with neon gas, (b): without neon gas.

Fig. 9. Result of the wavelength calibration of the xuv-spectrometer.

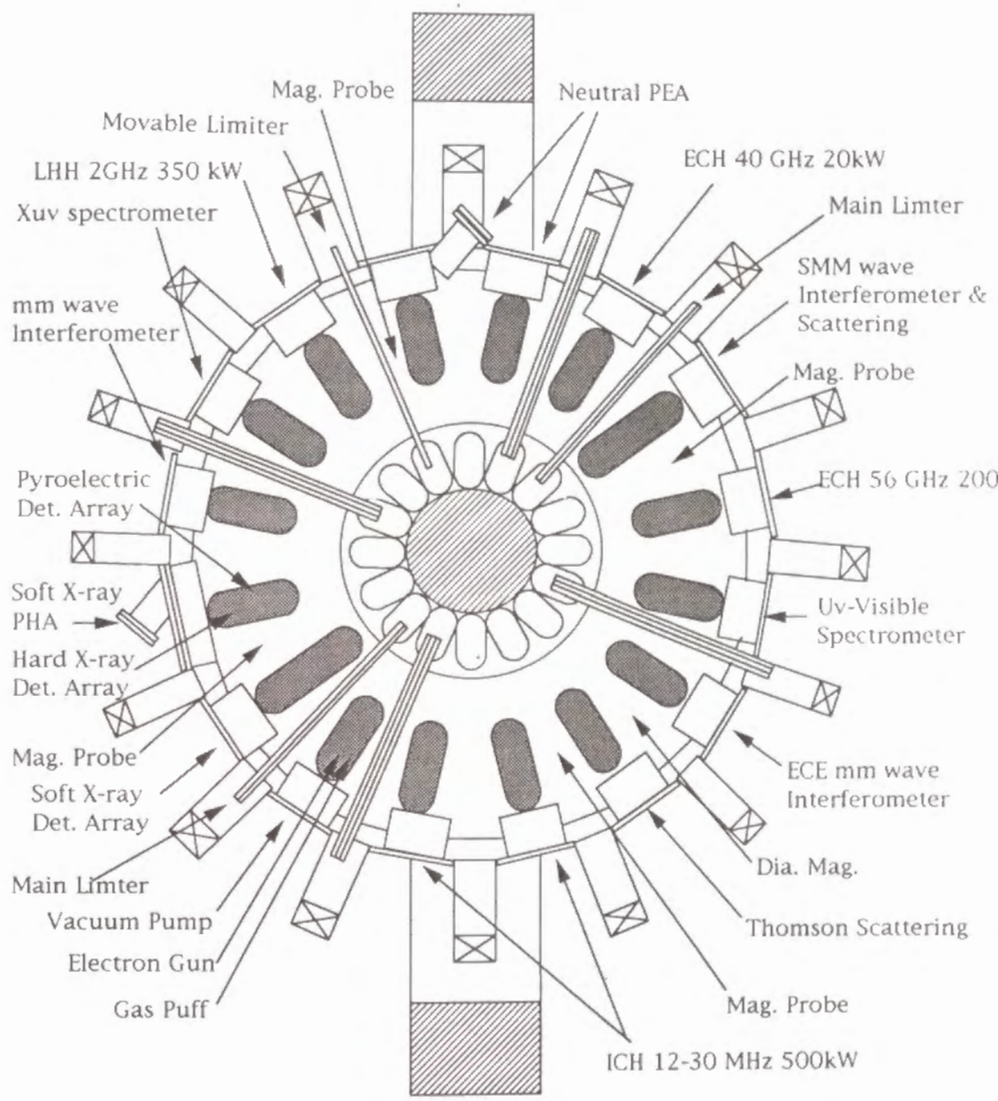

Fig. 1 Top View of WT-3 Tokamak Device

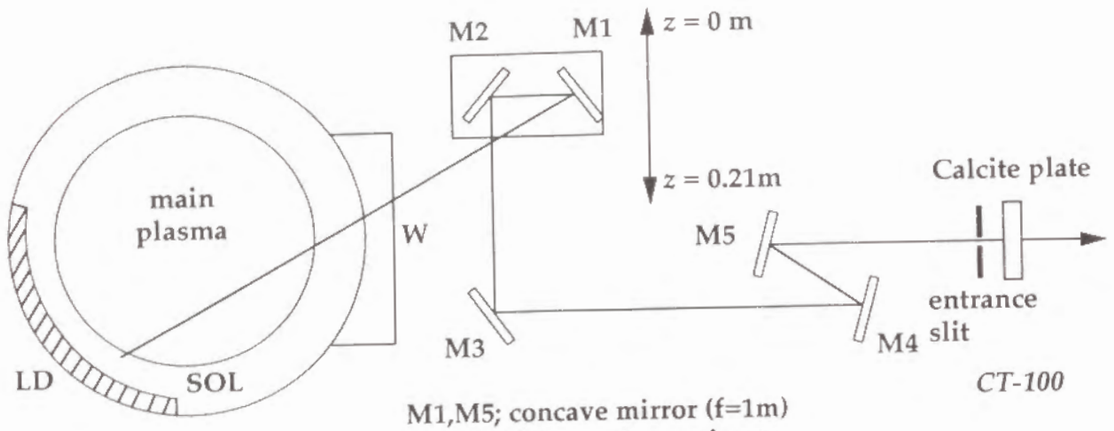

M1,M5; concave mirror (f=1m)
M2,M3,M4; plane mirror
W ; fused quartz window
LD ; light damper

Fig. 2

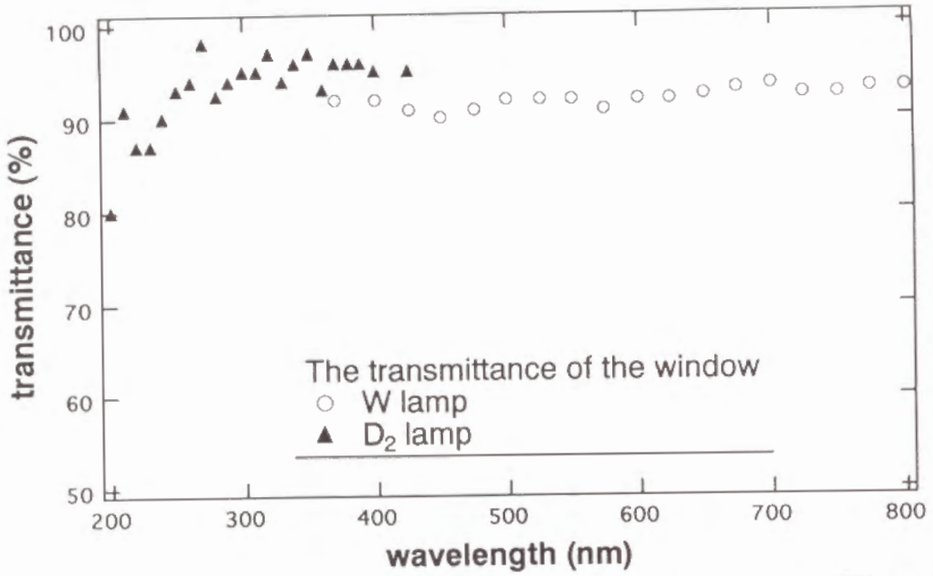

Fig. 3

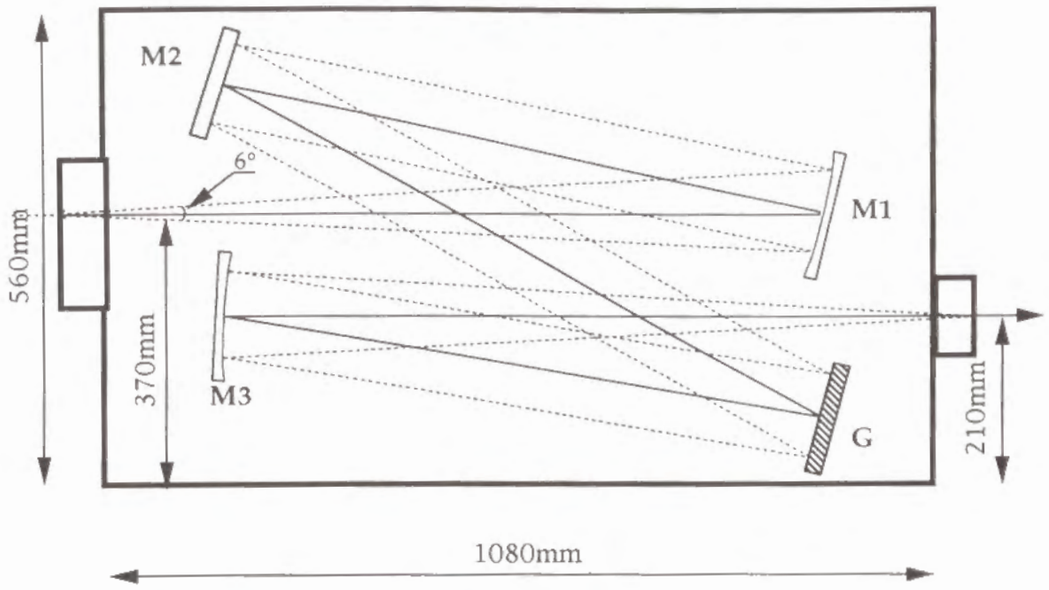

M1: concave mirror, M2: flat mirror
G : grating, M3: concave mirror

Fig. 4

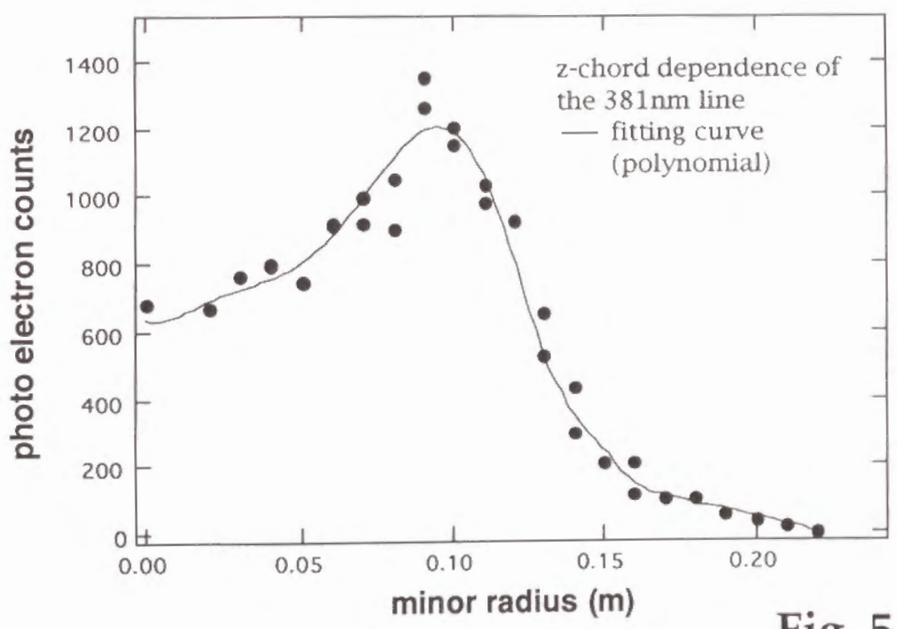

Fig. 5

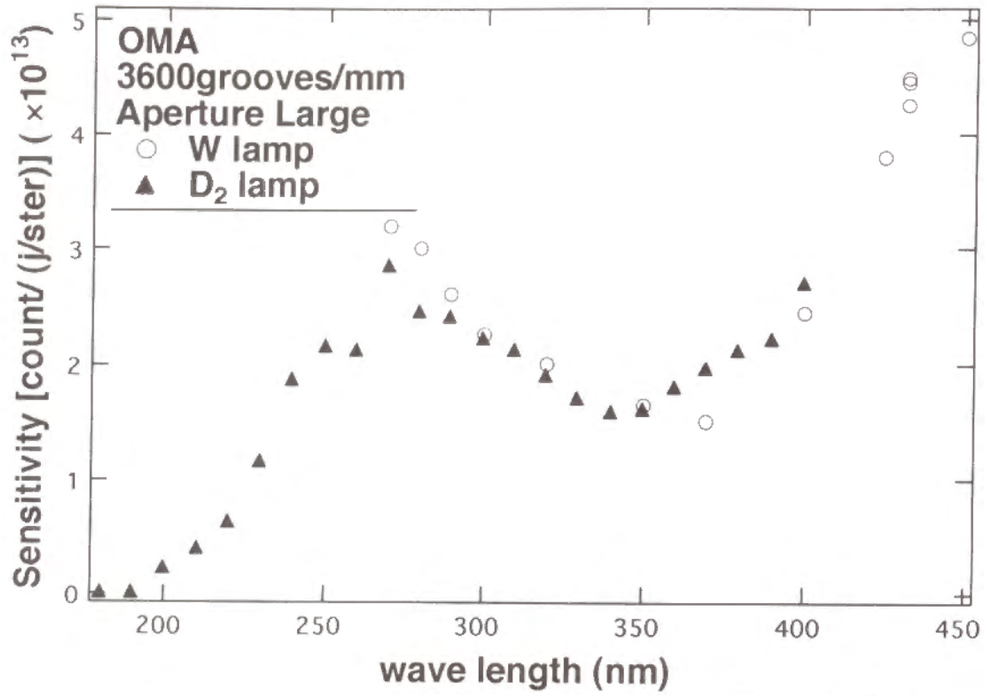

Fig. 6 (a)

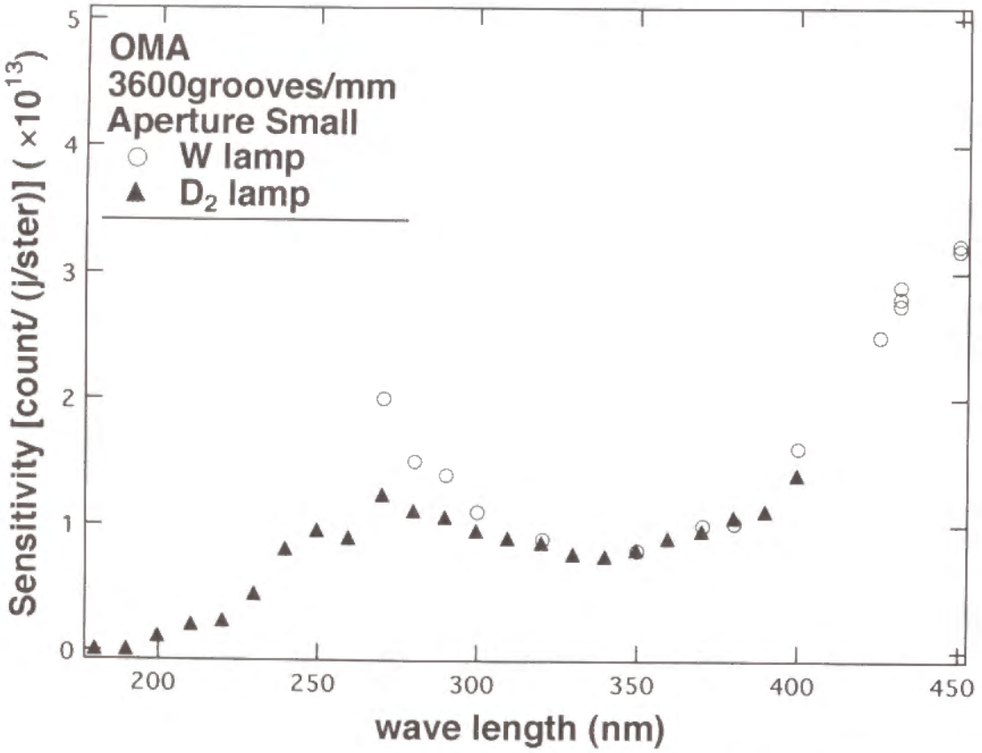

Fig. 6 (b)

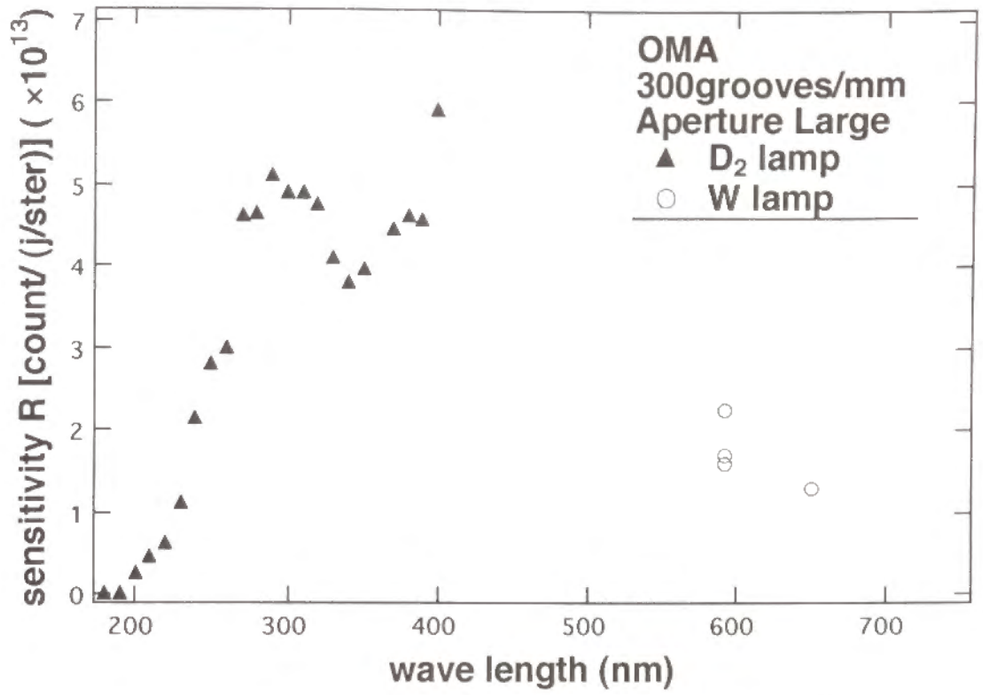

Fig. 6 (c)

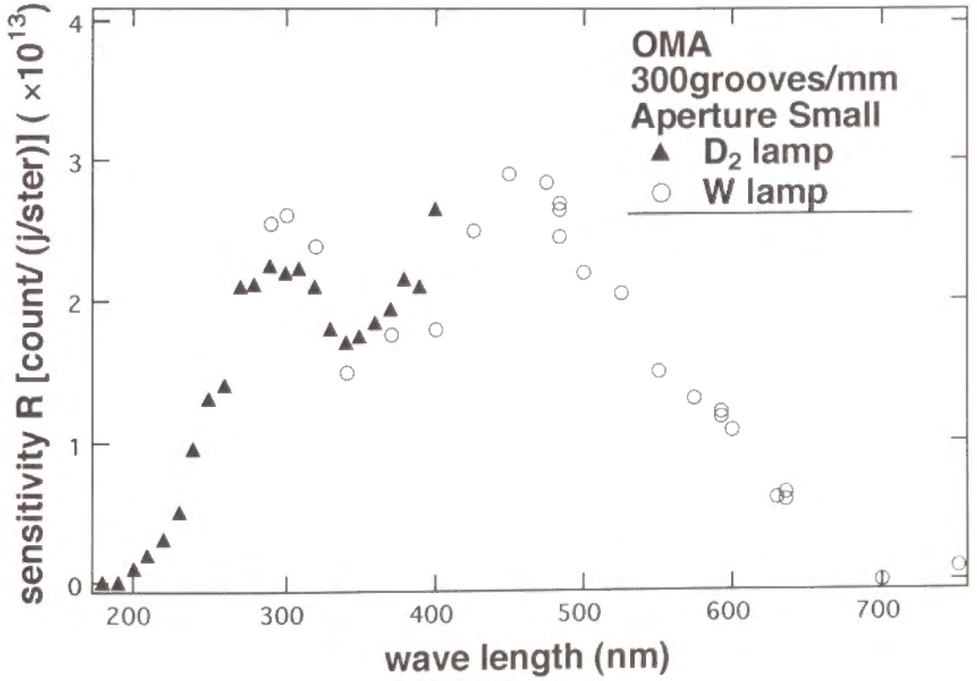

Fig. 6 (d)

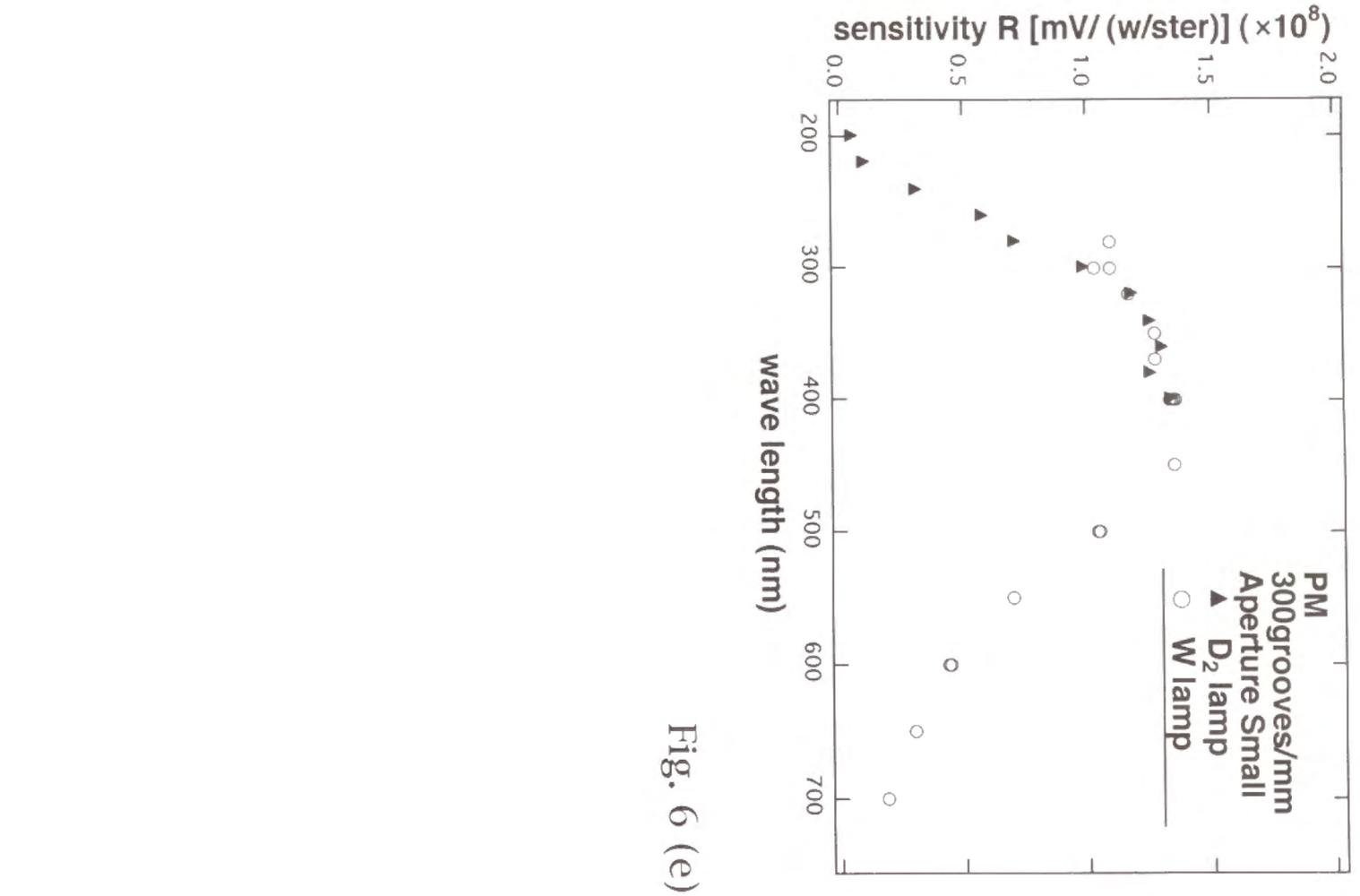
PM
300grooves/mm
Aperture Small
▲ D2 lamp
○ W lamp
sensitivity R [mV/ (w/ster)] (×10^8)
2.0
1.5
1.0
0.5
0.0
200
300
400
500
600
700
wave length (nm)

Fig. 6 (e)

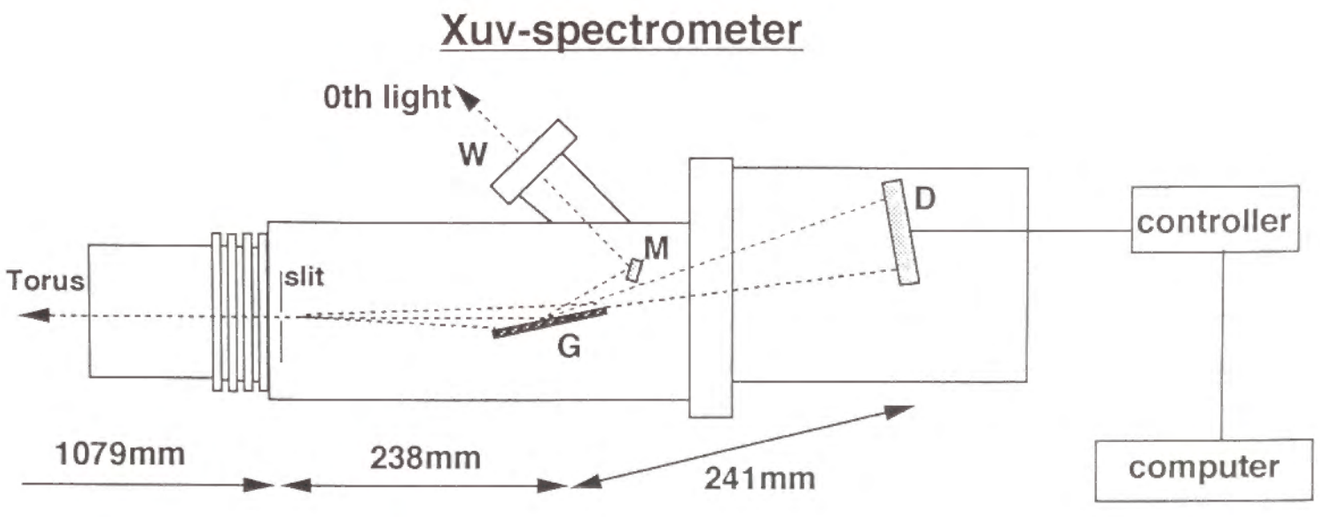
Xuv-spectrometer
0th light
W
M
D
controller
Torus
slit
G
1079mm
238mm
241mm
computer

Fig. 7

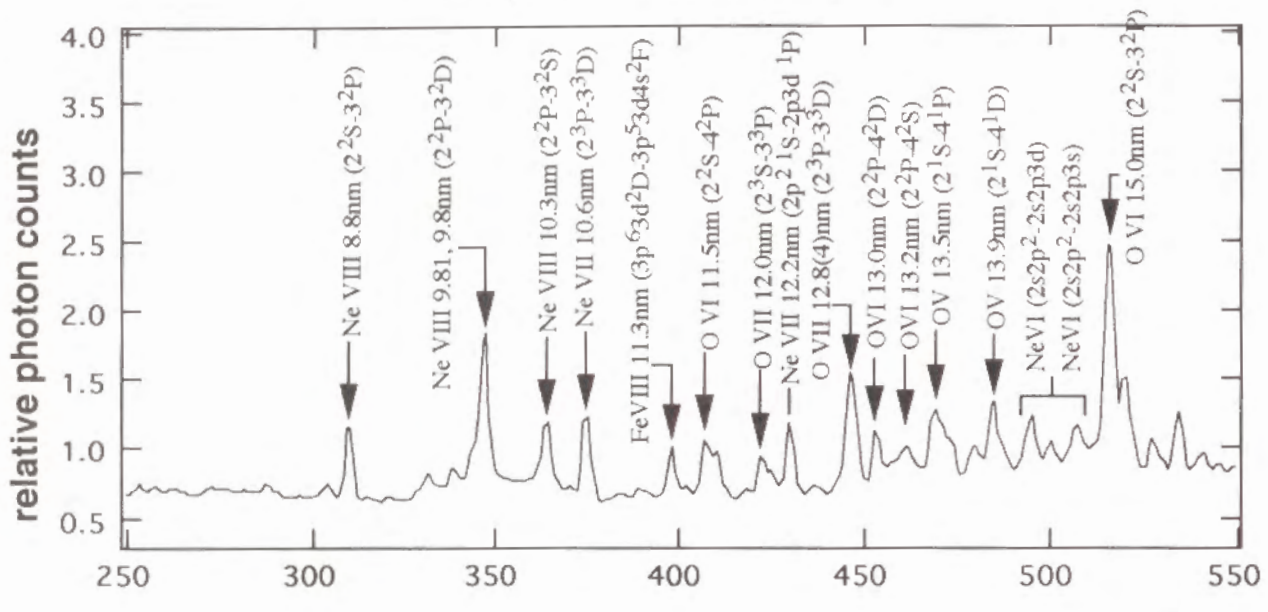

Fig. 8 (a)

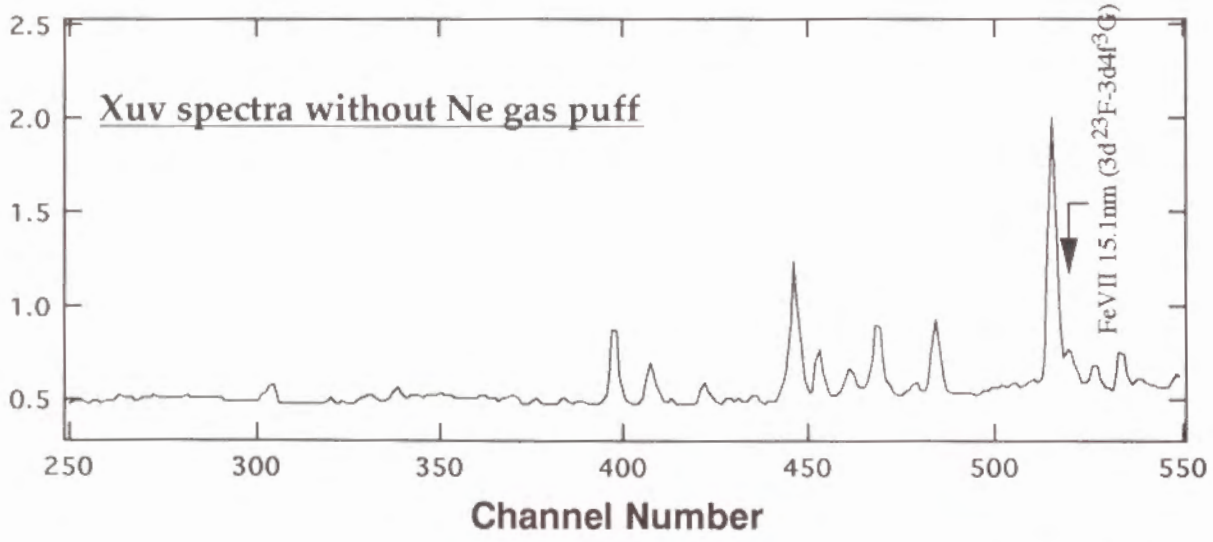

Fig. 8 (b)

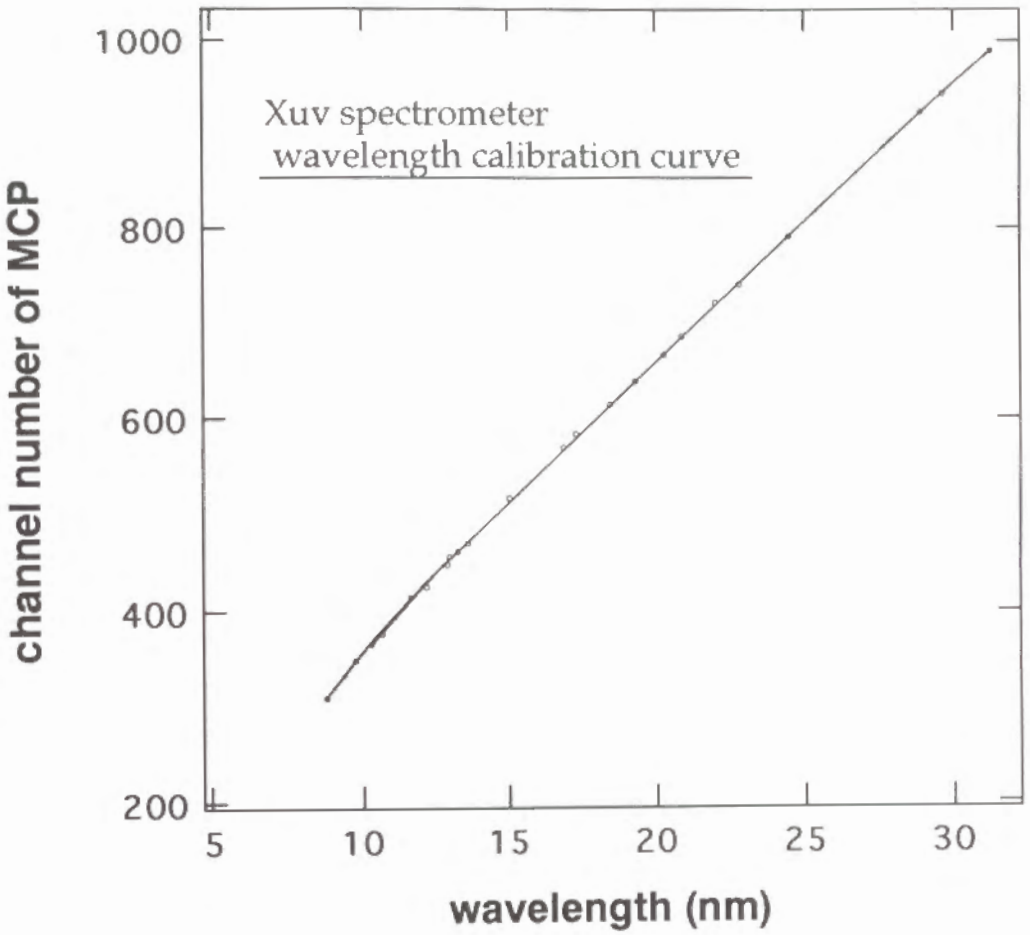

Fig. 9

CHAPTER IV.

In Situ Sensitivity Calibration of an Xuv Spectrometer

(Measurement of Charge Exchange Recombination Rate Coeffieicnt between Highly Charged Ions and Hydrogen Atoms or Molecules)

Abstract We have observed spectra of lithium-like oxygen and carbon ions from the WT-3 tokamak plasma with the xuv spectrometer. On the basis of the branching ratios to visible-uv spectral lines and the collisional-radiative model calculation for excited level populations, we have determined the absolute sensitivity of the spectrometer over 11.5 nm through 31.2 nm. From the line intensities emitted from the scrape-off layer plasma, we have estimated the charge exchange recombination rate coefficients of helium-like oxygen ions colliding with neutral hydrogen atoms or molecules.

I. INTRODUCTION

In order to conduct quantitative spectroscopy in the xuv region, the sensitivity of our detection system must be calibrated absolutely.

For the purpose of sensitivity calibration, a light source, the intensity of which is known beforehand, is necessary. The synchrotron radiation is an ideal source. However, the spectrometer to be calibrated should be moved to the facility, which may cause some practical difficulties. Furthermore, the polarization characteristics of the radiation sometimes make the calibration procedure, at least, complicated. The conventional branching ratio method has been used in many laboratories: The observed intensity of one of the pair lines having the common upper level is used for prediction of the intensity of another line. (We call this latter line the secondary line.) This method, however, is accompanied by various intrinsic difficulties. Besides the geometrical problem commonly recognized and the fact that we can find, in almost all the cases, only a small number of pair lines available, the plasma light source is prone to various adverse effects which may affect the line intensities. Hydrogen-like ion lines are used in some cases. For plasmas with electron density of the order of, say, $10^{20}m^{-3}$, the statistical population distribution among the different-l levels is unlikely to be established. The "branching ratio" of the sponteneous transition probabilities is then different from the value predicted on the assumption of the statistical distribution. For the case that the Lyman β line ($n = 1 - n = 3$) is used as the secondary line an error of 30 % could result for a plasma in the ionizing phase [1].

In order to realize the statistical population distribution in the hydrogen-like ions we have to employ a plasma with much higher electron density. Under such a condition, the ion density also tends to be high and, accordingly, the Lyman lines may be affected by radiation reabsorption. Thus, the secondary line intensity as obvserved by our detector may become lower than the value predicted on the assumption of the optically thin condition. If we use other ions, *e.g.*, helium-like ions, the above difficulty concerning the statistical distribution may be absent, but a similar problem concerning the population distribution over the fine structure levels may arise, besides the radiation trapping effect.

The drawback of the branching ratio method, *i.e.*, a limited number of suitable line pairs as mentioned above, may be overcome if we can predict intensities of the lines emitted from the plasma other than those of the

secondary lines. This can be accomplished if we understand the plasma characteristics, *i.e.*, what are the spatially dependent electron density and temperature as well as whether this plasma is ionizing or recombining , and if we have a reliable atomic model for the population distribution among the excited levels of the ion concerned. Helium-like ions can be an immediate candidate for a reliable atomic model, the collisional-radiative (CR) model [2]. In this case, however, excited-level populations, especially that of the triplet levels are strongly affected by the metastable level population. For transient plasmas or for plasmas in which spatial transport of ions is important, as is the case for a tokamak plasma, the metastable level population itself is the subject of investigations, and a straight-forward application of the CR model is impractical. Beryllium-like ions have a similar difficulty.

A tokamak plasma is effectively a diffuse light source and has a good geometrical symmetry so that the geometrical problem may be solved rather easily. This plasma is well diagnozed. This plasma is a hydrogen plasma containing impurities in the level of the order of a percent. Thus, the impurity lines are free from the effect of radiation reabsorption. It is well established that, in a small tokamak, the ions are in the ionizing plasma phase in the central part of the plasma. Lithium-like ion lines are common prominent impurity lines. At least one pair of lines, *i.e.*, $2s$-$3p$ and $3s$-$3p$ lines, is available for the branching ratio method. This ion has no metastable level, and a quantitatively reliable CR model has been established in Chapter II [3,4]. Thus, by using our own tokamak plasma and employing the CR model, we may calibrate sensitivity of our xuv spectrometer over substantially wider wavelength regions than is possible by the direct application of the branching ratio method.

In the following, the experimental procedure is given, the CR model is briefly described, and the result is given. By using this calibration result, information concerning the charge exchange recombination is obtained from the observed spectrum of the scrape-off layer (SOL) plasma.

II. EXPERIMENT

The details of experimental apparatus have been given in Chapter III.

In the present experiment the minor radius was set at 0.15 m. The toroidal magnet field was 1.7 T, and the plasma current was 80 kA in a joule heating mode for 50 - 100 msec from the start of the discharge. Electron density (n_e) was measured by an HCN laser interferometer. Electron temperature (T_e) was measured by Thomson scattering in the central region, and by an electric probe in SOL. n_e and T_e were 5×10^{19} m^{-3} and 500 eV at the plasma center, respectively (See Fig.1).

We used the 3600 grooves/mm grating (grating 1) for observation of the λ = 381 nm and 383 nm lines of lithium-like oxygen (OVI) ions which correspond to transitions $3s^2S_{1/2}$ - $3p^2P_{3/2}$ and - $3p^2P_{1/2}$, respectively, and 300 grooves/mm grating (grating 2) for the λ = 580 nm line of lithium-like carbon (CIV) ions ($3s^2S_{1/2}$ - $3p^2P_{1/2,3/2}$), where the fine structure components were unresolved. The width of the entrance slit was set at 300μm for both the cases. Figure 2 shows the r -dependence for the OVI (λ = 381 nm) line as derived from the z-dependence shown in Fig. 5 in chapter III. The ordinate is the population of the $3p^2P_{3/2}$ level. This was taken in the period of 70 - 84 msec from the start of the discharge, when the plasma was stationary. Figure 3 shows the spectra of the 381nm and 383nm lines in the central chord. The width of these spectra are mainly determined by the instrumental function of the spectrometer. The ratio of the photoelectron counts for the 381nm line to those for the 383nm line was 2.04±0.10. The uncertainty is mainly due to plasma fluctuation. From the intensity ratio of these lines, we confirmed that their upper levels had the statistical populations. This statistical distribution is consistent with our calculation shown in Fig. 16 (b) in Chapter II.

An example of the xuv spectra for the same discharge as for Figs.2 and 3 is shown in Fig.4 (a). The fine structure components, *e.g.*, 15.0089 nm and 15.0124 nm for $2s$ - $3p$ of lithium-like oxygen ions, were unresolved owing to the rather poor resolution ($\Delta\lambda$ = 0.06 nm) of this spectrometer. In the vicinity of the 15.0 nm line, the resonance line of CrXXI ions (14.9 nm) could appear. However, in the present discharge, the maximum temperature of 500 eV was unlikely to produce the CrXXI ions. The 17.2 nm line might be blended with the FeIX line (17.1 nm) or the OV line (17.3 nm), but the resolution of our spectrometer was barely enough to resolve these lines from the OVI line. (See Fig.4 (a)) The 13.2 nm line was blended with FeVII (13.1 nm) and OV lines (13.3 nm). We assumed the gaussian profile and subtracted the contributions from these nearby blending lines and the background signal. Figure 4 (b) and (c) shows a typical example of fitting (for the 13.0 nm, 13.2 nm lines and the 18.4nm line).

By the branching ratio method for the $2s$ - $3p$ and $3s$ - $3p$ lines, the absolute sensitivity of the xuv spectrometer was established as shown with the closed circles in Fig.5; for the OVI 15.0 nm ($2s$ - $3p$) line, the 381 nm ($3s$ - $3p$) line observed in the central chord served as reference, and for CIV 31.2 nm ($2s$ - $3p$) line, the 580 nm ($3s$ - $3p$) line served as reference. The 381 nm and the 580 nm line intensities were averages of 10 shots for each line, and they were reproducible within 5 %. The fluctuation was obviously due to the small photon numbers and plasma fluctuation (3 %). The 15.0 nm and 31.2 nm line intensities were averages of 20 shots and were reproducible within 3%. The fluctuation was due mainly to the plasma fluctuation. Because the uncertainty for the absolute sensitivity of the uv-visible spectrometer is 20%, the results in Fig.5 are accompanied by uncertainties of 21 %.

In the edge or SOL plasma where electron temperature was less than 20 eV, the spectra due to the recombining plasma component might be substantial. The "shoulder" in Fig.2 for 0.18 m $\leq r \leq$ 0.21 m is suggestive; radiative recombination (RR) of the helium-like ions and charge exchange recombination (CXR) by collisions with neutral hydrogen atoms or molecules can be responsible. Three body recombination and dielectronic recombination are ineffective in these regions ($n_e = 10^{19}$ m^{-3}, $T_e < 200$ eV). To subtract from the spectra in the central chord the contribution from the SOL plasma that may include the recombining plasma component, we changed the sight area of the xuv spectrometer and observed the spectra from the SOL plasma. The observed area was from r = 0.17m to 0.21m. The spectra of 13.0 nm ($2p$ - $4d$), 13.2nm ($2p$ - $4s$) and n = 2 - 3 transitions could be identified for OVI ions and 31.2nm ($2s$ - $3p$) for CIV ions. The 11.5 nm ($2s$ - $4p$) was too weak to be identified. Figure 6 shows spectrum including the 13.0 nm and 13.2 nm lines from the SOL plasma.

A different series of discharges was used for this observation of the SOL plasma. The amount of the oxygen impurity was higher in this series by about 20% and the carbon level stayed the same. For 381 nm line of OVI ions, the averaged intensity through the chord of z = 0.17 m to 0.21 m was 7 % of that in the central chord. (*c.f.* Fig.2) We normalized the observed xuv line intensities from the SOL plasma so that the 15.0 nm line intensity became 7 % of that in the central chord. We then subtracted these intensities from those observed in the central chord. For the 31.2 nm line of CIV ions, the contribution from SOL was estimated to be 5% of that in the central chord.

III. COLLISIONAL-RADIATIVE MODEL

We used our collisional radiative model for lithium-like ions for the analysis. The details have been described in Chapter II. From the r - dependent population of the excited OVI ions as shown in Fig.2 and a similar result for $3p$ of CIV ions and the r - dependent electron density and temperature shown in Fig. 1, we derive by the collisional-radiative model calculation the r - dependent ion densities of OVI and CIV ions for the range of r = 0.06 m to 0.17 m under the assumption that the ions are in the ionizing plasma phase, *i.e.*, excited level population is proportional to the ground state ion density. The result is shown in Fig. 7; in this figure, the result for $r > 0.17$m is also shown for reference. The populations of the $3s$, $3d$, $4s$, $4p$ and $4d$ levels for OVI ions and $4s$, $4p$ and $4d$ levels for CIV ions are then calculated.

IV. RESULT AND DISCUSSION

A. Absolute calibration of xuv-spectrometer

Figure 8 shows the T_e - dependence of photon emission ratios of OVI and CIV ions. We assume the ionizing plasma. In tokamak plasma, electron density is too low for a density effect on the population of excited levels to be significant, and we assume $n_e = 1.0 \times 10^{13}$ cm^{-3}. The similar result by Zastrow *et al.* [5] is attached.

We calculate the emissivities of lines $2s$ - $4p$, $2p$ - $3s$, $2p$ - $3d$, $2p$ - $4s$, and $2p$ - $4d$ of OVI ions and those of $2s$ - $4p$, $2p$ - $4s$, $2p$ - $4d$ of CIV ions in the r = 0.06 - 0.17m region from the radial distributions of the population of their upper levels, and derive the intensity as observed in the central chord. From the comparison between the observed, *i.e.*, Fig.4 (a) subtracted by the contribution from the SOL plasma, and the calculated intensities, we derive the absolute sensitivity of our spectrometer at each wavelength. The result is given with the open circles in Fig.5.

Uncertainty in this calibration is mainly due to the statistical fluctuations of the observed intensities, the uncertainty of excitation cross sections and the uncertainty of the sensitivity of our visible-uv spectrometer. The excitation cross sections by Zhang *et al.* are claimed to be accurate within 10 %, except $2s$ - $4p$ excitation cross sections whose accuracy is within 17 % for OVI. The results by Clarke, Abdallah and Csanak (C,A,C. See also Chapter II) are in good agreement with those by Zhang *et al.* and the accuracy of the results by C,A,C is

estimated to be similar to that by Zhang *et al.* The sensitivity points (open circle) in Fig.5 carry only the relative uncertainty. We estimate that the total uncertainty of the calibration is about 27 % at 11.5 nm and 24.4 nm, and about 23 % for other points.

B. Estimate of charge exchange recombination rate coefficients of OVII + H, H_2

In the spectra from SOL, the intensity ratio of the 13.2nm ($2p$ - $4s$) line to the 15.0nm ($2s$ - $3p$) line was 0.20. This value is substabtially larger than that predicted from the CR calculation under the assumption of the ionizing plasma (See Fig.8. T_e of the SOL plasma is less than 20eV as shown in Fig. 1). We conclude that the recombining plasma component is responsible for those ratios.

We calculate the ground state density of the OVII ions by the transport code "MIST" [6]. We assume that the impurity source is limiter (r = 0.15 m). In the case of D = 2.0 m^2/s and C = 1, the code calculation reproduces the r - dependence of the OVI ion ground state density resonably well in the main plasma (0.07m≤ r ≤0.15m) as shown in Fig. 9. In this figure, the error bars for the experimental r -dependence of the OVI ion ground state density are attached. These error bars are due to the uncertainty of T_e and n_e, and do not include the uncertainty in Abel inversion. It is concluded that the experimental $3p$ populations in $r \leq 0.17$m shown in Fig. 2 may be explained from the calculated OVI ion densities in Fig. 9. If we intend to do the same in the region of $r \geq 0.18$m, we have to assume higher T_e in r = 0.19m and 0.20m than in r = 0.17 and 0.18m. This is judged unlikely. It is thus concluded that these $3p$ populations in $r \geq 0.18$m cannot be explained within the framework of the ionizing plasma. Rather, they should be explained from the recombining plasma component. This conclusion is consistent with the earlier assumption. We now adopt the MIST calculation for the ion densities. By use of the CR calculation, the r - dependence of the ground state density of OVI ions and electron density and temperature, the ionizing plasma component in the SOL plasma is calculated. We subtract it from the spectra from the SOL plasma (See Fig. 6) to derive the spectra for the pure recombining plasma component. The contribution from the ionizing plasma component is about 80% for the n=2-3 lines, 20% for the $2p$-$4s$ line, 30% for the $2p$-$4d$ line, and about 45% for the other$n$=2-4 lines. First, we estimate the intensities of the lines which are

produced by RR. We find these are too weak to account for the observation, by more than one order. Recent experimental measurements [7-9] of the total CXR cross section between OVII ions and neutral hydrogen atoms show that the total cross section is of the order of 10^{-19} m^2 in the collision energy range of 10eV/amu to 10keV/amu. Theoretical calculations [10-12] suggest that, in the collision energy less than 1keV/amu, the recombination into the n = 4 levels is dominant and the recombination into the n = 3 levels is ignorably small. This suggests that the CXR process can be the dominant recombination process in SOL.

The densities of neutral hydrogen atoms and molecules are determined by the r-dependence of the intensities of H_α, H_β and H_γ [13], and these values are 3.0×10^{16} m^{-3} and 7.0×10^{17} m^{-3}, respectively.

In this experiment, we can not separate the contributions from hydrogen atoms and that from molecules, we can only derive an "averaged" rate coefficient. We take the averaged CXR rate coefficient into n = 4 levels $\gamma(4s)$, $\gamma(4p)$, $\gamma(4d)$ and $\gamma(4f)$ as fitting parameters, and we reproduce the intensities from the recombining plasma component. We ignore the CXR process into n = 3 levels. The result is shown in TABLE 1. In our results, the dominant channel of CXR in this experimental condition is to the 4s level. The CXR into the $4p$ and $4f$ levels are smaller by more than one order than that into the 4s level.

We estimate the CXR cross section into the n = 4 levels. Collision velocity between the OVII ions and neutral hydrogen atoms are estimated from the Doppler broadening of the H_γ and 381 nm lines; the velocities are about 1.2×10^4 m/sec (2 eV/amu) for both the atoms and ions. When we assume the same velocity for hydrogen molecules, the total CXR cross section into n = 4 levels of OVI ions is 1.2×10^{-19} m^2.

References

[1] K. Sawada, *thesis*, Kyoto University (1994)
[2] T. Fujimoto and T. Kato, *Phys. Rev. A* **30**, 379 (1984)
[3] T. Kawachi, T. Fujimoto and G. Csanak, *Phys. Rev. E* (in press)
[4] T. Kawachi and T. Fujimoto, *Phys. Rev. E* (in press)
[5] K-D. Zastrow, J. H. Brzozowski, E. Kallne and H. P. Summers

TRITA-PFU-91-09, Stockholm, Sweden (1990)
[6] R. A. Phaneuf, I. Alvarez, F. W. Meyer, and D. H. Crandall, *Phys. Rev. A* **26** 1892-1906 (1982)
[7] C. C. Havener, M. S. Huq, H. F. Krause, P. A. Schulz, and R. A. Phaneuf, *Phys. Rev. A* **39** 1725-1740 (1989)
[8] D. Dijkkamp, D. Ciric, F. J. De Heer, and E. Vlieg, *Nucl. Instr. Method B* **9** 403-407 (1985)
[9] J. Burgdorfer, R. Morgenstern and A. Niehaus, *J. Phys. B.* **19** L507-513 (1986)
[10] C. Harel and H. Jouin, *J. Phys. B.* **21** 859-883 (1988)
[11] E. J. Shipsey, J. C. Browne and R. E. Olson, *J. Phys. B.* **14** 869-880 (1981)
[12] R.A. Hulse, *Nucl. Tech/Fusion*, **3**, 259-272 (1983)
[13] T. Fujimoto, K. Sawada, K. Takahata, K. Eriguchi, H. Suemitsu, K. Ishii, R. Okasaka, S. Tanaka, T. Maekawa and Y. Terumichi, *Nucl. Fusion*. **29**, 1519 (1989)

Table 1. Charge exchange recombination rate coefficient (m^3s^{-1})

level	4^2S	4^2P	4^2D	4^2F
rate coefficient	8.9×10^{-16}	less than 1×10^{-17}	4.8×10^{-16}	2.1×10^{-17}

Figure Captions

Fig. 1. r-dependence of T_e and n_e for the experimental plasma condition.

Fig. 2. r -dependence of the $3p^2P_{3/2}$ level population of OVI ions.

Fig. 3. Spectra of (a) 381nm; and (b) 383nm; lines observed in the central chord. The upper level of these lines are $3p^2P_{3/2}$ and $3p^2P_{1/2}$, respectively.

Fig. 4. (a) Xuv spectra in the central chord. (b) Gaussian fitting for the 13.0 and 13.2nm lines and (c) the 18.2nm line in the central chord. Solid curves show the OVI spectra, and dotted ones are the blending lines.

Fig. 5. The result of the absolute sensitivity calibration of the xuv spectrometer. Closed circles are given directly by the branching ratio method and open circles are given from the CR model calculation combined with the branching ratio method. The uncertainty of the sensitivity of the visible-uv spectrometer is included in the error bars of the closed circles but is not included in the error bars of the open circles.

Fig. 6. Gaussian fit for the spectra from the SOL plasma. The explanation is the same as for Fig.4 (b).

Fig. 7. The ground state density of the CIV ions derived on the assumption of the ionizing plasma. The result of the transport code "MIST" is included. (We assume the diffusion coefficient D=2.0 m^2/sec and convective velocity parameter C=1.0.)

Fig. 8. (a) Photon emission ratios driven from the CR calculation for OVI ions, and (b) for CIV ions.

Fig. 9. The calculation result by the MIST code for oxygen. We assume that the diffusion coefficent and convective velocity parameter are D=2.0 m^2/s and C=1.0, respectively. We also assume that the impurity sourse is a limiter. "Experimental" density of OVI ions as derived from the measured $3p$ populations and T_e and n_e is also shown. The error bars of the closed circles are due to the uncertainty of T_e and n_e.

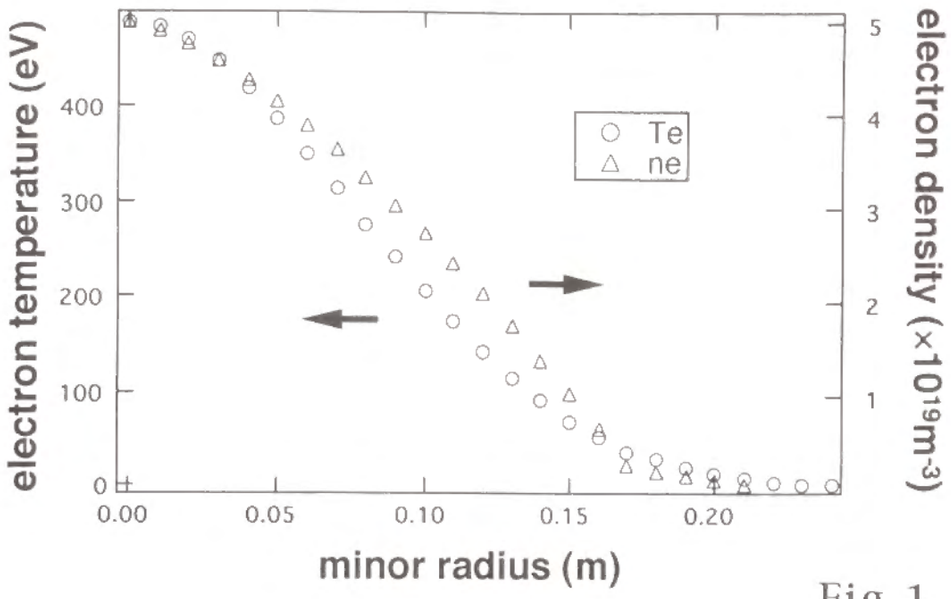

Fig. 1

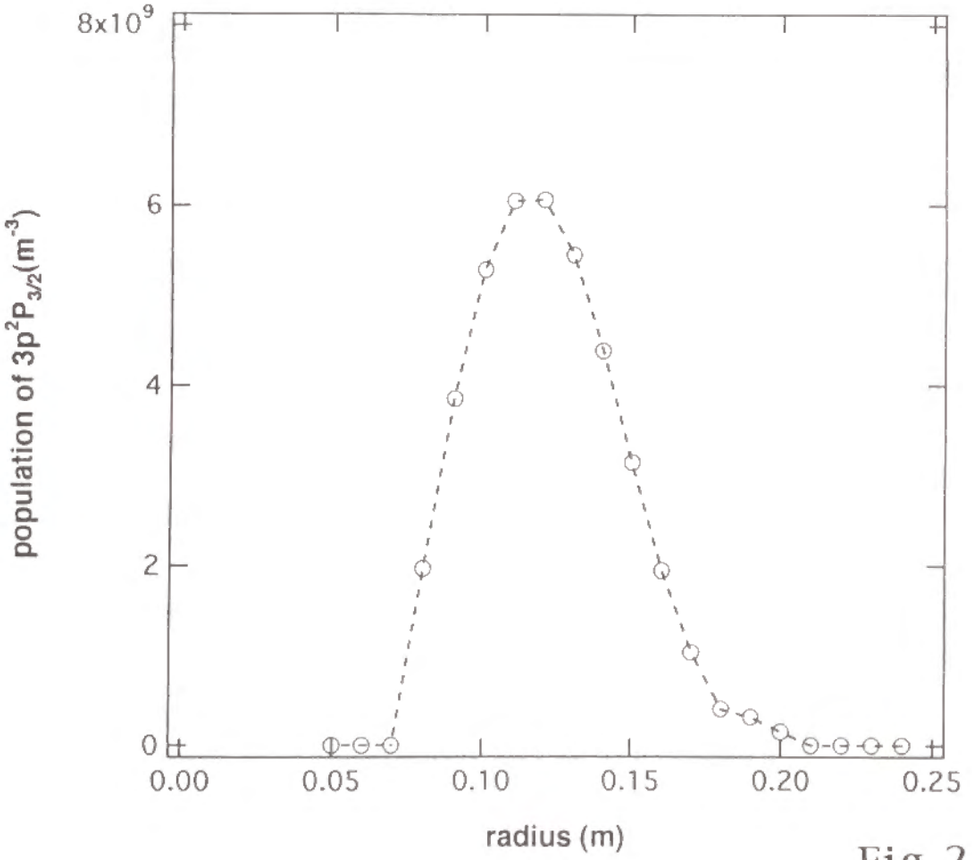

Fig. 2

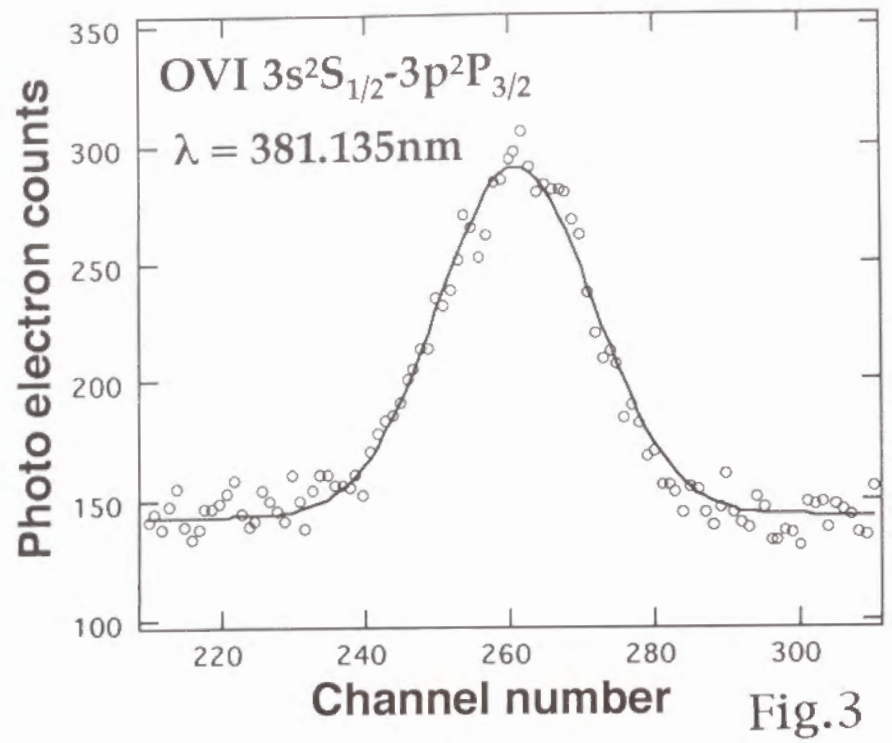

Fig.3 (a)

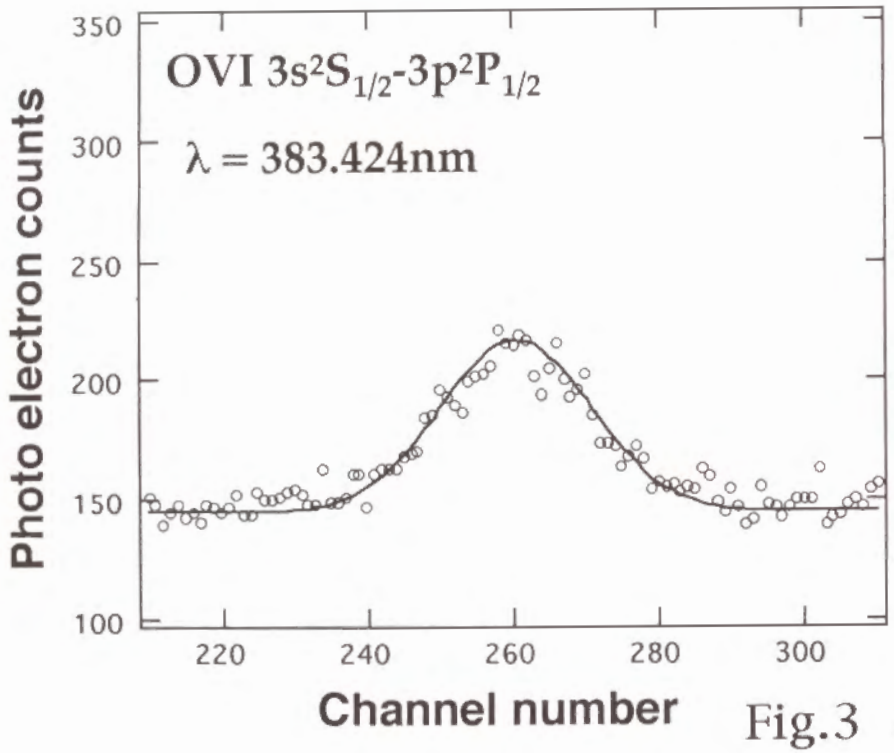

Fig.3 (b)

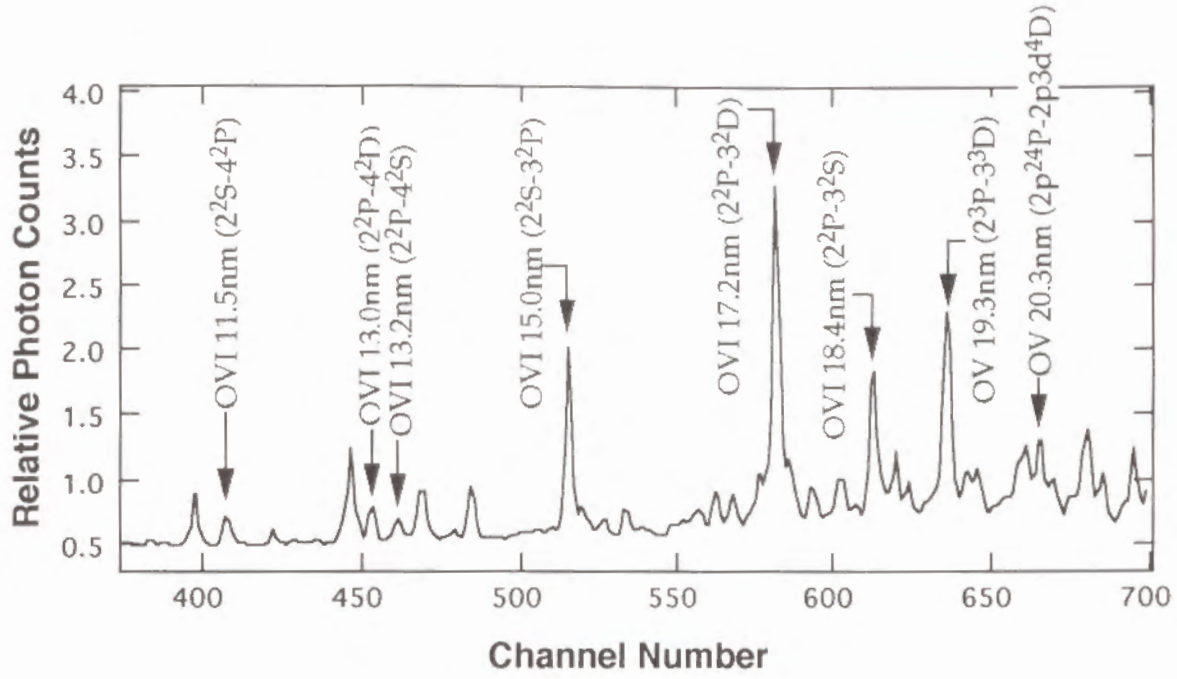

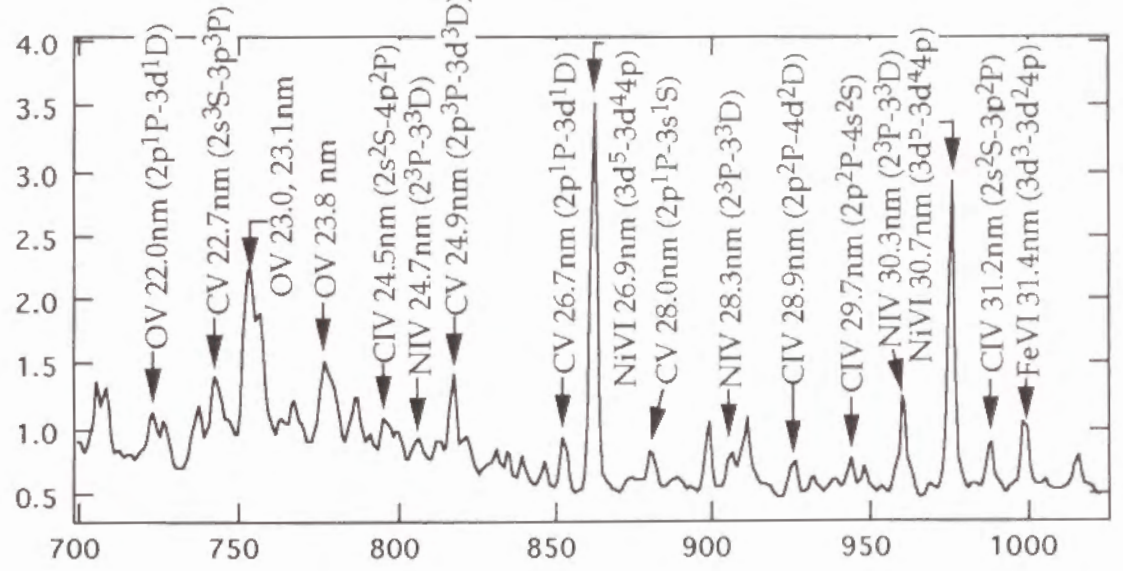

Fig.4 (a)

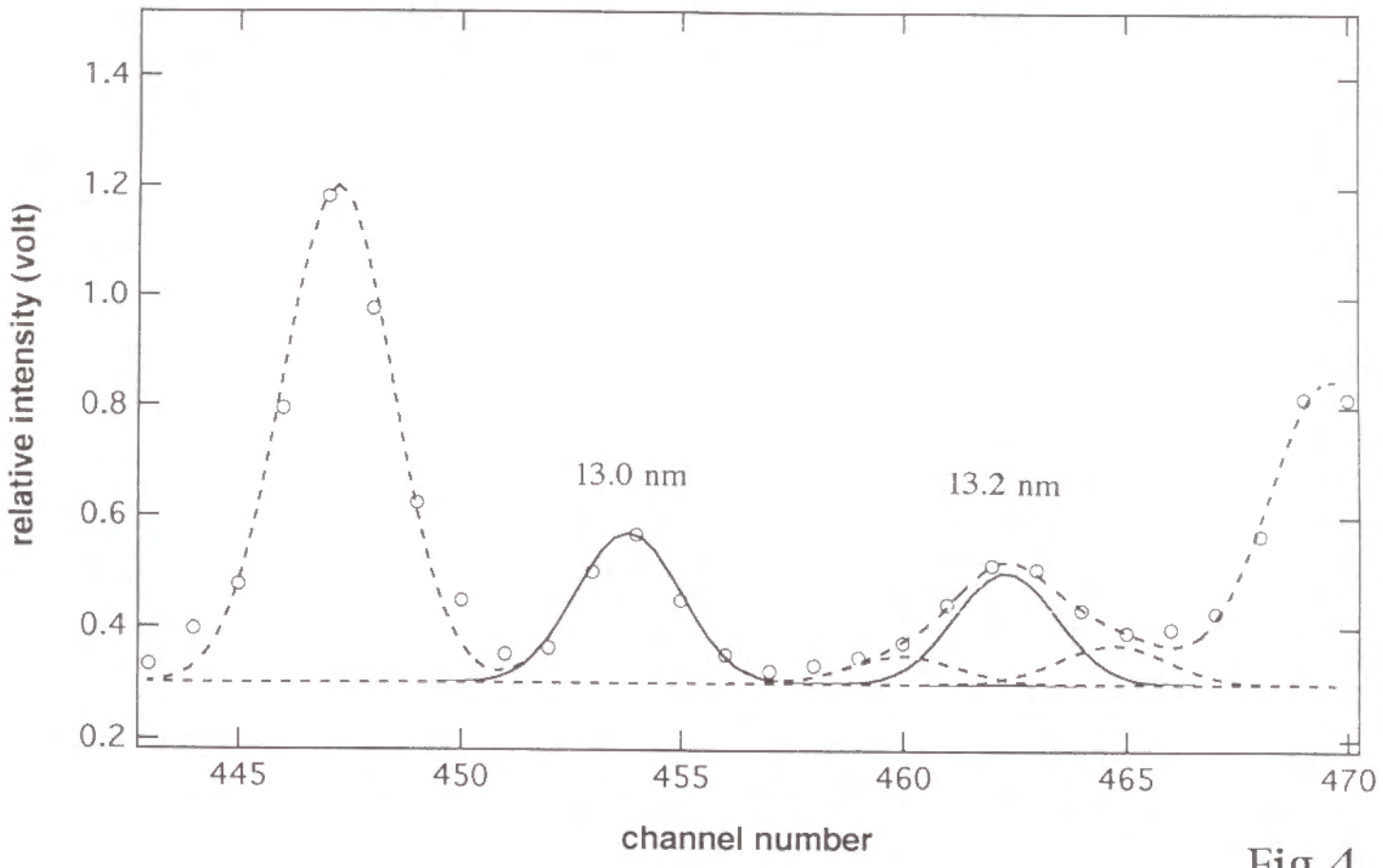
relative intensity (volt)
1.4
1.2
1.0
0.8
0.6
0.4
0.2
13.0 nm
13.2 nm
445
450
455
460
465
470
channel number

Fig.4 (b)

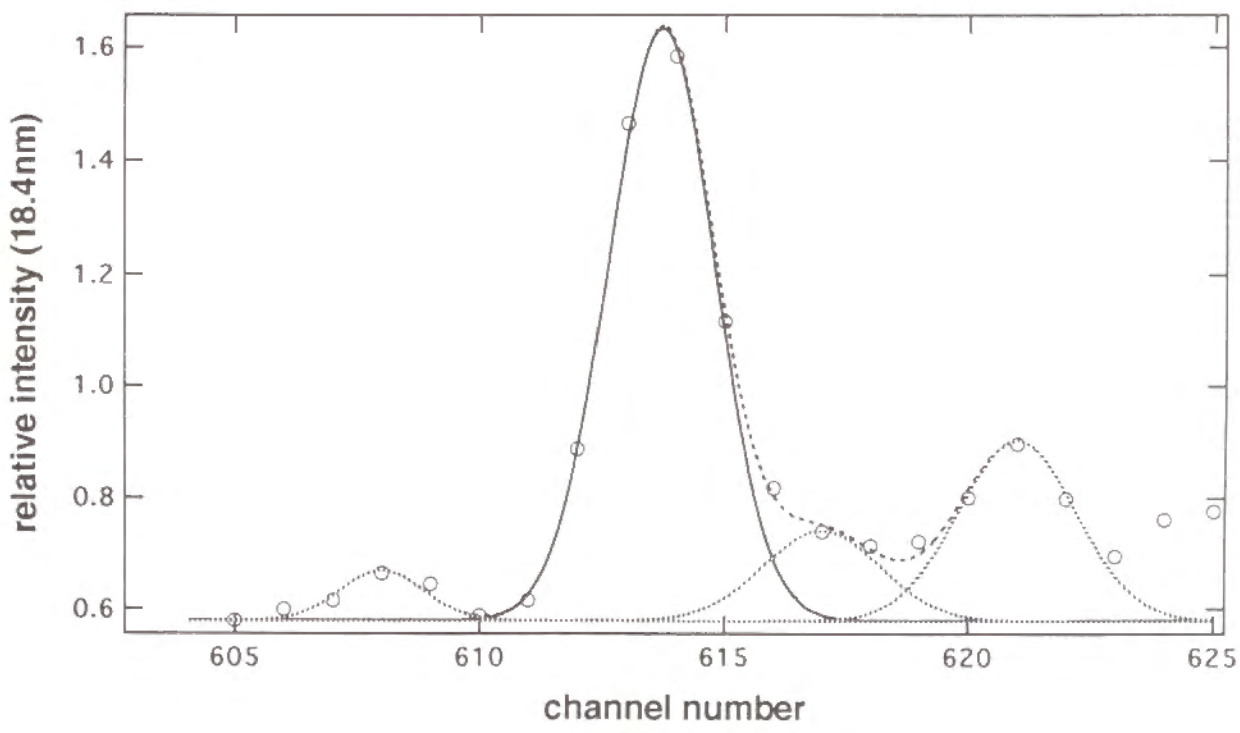
relative intensity (18.4nm)
1.6
1.4
1.2
1.0
0.8
0.6
605
610
615
620
625
channel number

Fig. 4 (c)

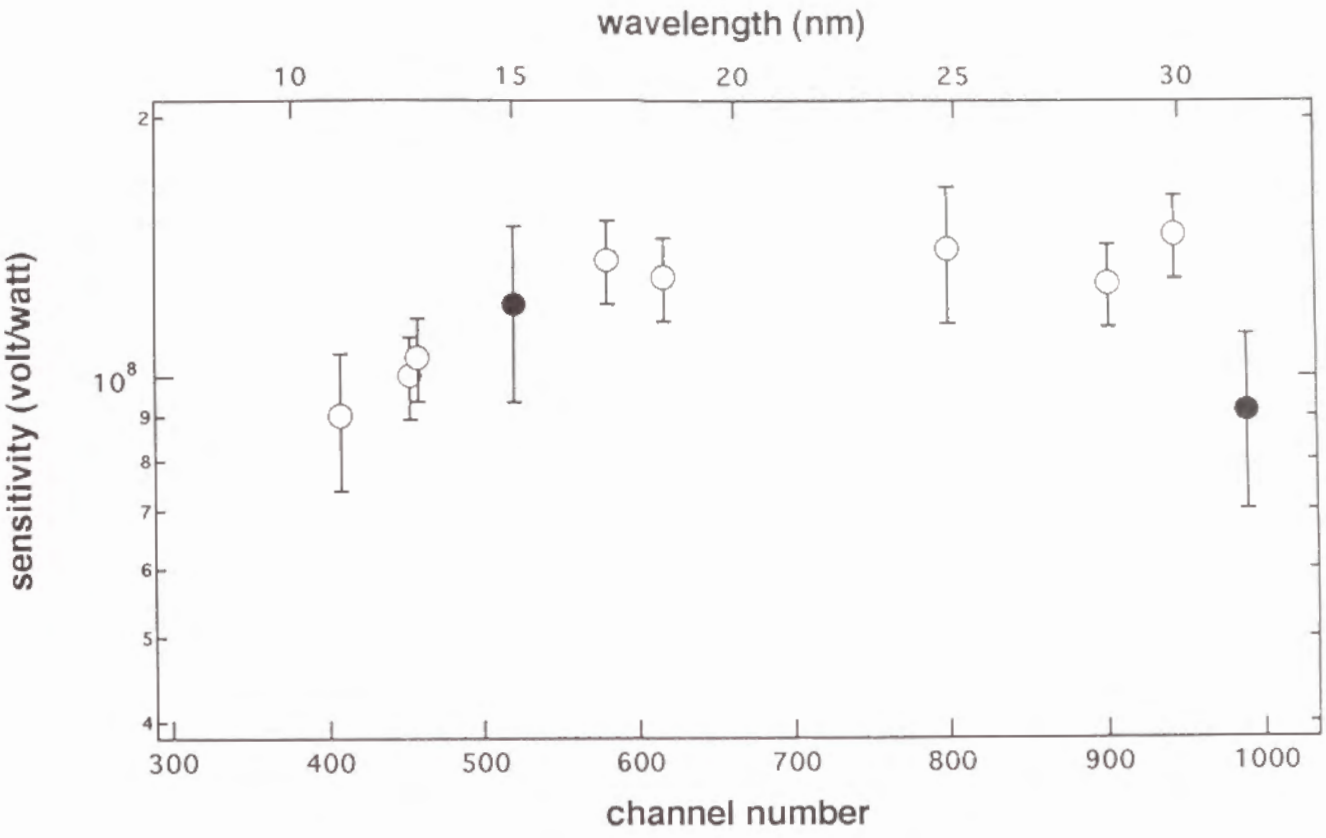
wavelength (nm)
10
15
20
25
30
sensitivity (volt/watt)
10^8
2
9
8
7
6
5
4
300
400
500
600
700
800
900
1000
channel number

Fig.5

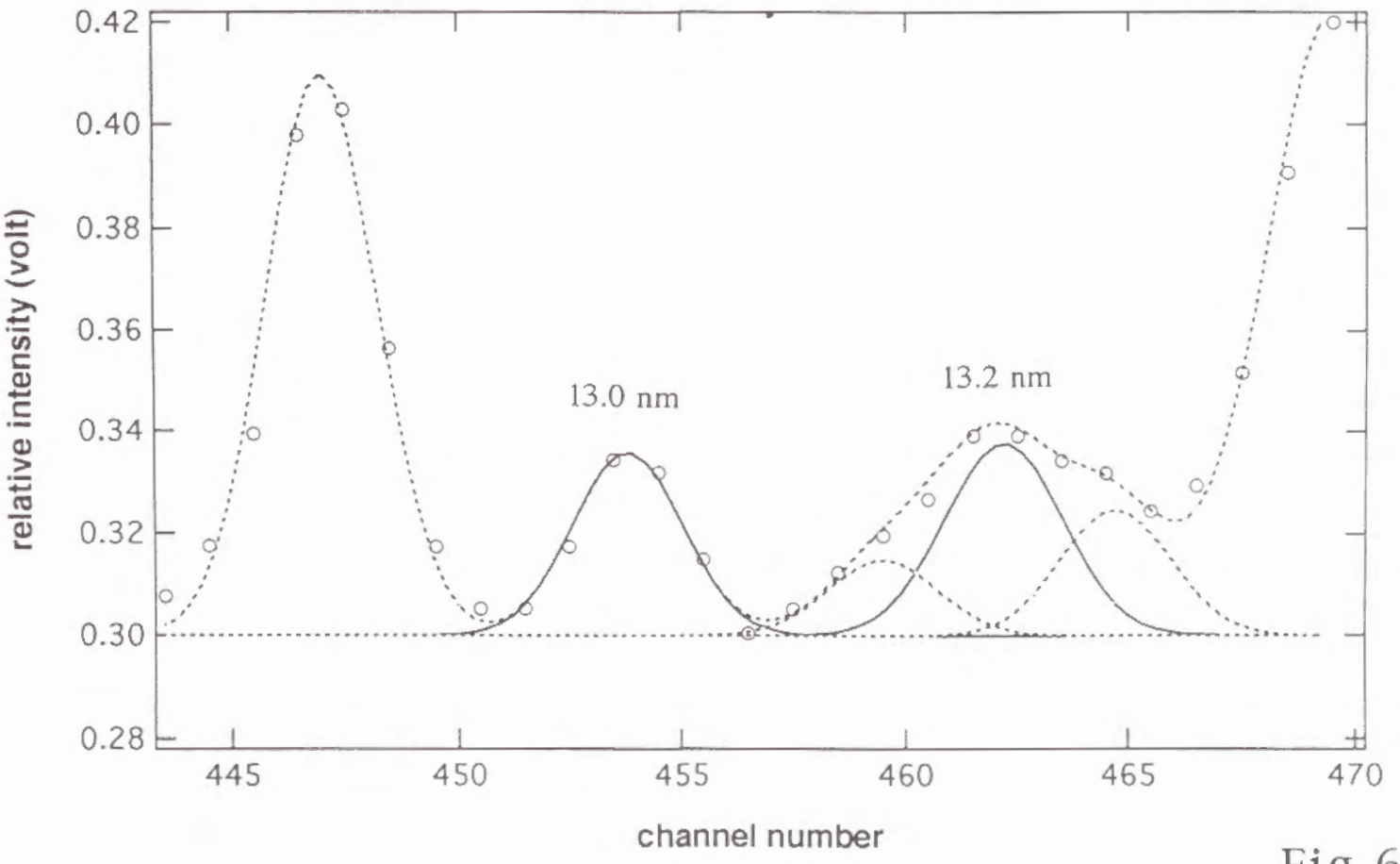
relative intensity (volt)
0.42
0.40
0.38
0.36
0.34
0.32
0.30
0.28
13.0 nm
13.2 nm
445
450
455
460
465
470
channel number

Fig.6

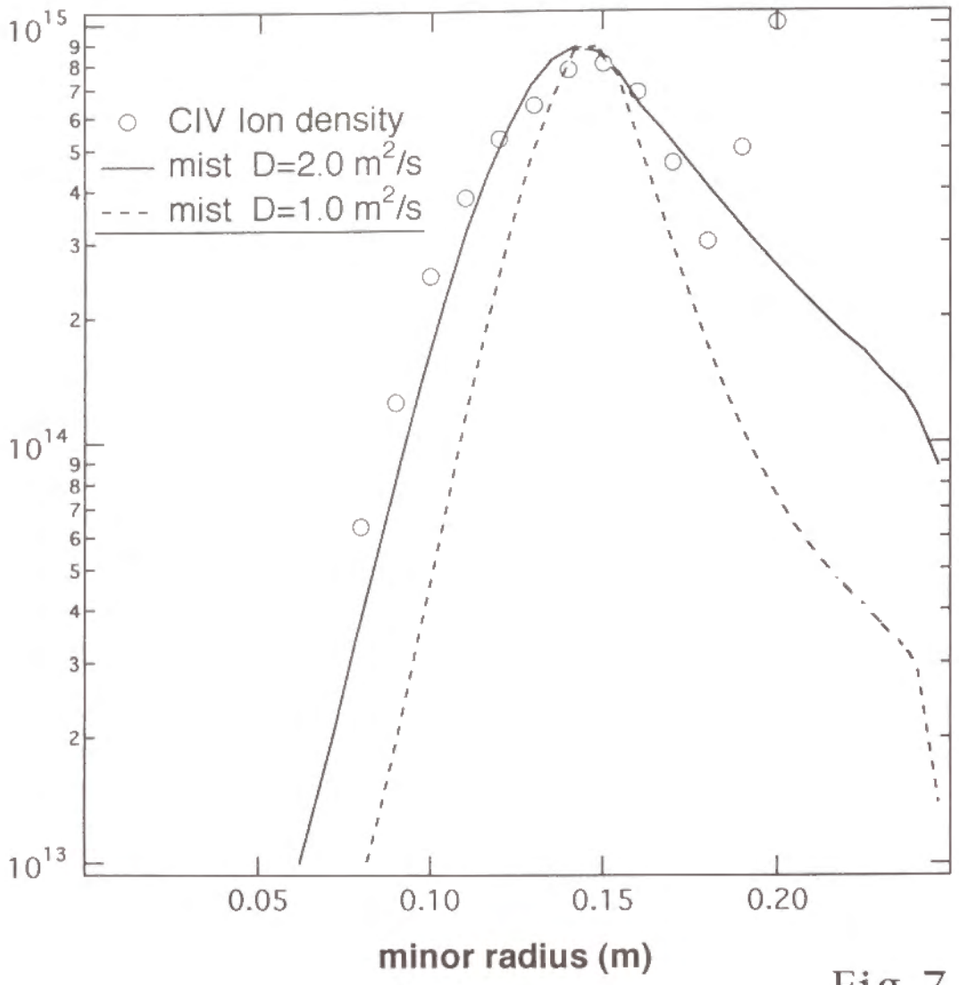
CIV Ion density
mist D=2.0 m²/s
mist D=1.0 m²/s
10¹⁵
10¹⁴
10¹³
0.05
0.10
0.15
0.20
minor radius (m)

Fig.7

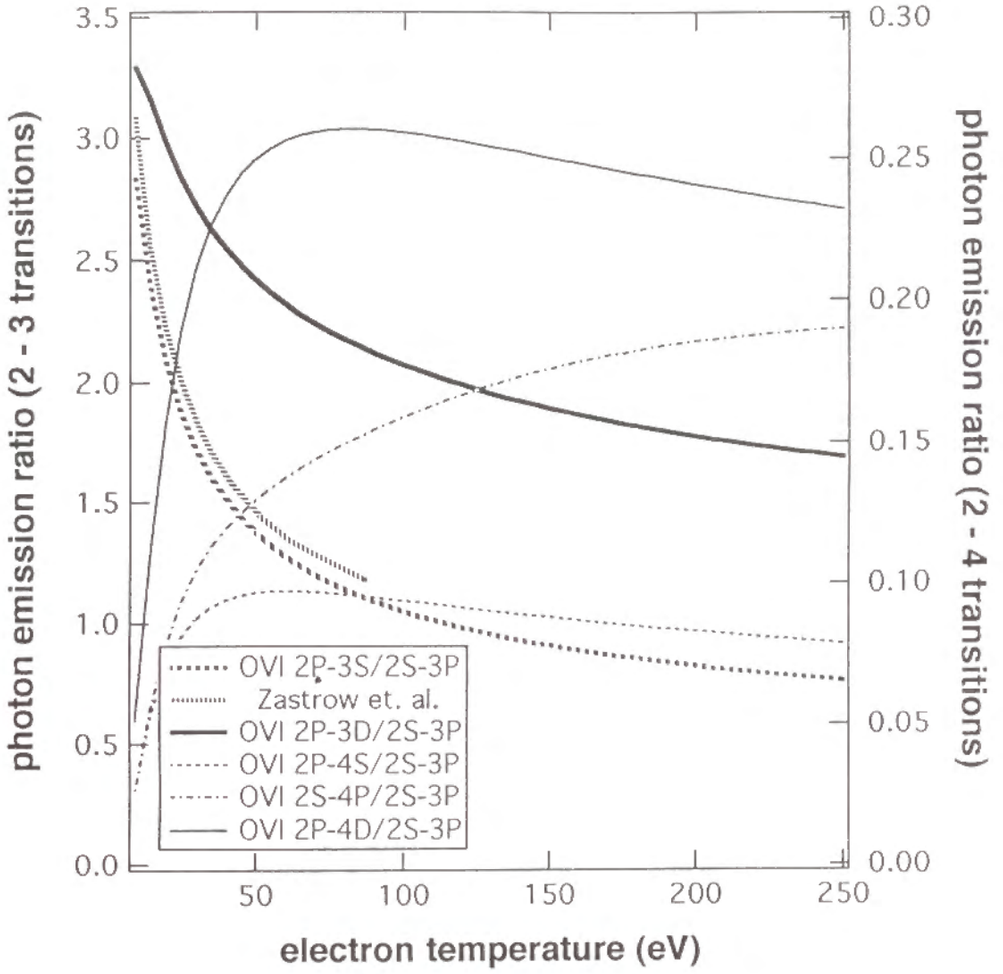
photon emission ratio (2 - 3 transitions)
photon emission ratio (2 - 4 transitions)
OVI 2P-3S/2S-3P
Zastrow et. al.
OVI 2P-3D/2S-3P
OVI 2P-4S/2S-3P
OVI 2S-4P/2S-3P
OVI 2P-4D/2S-3P
3.5
3.0
2.5
2.0
1.5
1.0
0.5
0.0
0.30
0.25
0.20
0.15
0.10
0.05
0.00
50
100
150
200
250
electron temperature (eV)

Fig.8 (a)

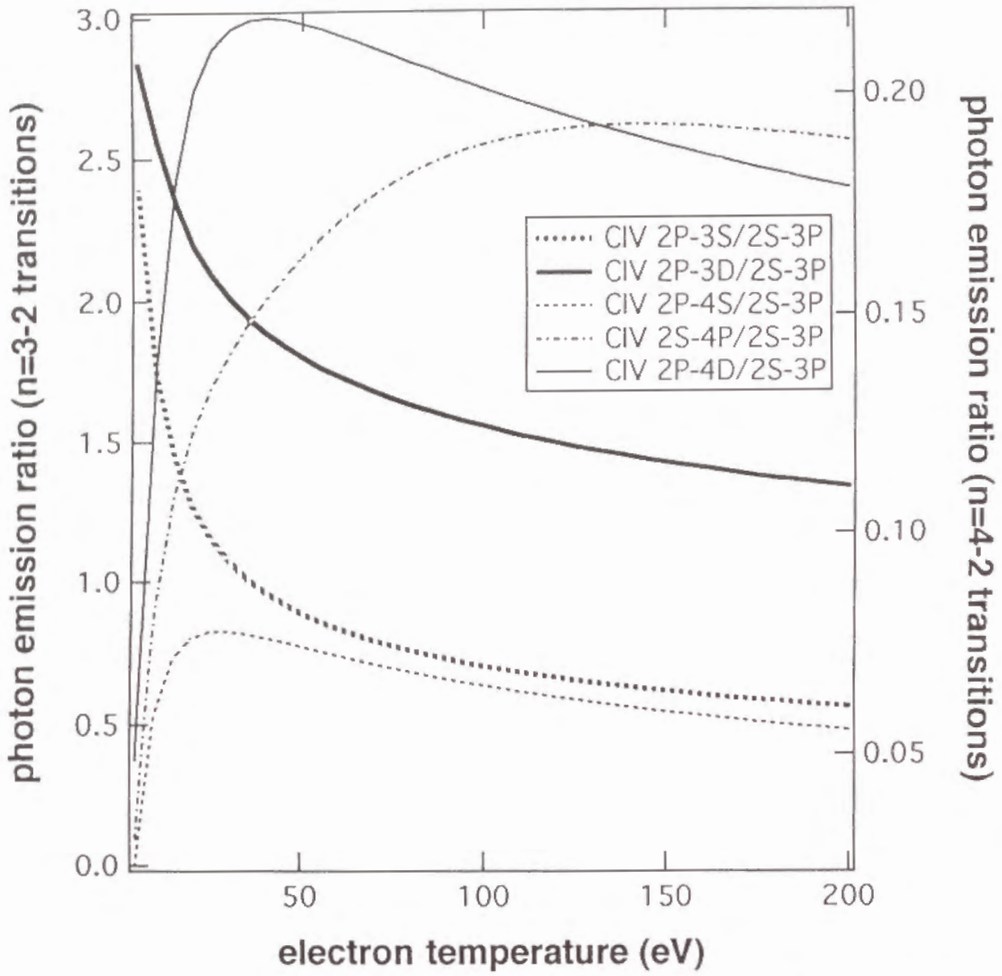
photon emission ratio (n=3-2 transitions)
photon emission ratio (n=4-2 transitions)
electron temperature (eV)
CIV 2P-3S/2S-3P
CIV 2P-3D/2S-3P
CIV 2P-4S/2S-3P
CIV 2S-4P/2S-3P
CIV 2P-4D/2S-3P
3.0
2.5
2.0
1.5
1.0
0.5
0.0
0.20
0.15
0.10
0.05
50
100
150
200

Fig.8 (b)

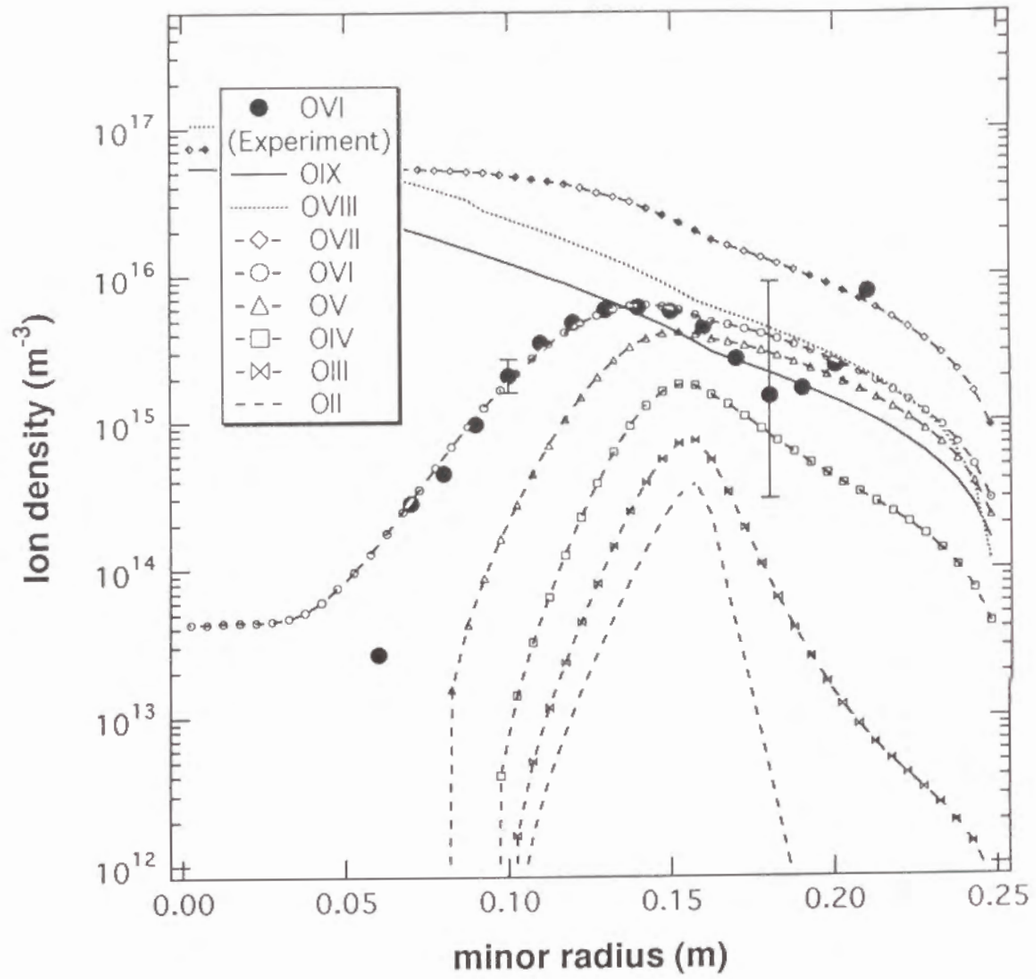
Ion density (m^{-3})
minor radius (m)
OVI
(Experiment)
OIX
OVIII
OVII
OVI
OV
OIV
OIII
OII
10^{17}
10^{16}
10^{15}
10^{14}
10^{13}
10^{12}
0.00
0.05
0.10
0.15
0.20
0.25

Fig. 9

CHAPTER V.

Plasma Polarization Spectroscopy

Abstract We have constructed a framework of a new method for plasma diagnostics, PPS (*plasma polarization spectroscopy*). For axially symmetric plasmas on the basis of the density matrix theory, we treat a rate equation of a relaxation process of an ensemble of atoms. In order to solve this equation, we introduce a "superoperator", and derive the explicit expressions of the relaxation matrix elements or rate coefficients for transitions of population and alignment between levels. We derive a collisional-radiative model for population and for alignment of the excited levels. We conducted a preliminary experiment of PPS on the WT-3 tokamak, and measured polarization of the beryllium-like oxygen (OV) ion lines ($3s^3S_1$- $3p^3P_{0,1,2}$) by use of a calcite polarizer. We made a simplified alignment CR model for these ions, and calculated the alignment of these levels for several cases of anisotropic electron velocity distributions.

I. INTRODUCTION

For a tokamak plasma, Lammeren *et al.* [1] measured the electron temperature by the method of Thomson scattering, and they found that the toridal temperature was slightly higher than the poloidal one. This is an example of spatial anisotropy of plasma. When the electron velocity distribution is anisotropic like this example, atoms and ions (simply called atoms) in it are subjected to collisions more frequently in one direction than in other directions. If these atoms are excited by these collisions the excited atoms are polarized, aligned in this case, and emitted radiation from these excited atoms is polarized, linearly polarized in this example.

The polarization of radiation emitted from plasma has been ignored so far in plasma research except for a few cases [2, 3]. Since the polarization of radiation is directly related with the anisotropy in plasma as discussed above, a method to treat plasma anisotropy by use of the polarization characteristics of radiation, which we call PPS (*Plasma polarization Spectroscopy*) [4], should be a powerful new tool for plasma diagnostics.

In order to treat quantitatively the anisotropy of the plasma from the polarization in the excited atom state, a new framework is needed; in this framework alignment would be treated on the same basis as population, *i.e.*, by a kind of collisional-radiative model. Furthermore, when the electron velocity distribution is anisotropic, for example, we need various kinds of rate coefficients and those for excitation should be different from those on the assumption of isotropic plasma or isotropic Maxwell distribution. Thus, we should assess these rate coefficients of population and alignment for given electron velocity distribution.

In the following, we show the formulations of the rate coefficients and the new CR model for axially symmetric case and an example.

II. THEORY

We assume an axially symmetric situation with no electric or magnetic field present. Throughout this section, we rely on the textbooks by Messiah [5], Omont [6] and Blum. [7]

A. Density matrix and rate equation

The state of an ensemble of atoms or ions (simply called atoms henceforth) is described by the density matrix.

$$\rho = \sum_{\alpha FM \beta GN} <\alpha FM\ |\rho|\beta GN>|\alpha FM><\beta GN| \tag{1}$$

where ρ is a density operator, F and G are the total angular momenta of the Zeeman multiplets of an atom in the ensemble, and M and N are their z-components, respectively. α and β represent all the other variables which are necessary for a complete specification of the states. An operator or a vector in product space (Liouville space), $|\alpha FM><\beta GN|$, can be expressed in terms of an irreducible tensor operator $T(\alpha F\beta G)_{kq}$ with rank k and its z-component q, (k =0, 1, 2, ..., $-k \le q \le k$.)

$$|\alpha FM><\beta GN| = \sum_{k,q} (-)^{F-M} <F\ G\ M-N|k\ q>T\ (\alpha F\ \beta G)_{k\,q} \tag{2}$$

where $<FGM\text{-}N|kq>$ is the Clebsch-Gordan coefficient.

By use of eq.(2), the density matrix is described as,

$$\begin{aligned}\rho &= \sum_{\alpha F\beta Gkq}\left[\sum_{MN} <\alpha F\ M|\rho|\beta G\ N>(-)^{F-M} <F\ G\ M-N|k\ q>\right] T\ (\alpha F\ \beta G)_{k\,q} \\ &= \sum_{\alpha F\beta Gkq} \rho^{k}_{q}(\alpha F\ \beta G)\ \ T\ (\alpha F\ \beta G)_{k\,q}\end{aligned} \tag{3}$$

where ρ^{k}_{q}'s are called state multipoles or irreducible components of the density matrix. The term with k = 0, 1 and 2 corresponds to population, orientation vector and alignment tensor, respectively, of ρ in the space spanned by αF and βG. The irreducible components of density matrix are expressed in terms of the dyadic representation of the matrix elements as

$$\rho^{k}_{q}(\alpha F\ \beta G) = \sum_{M} (-)^{G-N} <F\ G\ M-N|k\ q>\ \rho_{\alpha FM\ ,\ \beta GN} \tag{4}$$

In the case of axial symmetry along the z-axis, because the density operator must be invariant under the rotation along the z-axis and under the inversion, *i.e.*, $z \rightarrow -z$, all the components other than the q=0 components vanish, and k must be even, that is,

$$\rho\ (\alpha F\beta G) = \rho^{0}_{0}(\alpha F\beta G)\ T\ (\alpha F\beta G)_{00} + \rho^{2}_{0}(\alpha F\beta G)\ T\ (\alpha F\beta G)_{20} + \cdots \tag{5}$$

We consider the time development of the ensemble which is subjected to relaxation; *i.e.*, the processes of radiative decay, electron impact excitation and deexcitation, etc. This relaxation process may be expressed as

$$\frac{d\rho}{dt} = -\,G\,\rho \tag{6}$$

where G stands for the relaxation matrix. This equation can be expressed in terms of the dyadic representation as

$$\frac{d\rho_{ij}}{dt} = -\sum_{rs} G_{ij\,,\,rs}\rho_{rs} \tag{7}$$

The matrix element $G_{ij,rs}$ means that the operator $|r><s|$ is transformed into the operator $|i><j|$ by G.

For the isotropic relaxation case, *e.g.*, radiative processes in the optically thin plasma, the transfer rate $g_k(FG, F'G')$ for the irreducible components is defined by use of $G_{ij,rs}$ as

$$\begin{aligned}&T\ (\alpha F\ M, \beta G\ N)_{k\,q}\ G\,T\ (\alpha'F'\ M', \beta'G'\ N')^{+}_{k\,q} \\ &= g_{\ k}(FG\ F'G')\ \delta_{kk'} \\ &= \sum_{M,M'} (-)^{G+G'+M+M'} <F\ G\ M\ (q-M)|k\ q><F'\ G'\ M'\ (q-M')|k\ q> \\ &\qquad \times G_{\alpha F\ M\ \beta G\ M-q\ ,\alpha'F'\ M'\beta'G'\ M'-q}\end{aligned} \tag{8}$$

Equation (8) shows that there is no mixing between the different k-components in the isotropic relaxation process.

We now assume axial symmetry and no coherence between the different Zeeman multiplets. G is rotational invariant, and we can put the initial and final atomic states diagonal, *i.e.*, αF=βG and $\alpha'F'$=$\beta'G'$.

$$g_q(k\,k') = \sum_{M,M'} (-)^{F+F'+M+M'} \langle F\,F\,M\,(q-M)|k\,q\rangle \langle F'\,F'\,M'\,(q-M')|k'\,q\rangle \times G_{\alpha F\,M\,\alpha F\,M-q,\alpha' F' M'\,\alpha' F' M'-q} \tag{8 a}$$

From eqs. (4), (7) and (8 a), we obtain the rate equation, where we note $\rho_{ij} = 0$ except for $i=j$, because of the absence of coherence.

$$\frac{\mathrm{d}}{\mathrm{d}t}\rho_q^k(\alpha F\alpha F) = -\sum_{\alpha' F'}\left[\sum_{k'} g_q^{kk'}(\alpha' F'\alpha' F', \alpha F\alpha F)\,\rho_q^{k'}(\alpha' F'\alpha' F')\right] \tag{9}$$

where the expression $-g_q^{kk'}(F'F,'FF)$ means $-g_q(kk')$ for the transition from the level $\alpha' F'$ to the level αF. (Note that the order of F' and F in $g_q^{kk'}$ has been reversed. This notation is consistent with those of the rate coefficients in Chapter II.) Equation (9) is the basic formula for the rate equation in the "Alignment collisional-radiative model in axial symmetry" which we develop in the following sub-sections.

B. Irreducible representation of the rate coefficient

We consider the electron impact excitation process. A collision matrix (we define it by S) describes the process that an atom in state i transfers into another state f after the collision,

$$|\psi_f\rangle = S\,|\psi_i\rangle \tag{10}$$

In the semi-classical approximation, temporal development of the atomic ensemble by various collision processes is expressed by use of S with the collision velocity, v, and the impact parameter, b, as

$$\frac{\mathrm{d}\rho}{\mathrm{d}t} = -G_c\rho = 2\pi N_p\{v\int_0^\infty b\,\mathrm{d}b\,[S(b,v)\,\rho\,S(b,v)^+] - \rho\} \tag{11}$$

where $\{\ \}$ means average over the velocity distribution of electrons which collide with the atoms. N_p is the number of the perturbers. (In this case, these are electrons.) We assume excitation by an electron beam; the direction of which is parallel to the quantization (z-) axis with the speed v, and b perpendicular to z. We introduce an intermediate "super operator", an operator in the Liouville space, Π', which is defined as

$$\Pi'(b,v)\,\rho = \rho - [S(b,v)\,\rho\,S(b,v)^+]_{\text{Ang. ave}} \tag{12}$$

where $[\ ]$ means the average over the direction of b around the collision axis. The matrix element of Π' is expressed as,

$$\Pi'_{\alpha F\,M\,\beta G\,N,\,\alpha' F' M'\,\beta' G' N'} = \delta - \langle\alpha F\,M|S|\beta' G' N'\rangle\langle\alpha F\,M-q|S|\beta' G' M'-q\rangle^*\,\delta_{M-N,\,M'-N'} \tag{13}$$

where $\delta = \delta_{\alpha\alpha'}\,\delta_{\beta\beta'}\,\delta_{FF'}\,\delta_{GG'}\,\delta_{MM'}\,\delta_{NN'}$

The irreducible representation is expressed in terms of this dyadic representation in the similar way to eq. (8 a), *i.e.*,

$$\Pi'_q(k\,k') = \sum_{M,M'} (-)^{F+F'+M+M'} \langle F\,F\,M\,(q-M)|k\,q\rangle \langle F'\,F'\,M'\,(q-M')|k'\,q\rangle \times \Pi'_{\alpha F\,M\,\alpha F\,M-q,\,\alpha' F' M'\,\alpha' F' M'-q} \tag{14}$$

(Note that $q = q'$ and we denote Π' as $\Pi'_q(kk')$.)

where we assume that there is no coherence among the different Zeeman multiplets and put $\alpha' F' = \beta' G'$ for the initial level and $\alpha F = \beta G$ for the final level.

Here, we define the cross section as

$$\sigma_q(k\,k') = 2\pi\int_0^\infty \pm\Pi'_q(k\,k')\,b\,\mathrm{d}b \tag{15}$$

The plus sign applies to the case of $\alpha F = \alpha' F'$ and the minus sign applies to $\alpha F \neq \alpha' F'$. In the case of $\alpha F \neq \alpha' F'$, $\Pi'_q(kk')$ and corresponding cross section $\sigma_q(kk')$ for various k and k' are given as follows.

$$\Pi'_0(0\,0) = -\sum_{MM'} (-)^{F+F'+M+M'} \langle FFM-M|00\rangle\langle F'F'M'-M'|00\rangle \times |\langle\alpha F\,M|S|\alpha' F' M'\rangle|^2 = -(2F+1)^{-1/2}(2F'+1)^{-1/2}\sum_{MM'}|\langle\alpha F\,M|S|\alpha' F' M'\rangle|^2 \tag{16 a}$$

$$\sigma_0(0\,0) = (2F+1)^{-1/2}(2F'+1)^{-1/2}\sum_{MM'} Q_{\alpha FM,\,\alpha' F' M'} \tag{16 b}$$

where $Q_{\alpha FM,\ \alpha'F'M'}$ is the excitation cross section from Zeeman sublevel $\alpha'F'M'$ to another αFM, which is defined as

$$Q_{\alpha FM,\alpha'F'M'} = 2\pi \int_0^\infty |<\alpha FM|S|\alpha'F'M'>|^2 b\ db$$

Similar relation is found for other processes.

$$\Pi_0'(2\,0) = -(2F'+1)^{-1/2} \sum_{MM'} (-)^{F-M} <FFM-M|20> |<\alpha F\ M|S|\alpha'F'M'>|^2 \quad (17\text{ a})$$

$$\sigma_0(2\,0) = (2F'+1)^{-1/2} \sum_{MM'} (-)^{F-M} <FFM-M|20>\ Q_{\alpha FM,\alpha'F'M'} \quad (17\text{ b})$$

$$\Pi_0'(0\,2) = -(2F+1)^{-1/2} \sum_{MM'} (-)^{F'-M'} <F'F'M'-M'|20> |<\alpha F\ M|S|\alpha'F'M'>|^2 \quad (18\text{ a})$$

$$\sigma_0(0\,2) = (2F+1)^{-1/2} \sum_{MM'} (-)^{F'-M'} <F'F'M'-M'|20>\ Q_{\alpha FM,\alpha'F'M'} \quad (18\text{ b})$$

$$\Pi_0'(2\,2) = -\sum_{MM'} (-)^{F+F'-M-M'} <FFM-M|20><F'F'M'-M'|20>|<\alpha FM|S|\alpha'F'M'>|^2 \quad (19\text{ a})$$

$$\sigma_0(2\,2) = \sum_{MM'} (-)^{F+F'-M-M'} <F\ F\ M-M|20><F'F'M'-M'|20>\ Q_{\alpha FM,\alpha'F'M'} \quad (19\text{ b})$$

and

$$\sigma_q(2\,2) = \sum_{MM'} (-)^{F+F'-M-M'} <F\ F\ M\ q-M|2q><F'F'M'q-M'|2q> \times 2\pi \int <\alpha FM|S|\alpha'F'M'><\alpha FM-q|S|\alpha'F'M'-q>^* b\ db \quad (\text{for } q\neq 0) \quad (19\text{ c})$$

Equations (16), (17), (18) and (19) correspond to the processes of "population transfer", "alignment production from the population", "population production from the alignment, or correction term for eq.(16)", and "alignment transfer", respectively. It is noted that eq. (19 c) cannot be expressed in terms of the Zeeman sublevel-Zeeman sublevel cross sections. Rather, the S-matrix elements need to be known.

For the case of $\alpha F = \alpha'F'$,

$$\Pi_0'(00) = \frac{1}{(2F+1)} \sum_{M'} \sum_{M} \{\delta_{MM'} - |<\alpha FM|S|\alpha\ F\ M'>|^2\} \quad (20\text{ a})$$

where the sum over M corresponds to the total depopulation from the level $|\alpha FM'>$ to other Zeeman multiplets, or to all the levels with $F\neq F'$. By use of eq. (15) with the plus sign, the cross section corresponding to eq. (20 a) is given as,

$$\sigma_0(00) = \frac{1}{(2F+1)} \sum_{M'} D_{FM'} \quad (20\text{ b})$$

where $D_{FM'}$ is defined as,

$$D_{FM'} = 2\pi \int_0^\infty \sum_{M} \{\delta_{MM'} - |<\alpha FM|S|\alpha\ F\ M'>|^2\} b\ db$$

Similar relation is found for other processes.

$$\Pi_0'(20) = (2F+1)^{-1/2} \sum_{M'} \sum_{M} (-)^{F-M} <F\ F\ M-M|20> \{\delta_{MM'} - |<\alpha FM|S|\alpha\ F\ M'>|^2\}$$
$$= (2F+1)^{-1/2} \sum_{M'} \sum_{M} (-)^{F-M'} <F\ F\ M'-M'|20> \{\delta_{MM'} - |<\alpha FM|S|\alpha\ F\ M'>|^2\}$$
$$+ (2F+1)^{-1/2} \sum_{M'} \sum_{M} \{(-)^{F-M'} <F\ F\ M'-M'|20> - (-)^{F-M} <F\ F\ M-M|20>\}\ |<\alpha FM|S|\alpha\ F\ M'>|^2 \quad (21\text{ a})$$

$$\sigma_0(20) = (2F+1)^{-1/2} \sum_{M'} (-)^{F-M'} <F\ F\ M'-M'|20>\ D_{FM'}$$
$$+ (2F+1)^{-1/2} \sum_{M'} \sum_{M} \{(-)^{F-M'} <F\ F\ M'-M'|20> - (-)^{F-M} <F\ F\ M-M|20>\}\ Q_{\alpha FM,\alpha FM'} \quad (21\text{ b})$$

$$\Pi_0'(02) = (2F+1)^{-1/2} \sum_{M'} (-)^{F-M'} <F\ F\ M'-M'|20> \sum_{M} \{\delta_{MM'} - |<\alpha FM|S|\alpha\ F\ M'>|^2\} \quad (22\text{ a})$$

$$\sigma_0(02) = (2F+1)^{-1/2} \sum_{M'} (-)^{F-M'} <F\ F\ M'-M'|20>\ D_{FM'} \quad (22\text{ b})$$

$$\Pi_0'(20) = \sum_{M'} \sum_{M} (-)^{F+F'-M-M'} <F\ F\ M-M|20><F\ F\ M'-M'|20> \{\delta_{MM'} - |<\alpha FM|S|\alpha\ F\ M'>|^2\}$$
$$= \sum_{M'} \sum_{M} <F\ F\ M'-M'|20>^2 \{\delta_{MM'} - |<\alpha FM|S|\alpha\ F\ M'>|^2\}$$
$$+ \sum_{M'} \sum_{M} <F\ F\ M'-M'|20> \{<F\ F\ M'-M'|20> - (-)^{M-M'} <F\ F\ M-M|20>\} |<\alpha FM|S|\alpha\ F\ M'>|^2 \quad (23\text{ a})$$

$$\sigma_0(22) = \sum_{M'} (-)^{F-M'} \langle F\ F\ M\ -M'\ |20\rangle^2\ D_{FM'}$$
$$+ \sum_{M'} \sum_{M} \langle F\ F\ M\ -M'\ |20\rangle \{\langle F\ F\ M'\ -M'\ |20\rangle - (-)^{M-M'} \langle F\ F\ M\ -M\ |20\rangle\} Q_{\alpha FM,\ \alpha FM'} \quad (23\ b)$$

and

$$\sigma_q(22) = \sum_{MM'} (-)^{F+F-M-M'} \langle FFM\ q\ -M\ |2q\rangle \langle FFM'\ q\ -M'\ |2q\rangle$$
$$\times 2\pi \int_0^\infty [\delta_{MM'} - \langle \alpha FM\ |S|\ \alpha FM'\rangle \langle \alpha FM\ -q\ |S|\ \alpha FM'\ -q\rangle^*]\, b\, db$$
$$(q \neq 0) \quad (23\ c)$$

In eq. (21 b), the first and second terms on the right-hand side are understood to be the cross section of "alignment production from the depopulation" and that of "alignment production by elastic collisions", respectively. Equation (22 b) is the correction term to the depopulation process for the presence of alignment of the initial state. In the right-hand side of eq. (23 b), the first and second terms correspond to the cross section of "alignment destruction by the depopulation" and that of "disalignment", respectively.

We now turn to actual plasmas. We define an "super operator", $\Pi_q(kk')$, which describes the excitation, deexcitation or elastic collision process in an axial symmetric plasma. $\Pi_q(kk')$ is expressed in terms of $\Pi'_q(kk')$ as

$$\Pi_q(k\,k') = \sum_{q'} (-)^{q-q'} \Pi'_{q'}(k\,k')$$
$$\sum_K \langle k\,k'\,q-q\,|K\,0\rangle \langle k\,k'\,q'-q'\,|K\,0\rangle$$
$$\times \int_0^\pi f(v,\theta)\, P_K(\cos\theta)\, \sin\theta\, d\theta \quad (24)$$

Here $f(v,\ \theta)$ is the distribution of electron velocities over the speed and the direction, and $P_K(\cos\theta)$ is the Legendre polynomial. It is convenient that the integral in eq.(24) is expanded in K-multipole components. We first expand $f(v,\theta)$ as

$$f(v,\theta) = \sum_K f_K(v)\ P_K(\cos\theta) \quad (25)$$

then, we have

$$\int_0^\pi f(v,\theta)\, P_K(\cos\theta)\, \sin\theta\ d\theta$$
$$= f_K(v) \int_{-1}^{1} P_K(x)\, P_K(x)\, dx = \frac{2}{2K+1} f_K(v) \quad (26)$$

Thus, the irreducible components of the super operator Π are given from eqs. (24) and (26) as

$$\Pi_0(00) = 2 f_0(v)\, \Pi'_0(00) \quad (27\ a)$$
$$\Pi_0(02) = \frac{2}{5} f_2(v)\, \Pi'_0(02) \quad (27\ b)$$
$$\Pi_0(20) = \frac{2}{5} f_2(v)\, \Pi'_0(20) \quad (27\ c)$$
$$\Pi_0(22) = \left(\frac{2}{5} f_0(v) + \frac{4}{35} f_2(v) + \frac{4}{35} f_4(v)\right) \Pi'_0(22)$$
$$+ \left(\frac{2}{5} f_0(v) + \frac{2}{35} f_2(v) - \frac{8}{105} f_4(v)\right) \Pi'_1(22)$$
$$+ \left(\frac{2}{5} f_0(v) - \frac{4}{35} f_2(v) + \frac{6}{315} f_4(v)\right) \Pi'_2(22) \quad (27\ d)$$

We now substitute the superoperator $\Pi'_q(kk')$'s by the corresponding cross sections in eqs. (16)-(23), then we define the rate coefficients corresponding to these processes

$$C^{kk'} = \int_0^\infty f_K(v)\ \sigma_q(k\,k')\, v^3\, dv \quad (28)$$

C. Example

We assume that the neutral helium beam with the velocity of 4×10^6m/s is penetrating into the isotropic hydrogen plasma along the -z-direction. The electron and proton temperature are assumed to be 10keV ($v_p = 8.2\times10^5$m/s; v_p is the thermal proton velocity.), and the electron and proton densities are 1.0×10^{19}m^{-3}. In this situation, the electron and proton velocity distributions are "shifted-Maxwellian" as viewed by the beam particles. Figure 1 shows the shifted Maxwellian distribution of the plasma protons, $f(v_x, v_z)$. In this figure, the curve cutting the distribution function is the circle whose center is at the origin, and its radius corresponds to the collision speed of 2.5×10^6m/s taken as an example between the protons and helium beam atoms. Obviously, the

collisions in the z-direction occur more frequently than those in the x- and y-directions, *i.e.*, the collisions are anisotropic. (For electron collisions, the electron temperature is so high under this plasma condition that the anisotropy in the collisions is not substantial.)

For the distribution $f(v, \theta)$ of Fig.1, we calculate the multipole components, f_K's in Fig.2. (See also eq.(26)) The zero-th component for the isotropic Maxwellian distribution with the same proton temperature is attached. In this case, the higher order components are, of course, absent.

We calculated $\sigma_0(00)$ and $\sigma_0(20)$ for the transition from the ground state (1^1S) to the 2^1P level. $\sigma_0(00)$ is derived from the proton impact cross section data by Fritsch [8], and $\sigma_0(20)$ are obtained from the velocity scaling of the longitudinal alignment data for positron collisions by Csanak. [9] The result is shown in Fig. 3.

D. Formulation of the alignment collisional-radiative model

In this section, we show a formulation of the alignment collisional-radiative model by use of the rate coefficients which we presented in the previous section. Previously, Kazantzev and co-workers constructed a similar model for simple cases. [10-12]

The basic rate equation for the axial symmetric case has been shown in eq.(9). We introduce population $n(p)$ in place of $\rho^0_0(p)$,

$$n(p) = \sqrt{2J_p+1}\,\rho^0_0(p) \qquad (J_p = \text{total angular momentum of } p) \tag{29}$$

and substitute $\rho^0_0(\alpha F \alpha F)$ in eq. (9) by $n(p)$. We now re-define the cross sections originally given by eq. (16 b), (17 b), (18 b), (21 b) and (22 b) as,

$$\sigma_0(0\,0) = (2F'+1)^{-1} \sum_{MM'} Q_{\alpha FM,\,\alpha' F' M'} \tag{16' b}$$

$$\sigma_0(2\,0) = (2F'+1)^{-1} \sum_{MM'} (-)^{F-M} \langle FFM\,-M\,|20\rangle\, Q_{\alpha FM,\,\alpha' F' M'} \tag{17' b}$$

$$\sigma_0(0\,2) = \sum_{MM'} (-)^{F'-M'} \langle F'F'M'\,-M'\,|20\rangle\, Q_{\alpha FM,\,\alpha' F' M'} \tag{18' b}$$

$$\sigma_0(20) = (2F+1)^{-1} \sum_{M'} (-)^{F-M'} \langle F\,F\,M'\,-M'\,|20\rangle\, D_{FM'}$$
$$+ (2F+1)^{-1} \sum_{M'} \sum_{M} \left((-)^{F-M'} \langle F\,F\,M'\,-M'\,|20\rangle - (-)^{F-M} \langle F\,F\,M\,-M\,|20\rangle\right) Q_{\alpha FM,\,\alpha' F' M'} \tag{21' b}$$

$$\sigma_0(02) = \sum_{M'} (-)^{F-M'} \langle F\,F\,M'\,-M'\,|20\rangle\, D_{FM'} \tag{22' b}$$

Note that, in these expressions, $\sigma_0(00)$ in eq. (20 b) and $\sigma_q(22)$'s in eqs. (19 b), (19 c), (23 b) and (23 c), are identical to the original cross sections. The rate coefficient, eq. (28), is re-defined accordingly. From now on, we use these new definitions.

The rate equations for the population, $n(p)$, and the alignment, $\rho^2_0(p)$, are given as follows: For the population,

$$\begin{aligned}
\frac{dn(p)}{dt} &= \sum_{q \neq p} [C(q, p)\, n_e + A(q, p)]\, n(q) \\
&- \left(\sum_{q \neq p} [C(p,q)\, n_e + A(p,q)] + \Lambda(p) \right) n(p) \\
&+ \sum_{q \neq p} C^{02}(q, p)\, n_e\, \rho^2_0(q) \\
&- C^{02}(p, p)\, n_e\, \rho^2_0(p)
\end{aligned} \tag{30}$$

where p or q means Zeeman multiplets or the fine structure levels.
For the alignment,

$$\begin{aligned}
\frac{d\rho^2_0(p)}{dt} &= \sum_{q \neq p} C^{20}(q, p)\, n_e\, n(q) - C^{20}(p, p)\, n_e\, n(p) \\
&- \left\{ \sum_{q \neq p} A(p,q) + \Lambda(p) + C^{22}(p, p)\, n_e \right\} \rho^2_0(p) \\
&+ \sum_{q \neq p} \left[C^{22}(q, p)\, n_e + A^{22}(q, p) \right] \rho^2_0(q)
\end{aligned} \tag{31}$$

The additional term $\Lambda(p)$ in eq. (30) and (31) is the rate coefficient of the population flow out of the system, *i.e.*, the ionization process. We have assumed that the plasma is in the ionizing phase and the recombination processes have been ignored.

The alignment destruction rate coefficient $C^{22}(p,p)$ consists of two parts: depopulation and disalignment. (See eq. (23 a) or (23 b)) The latter contribution can be estimated from the Stark broadening of this level [13]. According to ref [14], the rate coefficient for Stark broadening is expressed in terms of the absorption oscillator strength, f, of the most frequent collisional transition as,

$$\omega_{1/2} = \left(\frac{\pi}{2}\right)^{5/3} \Gamma\left(\frac{1}{3}\right)\left(\frac{2e^2 a_0^2}{\hbar} f\left(\frac{Ry}{\Delta E}\right)\right)^{2/3} \langle v \rangle^{-2/3}$$
$$= 5.7\left(\frac{2e^2 a_0^2}{\hbar} f\left(\frac{Ry}{\Delta E}\right)\right)^{-2/3} \langle v \rangle^{-2/3} \quad (32)$$

In the spirit of the CR model, the left-hand-side of eq. (30) and (31) is put equal to zero for excited levels, and the coupled-differential equations become coupled equations for these levels.

III. EXPERIMENT

A. Preliminary experiment on the WT-3 tokamak

The system for the experiment has been described in Chapter III. In this experiment, the joule heating was cut off at 30ms from the start of the discharge, and the lower-hybrid (LH) wave of 2GHz was injected to sustain the plasma current. (*i.e.*, LHCD) The plasma current was about 45kA for the time region of 35-100ms. The electron temperature and density at the center of the plasma for this time region were about 200eV and 5.0×10^{18}m^{-3}, respectively. Figure 4 shows the temporal evolution of the plasma current (I_p), loop voltage (V_L), hard x-ray (HX) signal (E=35keV), and the chord integrated electron density in the central chord. The increase in the HX signal starting from 30ms corresponds to the increase in the number of the high energy electrons which were created by the LH wave.

We used the CT-100 visible-uv spectrometer with the OMA detector system, and observed the plasma in the central chord. The width of the entrance slit was 200μm. The storage time was 17.44ms, and we took the spectra for each 20ms period. Observed lines were the $3s^3S_1$-$3p^3P_{0,1,2}$ triplet lines (278.985, 278.699, 278.101nm, respectively) of beryllium-like oxygen ions (OV). Typical spectrum is shown in Fig. 5.

We took the toroidal direction (z) as the quantization axis, and we assumed the axial symmetry along this axis. The components linearly polarized in the direction parallel and perpendicular to the quantization axis were defined as the π and σ light, respectively. To observe the two polarization components of the spectral lines in a single discharge shot, we set the calcite plate (20mm×22mm×5.4mm) just behind the entrance slit. [15] The transmittance of this plate at 278nm was about 90%. The angle of the optical axis of the plate

was 60° with respect to the surface. (See Fig. 6) The emission of the spectral lines passing through the plate was divided into the o-ray (σ-component) and the e-ray (π-component), and these two components were focused at the different positions on the detector. Figure 7 shows the separation of the focusing positions between the o- and e-ray against the wavelength of the incident light.

Figure 8 (a) shows the typical spectra of the OV ions taken in the period of 30-50ms. The e-ray was focused on the right-hand side of the o-ray. In this experiment, the plate was tilted by 20° from normal incidence so as to obtain the best separation of the lines. We fitted these spectral lines by Gausssian profiles and derived the photoelectron counts for each line. The uncertainty was about 2% which was due to the fitting error. Our spectroscopic system was expected to have different sensitivities for the different polarization components. In principle, we should be able to calibrate the relative sensitivities by use of the photoelectron counts of the J=1-0 line which is never polarized for the case of oxygen (Possible effects from the non-zero nuclear spin, I, are well neglected. The abundance of the ^{16}O, ^{18}O (I=0) and ^{17}O (I=5/2) are 99.96% and 0.04%, respectively.). We assumed that these sensitivities are equal for the time being. From the comparison of the photoelectron counts of the two polarization components, we found that the π-component was stronger than the σ-component by 15% for the J=1-2 line and by 12% for the J=1-1 line. For the J=1-0 line, the photoelectron counts of π and σ-components were equal within 5%.

To check possible effects from blending lines, we rotated the calcite plate by 180°, and measured the same lines for a joule heating discharge. (See Fig. 8 (b)) In this case, the e-ray was focused on the other side of the o-ray.

Figure 9 shows the temporal evolutions of the experimental results. The abscissa is the time from the start of the discharge and the ordinate is the *apparent* longitudinal alignment which is defined as

$$A_L = \frac{I_\pi - I_\sigma}{I_\pi + 2I_\sigma} \quad (33)$$

where I_π and I_σ are the photoelectron counts of the π and σ polarized components, respectively. In Fig. 9, the open symbols are original data and the closed symbols are the data with the calcite plate reversed.

In view of Fig. 9, the *apparent* longitudinal alignment for the J=1-0 line for the two cases are different each other. A change of the sensitivity of our spectrometer by the rotation of the calcite plate is unlikely, *i.e.*, the difference may be due to plasma fluctuation or effects of blending lines. It is our subject in near future to reduce the these effects.

B. Example of the alignment CR model

We have constructed a preliminary alignment CR model for the OV ions. We include the four levels, $2s^1S$, $2p^3P$, $3s^3S$ and $3p^3P$, in this model. (See Fig. 10) We calculate the populations of the excited levels ($n(p)$) by use of the population collisional-radiative model for these ions. [16] By use of this calculation result for the population ratio of the $2p^3P$ metastable state to that of the ground state, we derive the alignment ($\rho\ ^2_0$) defined by eq. (4) of the $3p^3P_{0,1,2}$ levels according to eq.(31). On the right-hand side, we include the radiative transitions, the electron impact excitation and deexcitation processes and the disalignment process by elastic collisions.

The electron impact excitation or deexcitation cross section between all the Zeeman sublevels of the fine-structure levels for these four levels is calculated by Dr. Grabbe (Kansas University) and Dr. Csanak (Los Alamos National Laboratory). From these data we calculate the rate coefficient $C^{kk'}(p,q)$.

In a LHCD discharge, it is proved experimentally that the high energy tail electrons of $E \geq 100$keV are created. Figure 11 shows the electron distribution in momentum space for a typical LHCD discharge: this has been constructed from the hard x-ray measurement in LHCD experiments on the WT-3 tokamak. [17] It is understood that the accelerated electrons in the toroidal direction come to have a momentum in the poloidal direction by the collisions with the plasma particles. This high energy electrons ($E \geq 100$keV) are running predominantly in the direction about 45° with respect to the toroidal axis. Although the velocity distribution in the low energy region ($E < 100$keV) is of interest in physics of LHCD, this conventional method cannot provide information of these regions, since the detector of NaI is insensitive to electrons of E <100keV.

The alignment in the $3p^3P_{1,2}$ levels of OV ions is expected to be sensitive to electrons whose energy is less than 2~3 keV, because the higher energy electrons are ineffective for the excitation processes. (The transition energy of the $3p^3P_{0,1,2}$ levels from the ground state is about 75eV.) As examples of

anisotropic electron velocity distributions, we assume two distributions: 1) different toroidal temperature, T_{et}, from poloidal temperature, T_{ep}. 2) thermal velocity distribution with mono-energetic beam electrons.

For the former case, the electron distribution is described as

$$f(v) = \sqrt{\frac{\hbar}{2\pi m k T_{et}}}\frac{\hbar}{2\pi m k T_{ep}}\exp\left(-\frac{m v_{tor}^2}{2kT_{et}}\right)\exp\left(-\frac{m v_{pol}^2}{kT_{ep}}\right) \quad (34)$$

where v_{tor} and v_{pol} are the electron velocities in the toroidal and poloidal directions, respectively. We assume n_e=1.0×10^{18}m^{-3} and T_{ep} =100eV where the OV ions are present dominantly. For the latter case, we assume that the bulk electron temperature is 100eV and the density of the mono-energetic component is 10% of that of the bulk. Figure 12 (a) and (b) illustrates these distributions.

The results of the alignment CR model calculation for both the cases are shown in Fig.13 (a) and (b). In Fig. 13 (a), T_{et} is varied from 50eV to 400eV. In Fig. 13 (b), the energy of the mono-energetic component is varied from 50eV to 1keV in Fig.13 (b). These results suggested that, for the former case, the method of PPS is rather insensitive to the velocity anisotropy, and for the latter case, the beam energy region where this method is sensitive is $E \leq 300$eV.

Acknowledgements

This work was done by the support of many people. Special thanks to Dr, Csanak (*LANL*, USA), Dr. Grabbe (*Kansas University* USA), Prof. Terumichi, Prof. Maekawa, Dr. Maehara, Mr. Goto, Mr. Sahara (*Kyoto University*) and Mr. T. Kallestenius (*KTH*, Sweden).

References

[1] A.C.A.P. Van Lammeren, C.J. Barth, Q.C. Van Est, F.C. Schuller, *Nucl. Fusion* **32**, 655 (1992)

[2] J.C. Kieffer, J.P. Matte, H. Pepin, M. Caker, Y. Beaudoin, T.W. Johnston, C.Y. Chien, S. Coe, G. Mourou and J. Dubau, *Phys. Rev. Lett.* **68**, 480 (1992)

[3] M.K. Inal and J. Dubau, *J. Phys. B* **20**, 4221 (1987)

[4] *Plasma Polarization workshop*, Los Alamos, Feb. in 1994

[5] A. Messiah, "Mécanque Quantique", *Dunod, Paris* (1959)

[6] A. Omont, *Prog. Quantum. Electron.* 5, 69 (1977)

[7] K. Blum, "Density Matrix Theory and Application", *Plenum Press*, (1981)
[8] W. Fritsch, *Phys. Lett. A* 160, 64 (1991)
[9] G. Csanak, (private communication.)
[10] S.A. Kazantev, A.G. Petrashen, N.T. Polezhaeva, V.N. Rebane and T.K. Rebane, *Opt. Spectrosc.* (USSR) **68**, 544 (1990)
[11] S.A. Kazantev, A.G. Petrashen, N.T. Polezhaeva, V.N. Rebane, *Opt. Spectrosc.* (USSR) **68**, 740 (1990)
[12] A.G. Petrashen, V.N. Rebane and T.K. Rebane, *Opt. Spectrosc.* (USSR) **58**, 481 (1985)
[13] A. Hirabayashi, Y. Nambu, M. Hasuo, and T. Fujimoto *Phys, Rev. A* **37**, 83 (1988)
[14] I.I. Sobelman, L.A. Vainstein and E.A. Yukov, "Excitation of Atoms and Broadening of Spectra" *Springer-Verlag* (1981)
[15] T. Kallstenius, *thesis*, Kungl Tejniska Høgskolan, Stockholm, Sweden (1995)
[16] T. Kato, J. Lang and K.E. Berrington **NIFS-DATA-2** (1990)
[17] T. Maehara *et al.*, *Physics Letter*, (to be published)

Figure Captions

Fig. 1. Proton velocity distribution in the case of a shifted Maxwellian distribution. The proton temperature is 10keV. We assume helium beam is injected into the isotropic plasma in the -z-direction with the velocity of 4×10^6m/s.

Fig. 2. The K-multipole components, $f_K(v)$, for K=0, 2 and 4 of the shifted Maxwellian distribution of Fig. 1. $f_0(v)$ for the normal Maxwellian distribution is also shown for reference.

Fig. 3. An example of $\sigma_0(00)$ and $\sigma_0(20)$ for the transitions from the ground state $(1s^1S)$ to the $2p^1P$ level of neutral helium atom.

Fig. 4. The plasma current (I_p), loop voltage (V_L), soft x-ray (E=1.4keV) signal, hard x-ray signal (E=35keV) for a typical LHCD discharge.

Fig. 5. Typical spectra of the $3s^3S_1$-$3p^3P_{0,1,2}$ OV ions for the joule heating mode of the LHCD discharge. (without the calcite plate)

Fig. 6. Schematic diagram of the optics of the calcite plate (blade). a; the divergence of the incident light. δy; the separation of the focusing positions between the o-ray and e-ray. (from ref. [15] ; Kallstenius.)

Fig. 7. The separation of the focusing positions between the o- and e-rays on the detector. Experimental data points by use of the mercury and neon lines are attached.
(from ref. [15] ; Kallstenius.)

Fig. 8. (a); Typical spectra of OV ions for the LHCD discharge with calcite plate. The spectral lines correspond to J=1-2, J=1-1 and J=1-0 from the right-hand-side. (b); The spectral lines of OV ions for the Joule heating discharge. The calcite plate has been rotated by 180°.

Fig. 9. The temporal evolution of the *apparent* longitudinal alignment of the J=1-2, J=1-1 and J=1-0 lines for the case of Fig. 8 (a) and (b).

Fig. 10. The partial energy level diagram of OV ions. The levels which we include in our preliminary alignment CR model are shown.

Fig. 11. The result for the electron distribution in momentum space for the LHCD discharge. (This is derived from the hard x-ray measurement.) $P_{/\!/}$ and $P_{\perp}$ are the momentum of the electrons in the toroidal and poroidal direction, respectively. In this scale, 1 corresponds to the energy of 200keV. Open area in the central region means that this method is not sensitive for the energy region below 100keV. The solid line shows the cut-off region of the LH wave. (from ref. [17]; Maehara *et al.*)

Fig. 12. Schematic representation of the electron velocity distributions. (a); The case that there are two Maxwellian components, *i.e.*, toroidal temperature is higher than the poloidal temperature. α is the ratio of the two temperatures. (b); The case that there is a mono-energetic component. We assume that the density of the component is 10% of the bulk electrons.

Fig. 13. The calculation result by the alignment collisional-radiative model for OV ions. The ordinate is the longitudinal alignment of the transition lines from the respective levels. (a); Abscissa is the poloidal temperature, $T_{tor.}$, and a = T_{et}/T_{ep}. (b) We assumed the poloidal electron temperature is 50eV and 100eV. Abscissa is the energy of the mono-energetic beam electrons.

Fig. 1

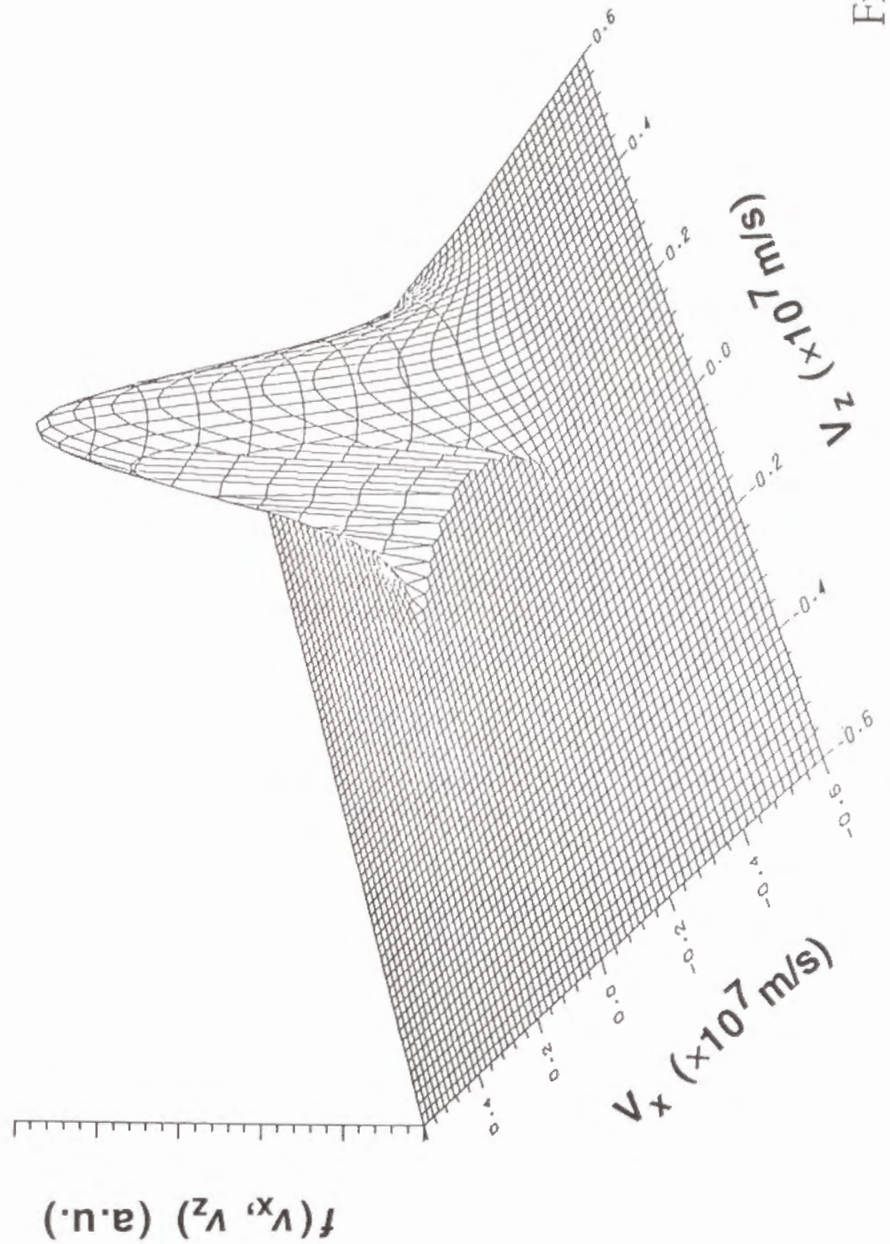

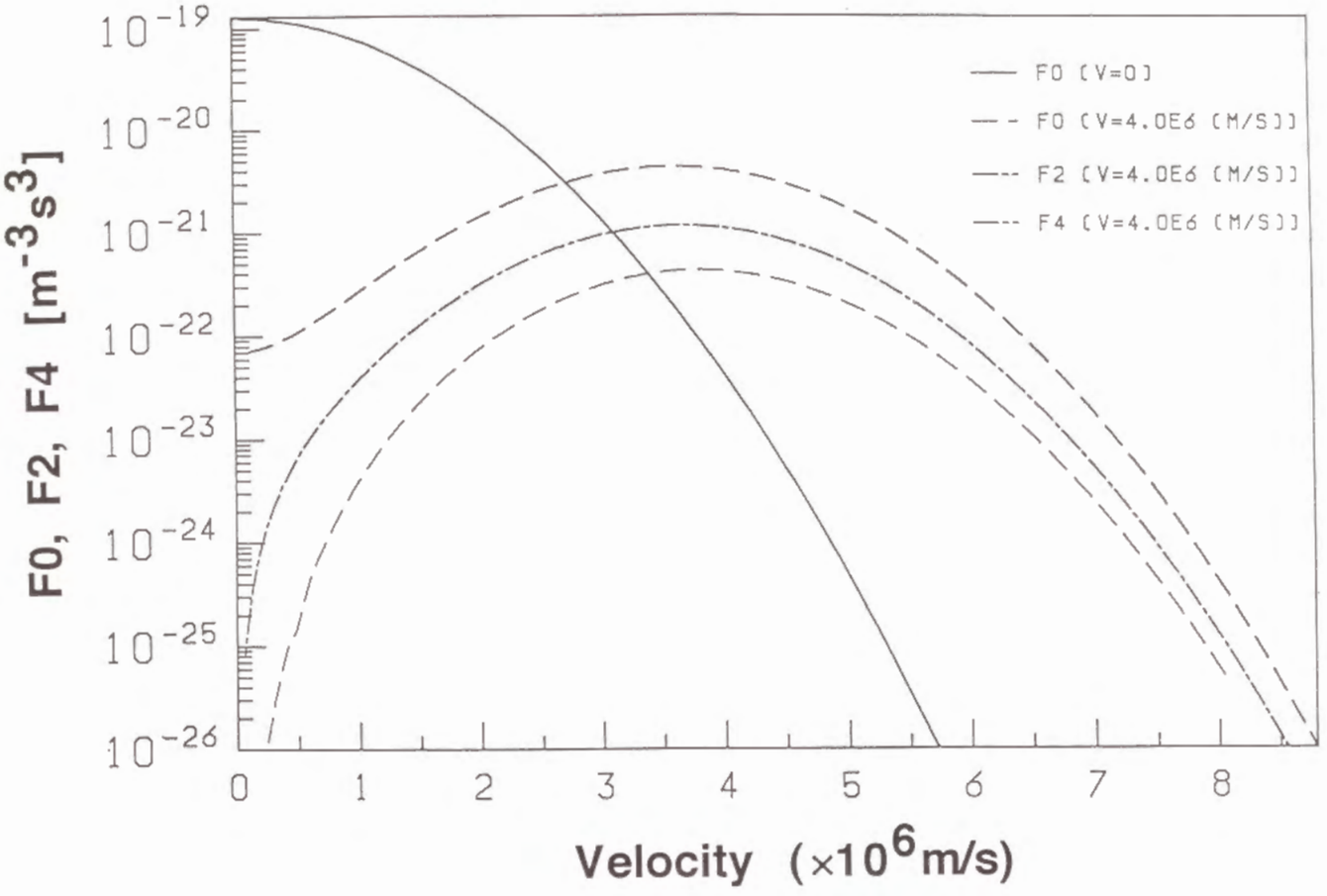

Fig. 2

He ($1s^1S$) + p → He ($2p^1P$) + p

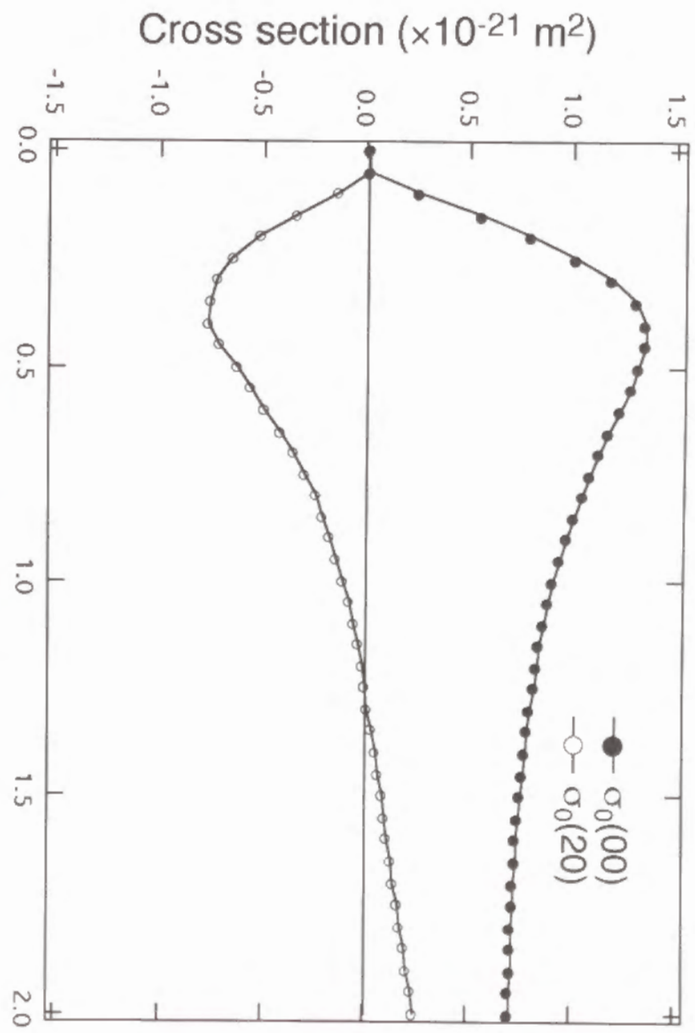

Fig. 3

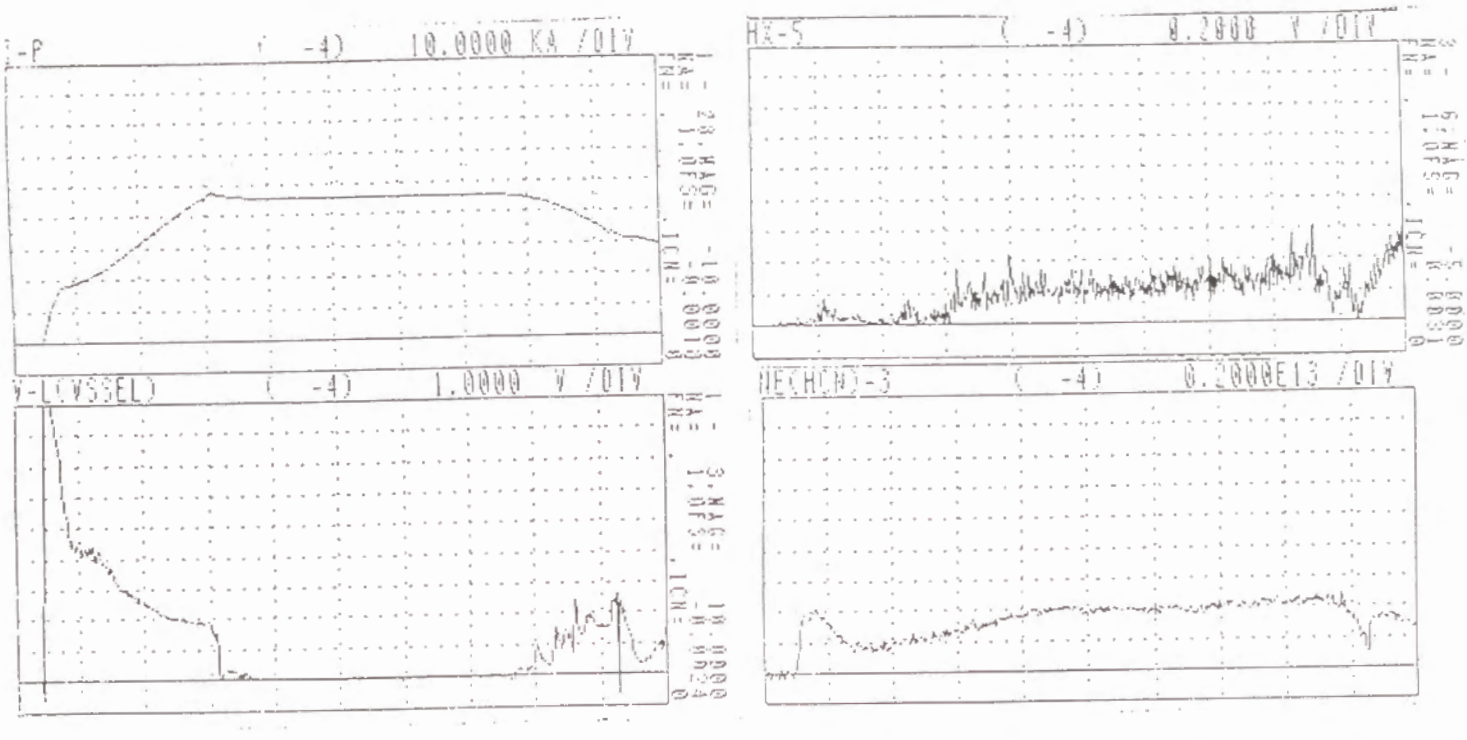
10.0000 KA /DIV
1.0000 V /DIV
0.2000 V /DIV
0.2000E13 /DIV

Fig. 4

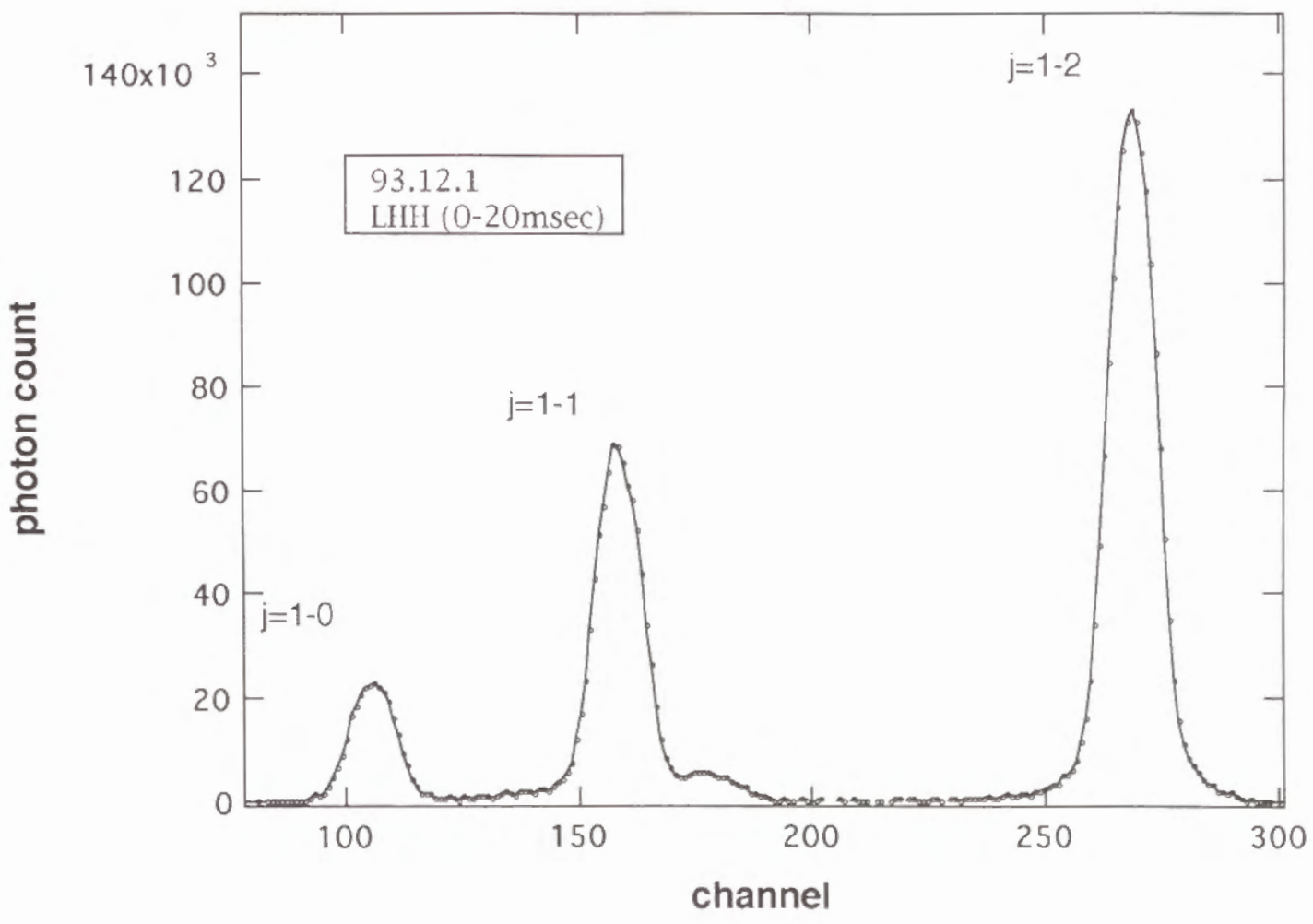
140x10 3
120
100
80
60
40
20
0
photon count
93.12.1
LHH (0-20msec)
j=1-0
j=1-1
j=1-2
100
150
200
250
300
channel

Fig. 5

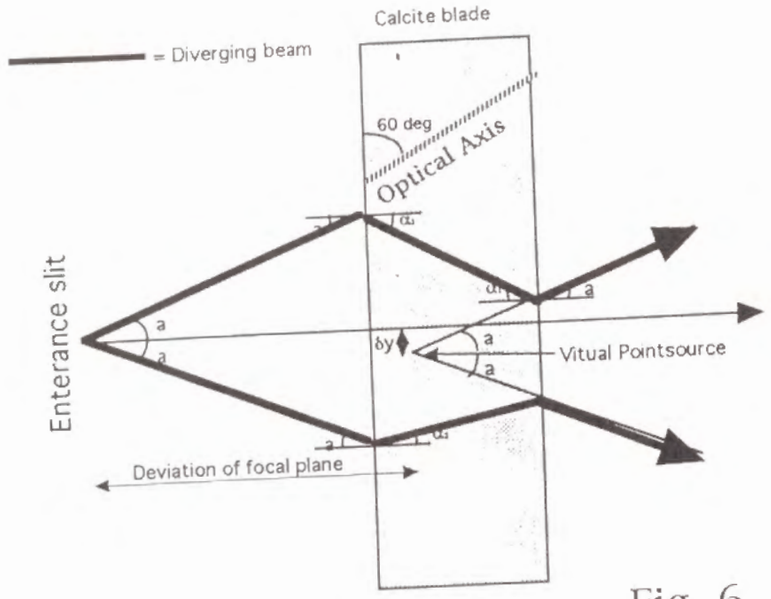

Fig. 6

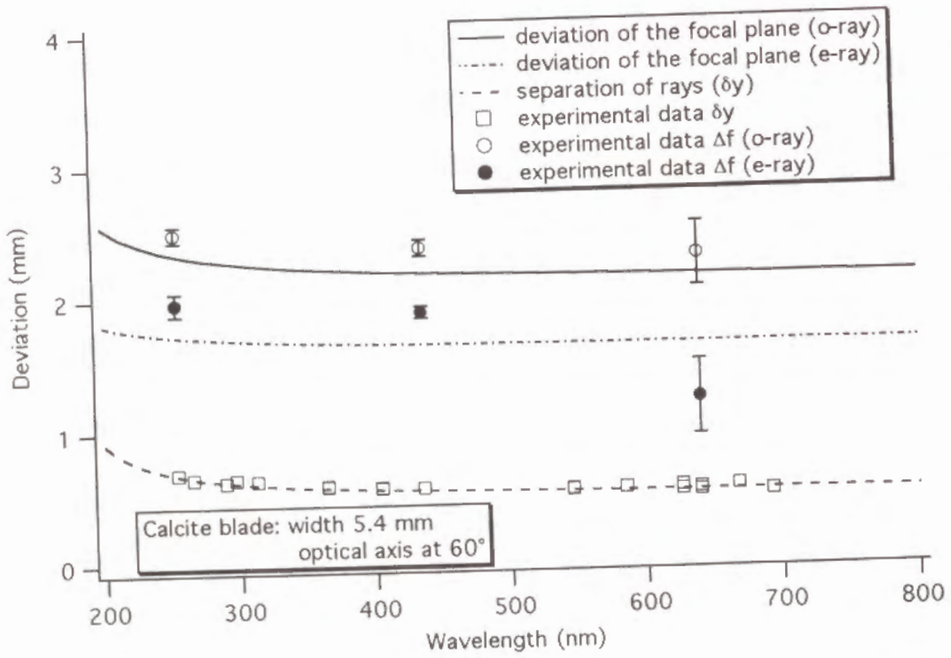

Fig. 7

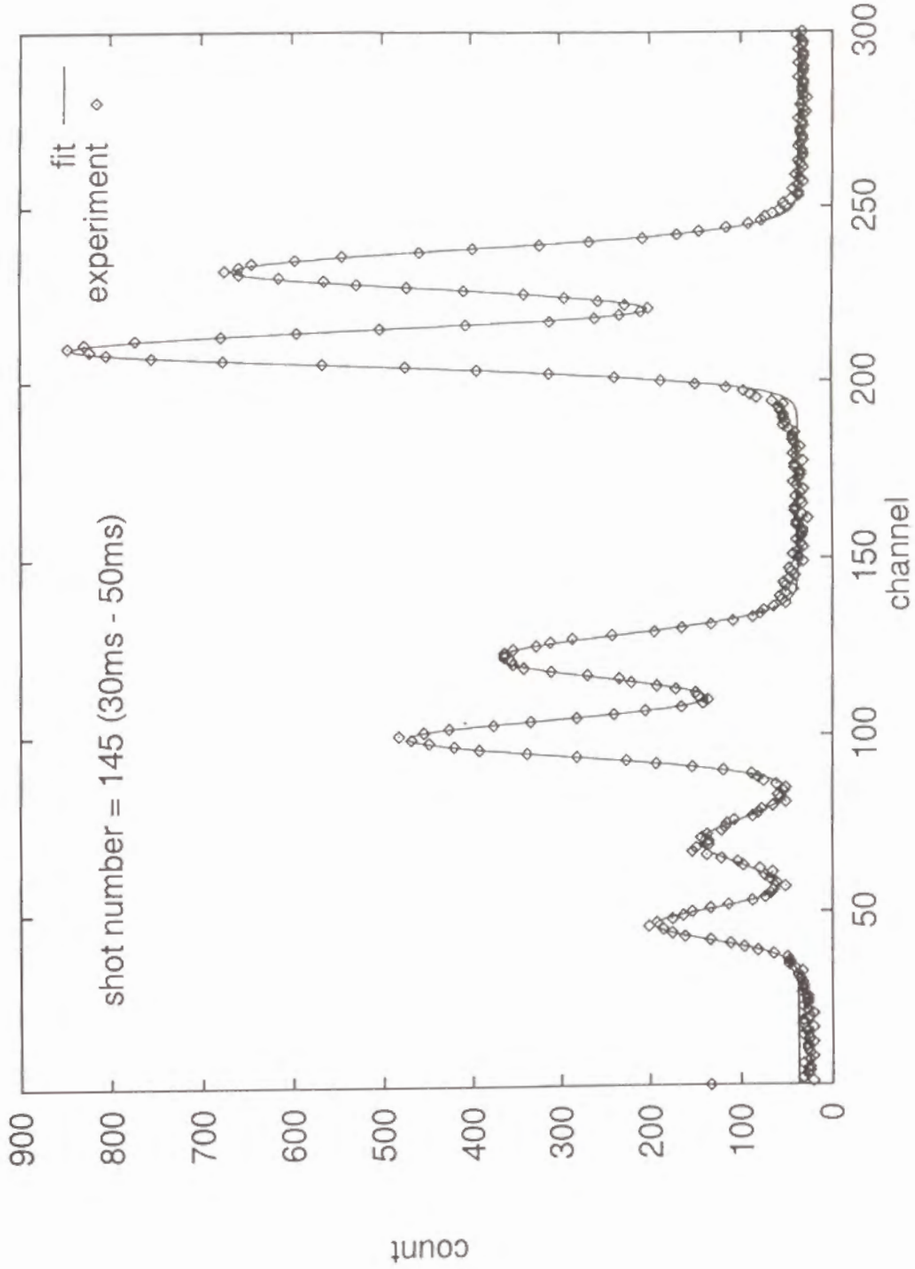

Fig. 8 (a)

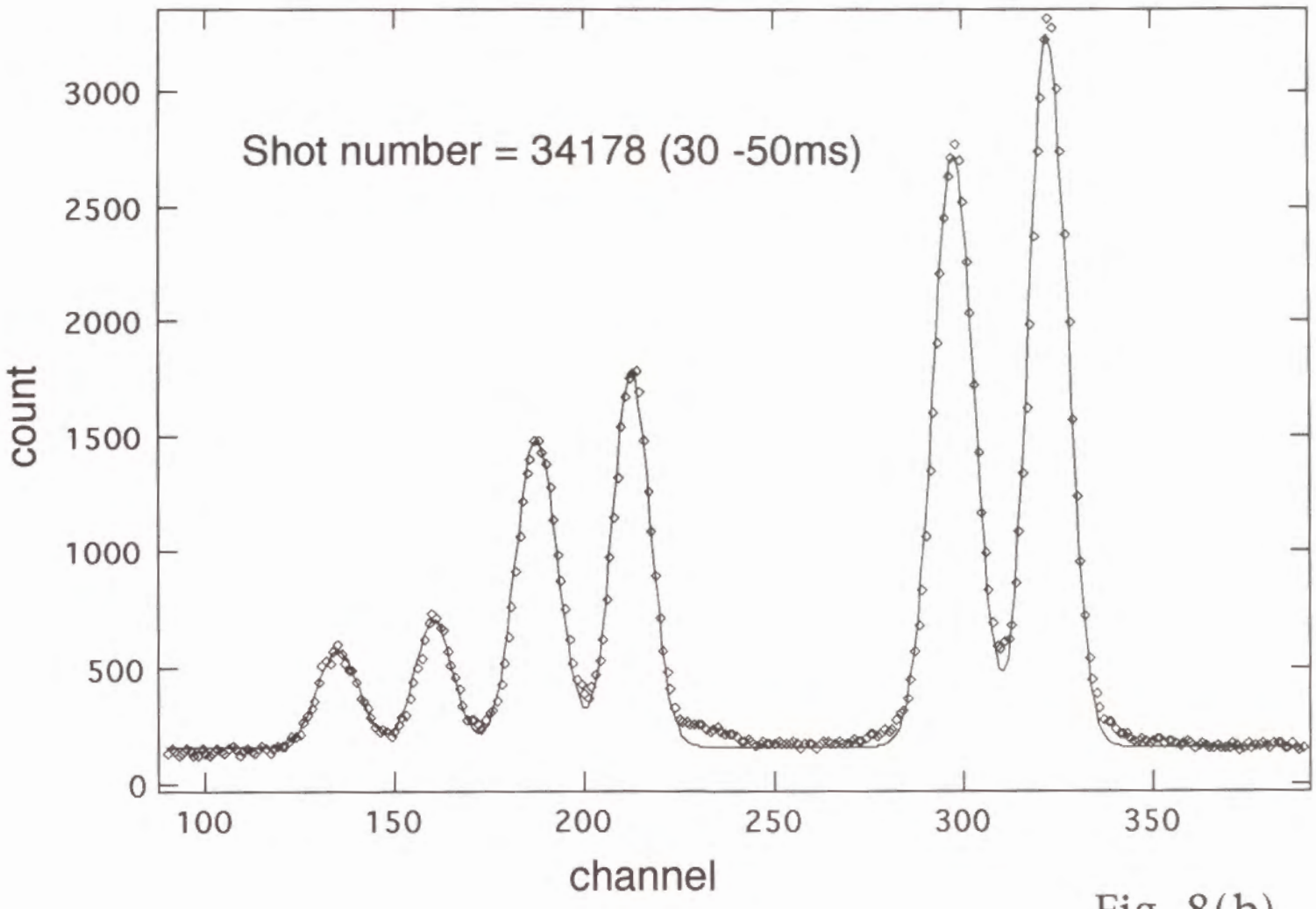
Shot number = 34178 (30 -50ms)
count
channel
0
500
1000
1500
2000
2500
3000
100
150
200
250
300
350

Fig. 8(b)

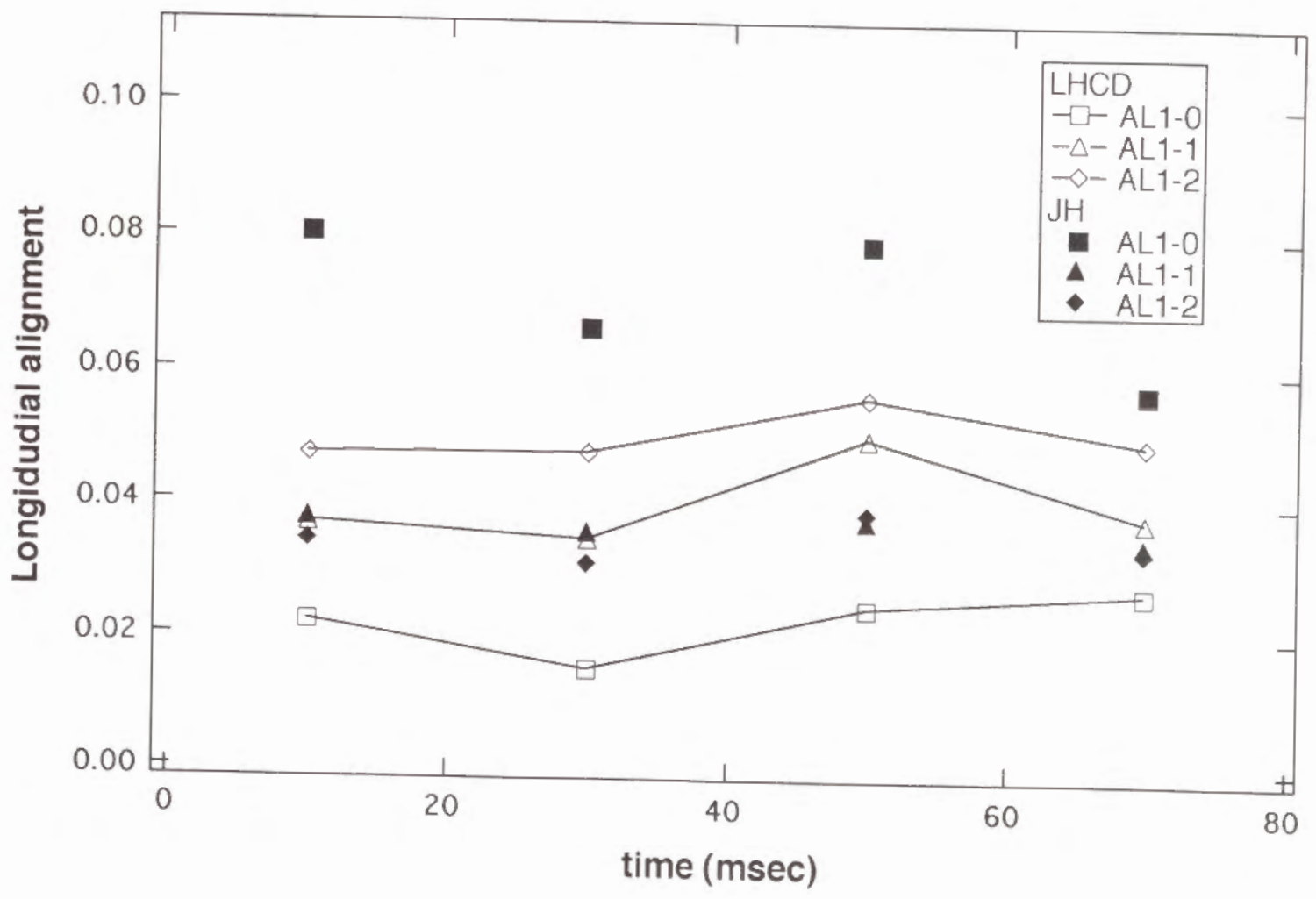
LHCD
AL1-0
AL1-1
AL1-2
JH
AL1-0
AL1-1
AL1-2
Longidudial alignment
time (msec)
0.00
0.02
0.04
0.06
0.08
0.10
0
20
40
60
80

Fig. 9

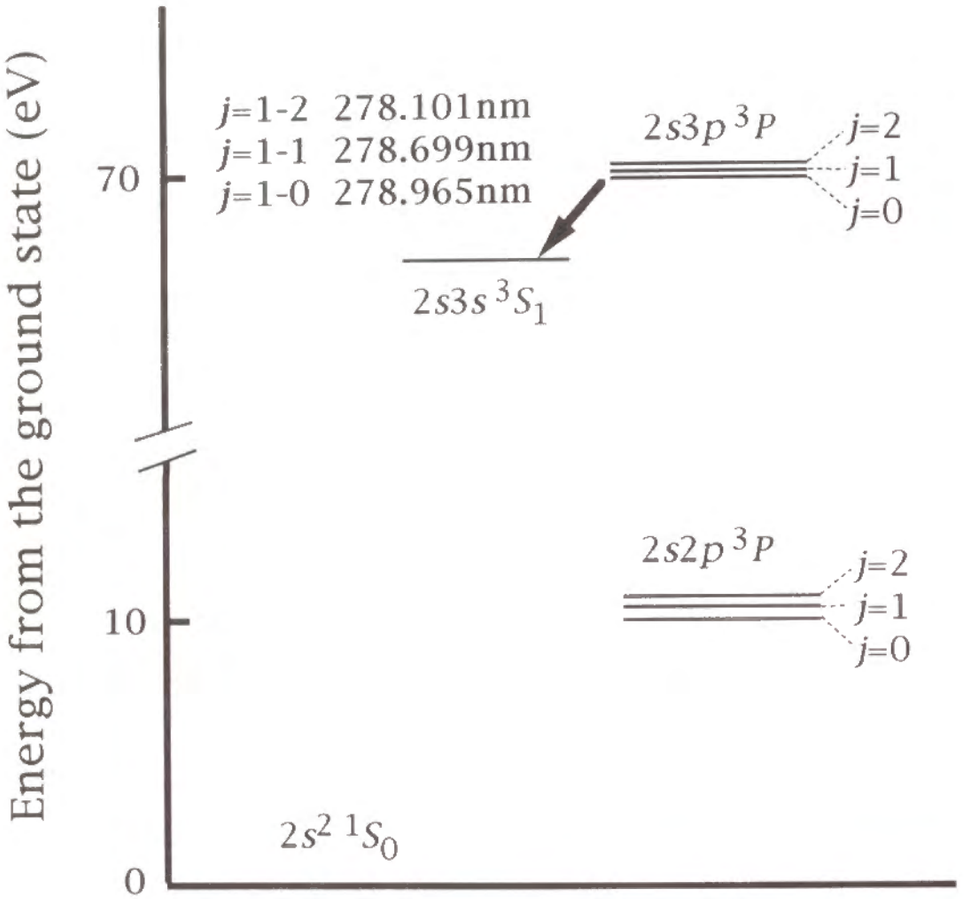
Energy level diagram of OV ions
Energy from the ground state (eV)
70
10
0
j=1-2 278.101nm
j=1-1 278.699nm
j=1-0 278.965nm
2s3p 3P
j=2
j=1
j=0
2s3s 3S1
2s2p 3P
j=2
j=1
j=0
2s2 1S0

Fig. 10

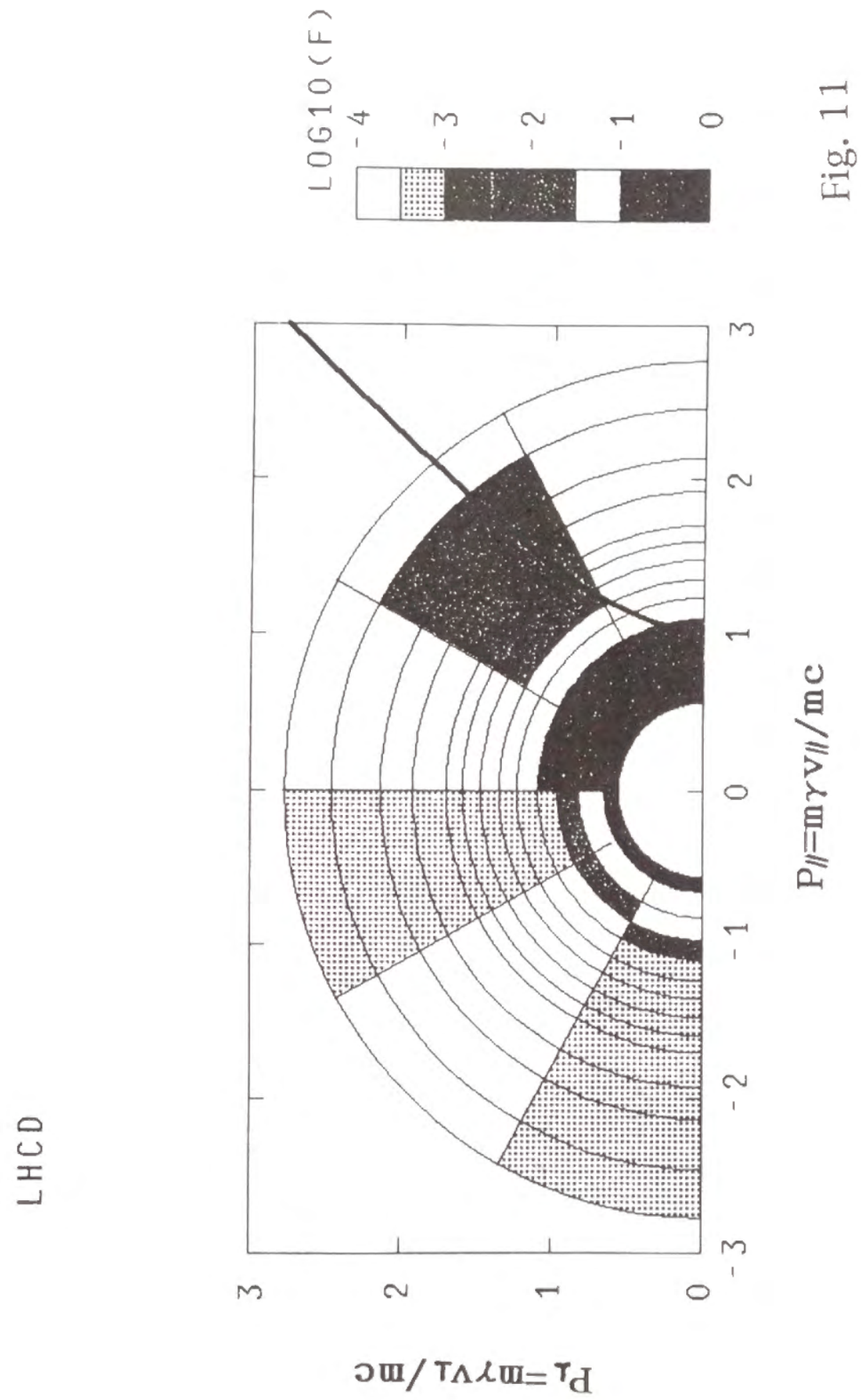
LOG10(F)
-4
-3
-2
-1
0
LHCD
P⊥=mγv⊥/mc
P∥=mγv∥/mc
3
2
1
0
-1
-2
-3

Fig. 11

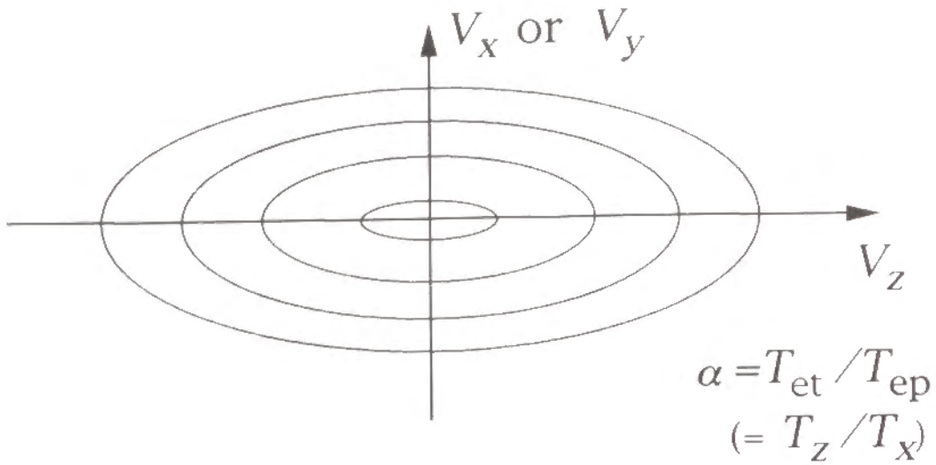

Case 1) Anisotropic Maxwell velocity distribution (Axial symmetric case)

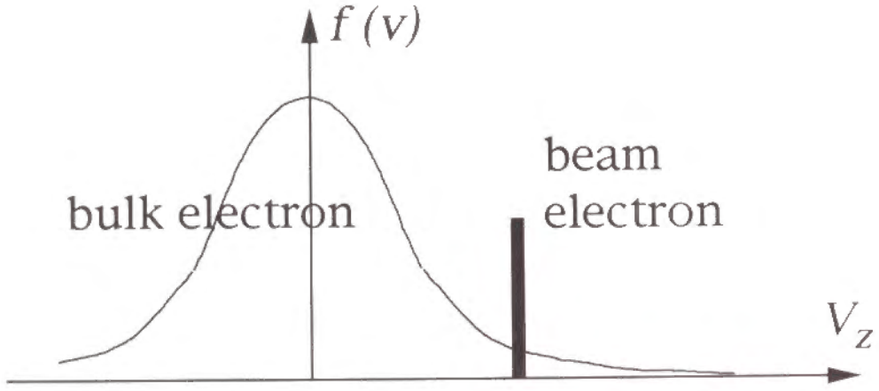

Case 2) Isotropic Maxwell velocity distribution and beam component in the z-direction

Fig. 12

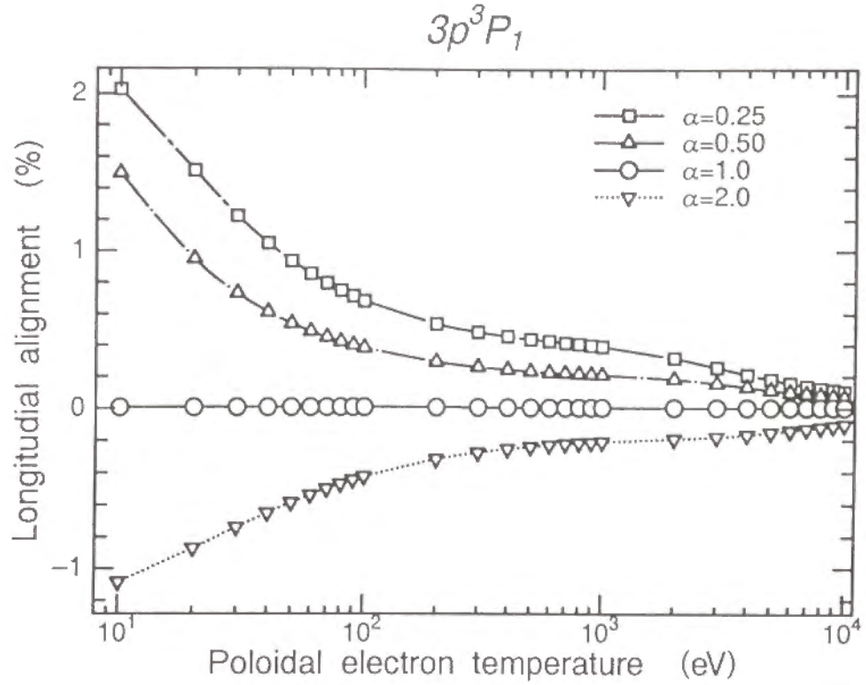

Fig. 13 (a-1)

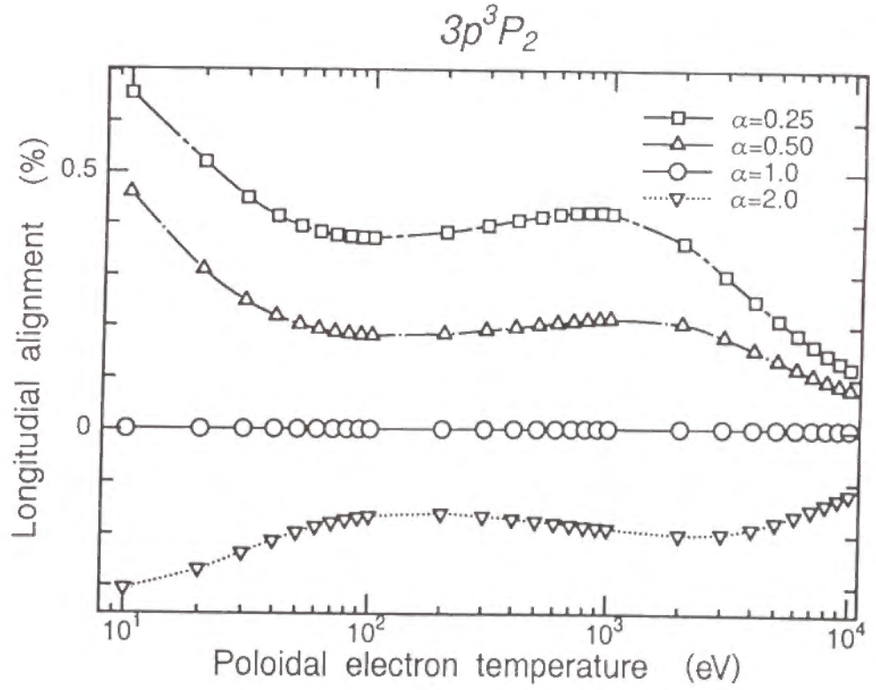

Fig. 13 (a-2)

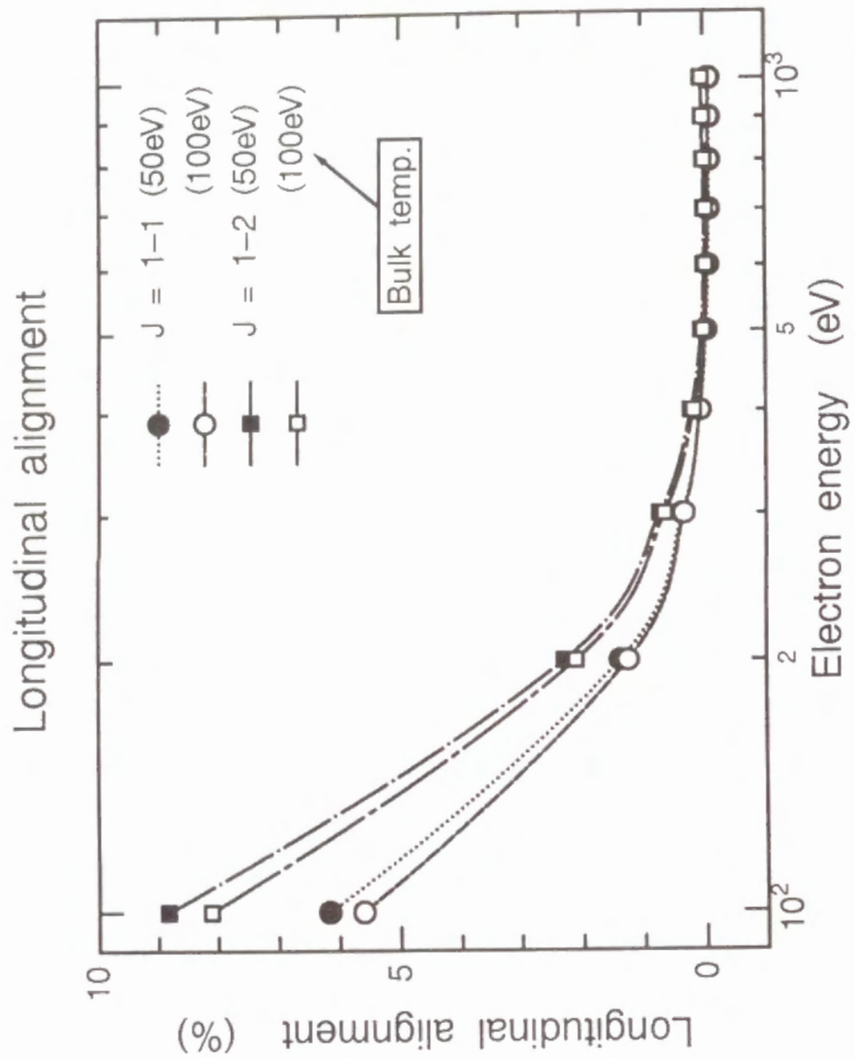

Fig. 13 (b)

CHAPTER VI.

Observation of Polarization of the Soft X-ray Laser Line in Neon-Like Germanium Ions

Abstract A 3cm-long germanium slab target was irradiated by 1.053μm glass laser light with irradiance of 2.9×10^{13}W/cm^2. The 19.6nm (J=1-0 transition) laser line from neon-like germanium ions was found to be linearly polarized by 53% in the direction perpendicular to that of the irradiating laser light. Since the spontaneous emission is unpolarized, the polarization is ascribed to a difference in the gains (by 13%) of the laser radiation with the different polarization directions. A Monte Carlo simulation, which treats the radiation trapping of the resonance line (J=0-1) in the expanding plasma with a velocity gradient of ions, shows that population imbalance develops among the magnetic sublevels of the lower level (J=1) of the laser transition, thus explaining the difference in the gains.

I. INTRODUCTION

Since the advent of the x-ray laser [1], continuing efforts have been directed to the development of high-performance x-ray lasers. We have now reached to a point where it is even feasible to conduct a plasma diagnostic experiment by using these lasers [2]. On the basis of advanced modellings, we are now able to analyze quantitatively the performance of these x-ray lasers. One example is the neon-like germanium laser of the collisional excitation scheme. [3] However, even for this well-studied laser a small discrepancy between theory and experiment still persists, that is, the gain of the 19.6nm line due to the $3s$-$3p$, J=1-0 transition (transition from $(2p_{1/2},3p_{1/2})_0$ to $(2p_{1/2},3s_{1/2})_1$) is predicted to be ~12cm^{-1}, much higher than experiment. (Figure 1 shows the energy level diagram of the neon-like germanium ions and the lasing lines.)

One of the phenomena that have called little attention so far concerning the laser produced plasma and the x-ray laser is the spatial anisotropy of the plasma and the resulting polarization of radiation. Kieffer *et al.* [4] produced an aluminum plasma with 1ps-pulsed laser irradiation, and found that the helium-like resonance line emission was linearly polarized. They interpreted this polarization as due to the spatial anisotropy of the velocity distribution of electrons in the plasma. With regard to the x-ray laser, Rus *et al.* [5] produced a germanium plasma with a 650ps pulse and a 1.6×10^{13}W/cm^2 irradiation intensity, and found virtually no polarization for the 23.2 and 23.6nm laser lines (J=1-2 transitions); the upper bound of the degree of polarization was (4±2)%. They employed a set of a multilayer polarizer and a normal incidence concave morror to relay the output into an amplifier. They found that the initial polarization degree of 97% of the seeded beam was conserved after the amplification. A similar experiment was conducted by Murai *et al.* [6]

In the following we report the first observation of the existence of polarization of the 19.6nm laser radiation of the neon-like germanium ions generated without any polarization seeding.

II. EXPERIMENT

Figure 2 shows the experimental set-up. A germanium slab target of a 1μm thick, 200μm wide and 3cm long stripe coated on a glass plate was bent cylindrically with a radius of curvature of 2.5m [7]. One beam of the GEKKO

XII Nd: glass laser of 1.053μm polarized counterclockwise 14.5° with respect to the y-direction irradiated the target from the z-direction. A cylindrical lens and an aspherical lens produced a line focus on the target along the y-axis of 6cm length and 100μm average width [8]. The laser light was composed of two Gaussian pulses of 0.1ns width (FWHM) separated by 0.4ns. The energy of the second pulse was stronger than that of the first by 10-20 %. The total energy on the 3cm length target was 170 J and the average irradiance of the second pulse was 2.9×10^{13}W/cm^2. X-ray amplification was observed at the second irradiation pulse which heated the plasma produced by the first irradiation pulse. This arrangement was effective in enhancing the 19.6 nm output [9]. The x-ray laser radiation was observed from the $-y$-direction by a high resolution flat-field recording grazing incidence spectrometer (HIREFS; Hettrick Scientific) [10]. The distance between the entrance slit and the grating G was 134cm and that from the grating to the focal plane was 409cm. The edge of the target was located at the position of 8.5cm in front of the entrance slit position, and in this experiment the slit was removed to take much laser light into the spectrometer. The laser beam was first reflected by a concave mirror M1, dispersed along the vertical (x) direction by an uneven-spacing grating of 375 grooves/mm and then reflected by a cylindrical mirror M2 to be weakly focused along the z-direction. The length of the spectral lines along the z-direction was approximately 1.5cm on the recording plane. The linear reciprocal dispersion was 0.58nm/mm. The central 0.6cm portion of the 19.6nm (J=1-0) laser line was then passed through a reflective linear polarizer placed at about 20cm in front of the recording plane. It consisted of two Mo/Si multilayer mirrors of 1.0cm×1.0cm square coated with 16 Mo layers and 15 Si layers, and in this experiment, the effective size of these multilayer mirrors was 0.6cm×0.6cm. These mirrors were calibrated with the synchrotron radiation at the UV-SOR facility of the Institute for Molecular Science. The angle of incidence of the light beam to these mirrors was 38° with respect to their surface normal. The reflectivity R_s for the light polarized in the direction perpendicular to the plane of incidence, was measured to be 25±5% for each of them, and the polarization efficiency, R_s/R_p is estimated to be >100 [5]. Here we have defined the direction of the oscillating electric field to be the direction of linear polarization. These mirrors, positioned parallel facing each other, were fixed in a housing which could be rotated around the entrance beam axis for measuring the x-ray laser intensities with different polarization

directions. The change of the angle of incidence due to rotation of the polarizer was less than 10mrad (0.57°), which might cause up to 9.7% relative uncertainty in the reflectivity of the polarizer. The exit light beam was displaced by 1.0cm in the direction perpendicular to the transmission axis of the polarizer. An Ilford Q-plate was used for recording the light intensity. This plate was located at the original focal plane. The increase in the optical path of 1.0cm by the polarizer together with the 8.5cm displacement of the light source from the entrance slit position made the image slightly off-focus. However, the quality of the image, as will be shown later, was satisfactory. The optical density against the exposure of the Q-plate was calibrated at 18.2nm by use of the spontaneous emission line of CVI, n=2-3 transition from a carbon plasma produced by a repetitive Nd: YAG laser. The result of the caliblation is shown in Fig.3 (a). The uncertainty in the measured intensity was estimated to be less than 17%. The relative transmittance of the spectrometer to the light polarized in the z-direction against that in the x-direction was determined to be $S_{/\!/}/S_{\perp}$=1.3±0.1 (See Fig.3 (b)): it was measured by use of the same polarizer with the CVI 18.2nm emission line which had been measured to be unpolarized [11]. Note that R_s/R_p of the polarizer at 18.2nm is about 80.

For the double-pulse, 170J irradiation, we first recorded with the polarizer removed the 19.6nm laser line as shown in Fig.4 (a). We then placed the polarizer, and recorded the intensity shot by shot with the transmission axis set in the direction parallel (//), perpendicular ($\perp$) and 45° to the z-axis. Figure 4 (b) shows the plates corresponding to the polarized components together with their densitometer traces scanned over the spectral line. A portion of the 19.6nm laser line which went by the side of the first polarizer mirror and transmitted through a 1.47μm thick aluminum filter was used to monitor the x-ray laser intensity (See Fig.2). This monitored intensity was used to normalize the measured intensity of the polarized component to give the relative intensity, $I_{/\!/}$, $I_{\perp}$ and $I_{45°}$ as given in Table 1 where the correction for $S_{/\!/}/S_{\perp}$ has been made. It is noted that the reproducibility of the laser energy is 4% over the three shots and that the monitored x-ray laser intensities are consistent with this small fluctuation. We conclude that our laser light is partially polarized in the perpendicular direction with polarization degree $P=(I_{/\!/}-I_{\perp})/(I_{/\!/}+I_{\perp})=-0.53\pm0.11$. The relative intensity with the transmission

axis in 45° is predicted to be 2.1±0.4, in agreement with the experimental value.

III. DISCUSSION

The upper level $3p$ of the 19.6nm line has the total angular momentum J=0, and the lower level $3s$ has J=1. (Germanium has virtually no nuclear spin: the abundance of the only isotope of odd mass number 73 with nuclear spin 9/2 is 7.8%.) It is noted that the spontaneous emission of the line of this angular momentum pair (J=1-0) is never polarized (See Fig.5). Thus, we can assume that the difference in the intensities of the polarized components of the laser output is due solely to a difference in the gains of these components. Let $g_{/\!/}$ and $g_{\perp}$ denote the gains for the parallel and perpendicular components, respectively. The ratio of the intensities, 3.3±0.7, indicates the difference in the gains to be $g_{/\!/}-g_{\perp} = -0.39 \pm 0.07 \mathrm{cm}^{-1}$.

Let M be the projection of J (=1 for $3s$) onto the quantization axis, z-axis, and $n(3s)_M$ be the population of the magnetic sublevel M. The upper level $3p$ has only one magnetic sublevel (M=0). We note that the relationships $g_{/\!/} \propto |n(3p)-n(3s)_0|$ and $g_{\perp} \propto |n(3p)-n(3s)_{\pm 1}|$ hold. (Fig.5) Our experimental result indicates that $n(3s)_0$ is larger than $n(3s)_{\pm 1}$ or the $3s$ level ions have negative alignment, $\sqrt{6}\,|n(3s)_{\pm 1}-n(3s)_0|/3$.

Our previous experiments suggest that, under the present experimental conditions, the gain of the 19.6 nm line is about $2\sim3\mathrm{cm}^{-1}$. If we assume $g_{\perp}=3\mathrm{cm}^{-1}$, we have $g_{/\!/}=2.61\pm0.07\mathrm{cm}^{-1}$. We now tentatively assume that the gain profile is given by a Voigt profile determined by the thermal Gaussian width with the ion temperature of 400eV (FWHM is $1.8\times10^{13}\mathrm{s}^{-1}$ in angular frequency units.) and the natural broadening, $2\times10^{12}\mathrm{s}^{-1}$. (FWHM are $2\times10^{11}\mathrm{s}^{-1}$ for the $3p$ level and $2\times10^{12}\mathrm{s}^{-1}$ for the $3s$ level.) It follows that $|n(3p)-n(3s)_{\pm 1}| = 2.81 \times 10^{15}\ \mathrm{cm}^{-3}$ and $|n(3p)-n(3s)_0| = (2.44\pm0.10) \times 10^{15}\ \mathrm{cm}^{-3}$. We assume the electron density of $4\times10^{20}\mathrm{cm}^{-3}$, the electron temperature 800eV and the ion density $n(2p^6)=2\times10^{19}\mathrm{cm}^{-3}$. We rely on the excitation cross section to the lower level $3s$ given in ref. [12]. We then obtain the lower level population $n(3s)\equiv |n(3s)_0+2n(3s)_{\pm 1}| = 1.33\times10^{16}\mathrm{cm}^{-3}$, where we have assumed corona equilibrium with the spontaneous transition probability decreased by a factor of 4.2 owing to the radiation trapping effect as described later. It readily follows that $n(3p)=(7.12\pm0.03)\times10^{15}\mathrm{cm}^{-3}$, $n(3s)_0=(4.68^{+0.13}_{-0.07})\times10^{15}\mathrm{cm}^{-3}$ and

$n(3s)_{\pm 1}= (4.31 \pm0.03)\times10^{15}\mathrm{cm}^{-3}$. These uncertainties do not include uncertainties in the determination of $n(3s)$.

Since our plasma was produced by relatively long pulse irradiation, spatial anisotropy in the velocity distribution of electrons is unlikely to develop, and the above alignment is not ascribed to anisotropic collisions. Instead, radiation trapping of the 0.98nm resonance line could create alignment in the $3s$ level ions.

Alignment created by radiation trapping in a spatially anisotropic geometry was first treated analytically in [13]. Recently, the similar phenomena has been treated by the Monte Carlo method [14]. We modify the Monte Carlo simulation code and apply it to the present case. It is well established by the hydrodynamic simulation [15] that our plasma has a streaming motion dominantly in the z-direction, resulting in a velocity gradient of the ions. (See Fig.6) In the present simulation we assume the following situation simplified from the hydrodynamic simulation result: The dimension of the plasma is 300μm in the z-direction and 60μm in the x-direction and the velocity gradient is only along the z-direction with 1.0×10^{7}cm/s per 100μm. We assume that the local absorption line profile is given by the thermal Gaussian shape (FWHM $3.6\times10^{14}\mathrm{s}^{-1}$; the natural width is $2\times10^{12}\mathrm{s}^{-1}$) and the frequency redistribution does not take place.

In our simulation an excited ion is treated as a classical oscillating electric dipole. This correspondence is exact for the $3s$-$2p^6$ (J=0-1) transition. An excited ion or a dipole is created at a random location (*i.e.*, chosen randomly from an appropriate probability function) with a random oscillating direction. After a certain random time corresponding to the natural lifetime of 0.50ps, it makes a spontaneous transition emitting a dipole radiation into a random direction. This photon traverses a random distance, and is absorbed there producing another dipole oscillating in the direction that is determined by the oscillating direction of the original dipole and the photon propagating direction. It is noted that the directions of the oscillating dipoles have been "quantized" into one of the x-, y- and z-directions. This procedure is repeated until the last photon escapes from the plasma. We repeat the similar series of procedures for about 6×10^{4} times, and count at each time after the start the number of the dipoles oscillating in a certain direction. Figure 7 shows the result of the simulation. We find that, after several lifetimes, the decay time constant of the total number of dipoles or $n(3s)$ reaches its final constant

value of 2.1ps, 4.2 times larger than the natural lifetime. We also find that the ratio $[n(3s)_0/n(3s)_{\pm1}]$ becomes constant; *i.e.*, $[n(3s)_0-n(3s)_{\pm1}]/[n(3s)/3]$ is 5% at T_e=400eV as shown in Fig. 8.

As seen above, our *experimental* ratio $[n(3s)_0-n(3s)_{\pm1}]/[n(3s)/3]$ was (8.4±2.2)%. In view of the many assumptions in the analysis of the experiment and the much simplification in the simulation, this disagreement may not be regarded serious.

As Fig.8 suggests, with an increase in the ion temperature the relative alignment decreases. This dependence is understood as follows: The plasma as viewed by a photon emitted at a certain location is a thin slab with boundaries parallel to the *x*-*y* plane. This is because: a photon can be absorbed only by ions that have the *z*-component of its velocity matching the frequency of this photon. Owing to the velocity gradient in the *z*-direction, these ions are restricted to a certain spatial region, the shape of which is a slab, and the thickness is determined by the Doppler width relative to the velocity gradient. In the present example the effective thickness of this slab is about 30μm in the *z*-direction, which is compared with the height in the *x*-direction of 60μm. An increase in the ion temperature leads to an increase in the effective thickness and, under the present conditions, to a decrease in the spatial anisotropy. This leads to the decrease in the relative magnitude of the alignment.

As shown in Table 1, we conducted a similar experiment with the higher irradiation laser energy of 190J for 3cm length target and found polarization degree to be P=-0.19±0.04. We do not present the discussion similar to the above except that the *experimental* ratio $[n(3s)_0-n(3s)_{\pm1}]/[n(3s)/3]$ is 3.2±1.0%. The agreement of this ratio with the simulation value of 4.3% would be fortuitous.

In order to obtain quantitative interpretation of the present experiment, various improvements are necessary: the Stark broadening ($1\times10^{11}s^{-1}$ for the resonance transition and $2\times10^{11}s^{-1}$ for the laser transition) and the isotope shifts should be included in the line profiles; a hydrodynamic simulation coupled with a collisional-radiative model with reliable rate coefficients should be employed to estimate various densities including the excited ion populations; and a more realistic plasma model should be adopted for the simulation, *e.g.*, we should take into account the disalignment (destruction of alignment) collisions. (This rate is approximately given by the rate for Stark broadening [16].) It should be noted that the electron-ion elastic collisions of the order of $10^{14}s^{-1}$ do not contribute to Stark broadening and thus to disalignment [17].

We estimate the polarization degree of the 23.2 and 23.6nm lines (J=1-2 transitions) under our experimental conditions. The Kastler diagram for this transition is shown in Fig.9. The upper level ions are assumed to be unaligned. The alignment of the lower level $(2p_{3/2}, 3s_{1/2})_1$ of 23.2nm is assumed to be equal to that of $(2p_{1/2}, 3s_{1/2})_1$ (the lower level of the 19.6nm and 23.6nm lines), *i.e.*, the M=0 level population is larger by 11.7% than those of the M=±1 levels. The averaged gain coefficients are assumed to be the same as that for 19.6nm. The expected polarization degree of the output laser of these J =1-2 transitions is 4%, which may be regarded consistent with the result by Rus *et al.* where the pulse duration was longer resulting in smaller velocity gradient (spatially less anisotropic) plasma formation.

References

[1] D. L. Matthews, P.L. Hagelstein, M.D. Rosen, M.J. Eckart, N.M. Ceglio, A.U. Hazi, H. Medecki, B.J. MacGowan, J.E. Trebes, B.J. Whitten, E.M. Campbell, C.W. Hatcher, A.M. Hawryluk, R.L. Kaufman, L.D. Pleasance, G. Rambach, J.H. Scofield, G. Stone and T.A. Weaver, *Phys. Rev. Lett.* **54** 110 (1985)

[2] L.B. DaSilva, J.A. Koch, D. Lehr, B.J. MacGowan and D.L. Matthews, *proc. SPIE* **2012**, 158 (1993)

[3] P.B. Holden, S.B. Healy, M.T.M. Lightbody, G.J. Pert, J.A. Plowes, A.E. Kingston, E. Robertson, C.L.S. Lewis and D. Neely, *J. Phys. B***27**, 341 (1994)

[4] J.C. Kieffer, J.P. Matte, H. Pepin, M. Chaker, Y. Beaudoin, T.W. Johnston, C.Y. Chien, S. Coe, G. Mourou and J. Dubau, Phys. Rev. Lett. **68**, 480 (1992): J.C. Kieffer, J.P. Matte, M. Chaker, Y. Beaudoin, C.Y. Chien, S. Coe, G. Mourou, J. Dubau and M.K. Inal, *Phys. Rev. E* **48** 4648 (1994)

[5] B. Rus, G.F. Cairns, P. Dhez, P. Jaegle, M.H. Key, C.L.S. Lewis, D. Neely, A.G. MacPhee, S.A. Ramsden, C.G. Smith and A. Sureau, Annual Report, **RAL**-94-042

[6] K. Murai, G. Yuan, R. Kodama, H. Daido, Y. Kato, M. Niibe, A. Miyake, M. Tsukamoto, Y. Fukuda, D. Neely and A.G. MacPhee, *Jpn. J. Appl. Phys.* **33**, L600 (1994)

[7] R. Kodama, D. Neely, Y. Kato, H. Daido, K. Murai, G. Yuan, A. G. MacPhee and C.L.S. Lewis, to be published in *Phys. Rev. Lett.*

[8] K. Murai, H. Shiraga, G. Yuan, H. Daido, H. Azuma, E. Miura, R. Kodama, M. Takagi, H. Tanabe, Y. Kato, D. Neely, D.M. O'Neill, C.L.S. Lewis and A. Djaoui, *J. Opt. Soc. Am.* (in press)
[9] H. Daido, R. Kodama, K. Murai, G. Yuan, M. Takagi, Y. Kato, I.W. Choi and C.H. Nam, to be published in *Opt. Lett.*
[10] M.C. Hettrick, J.H. Underwood, P.J. Batson and M.J. Eckart, *Appl.Opt.* **27**, 200 (1988)
[11] S. Nakayama, M. Yanagihara, M. Yamamoto, H. Kimura and T. Namioka, *Physical Scripta* **41**, 754 (1990)
[12] D. H. Sampson and H. L.Zhang, *Atomic Data &Nuclear Data Table* **41**, 1 (1989)
[13] V.I. Perel' and V.I. Rogova, *Sov. Phys. JETP* **34**, 965 (1972), **38**, 501 (1974)
[14] A. Hishikawa, T. Fujimoto and P. Erman, *Phys. Rev.A* (submitted)
[15] H. Takabe, Laser and Particle Beams, to be published.
[16] A. Hirabayashi, Y. Nambu, M. Hasuo, and T. Fujimoto, *Phys. Rev. A* **37**, 83 (1988)
[17] H.R. Griem, *Proc. 9th Int. Conference on Spectral Line Shapes*, Poland (1988)

Table 1 Relative intensities of the linearly polarized components of the 19.6nm laser line, normalized by the monitored intensity. The gain (target) length is 3cm.

energy	monitor	component	relative intensity
169 J	7.3	parallel	1
171 J	7.4	perpendicular	3.3
164 J	7.1	45 degree	1.9
187 J	15.3	parallel	4.1
195 J	14.9	perpendicular	6.0

Figure Captions

Fig. 1. Energy level diagram of the neon-like germanium ions.

Fig. 2. Experimental set up. Nd: glass laser irradiates along the z-direction a slab target and the 19.6nm line is amplified along the *y*-direction. M1: concave mirror, M2: cylindrical mirror, G: grating, P1 and P2: polarizer which can rotate around the *y*-axis for observation of the linearly polarized components of the laser output. The beam passing by the side of P1 is for intensity monitor.

Fig. 3. (a) The result of the calibration of the sensitivity of the Q-plate by use of the 18.2nm CVI (n=2-3) line. (b) The spectral intensity measured by HIREFS spectrometer with the polarizer. The parallel component is recorded stronger than that of the perpendicular component by 30%.

Fig. 4. (a) The 19.6nm laser output spectrum recorded with the polarizer removed, and its optical density at the peak, where z is the position along the z-axis. (b) Images of the polarized components and their densitometer traces, along with the accompanying monitored spectra. The units of the abscissa are μm. The densitometer scanned the portion of the spectral line indicated with the dotted line in (a).

Fig. 5. Kastler diagram for the 19.6nm laser transition and the 0.98nm resonance transition. Magnetic quantum number for each magnetic sublevel is indicated.

Fig. 6. The calculation result of the hydrodymanics simulation for the present case.

Fig. 7. The calculation result by the Monte Carlo simulation code. We treat 6×10^4 ions in it.

Fig. 8. The population imbalance among the magnetic sublevels of the 3*s* level against the ion temperature obtained by the Monte Carlo simulation.

Fig. 9. Kastler diagram for the 23.2 and 23.6nm laser transition. Magnetic quantum number for each magnetic sublevel is indicated.

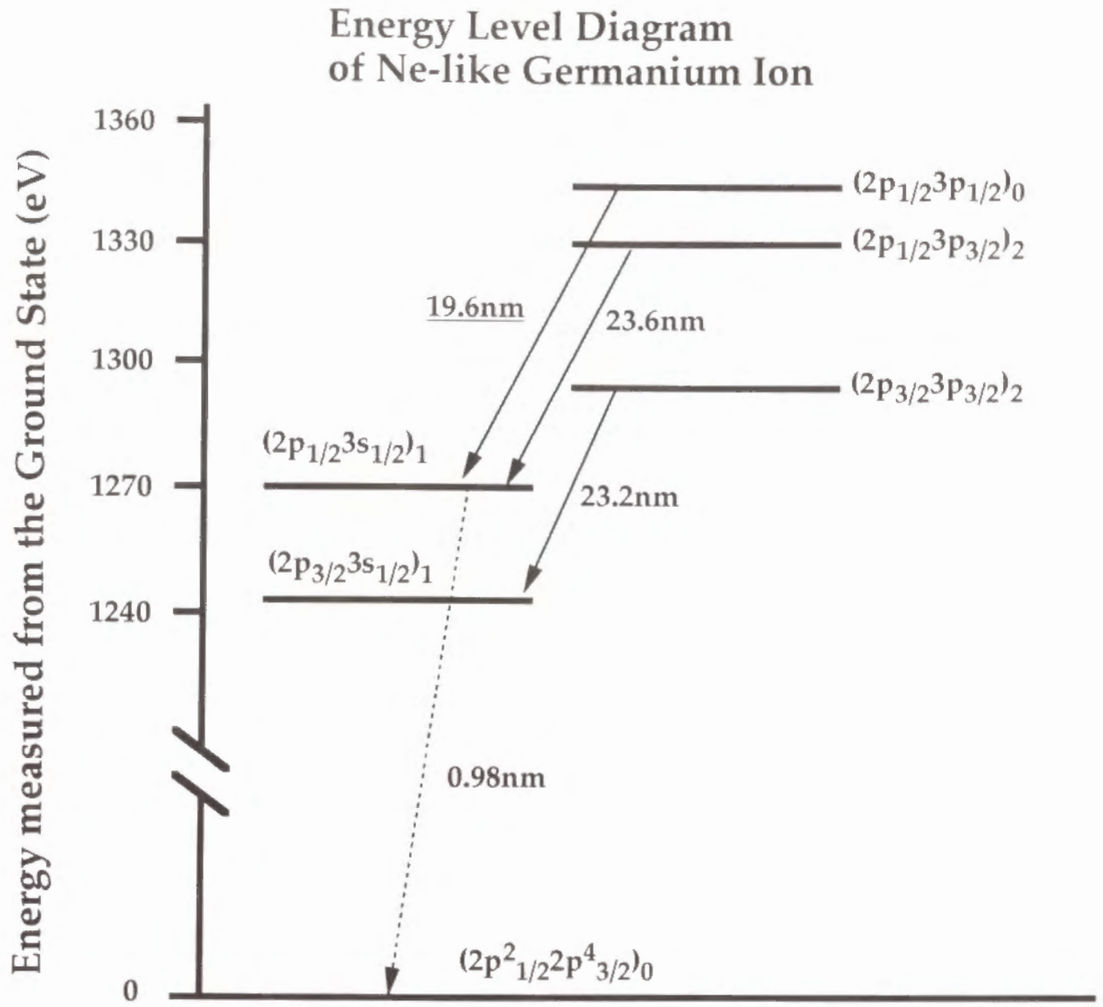

Fig. 1

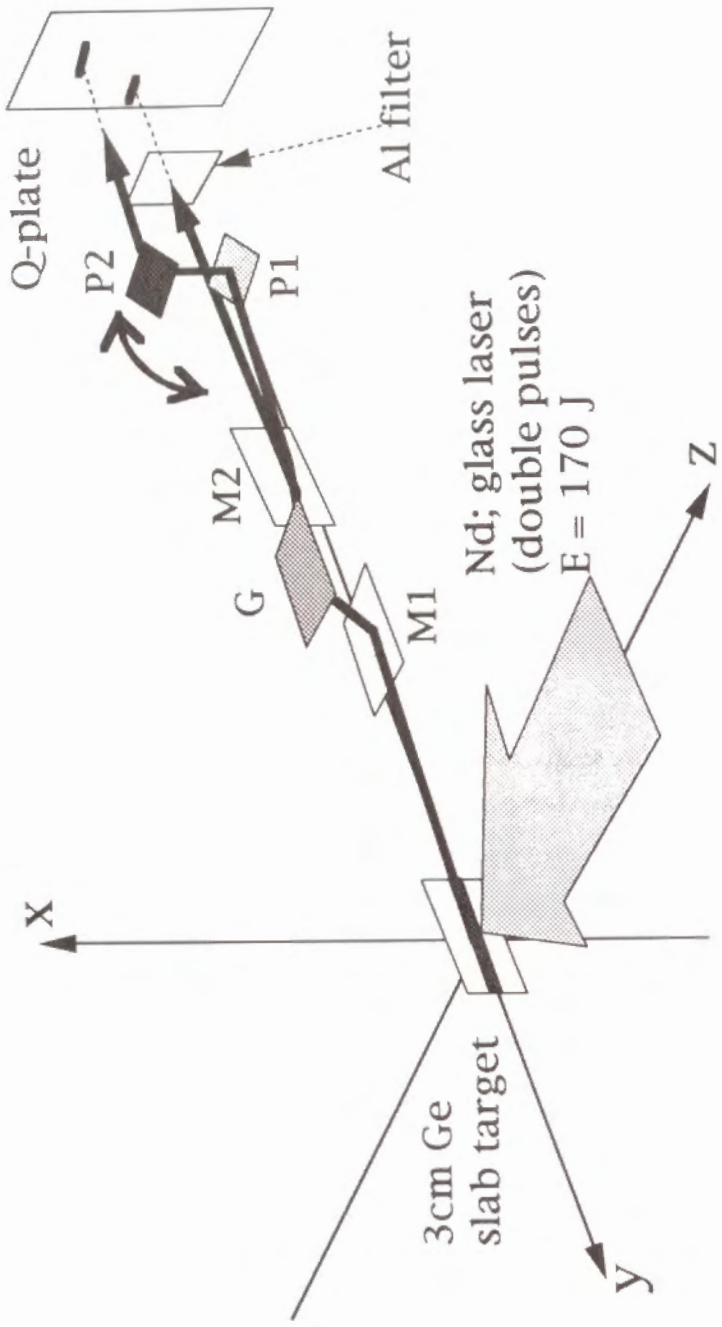

Fig. 2

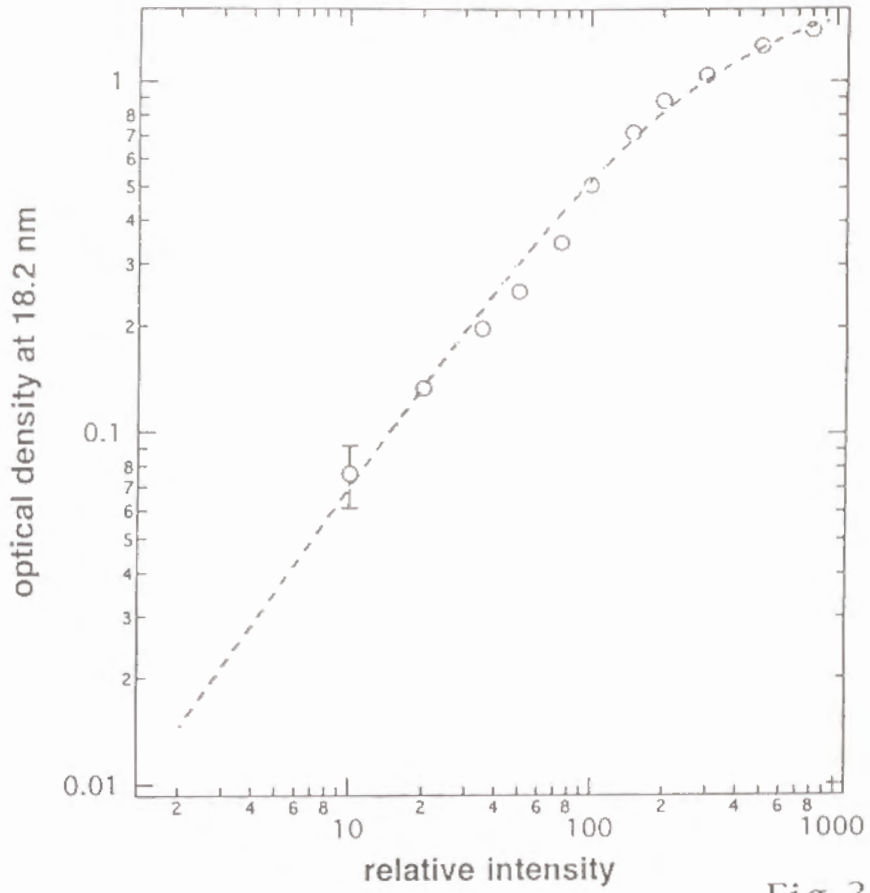

Fig.3(a)

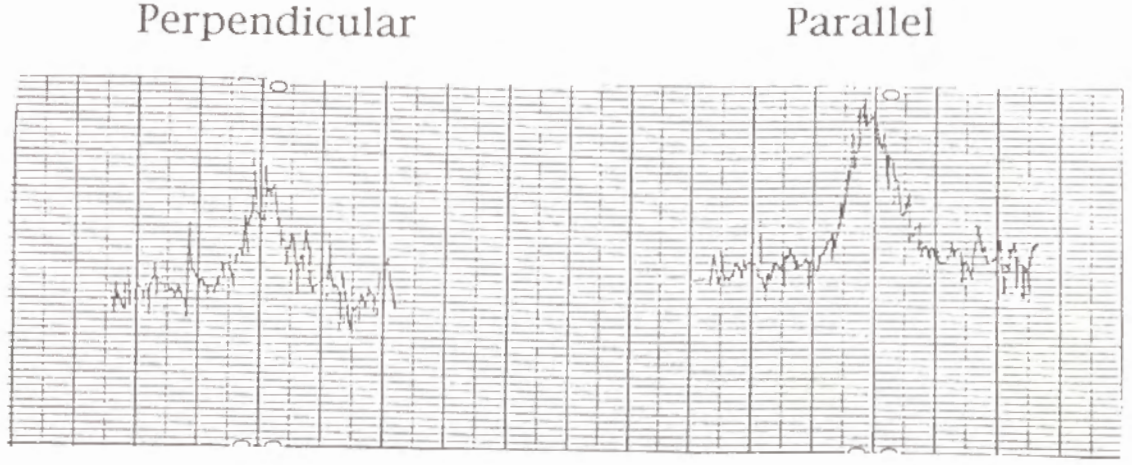

Fig.3(b)

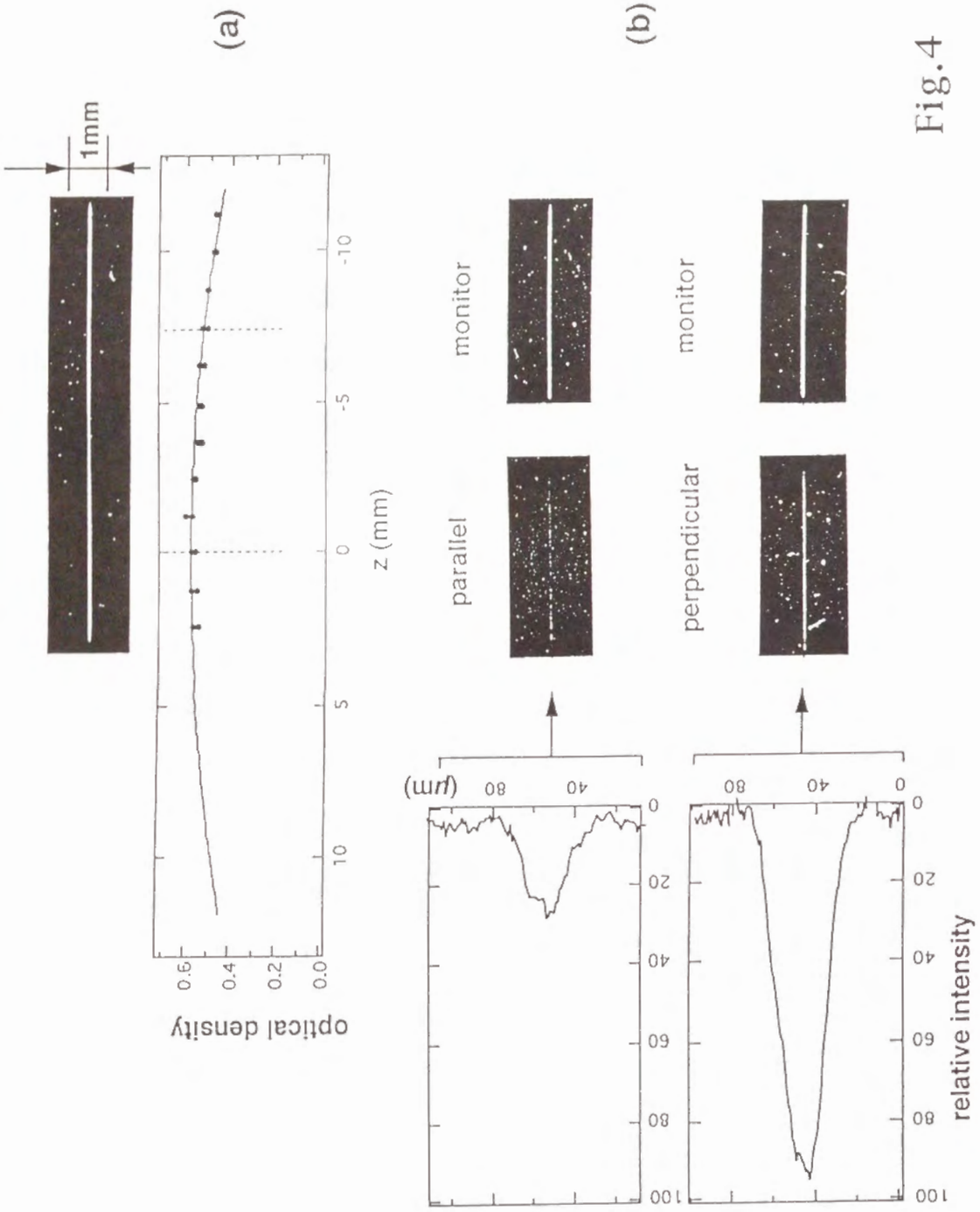
(a)
1mm
z (mm)
optical density
(b)
monitor
parallel
perpendicular
(μm)
relative intensity

Fig.4

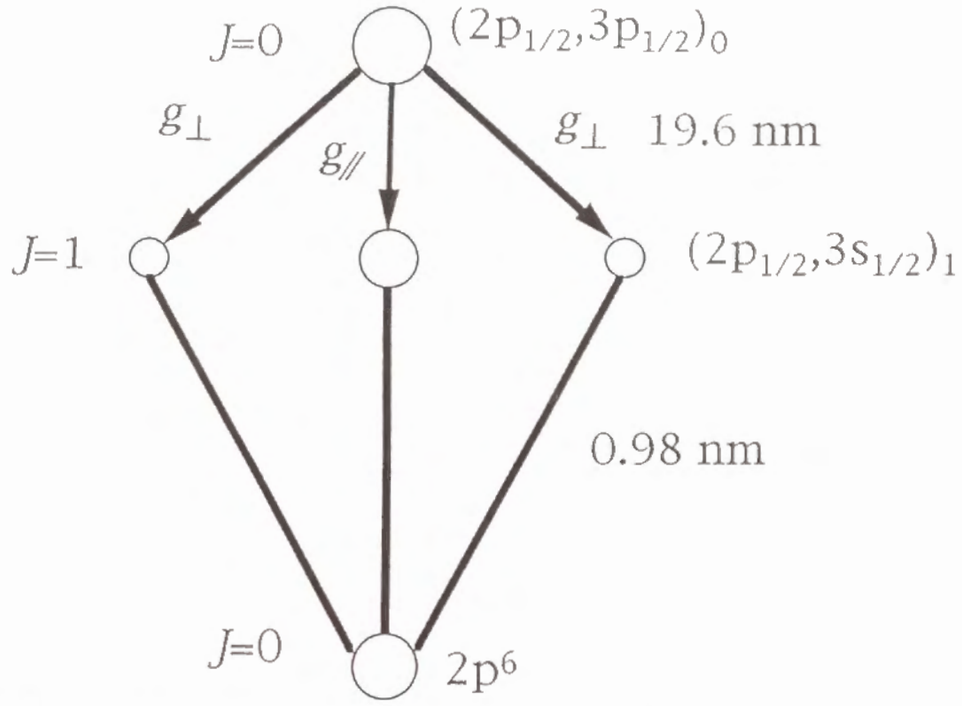
J=0
(2p1/2,3p1/2)0
g⊥
g//
g⊥ 19.6 nm
J=1
(2p1/2,3s1/2)1
0.98 nm
J=0
2p6
M = -1
0
+1

Fig. 5

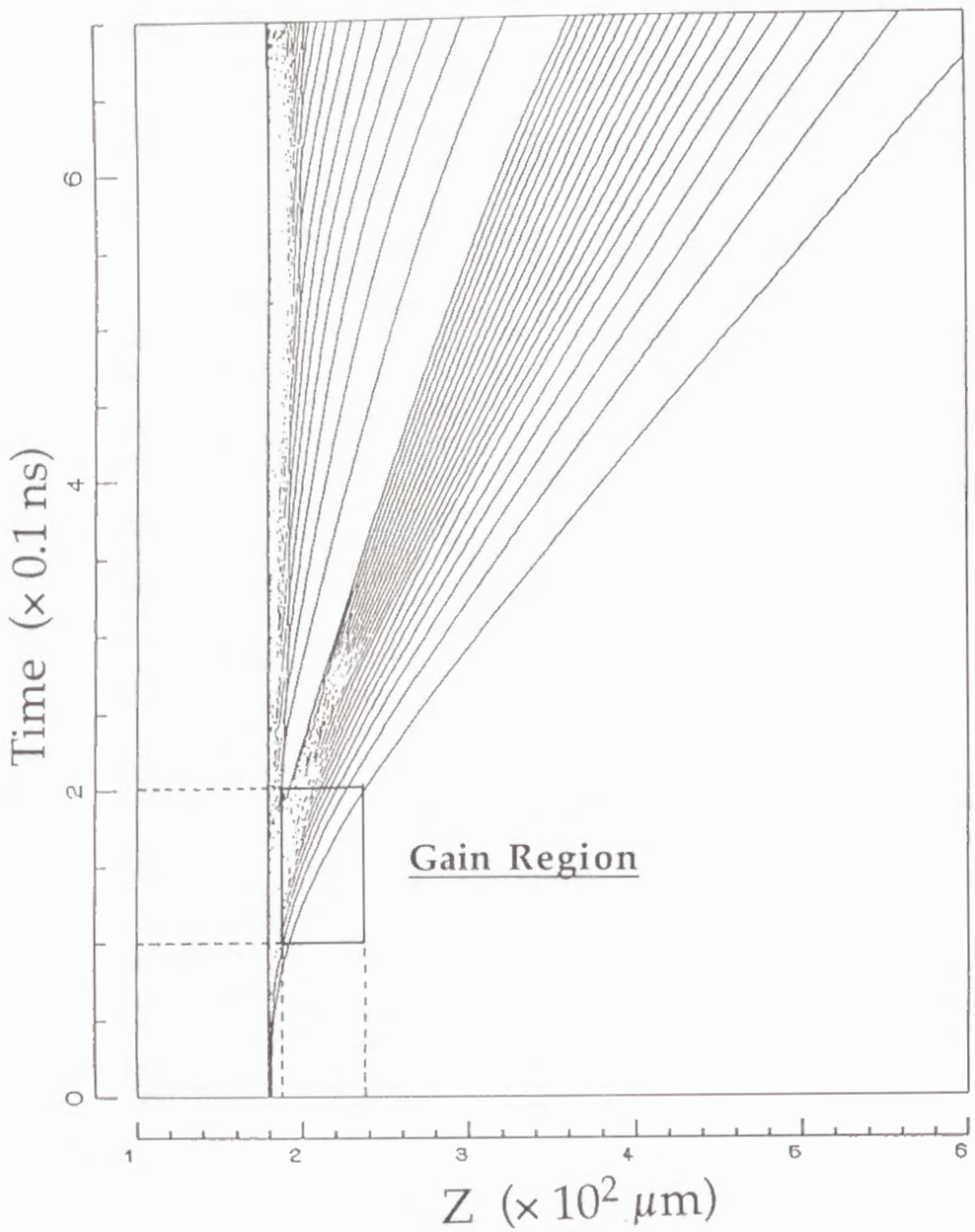
Time (× 0.1 ns)
0
2
4
6
Gain Region
1
2
3
4
5
6
Z (× 10² μm)

Fig. 6

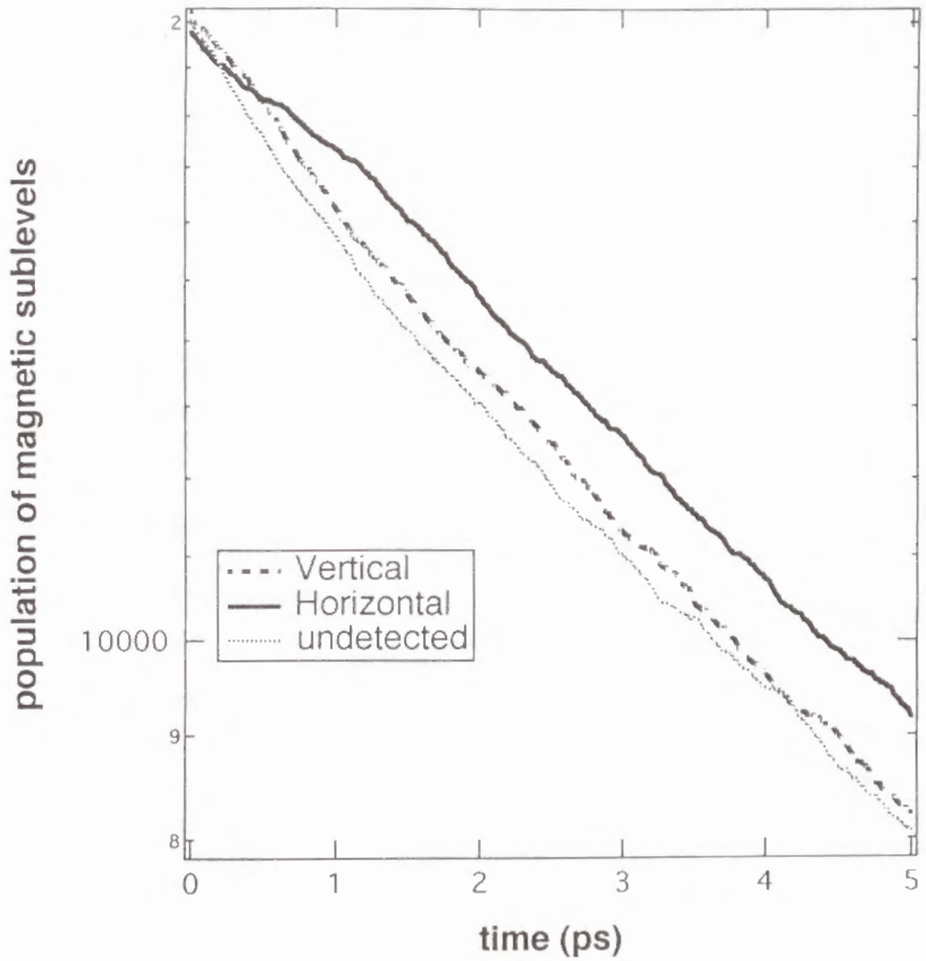
population of magnetic sublevels
2
10000
9
8
Vertical
Horizontal
undetected
0
1
2
3
4
5
time (ps)

Fig.7

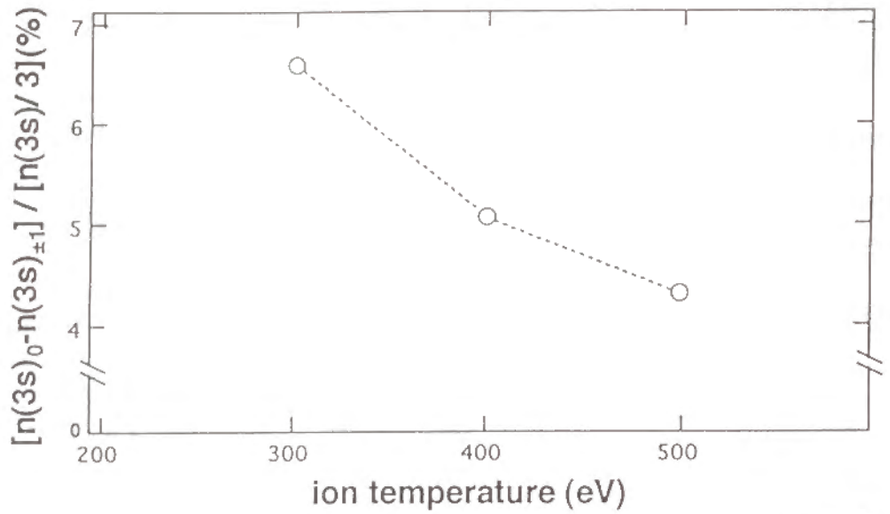

Fig.8

$(2p_{1/2}{}^3p_{3/2})_2$ or $(2p_{3/2}{}^3p_{3/2})_2$

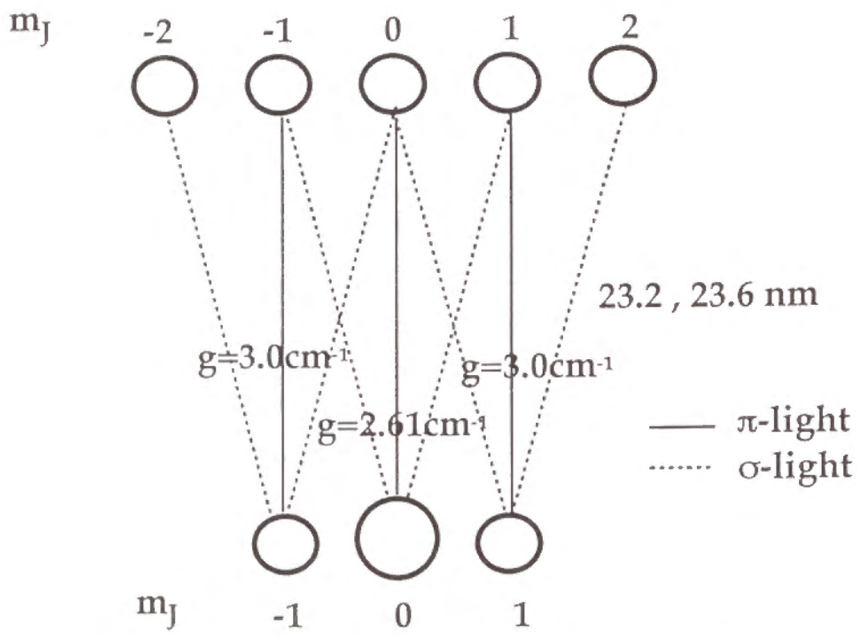

Fig.9